

UNIVERSITY OF OKLAHOMA  
GRADUATE COLLEGE

HIGH RESOLUTION SIMULATIONS OF THE MICROPHYSICS AND  
ELECTRIFICATION IN HURRICANE-LIKE VORTICES OVER WARM OCEAN  
AND AT LANDFALL.

A DISSERTATION  
SUBMITTED TO THE GRADUATE FACULTY  
in partial fulfillment of the requirements for the  
Degree of  
DOCTOR OF PHILOSOPHY

By  
ALEXANDRE OLIVIER FIERRO  
Norman, Oklahoma  
2007

UMI Number: 3291238



---

UMI Microform 3291238

Copyright 2008 by ProQuest Information and Learning Company.  
All rights reserved. This microform edition is protected against  
unauthorized copying under Title 17, United States Code.

---

ProQuest Information and Learning Company  
300 North Zeeb Road  
P.O. Box 1346  
Ann Arbor, MI 48106-1346

HIGH RESOLUTION SIMULATIONS OF THE MICROPHYSICS AND  
ELECTRIFICATION IN HURRICANE-LIKE VORTICES OVER WARM OCEAN  
AND AT LANDFALL.

A DISSERTATION APPROVED FOR THE  
SCHOOL OF METEOROLOGY

**BY:**

---

Dr. Lance Leslie

---

Dr. Evgeni Fedorovich

---

Dr. Pete J. Lamb

---

Dr. Edward Mansell

---

Dr. Bill Romanishin

©Copyright by ALEXANDRE OLIVIER FIERRO 2007  
All Rights Reserved.

## Acknowledgements

This work would not have been possible without the help and support of special individuals.

First of all, I would like to thank my advisor Dr. Lance Leslie for giving me the opportunity to complete this work through academical support. Most of all, I would like to show him my deepest appreciation for always being there when I needed and for helping me beyond my work in finding opportunities for my future career.

None of the analysis presented here would have been possible without the patience and assistance from Dr. Mansell and Dr. Straka, who provided continuous help and assistance with the model coding. I am also very thankful for their careful reviews that allowed me to better investigate the hypotheses from his earlier work and well as to express these ideas with more insight.

I would also like to thank Dr. H. Neeman and all the OSCER team (Oklahoma Supercomputing Center for Education and Research) for providing me with the computing resources and for helping me in understanding the concept of “supercomputing” and its technical aspects.

Again, I would also like to thank Dr. Fedorovich and the *Fulbright* Foundation for allowing me to be part of the SoM meteorology program here at OU.

Last but not least, I would like to show my deep appreciation to my friends and family for their continuous support.

## Table of contents

	<b>PAGE</b>
ACKNOWLEDGEMENTS	iv
LIST OF ILLUSTRATIONS	ix
ABSTRACT	xviii

## Chapter

I	INTRODUCTION	1
II	BACKGROUND	5
II.1	OVERVIEW OF TROPICAL STORMS INTERNAL STRUCTURE, DYNAMICS, AND THE FACTORS INFLUENCING ITS INTENSITY AND MOTION	5
II.1.1	TROPICAL CYCLONE DYNAMICS	5
II.1.2	TROPICAL CYCLONE FORMATION THEORIES	8
II.1.3	TROPICAL CYCLONE EYE CHARACTERISTICS AND FORMATION	12
II.1.4	TROPICAL CYCLONE RAINBANDS	15
II.1.5	MAIN EXTERNAL AN INTERNAL FACTORS INFLUENCING TROPICAL CYCLONE INTENSITY	17
II.1.6	FACTORS INFLUENCING TROPICAL CYCLONE MOTION	23
II.1.7	MAJOR CHANGES OBSERVED IN TROPICAL CYCLONE DYNAMICS AND KINEMATICS AT LANDFALL	26

II.2	PRESENT STATE OF KNOWLEDGE OF TROPICAL CYCLONE MICROPHYSICS AND ELECTRIFICATION	35
II.2.1	MODELING STUDIES OF TROPICAL CYCLONE MICROPHYSICS AND LIGHTNING	35
II.2.2	OBSERVATIONS OF CG AND IC FLASH PATTERNS IN TROPICAL CYCLONES AND THEIR RELATIONSHIPS TO STORM INTENSITY	38
II.2.3	RELATIONSHIPS BETWEEN LIGHTNING ACTIVITY, STORM DYNAMICS AND MICROPHYSICAL PROPERTIES	47
III	DESCRIPTION OF THE NUMERICAL MODEL	56
III.1	MODEL DYNAMICS	56
III.2	MODEL MICROPHYSICS	63
III.3	MODEL ELECTRIFICATION	64
IV	DESCRIPTION OF THE NUMERICAL SIMULATIONS AND THEIR RESPECTIVE INITIALIZATION PROCEDURES	66
IV.1	INTRODUCTION	66
IV.2	SQUALL LINE EXPERIMENTS SET UP	67
IV.3	HURRICANE EXPERIMENTS SET UP	74
V	NUMERICAL SIMULATIONS RESULTS	87
V.1	MARITIME TROPICAL SQUALL LINE SIMULATION	87
V.1.1	INTRODUCTION	87

V.1.2	RESULTS OF THE 600 M SQUALL LINE SIMULATION	88
V.1.3	CONCLUSIONS	105
V.2.	DEPENDENCE OF THE SIMULATED SQUALL LINE DYNAMICS, MICROPHYSICS AND ELECTRIFICATION ON THE HORIZONTAL GRID SPACING.	107
V.2.2	INTRODUCTION	107
V.2.2	RESULTS	108
V.2.3	CONCLUSIONS	129
V.3.	OCEAN EXPERIMENT	131
V.3.1	INTRODUCTION	131
V.3.2	RESULTS	132
V.3.3	CONCLUSIONS	163
V.4.	LAND EXPERIMENT	164
V.4.1	INTRODUCTION	164
V.4.2	RESULTS	166
V.4.3	CONCLUSIONS	180
V.5.	MAJOR ISSUES RAISED BY THE SIMULATIONS	181
VI	FUTURE WORK	184
VII	APPENDIX A: RECENT RESULTS FROM SIMULATIONS OF THE WEAKLY ELECTRIFIED 9 FEBRUARY 1993 TOGA COARE SQUALL LINE	189
VII.1	INTRODUCTION	189

VII.2	DESCRIPTION OF THE INITIALIZATION PROCEDURES	190
VII.3	RESULTS	193
	VII.3.1 KINEMATIC AND MICROPHYSICS EVOLUTION	193
	VII.3.2 LIGHTNING ACTIVITY AND CHARGE STRUCTURE	202
VII.4	CONCLUSIONS	215
VIII	REFERENCES	219
IX	NOMENCLATURE AND SYMBOLS USED	260

## List of illustrations

- Figure 1: Schematic of a mature TC cross section across the eyewall of precipitation processes, cloud distribution and flow structure. All symbols are explicitly described in the figure (From Black and Hallett, 1999). 6
- Figure 2: Observed radar reflectivity (panel a) and NLDN lightning composite (panel b) of Hurricane Charley, prior to landfall at 13Z, 14Z and 15Z, respectively on 13<sup>th</sup> August 2004. The legend on panel b indicates the age of the CG lightning flashes relative to the time of the scan, ranging from blue for the most recent flashes to pink for the oldest. Panels (c), (e) and (g) show time series of hourly eyewall total lightning flash rate detected by LASA (Los Alamos National Laboratory's Sferic Array) overlaid by NOAA central pressure for (c) Hurricane Katrina, (e) Hurricane Rita and (g) Hurricane Wilma as they intensified to category five status before making landfall. The plots in panels (c) and (e) and (g) were generously provided by Dr. Xuan Min Shao from the Los Alamos National Laboratory in New Mexico. The results were presented by Shao et al. in the 2006 AMS meeting in Atlanta during a poster session. Panel (d) and (f) show maps of CG flashes detected by the National Lightning Detection Network (NLDN) for an hour time period for (d) Hurricane Katrina and (f) Rita, on August 28<sup>th</sup> and September 21<sup>st</sup>, respectively. 42
- Figure 3: Skew-T log-p diagram of the 22<sup>nd</sup> February 1993 squall line case, from Honiara, Guadalcanal interpolated to the model grid. 71
- Figure 4: Sketch of the land/coast position and orientation at  $t = 1600$  min for the second simulation of the LAND experiment. 76
- Figure 5: (a) Gardiner et al (1985) NI scheme critical curve diagram adapted by Ziegler et al. (1991). The charging sign acquired by graupel particles colliding with ice crystals is shown by + and -, respectively. (b) Original Saunders and Peck (1998) For this scheme, there is no charging at temperature colder than -32.5 °C, (indicated by the grey dashed line and the 0). In the Gardiner et al. scheme, graupel is not allowed to gain charges below the line of constant values of  $q_c = 0.001 \text{ g kg}^{-1}$ . 78
- Figure 6: (a) Horizontal cross section of the initial wind vector field overlaid by the initial wind speeds at  $z = 1.028$  km and (b) vertical cross section ( $X-Z$ ) at  $Y = 300$  km of the initial wind speed. The wind speed scale is shown at the bottom of both panel (b). 81
- Figure 7: Original (modified) composite Skew-T log-p diagrams (shown in thick black (green) lines for original (modified) sounding) of the 13<sup>th</sup> August 2004, 00 UTC Owen Roberts airport, Grand Caiman Island and 00 UTC Kingston, Jamaica. 85

Figure 8: Horizontal cross section of radar reflectivity (dBZ) at  $z = 1,033$  km AGL shown for each hour of the simulation. Contours are ranging from 5 dBZ to 75 dBZ by increments of 5 dBZ. Locations of CG lightning strikes are also shown by a cross for -CG flashes and by a + for +CG flashes. The flash locations were plotted for a 30 min time interval until the cross section time. The black contour represents -1 K potential temperature perturbation at 50 m AGL, which depicts the cold pool near the surface. The horizontal thick black lines indicated by the grey arrows illustrate the location of the line averaging in Figs. 10c, d. 89

Figure 9: Horizontal cross section of the storm relative wind vector field at  $z = 50$  m AGL (a) at  $t = 10995$  s and (b) at  $t = 19995$  s. Panels (c) and (d) are as in (a) and (b) at  $z = 3.2$  km. Light red filled contours show vertical winds exceeding  $2 \text{ m s}^{-1}$  at  $z = 2$  km AGL. Light (dark) blue filled contours show wind speeds exceeding 5 (10)  $\text{m s}^{-1}$ . Because the density of wind vector is 1 out of 10, the maximum wind speed shown in the upper left corner of the panel does not exactly match the maximum magnitude of the wind vector. 92

Figure 10: Vertical cross section of radar reflectivity (in dBZ) at (a)  $Y = 105$  km at  $t = 10995$  s and (b)  $Y = 87.6$  km at  $t = 19995$  s. The quasi horizontal thin black lines in panels (a) and (b) show isotherms of 0, -10 and -20°C. The black contour depicts the cloud boundary ( $0.1 \text{ g kg}^{-1}$  which is the sum of cloud mixing ratio, snow mixing ratio, cloud ice mixing ratio and pristine ice mixing ratio). Similarly, line average reflectivity between  $Y = 60$  km and  $Y = 120$  km in the X-Z plane are shown at (c)  $t = 10995$  s and (d)  $t = 19995$  s. This line averaging consists of adding all the reflectivity values greater than a minimum threshold value (here set to 1) along the X or Y axis and then divide this sum by the number of grid points along this X / Y axis where the reflectivity values are greater or equal than this threshold. 94

Figure 11: Panels (a) and (b) are as in Figs. 10c and 10d for vertical wind in  $\text{m s}^{-1}$ . The threshold values for averaging the positive (negative) vertical velocities is  $0.1 \text{ m s}^{-1}$  ( $-0.1 \text{ m s}^{-1}$ ). Legends for shadings are shown in panel (a). The next to panels show vertical cross sections of vertical wind (in  $\text{m s}^{-1}$ ) and wind field vector (density of 1 out of 4) at (c)  $Y = 105$  km at  $t = 10995$  s and (d)  $Y = 87.6$  km at  $t = 19995$  s. Legend for vertical wind speed is shown below the panels and the scale for the wind vector is shown in the upper right corner of panel (c) and (d). 96

Figure 12: Panels (a) and (b) are as in Figs. 11a and 11b except for the line-averaged total graupel (sum of three categories) mixing ratio ( $\text{g kg}^{-1}$ ), line-averaged snow mixing ratio ( $\text{g kg}^{-1}$ ), cloud water content (CWC) in  $\text{g m}^{-3}$ . See legends below panels (a) and (b) for contours and shadings. The threshold values for averaging the total graupel mixing ratio, CWC and snow mixing ratio are  $0.1 \text{ g kg}^{-1}$ ,  $0.05 \text{ g m}^{-3}$  and  $0.05 \text{ g kg}^{-1}$ , respectively. The line-averaged visible cloud contour (which is the sum of cloud mixing ratio, snow mixing ratio,

cloud ice mixing ratio and pristine ice mixing ratio) of  $0.1 \text{ g kg}^{-1}$  is also shown. Panels (c) and (d) are as in Fig. 11c and 11d, except for snow mixing ratio ( $\text{g kg}^{-1}$ ), graupel mixing ratio ( $\text{g kg}^{-1}$ ), hail mixing ratio ( $\text{g kg}^{-1}$ ), rain mixing ratio ( $\text{g kg}^{-1}$ ) and potential temperature perturbation (K). The total graupel mixing ratio contours are plotted from  $0.5 \text{ g kg}^{-1}$  by increments of  $1 \text{ g kg}^{-1}$ . 98

Figure 13: Panels (a) and (b) are as in Figs. 9a and 9b but for the net amount of charge in  $\text{nC m}^{-3}$ . Legends for shadings and contours are shown below the figure. 101

Figure 14: As in Figs. 11a and 11b but for the total amount of positive and negative leader segments and lightning initiation locations. Light (dark) blue contour shows regions having more than 1 (10) negative leader segments. The same holds for the red contours. The leaders were summed for a time period of 10 min until the time of the cross section. The  $-1\text{K}$  ( $-2\text{K}$ ) perturbation temperature contours are also shown in a dark grey (black) line. 104

Figure 15: As in Fig. 8 for (a) the 300 m run, (b) 600 m run, (c) 1 km run and (d) the 2 km run. Note that the cross section time in panels (b), (c) and (d) are shown for  $t = 19995 \text{ s}$  while in panel (a) it is shown for  $t = 10998 \text{ s}$ . The flash locations were plotted for a 30 min time interval prior to the cross section time. The thick horizontal black lines and the grey arrows have the same meaning than in Fig. 8. Note that for all four panels, the longer thick marks on the  $X$  and  $Y$  axis represent a distance of 30 km. 109

Figure 16: As in Fig. 15 but for the line average of radar reflectivity (in dBZ) except with a threshold of 0 dBZ. This was done to eliminate the presence of isolated reflectivity maxima because, for the analysis in this section, we wish to establish a comparison of the main structure of squall line reflectivity profile. The averaging was performed in different portion of the line in a 30 km strip in the  $Y$  direction for all four cases. Details behind the averaging procedure are described in Fig. 10. For purpose of comparison, the thick marks in the  $Y$  axis represent a distance of 30 km for all cases. 111

Figure 17: As in Fig. 16, but for the total graupel mixing ratio ( $\text{g kg}^{-1}$ ), total liquid water ( $\text{g kg}^{-1}$ ) and vertical wind ( $\text{m s}^{-1}$ ). Shading and legends for the respective contours are shown at the bottom of the figure. The threshold value for the vertical wind and the graupel mixing ratio averaging was set to  $(+/-) 0.1 \text{ m s}^{-1}$  and  $0.1 \text{ g kg}^{-1}$ , respectively. For the total liquid water mixing ratio, the averaging threshold was set to  $0 \text{ g kg}^{-1}$ . Positive and negative values of vertical winds were summed separately in order to avoid unwanted cancellation. 113

Figure 18: Time series of 5-min IC and CG flash rate for the entire simulation for (a) the 600 m run, (b) 1 km run and (c) the 2 km run. The light gray (black) bars are

for – (+) CG flashes, respectively and the thin black line for IC flashes.

118

Figure 19: As in Fig. 17, but for the line-averaged total net space charge (in  $\text{nC m}^{-3}$ ). Light (dark) red shaded area show where positive net space charge exceeds  $1 \times 10^{-2}$  ( $0.1 \text{ nC m}^{-3}$ ). Likewise, light (dark) blue shaded area show where negative net space charge exceeds  $1 \times 10^{-2}$  ( $0.1 \text{ nC m}^{-3}$ ), respectively. The positive and negative values of net space charge were summed along the  $Y$  axis regardless of the sign of charge. This was done in order to still obtain an average of the *net* amount of charge across the line. The thick black line represents the line average visible cloud mixing ratio of  $0.1 \text{ g kg}^{-1}$ . 120

Figure 20: Time-height contour plot across the entire domain of the total updraft mass flux ( $\text{kg m s}^{-1}$ , in red shown for  $10^9$  contour only), rain mass ( $\text{kg}$ , blue shown for  $10^{10}$  contour only) and total graupel volume ( $\text{km}^3$ , with the 50, 100, 200 and  $400 \text{ km}^3$  shown in light gray to darker gray) for (a) 600 m run, (b) 1 km run and (c) the 2 km run. 122

Figure 21: As in Fig. 17 for the square root of the subgrid turbulence kinetic energy (TKE, in  $\text{m}^2 \text{ s}^{-2}$ ). We plotted the square root of TKE, because as mentioned in section III.1, the model predicts the square root of TKE rather than TKE. Moreover, the qualitative aspect of these plots won't be affected by this scaling. 125

Figure 22: Vertical cross section across the line in the  $X$ - $Z$  plane of equivalent potential temperature ( $\theta_e$ ) at  $t = 10998 \text{ s}$  for (a) the 300 m run at  $Y = 45 \text{ km}$ , and at  $t = 19995 \text{ s}$  for (b) the 600 m run at  $Y = 87.6 \text{ km}$ , (c) the 1 km run at  $Y = 90 \text{ km}$  and (d) the 2 km run at  $Y = 120 \text{ km}$ . 128

Figure 23: Horizontal cross sections of radar reflectivity at  $z = 1.028 \text{ km AGL}$  showing the time evolution of the TC in the model. 134

Figure 24: Time series for the first 27 h of simulation of (a) pressure at  $z = 100 \text{ m AGL}$  and (b) for the 1-min +CG, -CG and IC flash rate across the whole domain. 135

Figure 25: Horizontal cross of (a) perturbation pressure in mb at 100 m AGL and (b) vertical vorticity ( $\times 1000 \text{ s}^{-1}$ ) at  $t = 1300 \text{ min}$ . In panel (a), green contours range from 0 to -20 mb by increments of 4 mb. In a similar manner, light (dark) red contours range from -24 to -40 (-44 mb) by increments of 4 mb. For panel (b), the legend for the vertical vorticity magnitude is shown below the  $X$  axis. 138

Figure 26: (a) Vertical cross section in the  $Y$  direction at  $X = 326 \text{ km}$  of cloud mixing ratio ( $0.1 \text{ g kg}^{-1}$  contour in thick black line) and perturbation potential temperature (from initial base state). Panel (b) is as panel (a) for equivalent

potential temperature (indicated by shading). Note that the maximum altitude on the vertical axis goes until 18 km instead of 20 km for all the remaining model cross sections shown in this study. 139

Figure 27: Horizontal cross section of radar reflectivity (dBZ) at  $t = 1300$  min and  $z = 1.028$  km. Shading indicates reflectivity in 5 dBZ increments from 5 dBZ to 75 dBZ. Locations of CG lightning strikes are also shown by a cross for -CG flashes and by a + for +CG flashes. The flash locations were plotted for a 30 minutes interval up to the cross section time. A black line shows the location of the vertical cross section of the majority of the plots shown in this study. 141

Figure 28: (a) Vertical cross section at  $Y = 340$  km of and (c) horizontal cross section at  $z = 1.028$  km of the  $Y$ -component of the wind. Both panels (a) and (b) are shown for  $t = 1300$  min. As in Fig. 9, the maximum vector magnitude is smaller than the maximum windspeed because the density of the vector field is 1 out of 10. Panels (b) shows a cross section of the tangential winds (in  $\text{m s}^{-1}$ ) from a P-3 aircraft reconnaissance of Hurricane Katrina (2005) near 1800 Z and panel (d) shows interpolated horizontal winds (in knots) at the surface from various data sources. Images in panel (b) and (d) are courtesy of <http://www.aoml.noaa.gov/hrd>. 144

Figure 29: (a) Radar reflectivity in the vertical cross section across the eyewall in at  $X = 326$  km. Shading are as in Fig. 27. Panel (a) only shows a section of the total  $Y$  domain distance from 200 km to 500 km. The quasi-horizontal thin black lines represent isotherms at 0, -10 and -20°C, which depicts part of the mixed-phase region in which most of NI charging occurs. The thick black contours are for cloud mixing ratio of  $0.1 \text{ g kg}^{-1}$  which depicts the cloud boundary. Panel (b) shows radar reflectivity from a NASA ER-2 Doppler Radar (EDOP) overflight of Hurricane Emily on the 17<sup>th</sup> of July 2005 between 8h33-8h57 Z when the hurricane was a category 4. The data were collected by the EDOP during the Tropical Cloud Systems and Processes (TCSP) field program in 2005. Panel (c) shows another cross section of radar reflectivity from P-3 aircraft reconnaissance of Hurricane Katrina (2005) near 1800 Z. Image courtesy of <http://www.aoml.noaa.gov/hrd>. The flight level was near 3 km AGL, and hence reflectivity values below that level are considerably attenuated, while above that level an offset of 8 dBZ needs to be added to the computed reflectivity values (Dr. John Gamache, personal communication, 2006). 146

Figure 30: (a) Vertical winds indicated by shading in a horizontal cross section at  $z = 6.1$  km just above the melting level, and (b) a vertical cross section through the eye at the same location as in Fig. 29a. The thick black contours and thin black lines in panel (a) have the same meaning as in Fig. 29a. Panel (c) shows P-3 aircraft vertical wind observations across one side of the eyewall of Hurricane Katrina (2005) taken on the 28<sup>th</sup> of August 2005 near 1800 Z.

Image courtesy of <http://www.aoml.noaa.gov/hrd>. Legends for vertical winds magnitude are shown below each panel. 152

Figure 31: Horizontal cross-section at  $z = 1.028$  km AGL of horizontal convergence (red) and horizontal divergence (blue) at  $t = 1300$  min. 154

Figure 32: Vertical cross sections in the  $Y$  direction at  $X = 326$  km and  $t = 1300$  min for snow mixing ratio, total hail mixing ratio, total graupel mixing ratio and cloud water content (CWC in  $\text{g m}^{-3}$ ). Total mixing ratios are the sum of the mixing ratios of all the graupel (low, medium, and heavy density) and hail (small, large) categories. The thick black line depicts the cloud boundary ( $0.1 \text{ g kg}^{-1}$  cloud mixing ratio). The scale of shading for CWC is shown in the legend below the figure. Red (orange) contours show regions of the storm where the total graupel (hail) mixing ratio exceeds  $0.5 \text{ g kg}^{-1}$  in increments of  $1 \text{ g kg}^{-1}$  ( $0.2 \text{ g kg}^{-1}$ ). Light (dark) blue-filled shading shows snow mixing ratios greater than  $0.1 \text{ g kg}^{-1}$  ( $0.5 \text{ g kg}^{-1}$ ). 155

Figure 33: As in Fig. 32 but for cloud mixing ratio  $> 0.1 \text{ g kg}^{-1}$  (grey shaded area) and positive (negative) leader segments in red (blue) contours. Light (dark) blue contours show regions having more than 1 (20) negative leader segments. The same convention holds for red contours and positive leader segments. Thick black contours show locations having more than one flash initiation. Total flashes are plotted for a period of 30 minutes prior to the cross section time. 157

Figure 34: As in Fig. 32 but for the net total amount of net charge in  $\text{nC m}^{-3}$ . Light (dark) red filled contours show region where net charge exceeds  $4 \times 10^{-2}$  ( $0.4 \text{ nC m}^{-3}$ ). Likewise light (dark) blue filled contours shows where negative net charge magnitudes exceed  $4 \times 10^{-2}$  ( $0.4 \text{ nC m}^{-3}$ ). 158

Figure 35: As in Fig. 32 but for (a) total non-inductive and (b) total inductive charging rate in  $\text{pC m}^{-3} \text{ s}^{-1}$ . Positive (negative) contours are shown by the red (blue) contours in increments of  $2 \text{ pC m}^{-3} \text{ s}^{-1}$  starting at  $1 \text{ pC m}^{-3} \text{ s}^{-1}$ . Light to darker grey filled contours shows total graupel mixing ratio (see legend). 167

Figure 36: As in Fig. 24. The blue (red) line represents the land (no-land) case. 168

Figure 37: Vertical cross section (in  $X$ - $Z$  direction) at  $t = 1600$  min of perturbation pressure (in mb) for (a) the no-land and (b) land case. Panels (c) and (d) show the same field as in panels (a) and (b), except in the  $X$ - $Y$  direction. Green contours range from 0 to  $-20$  mb by increments of 4 mb. Likewise, light (dark) red contours range from  $-24$  to  $-40$  ( $-44$  to  $-52$  mb) by increments of 4 mb. 165

Figure 38: Vertical cross sections at  $Y = 339$  km of the  $V$ -component of the wind (in  $\text{m s}^{-1}$ ) for (a) the no-land case and (b) the land case. Panels (c) and (d) are as in

panels (a) and (b), except in the X-Y plane at  $z = 1.028$  km AGL. Shading legend for the wind speed scale is shown below. 169

Figure 39: As in Fig. 27 at  $t = 1600$  min for (a) the no-land case and (b) the land case. The flash locations were plotted for a 1 h 40 min time interval from the figure's cross section time. 172

Figure 40: As in Fig. 29a at  $t = 1600$  min for (a) the no-land case and (b) land case. 173

Figure 41: As in Figs. 38a and 38b but for CWC ( $\text{g m}^{-3}$ ), snow mixing ratio, total hail mixing ratio and total graupel mixing ratio. CWC is shown in grey shading with corresponding scale shown by the legend below the panel. Green (yellow) contours depict regions of the storm where the total graupel (hail) mixing ratio exceeds  $0.5 \text{ g kg}^{-1}$  ( $0.2 \text{ g kg}^{-1}$ ). Light (dark) blue-filled area shows snow mixing ratios greater than  $0.1 \text{ g kg}^{-1}$  ( $0.5 \text{ g kg}^{-1}$ ). 174

Figure 42: As in Figs. 38a and 38b but for the cloud mixing ratio ( $\text{g kg}^{-1}$  grey shaded area) and positive (negative) leader segments in red (blue) contours. The leader contours starts at 1 by increments of 10. Yellow contours show flash initiation locations greater than 1. The leader contours represent the total amount of leaders horizontally integrated for a time period of 1 h 40 min until the cross section time. This explains why a few leader contours are found outside the cloudy region. 175

Figure 43: As in Fig. 34 for (a) the no-land case and (b) the land case. 176

Figure 44: Time-height plot of the horizontally integrated IC and +/-CG flashes across the entire domain for the first 28 h of simulation for (a) the no-land case and (b) the land case. The time at which the landmass starts to enter the domain is indicated by a vertical light grey line in panel (b). 177

Figure 45: As in Fig. 44 for the total updraft mass flux (in  $\text{kg m s}^{-1}$ , in red shown for  $10^{10}$  contour only), rain mass (in kg, blue shown for  $10^{10}$  contour only) and total graupel volume (in  $\text{km}^3$ , see legend below panel b). Note that the  $8000 \text{ km}^3$  graupel volume contour is shown in a thicker green contour than for  $4000 \text{ km}^3$ . The thick dotted black line in panel (b) has the same meaning than the grey line in Fig. 44b. 179

Figure A1: Original (modified) Skew-T log-p diagrams of the 9 February 1993 R/V *Vickers* squall line case shown in the black (grey) thick line. Sounding data courtesy of the Earth Observing Laboratory, National Center of Atmospheric Research (NCAR). 191

Figure A2: Horizontal cross section of radar reflectivity (dBZ) at  $z = 1,033$  km AGL shown for (a)  $t = 1$  h 30 min, (b) 2 h 30 min, (c) 3 h 30 min and (d) 4 h 30

min. Contours range from 5 dBZ to 75 dBZ by increments of 5 dBZ. The flash locations were plotted for a 20 min time interval until the cross section time. Locations of -CG lightning strikes are also shown by a cross (Note that no +CG flashes were produced in the time frame for each plots). The black contour represents -1 K potential temperature perturbation at the ground, which depicts the cold pool at the surface. A compass indicates the orientation of the domain and the two thin black lines denoted by a double arrow indicates the region of the line averaging in Figs. A3-A5. 194

Figure A3: Vertical cross section of line-averaged radar reflectivity (in dBZ) between (a)  $X = 90$  km and  $X = 120$  km at  $t = 3$  h 30 min and (b) between  $X = 100$  and  $X = 130$  km at  $t = 4$  h 30 min. Legend for reflectivity is shown in panel (a). The line averaging consists of adding all the reflectivity values greater than a minimum threshold value (here set to 1 dBZ) along the  $X$  or  $Y$  axis and then divide this sum by the number of grid points along this  $X / Y$  axis where the reflectivity values are greater or equal than this threshold. The horizontal thin black lines show the average locations of the 0, -10 and -20°C isotherms. The 30 dBZ contour has been highlighted in a thicker black line. Panel (c) shows ship cross sections (11h32 Z) of composite maximum radar reflectivity through the observed squall line within a box of dimensions  $(x ; y) = (30,10)$  km. Reflectivity values are displayed in increments of 6 dBZ, with reflectivity values greater than 30 dBZ shaded. The dashed line indicates approximate location of the -10°C isotherm. Panel (c) from Petersen et al. (1999), used with permission. 196

Figure A4: As in Fig. A3, for the vertical wind component in  $\text{m s}^{-1}$ . The threshold value for the averaging of the positive (negative) vertical velocities is  $0.01 \text{ m s}^{-1}$  ( $-0.01 \text{ m s}^{-1}$ ). In Panel (c), velocities are contoured every  $1 \text{ m s}^{-1}$  with values  $\geq 5 \text{ m s}^{-1}$  shaded. The  $0.01 \text{ m s}^{-1}$  contour is also shown. Panel (c) from Petersen et al. (1999), used with permission. 199

Figure A5: As in Fig. A3 for line-averaged total graupel (sum of the three categories), mixing ratio ( $\text{g kg}^{-1}$ ), line-averaged snow mixing ratio ( $\text{g kg}^{-1}$ ), and total liquid water (LW) in ( $\text{g kg}^{-1}$ ). See legends in panel (a) for contours and shadings. The threshold value for averaging the total graupel mixing ratio, LW and snow mixing ratio is  $0.01 \text{ g kg}^{-1}$ . The line-averaged visible cloud contour (which is the sum of cloud mixing ratio, snow mixing ratio, cloud ice mixing ratio and pristine ice mixing ratio) of  $0.1 \text{ g kg}^{-1}$  is also shown in a thick black line. 201

Figure A6: Time-height contour plot across the entire domain of the total updraft mass flux (in  $\text{kg m s}^{-1}$ , in black shown from  $10^9$  until  $1.5 \times 10^9$  in increments of  $10^8$ ) and total graupel volume (in  $\text{km}^3$ , with the 50, 100, 200 and  $300 \text{ km}^3$ . shown in light gray to darker gray in the legend). 203

Figure A7: Charge density in  $\text{nC m}^{-3}$  for (a)  $t = 3 \text{ h } 30 \text{ min}$  at  $X = 114 \text{ km}$  and (b)  $t = 4 \text{ h } 30 \text{ min}$  at  $X = 87 \text{ km}$ . Panels (c) and (d) are as in panels (a) and (b) show the total count of positive (black) and negative (darker grey) leader segments for a 20 min time interval prior the time of the figure. The 1, 5 and 10 contours for the total number of leaders are shown. The lighter grey shaded area depicts the cloud mixing ratio of  $0.01 \text{ g kg}^{-1}$ . See legends in panels (a) and (c) for the meaning of the remaining contours and shadings. 205

Figure A8: As in Fig. A7, for total (i.e., all ice species) non-inductive charging rate (NICR) at (a)  $t = 3 \text{ h } 30 \text{ min}$  and (b)  $t = 4 \text{ h } 30 \text{ min}$  and for total inductive charging rate at (c)  $t = 3 \text{ h } 30 \text{ min}$  and (d)  $t = 4 \text{ h } 30 \text{ min}$  (in  $\text{pC m}^{-3} \text{ s}^{-1}$ ). The contours start at  $0.1 \text{ pC m}^{-3} \text{ s}^{-1}$  and increase by increments of  $0.5 \text{ pC m}^{-3} \text{ s}^{-1}$ . Contours and shadings are indicated by the legends in panel (a). 207

Figure A9: As in Fig. A7, for total cloud ice mixing ratio (i.e., sum of columns, plates and rimed ice particles, in  $\text{g kg}^{-1}$ ), total cloud ice charge and snow particles charge (in  $\text{nC m}^{-3}$ ) at (a)  $t = 3 \text{ h } 30 \text{ min}$  at  $X = 114 \text{ km}$  and (b)  $t = 4 \text{ h } 30 \text{ min}$  at  $X = 87 \text{ km}$ . Panels (c) and (d) are as in panels (a) and (b) for total graupel charge (i.e., the sum of low, medium and high density graupel species,  $\text{nC m}^{-3}$ ) and cloud water content (CWC, in  $\text{g m}^{-3}$ ). The meaning for contour and shadings are shown in the legends in panels (a) and (c). The cloud ice charge, snow charge and graupel charge are shown by increments of  $0.1 \text{ nC m}^{-3}$  starting at  $0.1 \text{ nC m}^{-3}$ . 208

Figure A10: Time series of maximum and minimum non-inductive charging rate (NICR) and inductive charging rate (ICR) overlaid by a time series of CG flash rate and 5-minute average IC flash rate. All time series are for the entire domain. The meaning behind each curve is shown in the legend. The circles filled with a cross indicates the time at which a -CG flash occurred (note, again, that no +CG flash was generated in the simulation). The label "IC0" in the legend means it is the 5 min average IC flash rate for the simulation carried out with inductive charging turned off. 211

Figure A11: Horizontal cross sections of positive and negative leaders segments as  $z = 4.67 \text{ km AGL}$  at (a)  $t = 3 \text{ h } 30 \text{ min}$  and (b)  $t = 4 \text{ h } 30 \text{ min}$ . The thick black curves line showed the location of the gust front ( $-1 \text{ K}$  perturbation temperature). The light grey shaded area shows cloud mixing ratio of  $0.01 \text{ g kg}^{-1}$ , and the horizontal black line shows the location of the vertical cross sections of Figs. A7-A9. Legends for leaders are as in Figs. 8c-d. 215

## **Abstract**

Cloud-to-ground (CG) lightning bursts in the eyewall of mature tropical cyclones (TCs) are believed to be good indicators of imminent intensification of these systems. While numerous well-documented observational cases exist in the literature, no modeling studies of the electrification processes within TCs have been made so far. At present, little is known about the evolution of charges and subsequent electrification in mature TCs. Towards this goal, a numerical cloud model featuring a 12-class bulk microphysics scheme and a three-dimensional branched lightning module is utilized to simulate the evolution of the microphysics fields and subsequent electrical activity in an idealized hurricane like vortex over ocean (OCEAN case). In a separate experiment (LAND case), two simulations were carried out at a slightly coarser resolution. The first simulation was similar to the OCEAN case, while in the second simulation, a simplistic landmass was introduced in the domain in order to investigate the effect of reduced sensible and moisture flux and enhanced drag on the TC's dynamics, microphysics and electrification.

Before carrying out these experiments, however, it was necessary to test the reliability of the model in maritime tropical environment. For this purpose, an additional idealized high-resolution simulation of a well-documented TOGA COARE squall line case was carried out. Moreover, for a single microphysical and electrical evolution, the latter experiment was carried out at three additional horizontal grid spacings to determine how the storm's dynamical, microphysical and electrical properties responded to these changes.

The simulated tropical squall line exhibited many features consistent with observations. In particular, the updraft speeds were generally much weaker than their

continental counterparts, which was in turn consistent with relatively shallow 30 dBZ echo tops and lower content of graupel and supercooled water droplets within the mixed phase layer. This general reduction of graupel and supercooled water was partly caused by a rapid depletion of liquid water by enhanced warm rain processes ahead of the line, in agreement with previous studies. The stratiform region was almost exclusively composed of light ice crystals and snow aggregates, with discrete regions, however, containing small amounts of graupel ( $\sim 0.1\text{-}0.3 \text{ g kg}^{-1}$ ). All of these factors combined resulted in a system producing overall little lightning.

As expected, the finer grid spacing simulation showed evidence of a more turbulent and more realistic flow structure. Most importantly, the analysis revealed that the overall squall line structure and evolution exhibited significant differences between each case. In particular, it was discovered that the amount of total lightning flash rate (intra-cloud plus cloud-to-ground) increased as the grid spacing increased (i.e., as resolution decreased), because of greater graupel production from more numerous and/or wider updraft cores at coarser resolution, particularly towards the end of the simulation. Also, as the horizontal grid spacing was increased, the squall line took more time to develop and became progressively more intense at the end of the simulation. Despite these results, the model was able to reproduce the basic structure of typical squall lines, such as a well developed gust front at its leading edge followed by a mature zone and later by a trailing stratiform region characterized by weak updrafts/downdrafts. Also, the overall charge structure and charging rates profiles across the line were qualitatively similar in all cases.

In summary, despite producing quantitatively different results, the qualitative aspects of the simulated squall line dynamics, microphysics and lightning were overall similar. This suggested that the hurricane simulations presented in this study could still provide a good and useful *qualitative* insight of the storm's dynamical, microphysical and electrical properties.

Preliminary results of the OCEAN TC case showed that the highest total lightning flash rate were primarily found within the eyewall but seldom within the stronger cells forming the outer rainbands where updraft speeds rarely exceeded  $10 \text{ m s}^{-1}$  and  $15 \text{ m s}^{-1}$ , respectively, consistent with observations. As expected, these regions of the storm were generally characterized by moderate total graupel mixing ratio ( $> 0.5 \text{ g kg}^{-1}$ ) and moderate cloud water content ( $> 0.2 \text{ g kg}^{-1}$ ). Using the Saunders and Peck non-inductive (NI) charging scheme and moderate inductive charging settings, the inner eyewall region exhibited a normal tripole charge structure (a mid-level negative charge layer amidst two positive charges regions) while a normal dipole (a positive charge region atop a negative charge region at mid-levels) was observed in the outer eyewall stratiform region and in the strongest cells forming the outer rainbands. The charges forming the normal dipole in the outer eyewall were generated within the eyewall via NI charging in the mixed-phase region at mid-levels (near the  $-15^\circ\text{C}$  isotherm).

In the LAND TC experiment the landfalling storm was, as expected, much weaker (higher surface pressure, weaker winds) and less organized than the storm evolving over ocean. The weaker landfalling storm was associated with smaller eyewall total updraft mass flux and shallower echo tops (particularly 30 dBZ and greater) in turn consistent with smaller total graupel volume aloft and an overall smaller total lightning activity.

Perhaps the most interesting finding of the LAND experiment was that several +CG flashes were produced after landfall, which was not observed in the control simulation over ocean. This indicated that, as suggested by observations, there exists a qualitative difference in the storm electrical behavior after landfall, which as we showed, was directly linked to its change in kinematical and microphysical fields. Observational studies, however, showed that this difference in lightning behavior over land versus over ocean varied from case to case, and therefore could not be generalized.

## **I. Introduction**

Severe tropical cyclones (TCs) are known for their destructive power particularly as they make landfall as TCs often are accompanied by extreme winds, storm surges and torrential rainfall. Accurate forecasting of TC landfall remains the major challenge meteorologists are faced with. Millions of dollars can be lost as a result of ill-timed evacuations (Whitehead, 2003) due to inaccurate forecasts. Most importantly, the confidence of the general public is also affected by systematic issuance of false alarms, which in a long term could make evacuation more difficult. Hence, it is crucial to provide the most accurate forecasts days in advance to sensitize the public.

Many populated coastal regions are threatened yearly by these extreme events. In particular the regions along the Gulf of Mexico, the islands of the Caribbean Sea, the southeastern United States, northwestern and eastern Mexico, the island of Taiwan, Philippines, Japan, Madagascar, the southern portion of Bangladesh and the northern coast of Australia. The 2004 and 2005 seasons have been particularly active in the Atlantic basin: The 2004 Atlantic hurricane season was described as “one of the most devastating on record” (Franklin et al. 2006), particularly given the loss of about 3000 lives in Haiti caused by extreme rainfall and mud slides resulting from intense deforestation as Hurricane Jeanne crossed the island (Lawrence and Cobb, 2005). Elsewhere a record ten typhoons affected southern Japan during the 2004 season (Kim et al. 2005). From its part, the 2005 hurricane season had the largest number of TC ever recorded on the Atlantic basin (28 TCs and subtropical storms formed, of which 15 became hurricanes), with the greatest number of category 5 storms (total of four, source:

<http://www.noaanews.noaa.gov/>). In particular, Hurricane Katrina made landfall as a category 4 storm in the Louisiana/Alabama coast on September 1, 2005, resulting more than 80 billions of dollars worth of damage making it the costliest hurricane and natural disaster on record in the US history together with an official death toll already exceeding 1800 people (Knabb et al. 2005).

Following these two unusually active seasons, many journal articles have been published in the last 2 years, about the possible links existing between this increase in hurricane activity and global warming (e.g., Emanuel 2005; Landsea 2005; Webster et al. 2005; Curry et al. 2006; Hoyos et al. 2006). This topic has fueled many debates and still raises many controversies, which are concisely summarized in an article by Curry et al. (2006). The role of the media in "promoting rather than reporting the work" and for "often looking for conflict or for an artificial balance in reporting on science issues", definitely shows its importance as most of the time they are the only direct link existing between the widely ignorant public and the scientists.

Probably one of the most cited study on this subject is the one conducted by Webster et al. (2005). They showed that, *globally*, although the total number of hurricanes dropped since the 1990s, the number of category 4 and 5 hurricanes worldwide nearly doubled over the past 35 years. They also found that this shift in category 4 and 5 numbers was correlated with a global sea surface temperatures increase over the same period. Dr. Curry, chair of the School of Earth and Atmospheric Sciences at Georgia Tech and coauthor of the study also stated that "category 4 and 5 hurricanes made up about 20% of all hurricanes in the 1970s, but over the last decade they accounted for about 35% of these storms." Despite this result, they found that the number

of TCs and TC days in all basins have decreased during the last decade, *except* the North Atlantic. This study alone illustrates the controversial nature of the subject.

With the advent of increasingly powerful computing resources, idealized numerical studies have reproduced with success many of the main features of TCs that are observed in nature (e.g., Braun 2002; Zhu 2002). The availability of increasingly detailed observational datasets, many of which are derived from satellites, is crucial in initializing and verifying these numerical experiments (e.g., Velden 1992).

Previous modeling work has focused mostly on the large-scale processes that control TC dynamics, and have led to significant progress in these areas (e.g., Emanuel et al. 1986, 1988; Zehnder et al. 1997; Blackwell 2000; Braun 2002; Wang 2002; Zhu 2002).

In comparison, there have been relatively few modeling studies that have explored the microphysical processes in TCs (e.g., MacFarquhar 2004; Rogers et al. 2007) and none of their electrification. Thus, little is known about these two physical aspects of the TCs, though better understanding of them may help improve short-term forecasts of their potential for severe weather, both at sea and at landfall. For instance, increasing total lightning flash rates (i.e., rates of intra-cloud plus cloud-to ground lightning) indicates an increasingly large volume of graupel/small hail aloft, indicative of strengthening updrafts and an increased probability of heavier rainfall (e.g., Lhermitte and Krehbiel 1979; MacGorman et al. 1989; Wiens et al. 2005). As a consequence, several observational studies have stressed the importance of a more systematic monitoring of any change in TC lightning flash rate, particularly in the eyewall, where an increase is often

accompanied with an intensification of the storm (e.g. Lyons et al. 1989; Molinari et al. 1994).

In the present study, emphasis is placed on increasing our knowledge of the *qualitative* aspects microphysical and electrical properties of TCs, as a significant novel step in the development of the next generation of TC models. These kinds of models are a necessary part of a research effort aimed at improving model forecasts of hurricane intensity before and during landfall.

In particular, the model used herein features a microphysical package having 12 separate hydrometeor species, which is an improvement over the widely used 3-ICE schemes (e.g., Lin et al. 1983). This increase in complexity was necessary for our study, because, as we will explain in more detail in the text, the magnitude and polarity of charge is highly dependent on the differential fall speed between the colliding particles. Therefore, having more particles types allows for a broader spectrum of fall speeds and hence allows for a more realistic representation of electrical structure of the storm, which is one of the main goals of this research.

## **II. Background**

### **II.1. Overview of Tropical storms internal structure, dynamics, and the factors influencing its intensity and motion.**

#### **II.1.1 Tropical cyclone dynamics**

To a certain degree, TCs may be approximated as rotating cylinders in hydrostatic and gradient-wind balance (mutual balance between centripetal acceleration, Coriolis acceleration and pressure gradient force for circular steady axisymmetric flows), with horizontal dimensions of the order of ~1000 km and a vertical depth of the order of the troposphere (~10-15 km). As a result, TCs are synoptic scale atmospheric features with embedded mesoscale and convective components. According to Wu and Wang (2004), TCs have three main components: (1) storm scale structures (local convection within the TC); (2) the inner core region or eyewall (mesoscale) and (3) the spiral rainbands (mesoscale to synoptic scale). However, understanding the physics involved in the smaller scales, such as convective or mesoscale features, is a key towards a better comprehension of TC dynamics. A complete understanding of TC dynamics would require a detailed knowledge of the interaction between the storm circulation, the ambient wind field, the convection distribution and the surface (e.g., land, orography, oceans, lakes).

In a mature TC the rapid rotation is produced by concentration of the vertical component of absolute vorticity by vortex stretching. To a first approximation, the

tangential wind is in gradient wind balance with the radial pressure gradient force (Willoughby 1990b). Also, hydrostatic balance implies that the vertical shear of the tangential velocity is a function of the radial temperature gradient through the thermal wind balance. Since hurricanes are warm cored lows, the thermal wind balance implies that in TCs the tangential winds decrease with altitude and that consequently, the strongest winds are found in the lowest kilometer in the boundary layer (BL).

In order to understand how pressure and wind balance each other on the horizontal in a mature TC, let's look at the balances of the forces involved in different regions of the storm.

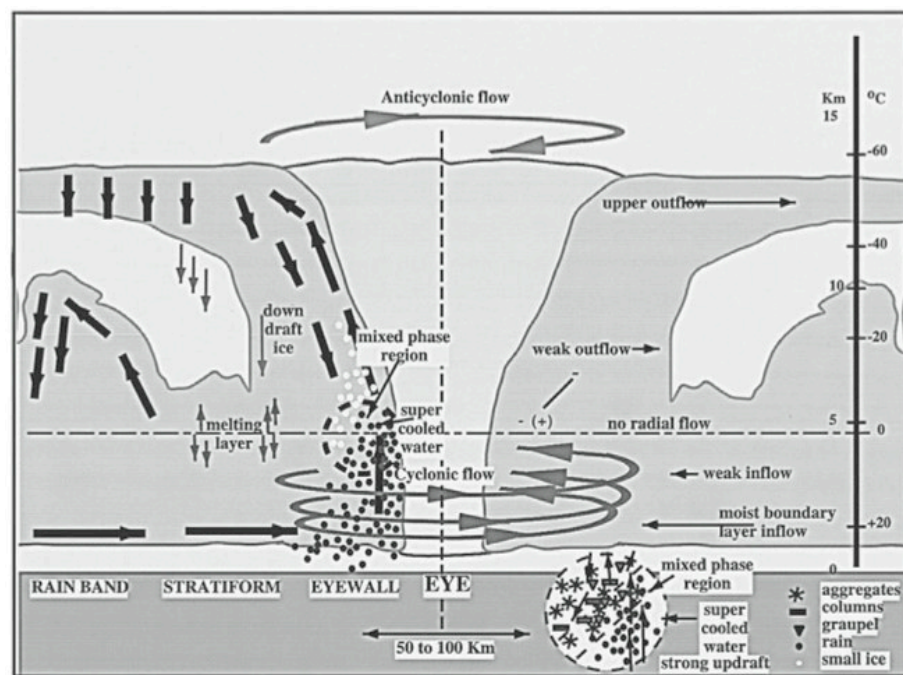


**Fig. 1.** Schematic of a mature TC cross section across the eyewall of precipitation processes, cloud distribution and flow structure. All symbols are explicitly described in the figure (From Black and Hallett, 1999).

For this analysis, let's only focus on the storm's eyewall and eye. (Fig. 1). In summary, the balances of forces occurring in a mature hurricane eyewalls are similar to that of a tornado.

The region of the vortex between approximately  $z = 1$  km (above the frictional layer) and  $z = 10$  km can be approximated as a solid body vortex in cyclostrophic balance:

$$\frac{1}{\rho} \frac{\partial p}{\partial r} = \frac{V^2}{r} \quad (1)$$

where the radial pressure gradient force (PGF) on the left hand side of (1) acts in opposite direction to the centrifugal force (on the right hand side of (1) ) that arises from the TC strong circulation. Hence, as the tangential winds ( $V$ ) increase, the radial PGF will increase as well, causing a pressure drop, which will be greater near the BL top where  $V$  is the largest (i.e.,  $z = 1$  km). This pressure drop tendency will then be transmitted to the surface (e.g., using isentropic potential vorticity (IPV) thinking).

Below the BL, additional terms have to be considered in the balance of forces: First near the surface, friction becomes important and second, one has to consider the advection of the inflowing (or radial) winds  $U$ :

$$U \frac{\partial U}{\partial r} + \frac{1}{\rho} \frac{\partial p}{\partial r} = \frac{V^2}{r} + \kappa \nabla^2 U \quad (2)$$

Near the surface,  $V$  tends to zero due to friction (no-slip boundary condition) and the radial PGF remains constant. Therefore, because of increasing friction near the surface, the advection term on the right hand side of (2) has to increase as well, leading to a cross isobaric flow converging near the radius of maximum winds underneath the TC eyewall. This inflowing air is crucial in continuously feeding the eyewall convection with BL air that has been moistened and warmed by strong surface latent heat and sensible fluxes.

As this inflowing air is forced to rise in the eyewall tilted updrafts, mass conservation near the tropopause results in strong upper level divergence (and strong anticyclonic flow) at storm top (see next section for more details).

These exceptionally low pressures in these storm systems can have non-negligible effects on environmental air that are otherwise not observed elsewhere. In particular, as an air parcel travels towards the TC center and becomes gradually exposed to lower environmental pressure, it will cool by adiabatic expansion (Gray, 1995). This cooling is so strong that the positive sensible heat flux from the underlying warm ocean is unable by itself to offset it (Gray 1995). As a result, it is often observed that ambient temperature beneath the hurricane eyewall is 3-4°C cooler than the ocean (Pudov, 1992; Black and Holland, 1995), which results in the environment within the hurricane to be more potentially stable (i.e. less CAPE) than outside.

## **II.1.2 Tropical cyclone formation theories**

On average, about 84 TCs form around the world and about two thirds of these reach severe stage (i.e., category 3 or greater, Neumann, 1993). Also, about 80-90% of the TCs form within 20° of the equator (Frank and Roundy, 2006). Zehr (1992) argued that during the formation stage of a TC, two stages needed to be considered: the genesis stage, where the storm evolves from a tropical disturbance to a named TC (winds of 15.5 m s<sup>-1</sup> and minimum sea level pressure of about 997 mb)

According to Frank and Roundy (2006), hurricane formation (i.e., genesis stage) does not require moist processes *initially*. Rather, the formation is strongly related to

enhanced activity of mixed Rossby-gravity waves, tropical depression-type or easterly waves, equatorial Rossby waves and the Madden Julian Oscillation (MJO). Furthermore they showed that each composite wave and the phase relationship between the wave and the cyclogenesis in all basins prone to hurricane formation (see their Fig. 3) was similar, suggesting consistent forcing mechanism in all these basins. All these four wave types also increased the amount of large-scale convection and low-level rotation in the region they were in. Holland (personal communication, 2005) also showed that where some of these easterly and westerly propagating waves (mixed Rossby-gravity waves and Rossby waves) reached a stagnation point (phase speed equals zero) in the Atlantic basin, sufficient amount of energy and relative vorticity can be accumulated (by looking at their respective group velocities) and trapped in the vertical, therefore setting the stage for the TC initial circulation development. Additionally, Frank and Roundy (2006) showed that the MJO and equatorial Rossby waves also produced a favorable easterly shear anomaly at the genesis location, which in turn modulated the time of TC formation within the Monsoon through (which, if unperturbed by one of these two wave types, can also eventually result in the formation of a few TCs by becoming unstable and breakdown, Wang and Frank, 1999).

Once the circulation (i.e., low-level relative vorticity) becomes strong enough (i.e.  $> 10^{-4} \text{ s}^{-1}$ , Zehr, 1992), moist processes already enhanced by the presence of these waves kick in (in particular conditional instability of the second kind or CISK), further increasing the TC intensity (intensification stage, Holland, 1993). The CISK process works as follows: once convection occurs, latent heat must be released during condensation as moist air parcels originating from the boundary layer rise into

progressively cooler and drier air above the level of free convection (LFC). This release of latent heat further warms this rising air parcel, thereby increasing the temperature gradient between the environment and the air parcel. This makes the air parcel more buoyant, which in turn result in more latent heat to be released and so on. This process, however, cannot continue indefinitely as many other factors will act to reduce the parcel's buoyancy. The most important of these factors is water loading resulting from falling raindrops within the convection cloud. Another factor reducing parcel buoyancy, is the downward directed pressure gradient force that arises from mass continuity within the convective cloud: low level convergence in the boundary layer results in a local low pressure area near the bottom of the cloud, while the upper level divergence near the tropopause causes a local high pressure zone to form there.

Unlike Frank and Roundy (2006), Gray (1995) argued that the TC genesis stage is not a gradual process, but rather an impulsive two-stage process: A first wind surge/shift in surface winds in the tropics, allows the formation of mesoscale convective systems (MCS) to develop. As this MCS weakens, a middle level cyclonic vortex (mesovortex, Maddox, 1980) sometimes extending to the sea level as a weaker vortex, will still persist a few days after the convection within the MCS dissipates. This will set the stage for the TC formation as a second wind surge (externally forced convergence) impinges on this pre-existing mesovortex. This second wind surge will also increase the water vapor amount by about 20%, making this second convective burst less prone to dilution by dry air entrainment and also transforms the initial cold cored disturbance at low levels into a warm cored one. The latter is possible because in the MCS's center, the vorticity and inertial stability at low levels are weaker than at upper levels, hence allowing this wind

surge to penetrate the MCS's center. This wind surge also concentrates the vorticity and low-level convergence of the MCS into a small area of Extreme Convection (or EC). This EC is then able to sustain itself by Internal Forced Convergence process (or IFC, similar to convective instability of the second kind), while having an embedded pre-existing cyclonic circulation at its center. IFC lowers pressure beneath the EC as updrafts increases due to increasing/enhanced release of latent heat energy during condensation in more humid environment at mid-to-upper levels, in turn increasing the inward mass flux into the EC area and so on. Once this positive feedback process kicks in, the disturbance becomes less dependent on the environmental condition in which it is embedded. Rather, this EC disturbance tends to protect itself from any dryer/colder air intrusion, which allows it to become almost isolated from its environment (provided that vertical shear remains weak). Hence, while the initial development of a TC is highly dependent on the ambient environment in which the disturbance evolves, the later (more impulsive) stage of the TC's development remains almost independent of the latter (provided that no strong shear exists).

Despite the differences in the genesis mechanisms, both theories seem to agree that after the genesis stage (i.e., once a well-defined low level cyclone has formed in an environment favorable for moist convection with weak shear and warm sea surface temperatures), CISK is the main mechanism involved in the intensification stage of the TC.

### **II.1.3 Tropical cyclone eye characteristics and formation**

Maybe the visually most attractive feature of these intense tropical low pressure systems is the presence of a cloud free region at the storm center commonly referred as an eye. The exact causes behind the formation of the TC eye are still unclear and many theories have been proposed in the last decades to attempt to explain in more details its formation process. A recent detailed literature review from Vigh (2006) classified most of the eye formation theories in four main groups: (1) the subsidence at the TC center is forced by kinematical and thermodynamic aspects of the intensifying storm, (2) boundary layer friction and geometry considerations which causes a preferred location for the convective forcing near the TC center, (3) Encircling rainbands or other changes in the TC convective morphology, which act to focus central subsidence, (4) distribution of vorticity, which acts as transport barrier and isolate the air in the eye from its surroundings (without, however, preventing mixing to occur with the surroundings).

Probably the most commonly accepted in the literature is hypothesis (1): Once the disturbance has developed into a well-defined (and named) tropical cyclone, the vertical motion at the center will increase progressively as frictional dissipation and positive outflow advection of tangential momentum aloft forces a mechanical increase in upward mass transport at the storm center in a in-up-in-out circulation fashion. Consequently, the largest the outflow to inflow ratio, the stronger and deeper the cyclone will be. As the upward mass flux at the storm center increases, the compensating subsidence in the storm's center causes a cloud free region (or eye) to form (Willoughby et al. 1982).

The temperature inside a TC eye in the upper-troposphere (near 12 km) is usually 10-15 C warmer than its surroundings due to adiabatic warming associated with this subsidence at these levels but is only 0-2 C warmer than the surface (Hawkins and Rubsam 1968). This large positive temperature anomaly at upper levels in the eye contributes to the surface pressure drop near the surface directly through hydrostatic balance (Willoughby, 1998). The pressure underneath the eyewall is usually about 85% as low than within the eye, increasing the inward mass flux into the eyewall. The formation of the eye at the storm center forces the strong convection there to organize into a solid ring of convection called the eyewall. The storm is able to resist the strong upper level warm anomaly in the eye by having updrafts tilting radially outward in the eyewall. That way, the updraft of the eyewall only has to overcome about 30% of this warming and continue to intensify further until the warming becomes too strong (Gray, 1995). The warm anomaly associated with the subsidence in the eye thereby sets a limit to the storm's intensity.

Willoughby (1998) showed that hurricane eye soundings exhibited an inversion typically near 500-850 mb which separates the dry warm air from aloft and the moist, cloudy air from below. Willoughby (1998) hypothesized that the dry air above the inversion became trapped by the TC as the eye formed, while the moist air present below the inversion arose from the evaporation of sea water, the frictional inflow of warm air in the BL and from moist downdrafts as condensate mixes into the eye.

As we described earlier, the eye is surrounded by an intense ring of convection, called the eyewall. TC eyewalls can exhibit various sizes and shapes and has also been discovered to undergo various evolution processes, which in turn influence on the TC

intensification (Willoughby et al. 1982; Willoughby 1990a; Willoughby, 1990b; Willoughby 1998). Polygonal eyewalls (Schubert et al. 1999) or ellipsoidal eyewalls, for instance, are believed to arise from the azimuthal propagation of vortex Rossby waves (VRW). Willoughby et al. (1982) also documented the so-called double-eyewall and the eyewall replacement (shrinking) processes: Assuming that the convective ring contains active diabatic heating, the wind speed will increase faster on the inward side resulting in a gradual contraction of the outer ring of wind maximum until the latter ultimately replaces the inner ring. The outer ring propagates inward because the adiabatic descent that accompanies the upward motion in the eyewall causes the pressure to fall just inside the outer convective annulus. Willoughby et al. (1982) hypothesized that the destruction of the inner eye by the outer one arose from the forcing of lower tropospheric air outflow and negative wind tendency towards the vortex center created by the outer contracting convective ring. The radius of maximum winds (RMW) and eyewall will shrink until the eye becomes too small to be able to vertically evacuate all the horizontally converging air from larger radius. There is also an upper limit to which the TC's eye is able to grow: As the eyewall gets bigger, the inward mass flux needed to balance the stronger ventilation flow aloft and the larger frictional drag below must also increase, which explains why eyes larger than 60 km are rarely seen (Weatherford and Gray, 1988). This eyewall replacement or shrinking is believed to be important in the storm meandering as it generally coincides with a temporal weakening or with a pause in the intensification trend in intense symmetric TC. Such (concentric and symmetric) eyewall replacement cycle was also well documented by Blackwell (2000) as Hurricane Danny made landfall near Mobile Bay (USA).

## II.1.4 Tropical cyclone rainbands

Another important feature of mature TCs mentioned earlier is the outer spiral rainbands. Powell (1990a, b) showed that outer hurricanes rainbands exhibit great similarities with tropical squall lines. They showed that these were mainly composed of individual convective cells moving downband, where stratiform (convective) rain was present on the outer (inner) side of the band main axis. This was consistent with environmental surroundings well outside the eye (~150 km) being similar to that of the subtropical atmosphere, which is more unstable and contains more dry air at midlevels. This apparent difference in convective regime between the eyewall and the outer bands arises partly from that the very high horizontal winds existing within the inner core region of hurricanes allows the eyewall to become stable to lateral displacement (slow variation in the circulation). This mechanism allows for a convective neutral state to develop, whereas the weaker rotation at outer radii of the hurricane center results in the convection to vary significantly (Shapiro and Montgomery, 1993). Shelton (2004) also showed that in the as Hurricane Bret (1999) evolved from a weak tropical depression to a Strong hurricane, that the convective instability increased with increasing strength of the storm. Also they found that the magnitude of the instability decreased towards the storm center, such that close to the center the atmosphere is close to (moist) neutral stability.

It was also shown that outer rainbands are relevant in the TC intensity evolution. May and Holland (1999) showed that high level of potential vorticity (PV) was generated within the stratiform regions associated with the TC outer rainbands. The downward surface flux associated with convective rainfall within the outer bands may directly

supply vorticity (thus PV) to lower levels, which in turn would strengthen the storm. This enhanced production of PV is coincident with shearing deformation of vertical vorticity resulting of the formation of a jet, which might account for the observed secondary horizontal wind maxima (SHWM) often observed in TCs (Samsury and Zipser, 1995). On the other hand, using aircraft observations of 20 Atlantic TCs, Samsury and Zipser (1995) posited that outer eyewall rainbands with SHWM could also act as a barrier to the inner eyewall inflow. Furthermore, the vertical motions associated with the convection in the rainbands would further modify this inflow air. Hence, since most of the radial mass transport is confined to the lowest 1000 m (i.e. the BL), these two factors combined would tend to weaken the storm. These results were consistent with the aircraft observations from Powell (1990a, b). They showed that the hurricane mixed layer (ML) thermodynamic structure is significantly modified by outer rainbands convective downdrafts located on the inner side of the band axis and that the complete restoration of the BL through heat and moisture supply by surface fluxes and entrainment at the ML top is not always guaranteed to occur. Also, the moistening effect of anvil rain evaporation from the rainbands can be overcome by differential evaporative cooling, further reducing the recovery of  $\theta_e$  in the ML. As a result, any intrusion of this lower equivalent potential temperature (hereafter,  $\theta_e$ ) air within the TC eyewall BL could cause a temporal weakening of the system.

Consistent with this, Sang and Smith (2004) showed that overall, shallow convection in a TC tended to dry and to warm the TC BL, thereby lowering  $\theta_e$  in the BL (as in Zhu and Smith, 2002). Additionally, it moistens and cools the air present in the lower troposphere, thereby increasing  $\theta_e$  above the BL, which in turn reduce the

convective instability within the TC. This process has been shown to delay the TC intensification by several hours and should thus be considered.

### **II.1.5 Main external and internal factors influencing tropical cyclone intensity.**

Most of the TC's kinetic energy comes from the conversion of latent heat energy from the underlying ocean (Emanuel, 1986, 1988). On the other hand, the potential energy conversion is achieved by the storm's transverse secondary circulation. Air spirals in towards the eye in the BL, ascends along constant momentum surfaces in the eyewall, and then slowly subsides outside. According to Emanuel (1986, 1988, 1991) mature TCs work like a Carnot heat engine, where the heat is ingested in the form of water vapor from the ocean and expelled at the top of the storm (air-sea interaction theory). They posited that the intensification and maintenance of TC only depends on heat transfer from the underlying warm ocean and hypothesized that TCs may be regarded as resulting from a finite air-sea interaction instability rather than linear instability involving potential buoyancy. This theory has been the source of controversy as for instance Gray (1995) hypothesized that hurricane intensity was not overly sensitive of the outflow temperature as the Carnot cycle theory implied. Furthermore, they posited that the Carnot cycle neglected the effect of buoyancy in sustaining eyewall convection.

Apart from being a major factor in the determination of TC track, ambient winds and particularly, vertical wind shear has many influences on TC internal dynamics. Gray (1968) stressed the importance of ambient vertical wind shear on TC demise by

hypothesizing that the condensational heat release crucial for TC maintenance will be advected away relative to the storm's low-level cyclonic circulation. Along this line, DeMaria (1996) showed that the primary effect of strong vertical wind shear is to tilt the upper (anticyclonic) and lower (cyclonic) PV anomalies, resulting in mid-tropospheric warming. This will increase the static stability at upper levels, in turn inhibiting the storm development. Wu and Emanuel (1993) confirmed the above result using a 2-layer, quasi-geostrophic (hereafter QG) model by showing that the principal effect of vertical shear is to displace the upper negative PV anomaly downstream of the lower cyclonic one. This in turn induces a mutual interaction between both circulations. In the Northern Hemisphere, this results in a drift (baroclinic drift) of the cyclone to the left of the vertical shear vector. It was also found that the direction of the vertical wind shear seems to be well correlated to the TC convective asymmetries within the inner region of the storm (Knaff and Zehr, 1999). Nevertheless, it is still important to emphasize that these convective asymmetries can arise without the presence of vertical shear; the frictional drag caused by the storm's translation across the BL will cause the wind field to be asymmetric, leading to asymmetrical drag and thus asymmetry in the BL winds and low level convergence (Shapiro, 1983). Using the MM5 cloud model, Frank and Ritchie (1999) showed that both vertical shear (mainly at low-to-mid levels) and the storm movement could cause major asymmetries in the TC core. Moreover maximum rainfall tended to be enhanced on the downshear-left side of the TC.

Since vertical wind shear has significant impact on TC evolution, an important question would be to know how much vertical shear a mature TC could withstand. Gray (1998) proposed that for identical environmental forcing (e.g. wind shear) a TC with

greater than average wind speed would intensify more rapidly than TCs having weaker outer winds.

Another process of relevance to TC evolution, and related to TC intensity, is the tendency for faster translation speeds to be correlated with weaker storms. On the premises that TC intensity is sensitive to the sea surface temperature (SST), Peng et al. (1999) hypothesized that the induced cooling of the upper ocean waters, resulting from upwelling from the strong wind stress occurring at the sea surface, will decrease the surface heat fluxes. Thus slow-moving storms will tend to weaken more rapidly due to prolonged interactions with the cooler sea-surface. Also, they hypothesized that storms moving too fast will tend to have enhanced asymmetries, which in turn will inhibit the TC from intensifying. Holland (2002) deduced from observations that the range of translation speed favorable for TC development lies between 3 and 6 m s<sup>-1</sup>.

Additional factor not discussed above, is the effect of water sea spray, which is also believed to have strong influence on TC strength. Since in situ measurements under high wind conditions are very difficult, little is known on this subject at present. From a theoretical approach, Anthes (1982) hypothesized that sea spray evaporation could produce strong cooling a few meters above the sea surface, which will increase the temperature gradient between the ocean and the air a few meters above. This larger vertical temperature gradient in turn will result in enhanced sensible heat transfer, which could strengthen the storm. Emmanuel (2003) showed recently that the exchange coefficients of heat and momentum (which governs the strength of the storm) should become independent in very high winds conditions. Indeed, Ginis et al. (2004) showed that the drag coefficient leveled off or even slightly decreases at high wind speeds in agreement

with observational results from Powell et al. (2003). This suggests that the drag coefficient and hence the momentum flux varies significantly depending of the position from the storm center. Other issues in using current drag coefficient parameterization, is that in situ wind profile measurement within Hurricane Isabel (2003) eyewall during the Coupled Boundary Layers Air-Sea Transfer (CBLAST) field program showed a quasi linear profile within the shallow mixed layer (~100 m, Black et al. 2004). The latter suggests that the log-wind profiles currently used to estimate surface roughness might be inadequate.

As we showed, hurricane intensity depends on many environmental factors that are constantly interacting with each other in a rather complicated manner. Initially, a theory of a TC “Maximum Potential Intensity” (or MPI) was proposed by Emanuel (1986). The latter is governed by SST, outflow temperature and surface RH. This theory assumes that with an initially convectively neutral atmosphere, the MPI is maintained by a balance between the surface friction and the air-sea exchange of the moist enthalpy (defined as  $C_p T + Lq$  where  $C_p$  is the heat capacity of air at constant pressure,  $T$  is air temperature,  $L$  is the latent heat of phase change of water vapor, and  $q$  is the specific humidity of air). Gray (1997) further hypothesized that MPI is limited by the process in which the increasing momentum requirements necessary to balance the intensifying TC’s, must balance the inner-core frictional dissipation and upwards transport of positive tangential momentum. Also the upper level warming associated with pressure fall tendency in an intensifying TC would decrease the convective instability within the inner core, thereby further limiting the storm’s MPI. Other limiting factors to MPI such as VRW and their coupling to the BL, the formation of secondary eyewall were also pointed

out by Camp and Montgomery (2000). Nevertheless, Bell et al. (2004) showed that the extreme winds recorded in Isabel were exceeding those predicted by the MPI theory of Emanuel (1986). Winds exceeding  $105 \text{ m s}^{-1}$  have been measured within Isabel eyewall and might indicate the presence of embedded strong mesovortices at the eyewall (Montgomery et al. 2002; Kossin et al. 2004). Following the MPI terminology, Isabel reached a so-called superintensity status. Bell et al. (2004) hypothesized that the very high  $\theta_e$  air reservoir present just inside the eyewall at low levels (trapped by the inversion and heated from the surface) becomes mixed inside the eyewall convection by these intense eyewall mesovortices, providing in turn an additional heat source for the hurricane (providing local convective instability). In hurricanes Isabel (2001), Hugo (1989) and Andrew (1992), three category 5 storms,  $\theta_e$  in the eye near the surface reached near 380 K, which was about 20 K greater within the eyewall at the same level (Aberson et al. 2006).

These mesovortices are also believed to protect the inner core from further mixing and are also able to advect high angular momentum present at the eyewall directly inside the eye where the angular momentum is low (Kossin et al. 2004).

Entrainment usually has a detrimental effect on convective systems by mixing environmental drier air within the buoyant moist updraft. In hurricanes, however, entrainment also imports high angular momentum air above the frictional inflow layer, thereby favoring the spin-up of the vortex and counteracting the detrimental effect of frictional dissipation.

Another important factor influencing on TC intensity is the effect of frictional drag. The most obvious manifestation of the effect of drag can be seen at landfall: the

increased surface roughness (together with much weaker surface latent heat and moisture fluxes) causes the storm to weaken quickly. Chao et al. (2002) showed that while higher surface friction rendered a weaker and smaller storm, it also resulted in earlier and lower minimum surface pressure development. They found that surface for a larger drag coefficient, low-level convergence was enhanced, while the total kinetic energy (KE) was reduced. Indeed, without surface friction, the converging air within the BL gains enough momentum to pick up sufficient amount of moisture, which makes the latter more convectively unstable, leading to the formation of a large eye (convection away from the center).

Using a simple coupled ocean–atmosphere axisymmetric model, Emanuel et al. (2004) explored the sensitivity of TC intensity upon various environmental factors, such as land surface characteristics, upper-ocean thermal structure and vertical wind shear. They found that TC intensity forecast became increasingly uncertain in the presence of large wind shear. They also showed that in particular cases, for which the SST departed significantly from climatological average, the forecast intensity showed large errors, suggesting the need of in situ upper ocean thermal structure observations for valid forecasts. Consistent with this, Gallacher et al. (1989) showed that a mere 2.5 K SST temperature drop in the TC core may suffice for its demise. Interestingly, Emanuel et al. (2004) clearly demonstrated that precise representation of land characteristics is warranted for accurate TC intensity forecast. In their model, it requires only a few meters of standing water (e.g. swamps or lakes) to significantly decrease the rate of decline of a landfalling TC. This is consistent with the greater enthalpy supply from these waters. Wang and Holland (1999) found similar results for the case of Hurricane Andrew (1992).

Moreover, it appeared that the intensity change of a landfalling TC could be a function of the storm current development stage.

## **II.1.6 Factors influencing tropical cyclone motion**

On the synoptic scale, TCs are embedded in an environmental flow of much larger dimensions. Thus, TC motion is mainly governed by the surrounding flow, which acts as a “steering” current (George and Gray, 1976).

Because a TC is a large scale vortex, its properties can be described using the vertical vorticity, which maximum is located at the storm’s center. Thus, for a TC embedded in a easterly flow in the Northern Hemisphere, maximum cyclonic vorticity advection will occur on the western side of the storm causing the latter to drift westward. In nature, such idealized constant horizontal flow at all levels is unrealistic, because environmental winds often display great variations in intensity and direction with height. To overcome this problem, numerical simulations studies usually average the environmental winds through a layer, with the depth depending on the TC intensity (Velden and Leslie, 1991). The latter approximation is also known as barotropic, where density and temperature surfaces are parallel to each other, preventing solenoidal (i.e., baroclinic) circulations to occur in the atmosphere.

However, observations of TC tracks from satellite imagery reveal that these systems tend to deviate from the mean steering flow (Chan, 1982). For instance, hurricanes in the Northern Hemisphere tend to drift towards the north while the mean steering current is towards the west, leading to a general northwest track of the TC

(Elsberry, 1987). Consequently, processes other than the steering mechanism must be present. On a rotating sphere such as the Earth, one has to consider the effects of the variations of the Coriolis force  $f$  with latitudes ( $df/dy$ ), which is known as the  $\beta$ -effect. This poleward displacement (known as the “propagation” component of the TC motion) is believed to arise from non-linear interactions between the flow associated with the vortex and  $f$ . Indeed, Fiorino and Elsberry (1989) approximate a hurricane being composed of “a set of symmetric/asymmetric circulations subsystems that move and sustain each other in a quasi balanced manner”. They found that the asymmetric advection of the asymmetric vorticity of an isolated barotropic vortex (with no basic state current) generate a dipole structure (called beta gyres). Fiorino and Elsberry (1989) found that the linear beta term is responsible for the initially east-west oriented asymmetric gyres. Later, the nonlinear advection of the asymmetric circulation by the symmetric vortex reorients these gyres in a NE-SW fashion, causing a so-called “ventilation flow” towards the NW rather than towards the south. This rotation of the gyres occurs because the nonlinear advection is in balance with the linear beta forcing. Ngan and Chan (1995) considered the possible influence of flow of higher wavenumbers on the TC vorticity tendency and found that the aforementioned two mechanisms (propagation and steering) alone cannot account for all TC motions.

This is motivated by the fact that the vertical flow structure of TCs is far from being uniform with height, implying that TCs are *not* barotropic. Indeed, because of mass continuity, the low level cyclonic (convergent) circulation must be accompanied with anticyclonic (divergent) flow at upper levels (Wu and Emanuel, 1993). Moreover, strong convective motions (updrafts and associated downdrafts) occurring within the storm will

result in significant amounts of heat and momentum transport at different altitudes, in turn changing the temperature profile (and thus the vertical wind shear profile) of the TC. Also, the latent heat release during condensation further changes the temperature profile. For these reasons another approach was introduced to study TCs (in particular TC motion) in a more consistent manner. The vertical wind shear, horizontal temperature gradients as well as latent heat release in convective clouds can all be included in PV (where  $PV = (\zeta + f) \partial\theta/\partial p$ , where  $\zeta$  and  $f$  are planetary and vertical relative vorticity, respectively). Wu and Emanuel (1993) approximated mature hurricanes as being “diabatically and frictionally maintained constant positive PV anomalies in the lower troposphere, with an expanding negative PV in the upper troposphere” (e.g. a cyclone overlaid by an anticyclone). Wu and Wang (2000) showed that baroclinic TCs tended to propagate into regions of wavenumber-one component of the maximum PV tendency (i.e. regions of strong cyclonic vorticity). Moreover, this PV maximum is not necessarily aligned with that of the ventilation flow. Hence, baroclinic-like vortices must include additional processes to account for their track evolution. Barotropic vortex motion is primarily controlled by the orientation and strength of the beta gyres, while for baroclinic features the latter is no longer valid.

Following the Fiorino and Elsberry (1989) approach, Chan et al. (2002) found that TC motion is mainly influenced by the horizontal advection of PV and the PV production associated with latent heating (previously suggested by Wu and Wang 2000). Diabatic heating alone cannot change the total mass-weighted PV of a TC. This mechanism is responsible only for redistributing the TC PV fields by horizontal and vertical transport such that the PV in a TC is enhanced below and weakened aloft. Chan et al. (2002)

proposed that in the cases of steady TCs, the horizontal PV advection (HA) is the dominant process steering the storm. In their analysis they divided PV HA into two parts: the asymmetric advection of asymmetric PV (AASPV); and the symmetric advection of symmetric PV (SAAPV). They showed that in the absence of significant diabatic heating (DH), the AASPV mechanism is dominant in steering the TC, whereas for increasing values of DH the SAAPV term has comparable contribution to the TC motion. Wu and Wang (1999) also showed that the asymmetric DH associated with vertical differential heating, can directly induce a positive PV tendency, thereby causing the storm to propagate towards regions of maximum differential heating rate.

To summarize the difficulty in studying TC motion, Shapiro and Franklin (1999) showed that the main factor contributing to the TC motion varies widely from case to case. Using PV cylinders of varying radii, Shapiro and Franklin (1999) showed that the motion of Hurricane Gloria (1985) and Andrew (1992) was primarily controlled by the presence of the upper level PV feature, while Hurricanes Debby (1982) was steered by more barotropic features. Other cases (Emily 1987 and 1993) also required a larger cylinder radius to determine their motion, suggesting larger scale environmental influences.

### **II.1.7 Major changes observed in tropical cyclone dynamics and kinematics at landfall**

In nature, observations shows that landfalling TCs experience very quick weakening since, in addition to enhanced surface drag over land, the heat energy supplied

for the warm waters of the ocean is suppressed over land (Farfan and Zehnder 2001). The additional effect of topographical inhomogeneities received considerable attention in the past 25 years. Recent numerical studies focusing on these aspects will be briefly presented below.

Using a primitive equations numerical model in an unsheared  $f$ -plane environment, Chang (1982) showed that typhoons approaching the island of Taiwan experienced dramatic changes in their path. As they approached the island, they tended to weaken and accelerate around the northern portion of the island to follow a cyclonically curved track. Their numerical simulation showed that this acceleration was due to strong easterly flow forming on the northern portion of the island as the TC flow interacted with it. Also, as the storm approached the mountain range before making landfall most of the low level flow became blocked by the escarpment. Thus, on the lee side of the ridge, a low level cyclone develops within the induced lee trough, while an anticyclonic circulation forms on the winward side of the mountain at low levels. The isotropic ascent forced by the escarpment on the winward side was also consistent with enhanced rainfall amount occurring there. The TC low level cyclone was blocked as the storm passed over the ridge, while the upper level anticyclone was not affected in its motion and continued in its original track. Hence, the storm's upper and low level circulations experienced a temporal shift in phase, until the upper level anticyclone became again vertically aligned with the lee cyclone on the lee side of the mountain. However, they were unable to investigate the inner core structure of the storm because of the relative coarse horizontal grid resolution (60 km) used in their model. Bender, Tuleya and Kurihara (1987) confirmed Chang's numerical results using a triple nested movable mesh model to

examine the track changes as TC made landfall on three different islands (i.e. Taiwan, Hispaniola and Luzon). They also found that entrainment of drier air originating from the mountain tops tended to weaken the TC further as they made landfall in all the three cases. The storm's weakening was also enhanced by the suppression of latent energy supply during landfall and by the vertical tilting of the upper and lower level circulations previously discussed in Chang (1982). However, once the TC left the island, the latter re-intensified only after the alignment of the cyclonic and anticyclonic circulations was re-established. Similar to Bender, Tuleya and Kurihara (1987) study, Cheng et al. (2004) performed idealized numerical simulation of Typhoon Zeb (1999) as it made landfall on Luzon. Their results confirmed observations in that Zeb's eyewall shrank before making landfall (due to increase in inflow in the coastal region) and then reformed as Zeb reentered the open waters. This eyewall contraction was coincident with a temporal weakening of the storm, also consistent with reduced heat flux over land. Such eyewall evolution may often occur whenever the terrain size is comparable to that of the vortex.

Moreover, Lin et al. (2002a) showed that weaker slow-moving storms tended to experience the largest variations in their track and intensity before, during and after landfall, while stronger entities such as superthyphoon Bilis (2000) tended to maintain their original track. Lin et al. (2002a) also showed that if the flow is perpendicular to the mountain range, the lee induced low pressure will tend to occupy the entire lee side of the mountains. Therefore, the secondary low formation was highly dependent upon the angle of the landfall, since thermal forcing associated with the orographic forcing governs the motion of the cyclonic vortex at low levels (and thus the hurricane itself). Kong and Soong (1997), however, argued that typhoon having continuous track or Type I track

(discontinuous track = Type II), were not only classified according to their intensity, but rather according to their Froude number ( $Fr = V^2 / g L$ , where  $V$  = velocity and  $L$  = characteristic length scale or fluid depth). Type I (II) typhoons were characterized by  $Fr > 3$  ( $<3$ ). A similar parameter defined as  $F = V_{max} / Nh$  was also proposed by Lin et al. (2001) and is the Froude number associated with the cyclone circulation. When  $F > 1.6$  ( $<1.6$ ) the storm track was continuous (discontinuous). Furthermore, Kong and Soong (1997) showed for typhoons approaching the southern portion of Taiwan, both surface friction and the  $\beta$ -effect had a significant role in the TC northward deflection. They also hypothesized that the friction over the mountain slopes could significantly alter the flow through a deep layer, in turn modifying the TC flow aloft more rapidly than over flat terrain. In a similar fashion, Jones (1987) used a 12-layer triple-nested moving-grid model on a  $f$ -plane to investigate landfalling hurricane structure and evolution. The main finding was the observed discontinuity displayed by the low levels winds along the coast. The latter was a consequence of higher drag coefficient over land than over water. Convergence (divergence) of anticyclonic (cyclonic) vorticity occurred of the right (left) side of the TC track. Consistent with this, tangential winds tend to decrease over land, while the radial component tended to increase (by Ekman pumping). In agreement with the above Powell (1987) found using various observation platforms, that in the case of Hurricane Alicia (1983), the land-sea roughness difference acted to oppose (reinforce) the mean vortex flow over land (water).

Farfan and Zehnder (2001) studied the evolution of Hurricane Nora, which made landfall in northwestern Mexico using the MM5 numerical model. In this case, the mountains of Baja California also caused the storm to deviate eastward. Additional

simulations carried out without the presence of orography did not reproduce this deflection, hence confirming the importance of the influence of these mountains in this case. Also, consistent with Chang's (1982) numerical study, a secondary circulation developed on the lee side of the mountains, which became coupled with the convection associated with the primary circulation as the storm moved across the ridge.

Zehnder (1993) investigated to what extent the flow divergence associated with large-scale topography influence on the track of TC. Towards this goal, Zehnder (1993) integrated numerically the shallow water equations on a  $\beta$ -plane (barotropic vortex). Two separate experiments were designed in which the TC first approached the mountain range from the east and then from the west. They found that when approaching the mountains from the east the vortex experienced a southward deflection, while vortices approaching from the west recurved and moved towards the east. They showed that the modification(s) of the beta gyres through vortex stretching as the flow associated with the vortex passed over the mountains was key to account for the simulated TC track displacement. For instance, a cyclone approaching from the east (in the northern hemisphere), the upslope (downslope) to the north (south) of the vortex resulted in the generation of anticyclonic (cyclonic) relative vorticity to the north (south) of cyclone. The vortex stretching strengthened the beta gyres and shifted the location of the vorticity maxima, resulting in the simulated southward deviation of the TC path. This result differed somewhat from Chang (1982) study, which found a northward deviation instead. Zehnder (1993) attributed this difference mainly to the steeper slope and smaller size of the mountains used in Chang's study. Zehnder (1993) also found that there was a component of motion oriented in the direction and to the left of the imposed PV gradient.

Because the mountains are regions of high PV, the storm will move south if approaching from the east.

Using the same numerical model, Geizler and Zehnder (1999) found similar track deviation trends for the case study of a strong barotropic vortex (Hurricane Gilbert 1988) approaching large scale mountain range (the Sierra Madre, Mexico) from the east. The same experiment was carried out for a much weaker storm (TC Hermine 1980) and showed disagreement with the observed and simulated track. They hypothesized that this discrepancy might likely be attributed to the fact that the steering current used in the simulations was averaged over a layer that was too deep for a weak TC like Hermine. Velden and Leslie (1991) have suggested that a shallower layer is needed for a better representation of the motion of weaker storms.

In the same framework, Zehnder and Reeder (1997) performed idealized simulations of barotropic vortex approaching large scale mountains (the Sierra Madre). They confirmed the results obtained in Zehnder (1993) in that the asymmetric vorticity distribution is greatly modified by the presence of the mountains. The resulting horizontal convergence (divergence) associated with the compression (stretching) of the vortex tubes as the flow crossed the ridge strengthened and reoriented the beta gyres, leading to a southward displacement of the TC. Interestingly, they found that as the slope of the mountains increased, the southward propagation component of the TC motion also tended to increase (as long as the ridge width was comparable to that of the beta gyres). Similar results were found when the angle of orientation of the mountain range with respect to the North-South axis was increased. The southward displacement was also enhanced as the static stability increased in the model. This was consistent with a subsequent increase

of the rigidity of the upper surface layer, thereby enhancing vortex stretching over the mountain.

When hurricanes made landfall in mountainous areas, enhanced rainfall amounts are often observed near the mountains (Chang, 1982). Geerts et al. (2000) provided a detailed airborne Doppler radar imagery of Hurricane George as it made landfall in the Dominican Republic. They found that the excessive rainfall amounts were indeed coupled with the presence of mountains (in the island of Hispaniola). They found that orographic lifting generated by the vortex flow interacting with the mountain released potential energy initially trapped below the eye's subsidence inversion, which resulted in deep convection to occur within George's eye on the mountain windward slopes. Consistent with the above results, Lin et al. (2002b) showed that in the case of superthyphoon Bilis (2000), the enhanced rainfall amounts observed in the vicinity of the Taiwan mountain range was primarily controlled by vertical orographic forcing. Wang (1999) showed (using MM5) that the simulated rainfall of typhoon Herb (1996) was enhanced by as much as a factor six during landfall on Taiwan. Observation of landfalling Hurricane Danny (1997) near Mobile AL found that the explosive development of supercells near its center resulted in tremendous amount of rainfall (700 mm in 12 h, Medlin and Blackwell, 1999), consistent with McCaul and Weisman. (1996) simulation study. Nevertheless, other factors not discussed above influencing on TC rainfall are the effect of storm motion and environmental shear. Using the MM5 numerical model, Rogers (2003) showed that when the shear is weak, the rainfall pattern showed a double maximum coincident with the eyewall convection and a minimum centered on the track of the storm. Also for strong along track (across track) shear the

rainfall is maximized on the left side of (centered along) the TC track. Moreover, Zipser and Jiang (2003) showed that the mean reflectivity vertical profile in TC stratiform and convective regions for 1-year TRMM (Tropical Rainfall Measuring Mission, Simpson 1988, 1996) and CAMEX-4 (Convection And Moisture Experiment, Kakar 2006) data tended to increase downward below 3 km and might be relevant for rainfall retrievals during landfall.

It should be emphasized that most of the above study mainly focused on the effects of mountainous areas but not flat land. Yau and Chen (2002) showed that the presence of flat terrain could produce positive (negative) PV ahead (behind) the hurricane by friction induced converging winds during landfall. Consequently, the convection and associated heating was enhanced in the front quadrant of the storm, which in turn increased the low-level PV ahead of the TC. This asymmetry in the convection caused the inner ring to break, which allowed low entropy air to enter and stabilize the TC center leading to the TC demise.

Using the 3<sup>rd</sup> version of the MM5 atmospheric model on a  $f$ -plane, Chan and Liang (2003) found that the change in sensible heat flux had little effect on a TC convective evolution. On the other hand, the decrease in moisture flux after landfall tended to have by far the greatest influence of the TC convective activity. They argued that the change in moisture supply modified the moist static stability of the atmosphere and hence the TC convection distribution. The three dimensional advection of dry air (from over land) around the TC destabilize further the atmosphere whenever dry air is present over moist air, in turn enhancing convective rainfall. In addition to being prone of producing heavier rainfall amounts during landfall, the land surface friction also tends to

enhance the probability for tornadoes to occur (mainly in the right front quadrant in the northern hemisphere). Using the Klemp-Wilhelmson cloud model (1978), McCaul and Weisman (1996) showed that even though environmental CAPE in hurricanes was relatively weak because of near-moist adiabatic lapse rates, development of shallow supercells was possible during landfall. They found that the vertical dynamic PGF contributed three times more in the updraft development of the simulated hurricane supercells than it did for their Great Plains cousins. They also found that hurricane supercells have much weaker cold pools than Great Plains supercells, which in turn limited surface vorticity development. Hence, this would explain why most of the tornadoes associated with hurricane supercells are generally weak (maximum F2 on the Fujita (1971) scale).

Wolff (2000) is one of the very few studies documenting the changes in lightning flash strokes over water versus over land. Interestingly, the percentage of lightning activity over land versus over water showed significant variations from storm to storm (using five cases of landfalling TC). Nevertheless, four of the cases showed the majority of the flashes occurring over the open sea.

## **II.2 Present state of knowledge of tropical cyclone microphysics and electrification**

### **II.2.1 Modeling studies of tropical cyclone microphysics and lightning**

Tropical cyclone dynamics (e.g., Willoughby et al. 1982; Willoughby 1998; Powell 1990a, b; Gray 1995; Shapiro and Franklin 1999; Wang 2002; Zhu 2002) and thermodynamics (e.g., Emanuel et al. 1986, 1988, 1991) has been the focus of many modeling studies, producing significant progress in these areas, while relatively few modeling studies of microphysical properties of mature TCs have been made (McFarquhar and Black 2004, Rogers et al. 2006a). In particular, no modeling studies have focused on the electrical properties of mature TCs.

McFarquhar and Black (2004) showed that the current parameterizations used in mesoscale models may not be suitable for simulating TC microphysics. Their hypothesis was motivated by the hypothesis that in TCs, the intercepts of the size distributions tend to increase with mass content, whereas the opposite is actually observed outside TCs (i.e., in the rainbands). Observations suggested that graupel and snow distribution could show significant variability within TCs. McFarquhar and Black (2004) showed that updrafts and downdrafts possessed larger graupel particles than stratiform regions. Based on these observations, they proposed that different microphysical parameterizations should be used in convective and stratiform regions, respectively. Using a hydrostatic primitive equation model, Wang (2002) showed that although the TC cloud structure, peak and areal coverage in precipitation was quite sensitive to the microphysics schemes selected

(Lin-Farley-Orville (1983)-type 3-ICE scheme or Kessler (1969)-type warm rain scheme), the intensification rate and final intensity were not, because all the microphysics schemes produced similar vertical heating profiles. They also found that both evaporation of rain drops and melting of snow and graupel were responsible for the generation of the TC rainbands. Witcraft et al. (2003) also found that the track and speed of the simulated TC was remarkably similar for four different microphysics schemes (Tao and Simpson 1993; Dudhia, 1989; Reisner, 1993; Reisner, 1998), thereby suggesting that choice of the microphysics is not very important in that case. Using a finer horizontal grid spacing than the two previous studies (2 km instead of 7 and 5 km, respectively) in the MM5 model, MacFarquhar and Black (2004) further supported that changing the microphysics scheme did not have any systematic impact on the TC final intensity. Rather, they argue that the choice of the surface fluxes parameterization may be more important.

Other modeling studies focusing on supercell storms clearly showed that improved knowledge of the microphysical processes was crucial in determining rainfall rate distributions and lightning activity of a storm (e.g., MacCumber et al. 1991; Gilmore et al. 2004). The latter hypothesis could therefore also be applied for TCs

One of the major challenges in modeling lightning is to possess a microphysical package that includes a spectrum of hydrometeor species that is broad enough to provide a wide spectrum of differential fall speeds. This is because separation of the charges occurs when the different hydrometeors collide with one other as they are advected by turbulent motions within the storm's drafts (e.g., Takahashi, 1978). Many investigators (e.g., Saunders and Peck, 1998) have shown that the sign and magnitude of the charge separated depends upon the differential speeds between the particles involved in the

collision among other factors such as ambient temperature and liquid water content (see later in the text for more details). In the current literature, the majority of the cloud modeling studies makes use of a 3-ICE microphysics scheme (from or similar to Lin et al. 1983). This scheme only features cloud ice and graupel/hail as separate ice categories. Therefore, due to its limited number of ice species, this scheme provides a limited differential fall speed spectrum, which as described earlier, is crucial for determining charging rates (and hence lightning distribution) within a storm. That is why we believe that using a 10-ICE scheme (see section III for details behind the microphysics package) instead of a more simplistic 3-ICE scheme, will give a better representation of the electrical properties within the simulated storms presented in this study.

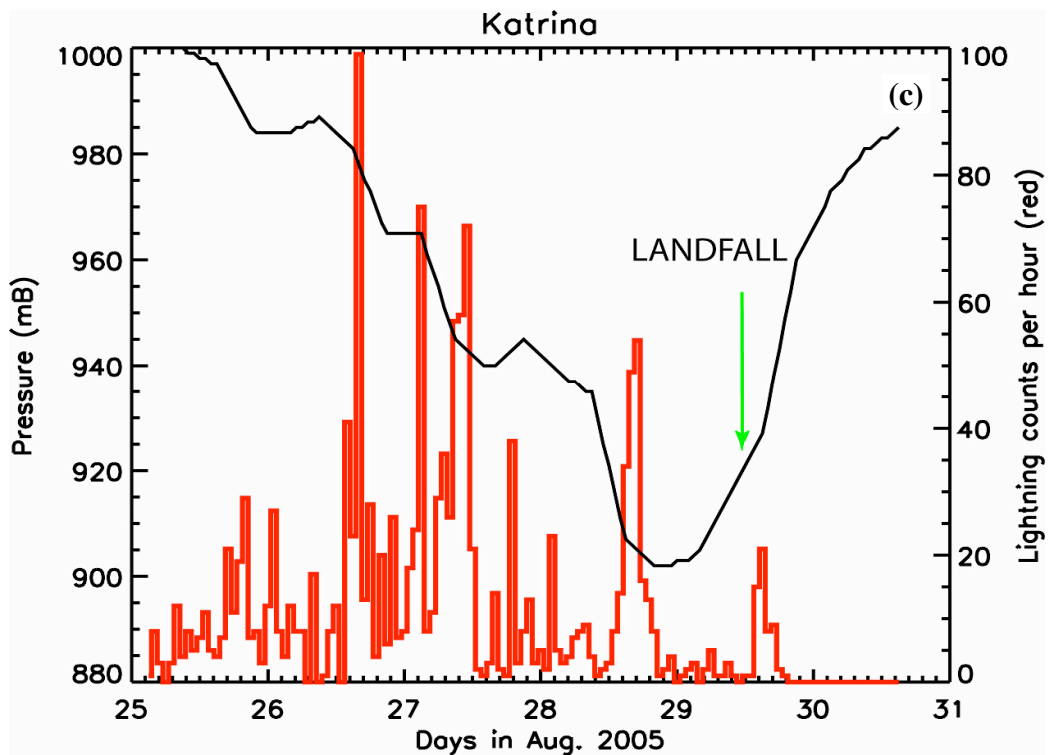
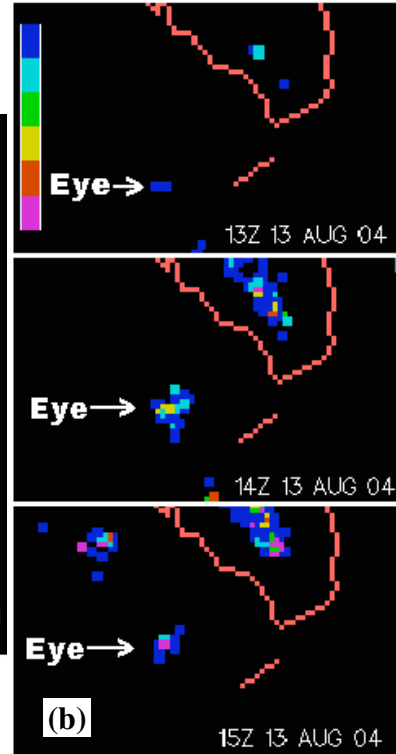
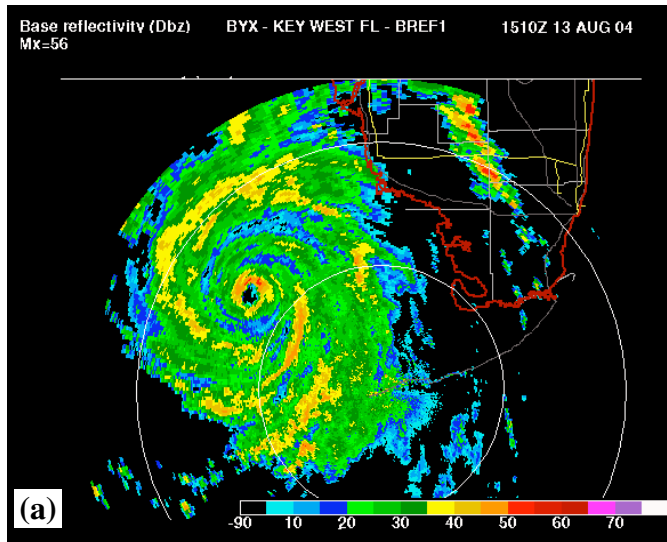
In summary, modeling microphysics and lightning within TCs remains an ambitious and difficult task. Compared to continental storms (such as squall lines, supercells and MCSs), *in situ* observations of microphysical and electrical properties within TCs are more difficult to obtain, primarily because these systems spend most of their existence over remote oceanic locations. Moreover, the horizontal scales of a TCs are much larger than for continental storms: ~1000 km compared to about a few 10's of km for supercell/multicell storms and 100's of km for a squall line.

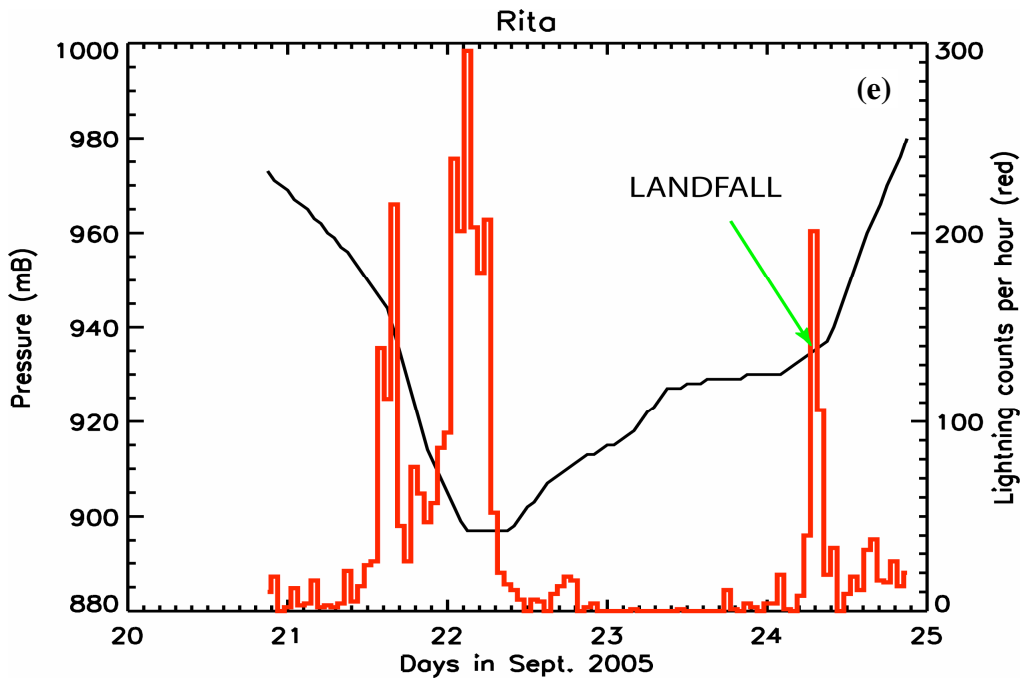
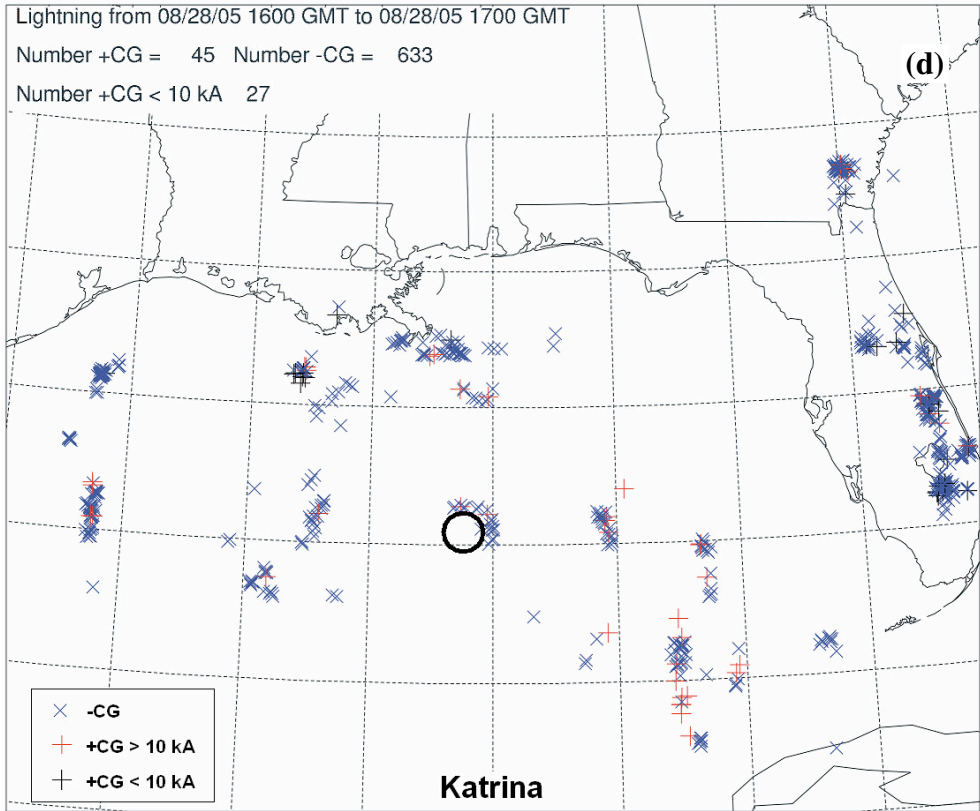
In the past 10-15 years, however, an increasing number of field experiments have been carried out to increase our knowledge on TC microphysics and dynamics, some of which will be described in more details in the next section. The data from these field experiments will provide the main source of comparisons for our results.

## **II.2.2 Observations of CG and IC flash patterns in tropical cyclones and their relationships to storm intensity.**

Samsury and Orville (1994) analyzed lightning evolution for weak TC Jerry (1989) and intense Hurricane Hugo (1989) within an 18 h window that included the periods before and after the storm made landfall. They found that, regardless of cloud-to-ground (CG) flash polarity, lightning primarily occurred within convective regions often associated with the largest reflectivity values. For both Jerry and Hugo, Samsury and Orville (1994) found that most of the lightning occurred on the east side of the storm. In contrast to hurricane Hugo, Jerry showed a significant increase in CG flash rate after making landfall by as much as a factor of three, which still remains far below continental systems. Molinari et al. (1999) confirmed that weaker TCs tended to increase their total flash rate prior landfall while no significant increase was observed for major hurricanes. Moreover, they found that three of the hurricanes showed clear evidence of lightning outbreaks within the eyewall as the latter underwent significant changes in its intensity or in its structure, such as an eyewall replacement cycle or eyewall contraction (Willoughby 1990a). Furthermore, using data from an experimental long-range lightning detection network from Vaisala, Demetriades and Holle (2005) showed that for 9 recent Atlantic Hurricanes (such as Lili and Isidore, 2002, Isabel and Fabian, 2003; Charley, 2004), eyewall lightning outbreak occurred in 11 of the 12 eyewall cycles present in the study (see Fig. 2 for TC Charley). They also found that eyewall lightning outbreak was occurring during the early intensification stage of the TC. Rodgers et al. (2000) also showed that for intensifying TCs, the closer the lightning is to the storm's center, the

more likely the TC will intensify, since these lightning flash burst are likely associated with explosive convective burst or convective band cycle (e.g., Lyons et al. 1989; Black et al. 1993; Simpson et al. 1998) or with explosive supercell growth (Lyons and Keen 1994). Henning (1997) posited that such explosive convective development might be caused by advection of destabilizing layer into the lower troposphere above an unusually moist BL with SSTs of at least 28°C, leading to a sudden local increase in convective available potential energy (CAPE) in the eyewall. Consistent with this, Kelley et al. (2004) suggested that extremely deep eyewall clouds (most likely to produce lightning) observed via TRMM satellite in the eyewall were coincident with a 70% likelihood of storm intensification. On the other hand, strong mature hurricane remaining in a quasi-steady state (e.g., Hurricane Isabel, 2003) exhibited small lightning flash rate in the eyewall (Molinari et al. 1999; Demetriades and Holle, 2005). Also, Willoughby (1990) showed that for weak TC or tropical depressions, convective eruption near the center could cause the intensification to falter and the cyclone path to become discontinuous. Hence for the case of weaker tropical systems, the lightning outbreaks accompanying strong convective bursts might precede the temporal weakening of the system and/or an imminent change in its track (as in Lei and Chan, 1999).





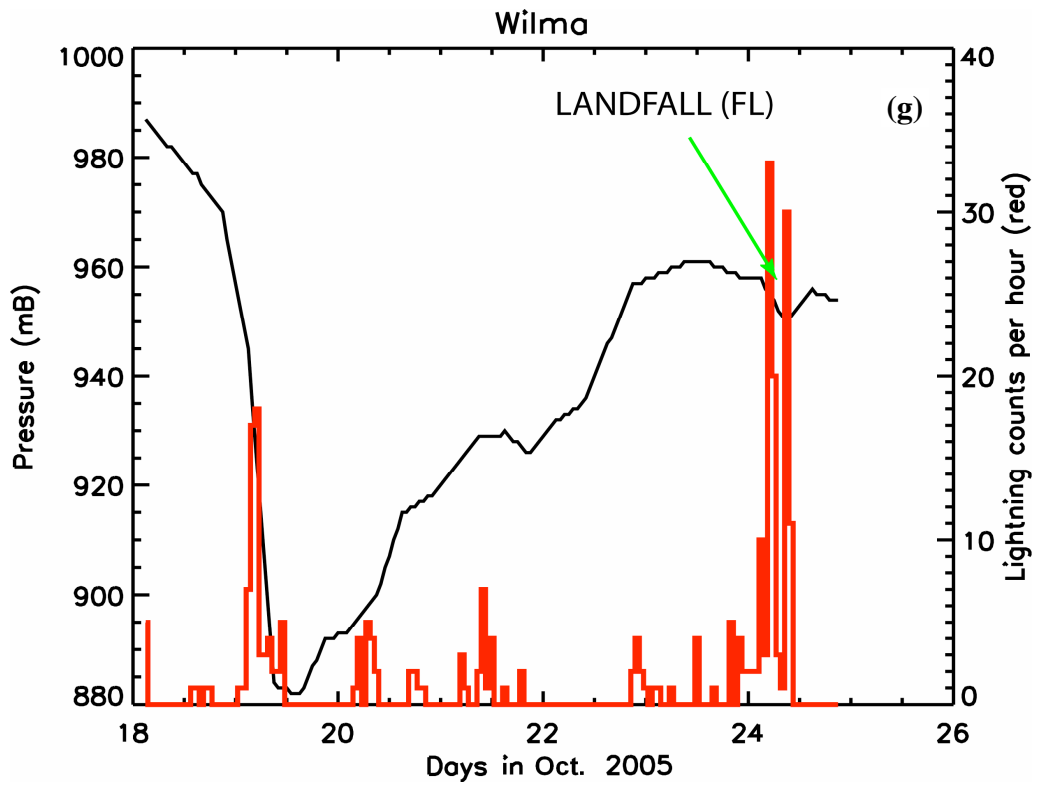
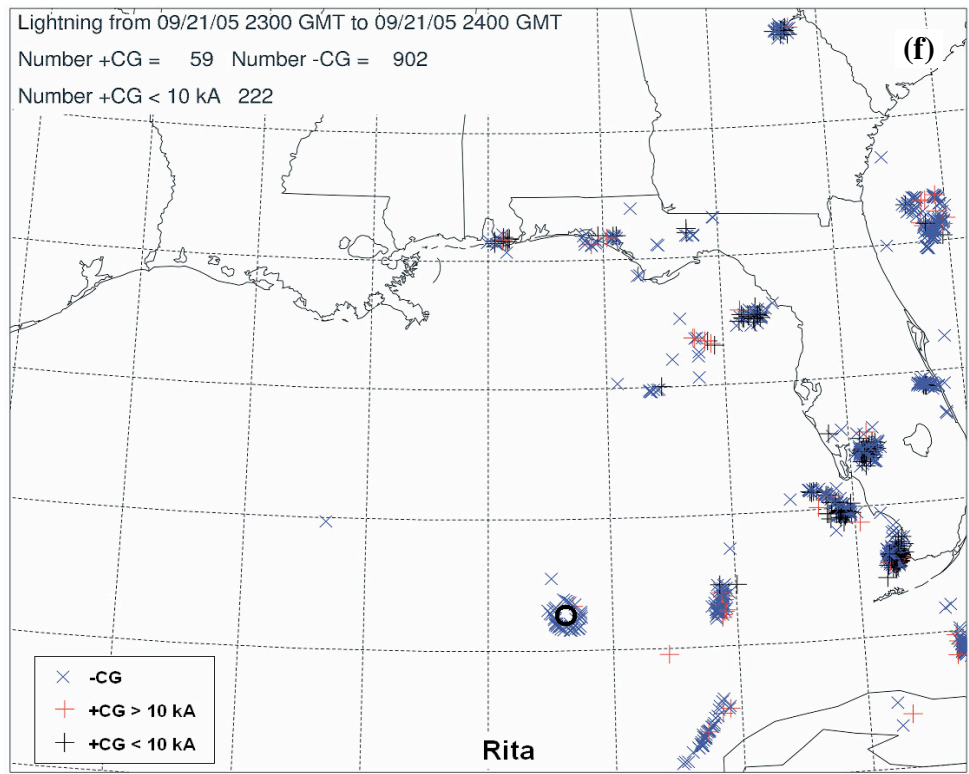


**Fig.2.** Observed radar reflectivity (panel a) and NLDN lightning composite (panel b) of Hurricane Charley, prior to landfall at 13Z, 14Z and 15Z, respectively on 13<sup>th</sup>

August 2004. The legend on panel b indicates the age of the CG lightning flashes relative to the time of the scan, ranging from blue for the most recent flashes to pink for the oldest. Panels (c), (e) and (g) show time series of hourly eyewall total lightning flash rate detected by LASA (Los Alamos National Laboratory's Sferic Array) overlaid by NOAA central pressure for (c) Hurricane Katrina, (e) Hurricane Rita and (g) Hurricane Wilma as they intensified to category 5 status before making landfall. The plots in panels (c) and (e) and (g) were generously provided by Dr. Xuan Min Shao from the Los Alamos National Laboratory in New Mexico. The results were presented by Shao et al. in the 2006 AMS meeting in Atlanta during a poster session. Panel (d) and (f) show maps of CG flashes detected by the National Lightning Detection Network (NLDN) for an hour time period for (d) Hurricane Katrina and (f) Rita, on August 28<sup>th</sup> and September 21<sup>st</sup>, respectively.

Fig. 2 shows examples of lightning outbreaks, particularly within the eyewall, in recent hurricanes that intensified rapidly before making landfall in the US coastline. For instance, as Hurricane Charley (2004) neared landfall, it intensified rapidly from a category 2 to a category 4 storm in only 8 h (not shown). This sharp deepening of the storm was accompanied with a CG lightning burst near and around the eye (Figs. 2a, b). Similar eyewall CG flash trends were also observed for three category 5 storms of the 2005 Atlantic season: namely, Hurricane Katrina (Figs. 2b, c), Rita (Fig. 2d, e) and Wilma (Fig. 2g), and also in strong typhoons that occurred over the Pacific basin (Solorzano et al., 2007) which highlights the relative frequency and importance of such events. The sferics signal amplitude of IC flashes is much smaller than for -CG flashes, and therefore, the accuracy of the LASA network in detecting IC flashes in remote locations over oceans is still quite poor. The accuracy of the LASA network for generic IC flash detection is only a few percent within a radius of 625 km compared to 85 % for CG flashes (Suszcynsky et al. 2005). The strong relationship of cloud flash rates and total lightning flash rates (in contrast with the lack of relationship of CG flash rates, Reap and MacGorman, 1989) with updraft intensification means that systems that map all lightning would be preferable for monitoring the potential for intensification of TCs

Based on studies made on continental systems (e.g., MacGorman et al 1989), we hypothesize that if IC flash rates were detected with a better efficiency (i.e., 60 % or greater), the observed peak in total lightning flash rate (IC+CG) within the hurricane, and particularly eyewall, would be much higher by more than a factor two (Dr. X. Shao and Dr. J. Molinari, personal communication, 2006). This is because IC flashes tend to generally outnumber CG flashes (Rutledge et al. 1992; Boccippio et al. 2001). Several investigators such as Mackerras et al. (1998) and Rutledge et al. (1992) showed that the IC:CG ratio exhibited relatively high values in the deep tropics and comparatively small values in the midlatitudes, which they hypothesized could be attributed to deeper cloud tops (higher mean tropopauses). This would cause the volume of cloud above the main negative charge region of the mixed phase region in tropical convection to be two to three times larger than in midlatitude storms, which combined with an exponentially decreasing breakeven electric field with height would be favorable for significant IC production. Rutledge et al. (1992) and Williams and Rutledge (1990) stressed, however, that cloud top height could be misleading and showed that instead, IC lightning flashes were most likely to occur in storms which 30 dBZ echo top height exceeded the melting level., which is indicative of an active mixed-phase region for NI collisional charging between riming graupel and ice crystals in the presence of supercooled water (e.g., Takahashi, 1978). Williams and Stanfill (2002) argued that the larger total flash rates in continental storm (i.e., compared to oceanic storms) was caused by a larger Bowen ratio (sensible heat over latent heat flux) and by more buoyant BL parcels which were able to convert CAPE more efficiently to kinetic energy within the storm's updraft. A detailed

discussion on the hypotheses of charging mechanisms occurring within hurricanes will be presented later.

Fig. 2 also shows that CG lightning does show preferential spatial patterns within hurricanes. Using the National Lightning Detection Network (NLDN) lightning data derived from 9 Atlantic hurricanes, Molinari et al. (1999) were able to establish the existence of three distinct convective regimes in mature hurricanes. These are also used by Cecil et al. (2002a, b) and are:

- The eyewall, having similar attributes to that of deep, weakly electrified, monsoonal convection
- The region outside the eyewall ( $\approx 90$  km radius) resembling MCS's trailing stratiform region with higher +CG flash rates relative to the two other regions of the TC mentioned here with a +CG : -CG ratio exceeding 25 %, which is still lower than for MCS (e.g., Holle et al. 1994).
- The outer bands ( $\approx 250$  km radius) producing the vast majority of the total ground flashes.

These examples in Fig. 2 also reveal that an intensification of the storm is not always accompanied by lightning bursts in the TC outer bands: In Hurricane Rita (2005) large total lightning flash rate were mainly found within the eyewall during its intensification stage (Figs. 2c, d, e, f, Shao et al. 2005; Demetriades and Holle, 2006). In a recent study from Molinari et al. (2006) they further hypothesized that a TC producing lightning mostly left of the vertical wind shear vector was indicative of a storm that was successfully resisting the wind shear and hence that was deepening. The opposite was true for lightning activity occurring to the right of the wind shear vector.

As shown earlier, many TCs exhibited CG lightning bursts in their eyewall prior to intensifying. Consequently, an important scientific question would be to know whether this lightning behavior can be generalized. Towards this goal, Orville and Coyne (1999) investigated the CG lightning flash characteristics and patterns in 34 TCs between 1986 and 1996. They found that as the TC became more organized, weak lightning activity was present in the eyewall, while the minimum (maximum) activity was observed in the inner band stratiform (outer band) regions. In a more recent study, Cecil et al. (2002b) used aircraft observation of 45 hurricanes during the TRMM field experiment to investigate intra-cloud (IC) and CG lightning activity and reflectivity patterns within the eyewall, inner and outer rainbands. They found that the total lightning flash rates in the eyewall and particularly within the outer rainbands were much higher (while still being much less than their continental cousins) than those within the inner band region mainly composed of stratiform precipitation and relatively weak updrafts. Higher lightning flash rates in the rainbands were also documented for Hurricane Andrew, (1992, Molinari et al. 1994) and Hurricane Lili (1996, Fritz and Morales, 1997). A significant result from this study was that lightning frequency measured within the TC 300 km and 50 km radius tended to indicate a state of hurricane intensification or temporary weakening. Using optical transient detector (OTD) observations, Cecil and Zipser (1999) showed that the greater flash rates in the eyewall were preferentially associated with strong TCs or weak tropical storms. Cecil and Zipser (1999) also found that a temporal lag existed between the production of ice scattering signature (proportional to convective intensity and lightning production) and the TC strengthening. Therefore, they argued that lightning activity

could be used as a reliable forecast tool as any changes in its patterns were likely associated with the TC change in intensity and even track.

A recent study from Chronis et al. (2006b) further showed using the very low frequency Zeus long-range lightning network (Chronis and Anagnostou, 2006a) that from all the African easterly waves (AEW) that evolved from the African continent to the Atlantic Ocean, the ones exhibiting the strongest total lightning activity were more likely to intensify and become TCs. Lightning activity peaks in late afternoon (Carnegie curve), therefore the waves exiting the African continent during this period of the day had more chance to become TCs over ocean as they were likely composed of convective elements having stronger updrafts.

### **II.2.3 Relationships between lightning activity, storm dynamics and microphysical properties.**

In the last 25 years, many studies have focused their attention on maritime tropical convection. These studies could provide a good insight on the kinematical and microphysical fields leading to significant electrification mainly within the TC outer rainbands. In TC eyewalls, however, one has to take into account the strong tangential winds at low-to-midlevels and the outwardly tilted nature of the updrafts. Nonetheless, the necessary ingredients for electrification within hurricane eyewalls should remain the same as for the outer bands.

Takahashi (2003) showed that in maritime convection, the ice crystals and graupel concentration, and hence lightning, was half that of open oceanic systems in Eastern

Asia. Takahashi (2003) therefore suggested that different precipitation processes should be expected between open oceanic and continental maritime convection. Petersen et al. (1999) also analyzed electric activity in oceanic convective systems during the Tropical Ocean Global Atmosphere Coupled Ocean-Atmosphere Response Experiment (TOGA COARE) field program and concluded that lightning occurrence in oceanic convection was preferentially observed in deep, vertically developed cells showing reflectivity values  $\geq 30$  dBZ lying above the  $-10$  C level (near  $z = 7$  km) for periods exceeding 10 min. Consistent with this, Bedrick and Burgett (1999) showed that the onset of lightning within super typhoon Keith (1997) typically occurred after that the 30 dBZ contour reached its maximum altitude in the mixed region (at about the  $-10$  C level). Petersen et al. (1999) also showed that, as in continental convection, CG occurrence was highly correlated with the progressive descent of the 30 dBZ reflectivity contour. In the same line, Cecil et al. (2002b) found that the larger flash rates observed within the rainbands of Hurricane Andrew (1992) and Lilly (1996) was coincident with larger reflectivity above the freezing level.

Petersen et al. (1999) findings for tropical convection also supports that of Simpson et al. (1998), who suggested that in the case of tropical storm Oliver (1993), strong updrafts above the melting level were crucial for significant electrification to develop. This finding was supported by Black and Hallett (1990), who argued that vertical velocities  $> 12 \text{ m s}^{-1}$  near the melting level were associated with substantial electrical activity in the cases of Hurricane Norbert (1984), Emily (1987) and Hugo (1989). Williams and Rutledge (1990) provided a detailed observational study of electrical activity of deep convection near Darwin, Australia, during the Down Under

Doppler and Electricity Experiment (DUNDEE) field program. They also found that convective strength (proportional to CAPE) was correlated to intense lightning activity within these cells. Williams and Rutledge (1990) hypothesized that the low lightning rates commonly observed in hurricanes resulted from low values of CAPE. This lower instability within hurricane centers is consistent with the presence of a warm core at upper levels, and which increases as the TC intensifies, (e.g. Jorgensen et al. 1985). Petersen et al. (1995) further proposed that for tropical MCSs, updraft velocities reaching  $6 \text{ m s}^{-1}$  near the 6 km level might be a threshold value required for significant electrification to occur, since this threshold equals that of the terminal fall speed of millimeter sized supercooled water drops.

At present, it is widely accepted that the relatively weak electrical activity of TCs is mainly caused by updrafts that are too weak in the mixed phase region to allow sufficient production and lofting of large graupel particles, and supercooled water necessary for large electric fields to develop initially via the NI charging process (Takahashi 1978; Saunders et al. 1991; Saunders and Peck 1998). Rogers et al. (2006a) showed that the majority of observed eyewall vertical motions were weak ( $|w| < 2 \text{ m s}^{-1}$ ) with 1-2% reaching  $6 \text{ m s}^{-1}$ , which was consistent with Black et al. (1996) who found that 70% of the vertical velocities from seven Atlantic hurricanes ranged between -2 and  $2 \text{ m s}^{-1}$ . The latter two investigators, however, showed that the broadest vertical velocity distribution was found in the eyewall with about 5% of vertical motions exceeding  $5 \text{ m s}^{-1}$ . Rogers et al. (2007) showed that in their dataset, modal values of vertical motions were negative in the lowest 2 km and positive above 9 km due to the reduction of liquid water loading caused by hydrometeor loss. Black et al. (1996) found that within TCs, updrafts

generally outnumbered downdrafts by at least a factor of two and that updrafts are wider and stronger than downdrafts. They further showed, that unlike updrafts, downdrafts did not exhibit any apparent radial sloping.

Nonetheless, it is not uncommon to find updrafts speeds exceeding  $10 \text{ m s}^{-1}$  in TC eyewalls, particularly when the storm is undergoing rapid intensification. Black et al. (1994) measured updraft / downdraft speeds reaching  $24 / 19 \text{ m s}^{-1}$ , respectively, in Hurricane Emily (1987) during its deepening phase. These unusually strong updrafts were associated with the presence of large supercooled water droplets (i.e., with a diameter ranging between 2-3 mm) at altitudes of about 12 km AGL (Black et al. 2003). Such occurrences are not rare; for instance, Bansemer et al. (2002) found high particle concentrations of about  $1000 \text{ L}^{-1}$  at temperatures as cold as  $-57^\circ\text{C}$  and large particles (7 mm) at altitudes up to 39000 feet in Hurricane Humberto (2001). Similarly, *in situ* aircraft microphysical data measured in Hurricane Bonnie (1998) suggested that supercooled water may exist at temperatures as low as  $-40^\circ\text{C}$  and that these particles were likely to be advected extremely rapidly there, preventing instantaneous freezing from occurring (Black and Heymsfield, 2002).

Consistent with overall weak updrafts, hurricane eyewalls generally contains little amount of supercooled water. Black (1984) showed that in the case of Hurricane Allen (1980) and Irene (1981), little amount of liquid water drops / droplets were formed within the updrafts above the melting level. They found that only updrafts wider than 1 km having vertical velocities greater than  $5 \text{ m s}^{-1}$  contained predominantly liquid water drops and droplets. Nevertheless, Black and Hallett (1986) found that in these two cases, *not all* updrafts having vertical velocities greater than  $5 \text{ m s}^{-1}$  contained appreciable amount of

liquid water droplets above the melting level. Supporting the lack of liquid water in hurricane updrafts above the freezing level, Black and Hallett (1986) showed that hurricane convection is largely glaciated even at temperatures reaching  $-5^{\circ}\text{C}$ . The sharp decrease in reflectivity with height observed within the eyewall and the outer rainbands further supports that most of the liquid water reaching the melting level becomes frozen below the  $-10^{\circ}\text{C}$  level, which is consistent with a recent study from Rogers et al. (2007). Jorgensen et al. (1985) hypothesized that the rapid falloff of radar reflectivity and cloud water content above the freezing level were attributed to warm-cloud coalescence processes, which should develop a full precipitation drop size spectrum before these reaches the freezing level. The relative weak mean updrafts caused an early fallout of the majority of the drops, before they reached the freezing level. Also, the smaller concentration of cloud condensation nuclei (CCN) over oceans will result in a droplet spectrum within maritime clouds having fewer small droplets (of radius  $< 10\ \mu\text{m}$ ) and greater amount of larger droplets (of radius  $> 20\ \mu\text{m}$ ), because fewer droplets compete for the same amount of available moisture (e.g., Rogers and Yau, 1989). Consequently, little amount of smaller and lighter droplets will be lofted above the freezing level in maritime clouds, which would prevent the formation of graupel pellets within the mixed-phase region. Moreover, the few large graupel often observed within the larger updrafts in TCs accrete cloud water quickly leading to progressively complete glaciation of the cloud in the mixed phase region ( $\approx -10^{\circ}\text{C}$ ). Black and Hallett, (1999) found that in the outwards region of TCs eyewalls, supercooled water was rapidly depleted due to the erosion of abundant amounts of ice present in downdrafts. In other words, they suggested that seeding by ice particles generated upstream of the radial flow limited the amount of

supercooled water within the eyewall. Consistent with this, observations made by May and Rajopadhyaya (1996) of a tropical squall line also revealed that mature cells were dominated by the effect of glaciation and that only significant updrafts having updrafts speed  $\geq 10 \text{ m s}^{-1}$  (which are relatively rare in TCs) contained appreciable amounts of supercooled water as much as 2 km above the freezing level.

During the NOAA and NASA Intensity Forecasting Experiment (IFEX, July 2005) aircraft field experiment campaign, *in situ* measurements showed that in the vicinity of Tropical Storm Dennis ragged “eyewall”, updrafts speeds at flight levels (between 4.2 and 5.8 km AGL) were reaching  $6 \text{ m s}^{-1}$  and that liquid (ice) particle concentration there were about  $6 \text{ g kg}^{-1}$  ( $4 \text{ g kg}^{-1}$ ). When the aircraft was at 5.5 km AGL ( $-4^\circ\text{C}$ ) they found a mixture of ice crystals and rimed particles with some having a diameter exceeding 1.6 mm (Rogers et al. 2006b). Houze et al. (1992) found that the ice particles at the 6 km level in Hurricane Norbert (1984) tended to be relatively large in both the eyewall and the outer rainbands. In the eyewall most of these particles were graupel, while in the outer more stratiform region the predominant particle type was aggregate in moderate concentration (consistent with Black 1984; Black and Hallett 1986; Willis and Heymsfield 1989). Houze et al. (1992) also hypothesized that the smaller and more abundant ( $100\text{-}300 \text{ L}^{-1}$ ) particles present between the eyewall and the outer stratiform region might have been produced by splintering of the graupel particle forming in the eyewall updraft. Graupel particles were coincident with the RMW because, unlike lighter aggregates, graupel particles were not as susceptible to azimuthal advection because of their relatively large terminal fall speed.

Black and Hallett (1986) suggested that the onset of lightning activity could be indicative of the presence of liquid water above the 0°C isotherm (Takahashi, 1978; Saunders et al. 1991). Also, strong updrafts were usually found nearby high reflectivity cores (30-40 dBZ echoes), while the opposite was not always true. Moreover, they found that these reflectivity cores primarily contained graupel and rounded ice particles but not liquid water, consistent with Willis and Heymsfield (1989).

Using trajectory analysis for the case of Hurricane Emily (1987), Willis and Heymsfield (1989) hypothesized that the ice particles growing and descending through the TC stratiform region were detrained by large reflectivity cores back into the lower levels of the eyewall. The high reflectivity values in the eyewall resulted from the fallout of graupel, raindrops and frozen drops close to their source. They also posited that the graupel confined in convective region was active in the nucleation (through rime splintering) of abundant supply of ice crystals, which initiated the aggregation process outside the convective region. Furthermore, Black and Hallett (1986) argued that most of the ice present in the eyewall updrafts originate from the “ice multiplication” mechanism and is then redistributed throughout the storm by the upper and midlevel anticyclones.

Using various data sources (e.g., TRMM, or CAMEX-3, Kakar 2006) Zipser and Jiang (2003) found that, in general, eyewall regions tend to have much more precipitation ice and liquid water mass than do the outer and inner rainbands. Nevertheless, liquid precipitation mass was still larger than ice precipitation mass within the eyewall.

Black and Hallett (1999) suggested that charge separation in TCs depends upon the relative mix of supercooled water in the eyewall updrafts and the ice particles that have been ejected from the eyewall inside the inner band stratiform region. They

proposed that the electrical activity is favored in a confined “mixed-phase region” between these updrafts and downdrafts near the storm’s core. Also, the strong horizontal winds in the eyewall will tend to spread the charged particles in a broader area, thus not allowing these particles to reside sufficiently long enough for sufficient charge separation to occur in a given layer in the eyewall. Consequently, this might explain why the vertical and horizontal electric fields observed within TC eyewalls are generally much weaker than in continental MCSs (Goodman and MacGorman 1986; Rutledge and MacGorman, 1988; MacGorman et al. 1989) and even supercells (MacGorman and Nielsen, 1991). For instance Goodman and McGorman (1986) showed that a single MCC could generate as much as 25% of the annual total lightning flashes at any sites it passes.

Based on the positive and negative CG flash (-CG and +CG, respectively) locations close to the eyewall (within 80 km), Molinari et al. (1994) hypothesized that the outward tilt of the updraft would cause the upper levels positive charge region to be advected radially outward towards the inner bands, producing more +CG there. In other words this would support the possibility of a normal dipole outwardly tilted along the sloping eyewall. However, Samsury and Orville (1994) found that in the case of TC Jerry (1989) and Hugo (1989), +CG flashes were not necessarily found to occur within the inner band stratiform region. Also, the tilted dipole hypothesis is nowadays not widely accepted because for instance, recent modeling work from Mansell et al. (2005) showed that a negative charge region must exist underneath the region of positive charge for +CG flashes to occur, the latter which is not a requirement in the tilted dipole hypothesis of Molinari et al. (1994). In the eyewall, Black and Hallett (1995) showed that in the deep

isolated convective cells of Hurricane Claudette (1991) graupel was carrying most of the negative charges at midlevels ( $\sim -5^{\circ}\text{C}$ ).

One of many other aspects not discussed here is the possible impact of the storm's own circulation on the lightning distribution and thus, the location respectively to the strongest updrafts. Corbosiero (1999) found that due to the storm's circulation, TCs tend to exhibit a downshear left azimuthal distribution of lightning flashes, so the lightning flash pattern appears slightly shifted from the downshear region where the lightning source (likely strong updraft) is located.

### III. Description of the numerical model.

#### III.1. Model dynamics.

The numerical cloud model used in this study (Straka Atmospheric Model, hereafter SAM) was developed by Straka and Mansell (2005). This model solves the quasi-anelastic (Anderson et al. 1985) Navier-Stokes equations for the three-dimensional wind field  $(u_1; u_2; u_3) = (u; v; w)$ :

$$\begin{aligned} \frac{\partial u_i}{\partial t} + u_i \frac{\partial u_j}{\partial x_i} &= -\frac{1}{\rho} \frac{\partial p'}{\partial x_i} + g \delta_{i3} \left[ \frac{\theta'}{\theta} + 0.608 q'_v - \sum q'_x - \frac{C_v}{C_p} \frac{p'}{p} \right] \\ &\quad + 2\Omega u_i \varepsilon_{ijk} + turb_{u_i} \\ turb_{u_i} &= -\frac{\partial \langle u_i'' u_j'' \rangle}{\partial x_j} \\ and \langle u_i'' u_j'' \rangle &= -K_M \left[ \left( \frac{\partial u_i}{\partial x_j} + \frac{\partial u_j}{\partial x_i} \right) + \frac{2}{3} \delta_{ij} e \right] \\ e &= \frac{1}{2} \langle u_i'' u_i'' \rangle \\ K_M &= C_K e^{1/2} l, \quad where \ C_K = 0.094 \ and \ l = (\Delta x \Delta y \Delta z)^{1/3} \\ \frac{\partial \theta}{\partial t} &= -\frac{1}{\bar{\rho}} \left( \frac{\partial (\bar{\rho} u_i \theta)}{\partial x_i} - \theta \frac{\partial (\bar{\rho} u_i)}{\partial x_i} \right) + turb_{\theta} + mphys_{\theta} \\ turb_{\theta} &= -\frac{\partial \langle u_i'' \theta'' \rangle}{\partial x_i} \\ where \ \langle u_i'' \theta'' \rangle &= -K_H \frac{\partial \theta}{\partial x_i} \\ and \ K_H &\approx 3 K_M \end{aligned} \tag{3}$$

The last term on the right hand side (rhs) of the momentum equation in (3) called ‘‘turb’’ is the subgrid-scale turbulence diffusion. All the variables inside brackets represent Reynolds average quantities over the grid volume  $\Delta x \Delta y \Delta z$  centered at the point of consideration. The primes denote local deviation from the constant horizontally

homogeneous base state, which are represented with overbars. The double primes are used for subgrid-scale quantities. The turbulent fluxes or covariance terms in the SAM model are parameterized using the downgradient K-theory (or Boussinesq analogy for molecular fluxes). The parameterization for the mixing length  $l$  is the same for stable and unstable conditions.  $K_M$  is the eddy diffusivity coefficient for momentum and  $e$  is the subgrid turbulence kinetic energy (for all the symbols used in the equations, the reader is referred to the nomenclature at the last page of the document). For practical purposes, however, some of the symbols will be described in the text.

The  $q_x$  terms in the momentum equation denote mixing ratios of the predicted microphysical quantities. The subscript  $x$  denotes the hydrometeor specie such as:  $r$  for rain,  $i$  for cloud ice,  $c$  for cloud water,  $s$  for snow,  $h$  for hail and  $g$  for graupel.

Mass continuity is written in terms of the perturbation pressure  $p'$  in flux form as follows:

$$\frac{\partial p'}{\partial t} = -C_{sound}^2 \frac{\partial(\bar{\rho}u_i)}{\partial x_i} \quad (4)$$

And the thermodynamic equation (in flux form) as:

$$\begin{aligned} \frac{\partial \theta}{\partial t} &= -\frac{1}{\bar{\rho}} \left( \frac{\partial(\bar{\rho}u_i\theta)}{\partial x_i} - \theta \frac{\partial(\bar{\rho}u_i)}{\partial x_i} \right) + turb_{\theta} + mphys_{\theta} \\ turb_{\theta} &= -\frac{\partial \langle u_i'' \theta'' \rangle}{\partial x_i} \end{aligned} \quad (5)$$

$$\text{where } \langle u_i'' \theta'' \rangle = -K_H \frac{\partial \theta}{\partial x_i}$$

$$\text{and } K_H \approx 3 K_M$$

$$q_{s,s} = \text{saturation vapor mixing ratio}$$

The last term on the rhs of (5) called  $mphys_\theta$  includes all diabatic heating effects (i.e., caused by sublimation, melting...etc) for each hydrometeor category, which are described in more details in Straka and Mansell (2005).  $K_H$  is the eddy diffusivity coefficient for scalars.

Dimensional pressure and potential temperature are the prognostic thermodynamic variables, while temperature and density are diagnosed.

For hydrometeors, the conservation equation (in flux form) is given by:

$$\frac{\partial q_x}{\partial t} = -\frac{1}{\bar{\rho}} \left[ \frac{\partial(\bar{\rho} q_x u_i)}{\partial x_i} - q_x \frac{\partial(\bar{\rho} u_i)}{\partial x_i} \right] + \frac{\partial}{\partial x_i} (K_H \frac{\partial q_x}{\partial x_i}) + \frac{1}{\bar{\rho}} \frac{\partial(V_x \bar{\rho} q_x)}{\partial x_3} + S \quad (6)$$

The first two terms on the rhs of (6) are the advection terms in flux form. The other remaining terms on the rhs represent turbulent mixing, fall out and source/sink terms, respectively.  $V_x$  is the terminal fall speed for the hydrometeor category  $x$ .

As mentioned earlier in the section, the SAM model solves the three-dimensional; non-hydrostatic, compressible equations of motion (which allows gravity and sound waves modes in the solution) using the time splitting procedure of Wilhelmson and Klemp (1978, hereafter WK78) on a Cartesian Arakawa C grid. This method uses a large time step (usually  $dt = 5$  to  $10$  s for  $dx = dy = 500$  to  $5000$  m) and a small time step to treat the sound wave mode separately as in WK78. This is done because sound waves usually impose severe restrictions on the time step (WK78, their equation 3.5) because of their fast velocity of about  $\sim 200$ - $300$  m s<sup>-1</sup>. Skamarock and Klemp (1992) demonstrated that WK78 time splitting method offered the best combination of stability, minimal filtering, simplicity and freedom from spurious noise or integrating the prognostic equations of motion. In general, many models prefer to use the anelastic approximation,

in which sound waves are removed from the compressible equations of motion, because larger time steps can be used (Anderson et al. 1985).

However, this approximation eliminates the more simple prognostic nature of the equation and yields to an elliptic equation for pressure (with non-linear terms acting as forcing terms) with constant coefficients, which is more complicated to code. WK78 showed that solving the fully compressible equations is computationally simpler than solving the elliptic equation by using their splitting method. An alternative between anelastic and fully compressible equation, called “quasi-compressible” has been developed by Chorin (1967) and applied by Anderson et al. (1985) into a numerical cloud model. The basic idea is to relax the pressure field to the anelastic pressure field by using a slow sound speed the Poisson equation for pressure. They showed that the quasi-compressible system exhibited comparable efficiency (in terms of the time steps) to an anelastic system while keeping the computer program and boundary condition simplicity of a fully compressible system. Also they found that the quasi-compressible solution rapidly converges to the anelastic solution when the speed of sound ( $C_{sound}$  in equation 4) was more than twice the fastest velocity simulated. Therefore, for our hurricane simulations, where horizontal wind speeds exceeding  $70 \text{ m s}^{-1}$  are common, we chose  $C_{sound}$  to be equal to about  $200 \text{ m s}^{-1}$ .

The simulation domain is translated at constant velocity as in Weisman and Klemp (1984). This was done in order to keep the squall line as close as possible to the center of the domain and hence, away from the boundaries. Except for the 300 m run, the model domain was translated with a constant speed of  $u = 11 \text{ m s}^{-1}$  and  $v = -4 \text{ m s}^{-1}$ . For

the 300 m we used of  $u = 13 \text{ m s}^{-1}$  and  $v = -5 \text{ m s}^{-1}$  for the first 7000 s of integration and  $u = v = 0$  for the remainder of the simulation.

The boundary conditions are as in WK78: open boundary conditions were applied at the lateral edges of the domain, in order to prevent an accumulation of energy in the domain from wave reflection. Because not all wavenumbers in the energy spectrum can escape the domain, this causes a few weak sporadic cells to develop along the lateral boundaries of the domain. As in WK78, the internal gravity wave mode with most energy (with corresponding intrinsic gravity wave phase speed  $c_{giw}$  set to  $30 \text{ m s}^{-1}$ ) is allowed to pass through the lateral boundary. That is, the local time rate of change of the velocity normal to that boundary does not vanish if  $(u+c_{giw}) > 0$  (meaning outflow). If the latter is  $< 0$  (inflow), we set  $du/dt = 0$  or  $dv/dt = 0$ . In summary, this means that no flow is allowed to enter the domain, while the gravity wave mode with most energy does not reflect back into the domain.

Rigid lid boundary conditions (i.e., all the kinematical variables vanish) were set at the top and at the bottom of the simulation domain. That is semi-slip for horizontal velocity and impermeable condition for the vertical velocity. Because we allow sufficient distance between the cloud top level and the model top (about 10 km) and because vertical transport of horizontal momentum is considered negligible, the rigid lid approximation at the top of the model is adequate.

The model uses a 1.5 order turbulence closure scheme. Diffusion of scalars is based on the prognostic equation for the *square root* of turbulence kinetic energy (TKE) following Deardroff (1980):

$$\begin{aligned} \frac{\partial E}{\partial t} = & -u_i \frac{\partial E}{\partial x_i} + \frac{1}{2E} [gu_3 \left( \frac{\theta'}{\theta} + 0.608q'_v - \sum q'_x \right)] + \frac{(C_M l)^2}{2} \left( \frac{\partial u_i}{\partial x_j} + \frac{\partial u_j}{\partial x_i} \right) \frac{\partial u_i}{\partial x_j} \\ & - \frac{1}{3} E \frac{\partial u_i}{\partial x_i} - \frac{\partial}{\partial x_j} \left( 2K_M \frac{\partial E}{\partial x_j} \right) - \frac{C_e}{2l} E^2 \end{aligned} \quad (7)$$

where  $E = e^{\frac{1}{2}}$  and  $C_e = 0.93$

The terms on the rhs of (7) are advection, buoyancy, hydrometeor loading, shear, divergence, mixing and dissipation. This equation was obtained by dividing the prognostic equation for the TKE “ $e$ ” by  $2e^{1/2}$  and using the following assumption:

$$\frac{1}{2E} \frac{\partial}{\partial x_i} \left( 2K_M \frac{\partial E^2}{\partial x_i} \right) = \frac{\partial}{\partial x_i} \left( 2K_M \frac{\partial E}{\partial x_i} \right) \quad (8)$$

Using an equation for  $e^{1/2}$  instead of  $e$  as many advantages. First, this avoids the necessity of taking square roots in calculating  $K_m$  (see equation (3)) and the dissipation rate  $\varepsilon$  at each grid point. Most importantly, we notice that the third term (or shear term) on the rhs of equation (7) is not a function of  $e$ . This term is a source term for turbulence and if we start the simulation with zero turbulence (i.e.,  $e = 0$ ), this term is able to generate TKE. In the prognostic equation for  $e$ , however, the shear term is multiplied by  $e^{1/2}$  and therefore all terms on the rhs of this equation will be zero, if no turbulence is present. As a result, one would need to “seed” turbulence initially by setting the buoyancy and/or shear term (i.e., the source terms) to small arbitrary values.

Once the model has computed  $e^{1/2}$ ,  $K_m$  and  $K_h$  are found using (3) and (5), respectively and are then used to compute  $e^{1/2}$  at the next time step.

In total, 42 scalars are advected using a 6th order flux conservative Crowley scheme (Tremback et al. 1987) with a monotonic limiter (Leonard, 1991) on a forward time step. These 42 scalars are: the potential temperature  $\theta$ , the water vapor  $q_v$ , the TKE

$e$ , the mixing ratios for the 12 hydrometeors species (see section III.2), the amount of charge carried by each of these 12 species, positive and negative ions, the time-averaged parcel cloud water content (used or riming conversion of graupel) and 12 time history variables (used to track particle density for riming and conversion to rain for rain water). The time history variables for rain, large hail and small hail are currently not used as hail and rain do not rime in the model. The flux conservative scheme has significantly less phase errors and amplitude error than the advective scheme. The 6<sup>th</sup> order scheme was shown to be the best balance between efficiency and accuracy (Tremback et al. 1987). For velocity, the model uses a leapfrog scheme with an Asselin filter in time, a 6th-order local spectral scheme in the horizontal and a 2nd-order box scheme in the vertical.

In the model, density and pressure are not filtered. Density is not filtered because it is considered anelastic (no  $X$  and  $Y$  variation). If density was filtered in the vertical it would become constant. In model, velocities are filtered, which essentially filters pressure. So filtering pressure would act like a second filter on velocity.

Also, a Rayleigh damping is applied to velocity and scalars in the stratosphere above 15 km to prevent spurious development, propagation and reflection of convective gravity waves (Fovell et al. 1992). Above that level (often called sponge layer), all of the vertical momentum flux through any level slowly tends to zero. Density and pressure are, however, not damped.

Furthermore, pressure divergence damping (e.g., Henshaw and Kreiss, 1995) is allowed to prevent the formation of low energy high amplitude pressure oscillations associated with transient computational modes, which usually occur after a sufficiently long integration time. In general, divergent damping is used to get rid of high frequency

low energy waves, which helps to keep the solutions stable.

### **III.2. Model microphysics**

The numerical cloud model features twelve discrete, bulk hydrometeor categories having an inverse exponential size distribution for all precipitation particles (Straka and Mansell, 2005). The model predicts total mass (mixing ratio) and diagnoses particle concentration from mixing ratio and assumed mean particle size (i.e., 1-moment model). Cloud ice number concentration is diagnosed using the (Meyers et al. 1992) parameterization for the number of active cloud nuclei, since the temperature dependent formulation of Fletcher (1962) frequently underestimates ice concentrations at warmer temperatures (Meyers et al. 1992). Furthermore the Fletcher formulation is not valid below -25 C and overprediction may occur if that curve had to be extrapolated to these temperatures. The main disadvantage of the Meyers parameterization is that crystal concentration is underestimated at warmer temperatures between -15°C to 0°C. In the model, the habit of any newly formed ice crystal is determined by ambient temperature only.

The microphysical package includes 12 separate categories for cloud water, rain, cloud ice (columns, plates, and rimed), snow particles, frozen drops, three graupel densities, and two size ranges of hail. This wide variety of cloud particles is important when modeling cloud electrification processes, since this allows a wider spectrum of terminal fall speeds and differential fall speeds, which directly influence the magnitude of charge separated during single collisions. In a more simplistic view, the model main

categories of hydrometeors are cloud water, raindrops, ice crystals, snow aggregates, graupel, frozen raindrops, and hail. The six sub-categories complement the main categories, based on various physical reasons. For example, there are columns and plates, which start to rime at different sizes, and rimed crystals. These rimed crystals are the ice crystals that can rime further to become graupel. The low-, medium- and high-density graupel categories are included to insure a differential fall out of graupel formed and grown in different strength updrafts and super-cooled liquid water contents. As mentioned earlier, these all influences electrical charging rates of graupel. Only the high-density graupel larger than 5 mm is converted to hail. Cotton and Anthes (1989) have noted “it is quite important, for example, to be able to distinguish between the occurrence of graupel and freezing rain, or the occurrence of numerous graupel and a few large hail stones.” In the model hail has sub-categories of small hail ( $5 < D < 20$  mm) and large hail ( $D > 20$  mm). The large hail category possibly is never active in TC simulations. The saturation adjustment of Tao et al. (1989) is used to deal with the influence of the phase change of bulk water to the vapor mixing ratio and ambient temperature.

### **III.3. Model electrification**

In the lightning model, bi-directional leaders propagate in a stochastic step-by-step fashion on a constant resolution grid (Mansell et al. 2002). The initiation of a lightning flash occurs when the ambient electric field at a given point in the storm exceeds the critical “runaway” threshold electric field (hereafter  $E_{crit}$ ). In the current study,  $E_{crit}$  was  $30 \text{ kV m}^{-1}$  at the top of the domain and was increased exponentially to

125 kV m<sup>-1</sup> at the surface. The model also features explicit treatments of small ions including attachment and drift motion following Chiu (1978) and Helsdon (1980). Additionally, corona emission, or point ion discharge currents, occurs whenever the magnitude of the vertical electric field component at a given point exceeds 5 kV m<sup>-1</sup>.

The primary electrification mechanism in simulated storms, at least initially, is the non-inductive (NI) mechanism involving collisions between riming graupel and cloud ice. In the model the following five NI charging parameterizations are currently available as an option: Riming Rate (Mansell et al. 2005), Gardiner (1985) modified by Ziegler et al (1991), Takahashi (1978), Saunders and Peck (1998) and Saunders et al. (1991) modified by Heldson (2001).

Electrification via inductive or polarization charging is also allowed when hail and graupel collide with cloud water as in Ziegler et al. (1991). The inductive charging strength is determined by the rebound efficiency ( $R_{eff}$ ) and average cosine of the angle of impact collision between the droplet and graupel (hail) particles (set to 0.40 degrees).

The magnitudes of the charge separated are very sensitive to the values of minimum and maximum ice concentration threshold (Mansell et al. 2005), which in the current version of the model are not explicitly predicted causing the actual amount of charge to be under-or-overestimated. In this study the minimum (maximum) ice concentration threshold is set to 500 (10 000 m<sup>-3</sup>).

## **IV. Description of the numerical simulations and their respective initialization procedures**

### **IV.1 Introduction**

Before carrying out the hurricane simulations it is important to stress that the current model has not been tested sufficiently for tropical, maritime storm simulations.

Moreover, recent modeling work from Bryan et al. (2003) showed that the large eddy simulation (LES) techniques used in cloud scale models (such as SAM) were not designed to perform at grid spacing ranging roughly between 500 m to about 10 km. They argued that in order for the LES schemes to perform well, a grid spacing of 100 m or less should be used. For our study, however, this finding is currently far beyond the current computing resources available, mainly because no message passing interface (MPI) version of the model is yet available. By going down to these very high resolutions (in the context of cloud scale or mesoscale systems modeling), one enables turbulence to occur, which result in a more detailed and more realistic looking structure of the convective system being modeled. For instance, phenomena such as cloud entrainment, Kelvin–Helmoltz billows are able to appear in the simulated storms, which can be important in redistributing for instance kinetic energy across the system. They were able to model these features because at these scales (100 m or less) a broader portion of the inertial subrange for subgrid kinetic energy can be explicitly reproduced on the model grid. Despite this problem, Bryan et al. (2003) still believe that numerical simulations carried out using grid spacing of 1 km or 2 km could offer a good insight on the basic

structure of the system even though quantities such as the magnitude of subgrid energy and subgrid water fluxes can be unacceptably large.

As mentioned earlier, the main goal of this study is to acquire a better qualitative view on TC microphysical and electrical properties. Therefore, we believe that choosing a horizontal grid spacing of 2-3 km for our idealized TC simulation (described later in section V.3) is adequate for our purpose.

## **IV.2 Squall line experiments set up**

In order to address the resolution dependence problem mentioned earlier and the necessity to test the model in reproducing maritime tropical convection, we chose to carry out several idealized squall line simulations of a well documented cases at four different grid spacings. We chose squall lines, because, unlike hurricanes, their overall dynamics is better understood (e.g., Thorpe et al. 1982; Rotunno et al. 1988; Xue 1990; 2000) and therefore the model results will be easier to compare with previous observations and numerical simulations. Another reason is related to CPU time as squall lines have a much smaller horizontal characteristic scale relative to hurricanes. Indeed, the hurricane simulations remain *extremely* expensive at horizontal grid spacings of 2 and 3 km. (For the 2 km run, between 8 h and 17 h of wallclock time were required to generate 200 s of cloud time, depending on the IC flash rate). The final reason is that there exists several well-documented cases (some even including electrification) of tropical squall lines in the literature.

In particular, on February 1993, several oceanic tropical squall lines were particularly well sampled by the TOGA COARE field program. One of these, namely the 22<sup>nd</sup> February 1993 maritime tropical squall line case of Trier et al. (1996) was particularly well sampled and simulated. Therefore this case provides an ideal basis for our study.

All the simulations presented herein were carried out using the 10-ICE microphysics scheme of Straka and Mansell (2005). We decided to make use of this more complex and more computationally expensive scheme, because one of the main goals of this study is to acquire a better overview of electrification properties within TCs (and also squall lines). Electrification (i.e., charge magnitude and polarity) resulting from charge separation during collisions between hydrometeors, particularly riming graupel pellets and ice crystals, is highly dependent on the differential fall speed between the colliding particles (among other factors such as ambient temperature). Therefore, the 10-ICE scheme provides a better test bed for evaluating electrification processes because its greater variety of hydrometeor species allows a broader spectrum of differential fall speeds. However, one important question needs to be addressed: Does the choice between the 3-ICE (i.e., LFO type scheme with snow aggregates, cloud ice and graupel/hail as the three distinct ice species) and 10-ICE scheme strongly influence the simulated storm dynamics? This can occur for example via differences in latent heat profiles resulting from more (or less) melting, freezing, riming, evaporation or condensation.

In order to address the scientific questions raised by Brian et al. (2003) work, 4 simulations of the Trier et al. (1996) TOGA COARE case were carried out using four different horizontal grid spacings of 300 m, 600 m, 1 km and 2 km. Except for the 300 m

simulation, we kept the vertical grid spacing and the domain size identical (of 132 x 210 x 24 km). The 300 m simulation was carried out in a smaller domain of 100 x 100 x 26 km and used 65 vertical levels instead of 60. These four simulations will also allow us to determine how grid asymmetry (i.e., when  $dx/dz$  or  $dy/dz > 1$ ) influences the simulated squall line dynamical and microphysical properties.

Except for the 300 m simulation, which was run up to 3 h, all the simulations were carried out for about 5 h and 30 min (20000 sec) of cloud time. The vertical grid spacing near the surface was set to  $dz = 100$  m and stretched to  $dz = 600$  m at and above 7 km AGL with an average spacing of 400 m. In all four simulations, the horizontal lightning grid spacing was set to half the horizontal grid spacing. The horizontal spacing for lightning is smaller (interpolated) so that the horizontal grid spacing ( $dx$  and  $dy$ ) and the vertical grid spacing  $dz$  are more comparable for propagation. As a consequence, the electric field estimates (i.e., potential gradients) around the channel points will be less biased by resolution differences.

The time step for the implicit solver in the vertical was set to 2 s for the 300 m case, and to 5 s for the remaining three simulations. The surface fluxes (i.e., of momentum, latent heat and moisture) for all the squall line simulations were turned off because an additional test runs carried out at a horizontal grid spacing of 1 km did not show any significant differences compared with the same simulation having the surface fluxes turned on. This finding is also in agreement with Trier et al. (1996). For our squall line study, however, we decided to include the effect of the Coriolis force as the latter showed to have a small but nonetheless relative important impact on the squall line dynamics (see next section for the details).

The initial environmental conditions were assumed to be the same for the entire simulation domain and were represented by the composite P-3 model sounding of Trier et al. (1996, their Fig. 2) from Honiara, Guadalcanal. This sounding is nearly moist adiabatic and has moderate to high convective instability (CAPE near  $1500 \text{ J kg}^{-1}$ ) and no convective inhibition. A low level jet of  $\sim 12 \text{ m s}^{-1}$  is located near 2 km AGL. Differences in the interpolated soundings are expected, since we use a different vertical grid spacing configuration than Trier et al (1996). After interpolation, the sounding we used (Fig. 3) has a CAPE of  $1856.5 \text{ J kg}^{-1}$  and a convective inhibition (CIN) of  $2.2 \text{ J kg}^{-1}$ . Because the 300 m simulations featured 5 more vertical levels than the remaining three, the CIN and CAPE values after interpolation to the grid revealed some small and negligible differences.

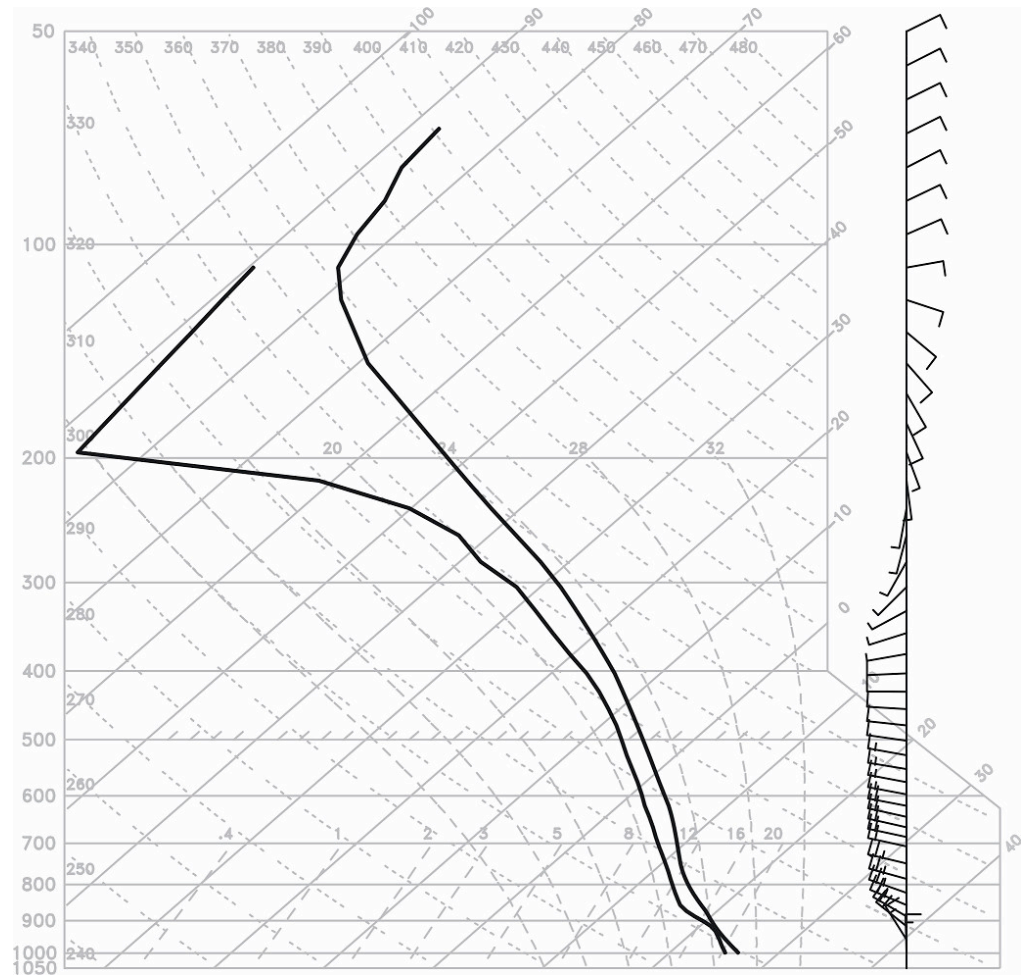


**Fig. 3.** Skew-T log-p diagram of the 22<sup>nd</sup> February 1993 squall line case, from Honiara, Guadalcanal interpolated to the model grid.

Similar to Trier et al (1996), a -7 K ellipsoidal temperature anomaly was used to trigger convection in the model. This cold anomaly, centered at  $z = 1500$  m, and except for the 300 m case had dimensions of 20 x 120 x 2 km and was placed at  $X = 60$  km and  $Y = 108$  km. For the 300 simulation the initial cold anomaly had dimensions of 20 x 50 x 2 km and was placed at  $X = 36$  km and  $Y = 49.5$  km. In all our simulations, the cold anomaly was oriented in a north-south manner, whereas Trier et al. (1996) had an initially 330°-150° oriented line of -8 K overlapping spheroidal cold anomalies, which maximized the squall line's relative inflow below 1 km. Separate test simulations, not presented here,

using Trier et al. method, showed that the resulting squall line was overall less organized and not as well developed after 5 h than with our simpler initialization procedure.

Our idealized *modus operandi* to trigger convection resulted in an initial development of convection along a North-South oriented line (see next section), as the gravity current caused by the collapse of the initial cold anomaly allowed this convection to persist along its leading edge, mimicking real squall lines. The magnitude of the cold anomaly rapidly decreased from -7 K to about -2 K due to mixing.

For the electrification, the SP98 NI charging scheme was selected along with moderate inductive charging settings (see later in the section for further detail). We chose the SP98 NI scheme because Mansell et al. (2005) found that the latter gave more varied results in most cases, particularly in terms of the polarities of CG flashes. RAR also is physically a more attractive variable than ambient CWC as it accounts for the rate of latent heat release and vapor supply from accreted droplets.

The analysis of the squall line simulations output will be separated in two parts: The first one will focus on describing the simulated squall line microphysical, dynamical and electrical properties. Particular focus will be directed towards the reflectivity profiles evolution, the depth of the convection, the wind profiles and the precipitation structure and intensity. For this analysis, the 600 m squall line was selected, because at this horizontal resolution, the average updraft width can be resolved on the grid. Indeed, Bryan (2006) showed that in continental storms, the average updraft width lied between 2 and 4 km and that for a horizontal grid spacing of  $dx$  ( $= dy$ ), numerical models were generally able to resolve updrafts width greater or equal to about  $4 \times dx$ . Therefore, if  $dx = 600$  m, the minimum updraft width than can be resolved on our grid will be about 2.4

km, which lies within the range of observed average updraft width. Nonetheless, Bryan (2006) found that for horizontal grid spacings ranging between 125 m and 8 km, his model produced in average the largest updraft speeds for  $dx$  lying between about 500 m and 1 km and also produced the largest upward mass fluxes for  $dx$  values between 1 km and 2 km. Indeed, at finer horizontal resolution (i.e.,  $< 500$  m), the majority of the simulated updrafts are smaller and hence, more prone to dilution by entrainment. Therefore, while typical average updraft sizes can be represented on our grid, the average strength of these updrafts will likely be overestimated.

The second part will focus on evaluating the differences in the dynamical, microphysical and electrical properties of the simulated squall line between the four different horizontal grid spacings selected. The 300 m simulation was intended to represent the lower limit at which the inertial subrange started to become crudely reproduced, although Bryan et al. stressed that 100 m was needed for this purpose. We decided not to go down to 100 m, because we also included lightning in this sensitivity study, which requires about 80% more CPU time.

Our squall line simulation will be best compared to Trier et al. (1996) “weak shear” case (defined with  $10 \text{ m s}^{-1}$  speed shear in the lowest 2.5 km), because in our case, the speed shear was less than  $5 \text{ m s}^{-1}$  in the lowest 3.5 km (Fig. 3).

As a separate experiment, a high-resolution simulation of another TOGA COARE squall line (one of the 9<sup>th</sup> February 1993 cases) was carried out and is presented in Appendix A. The results presented in this appendix supplement those shown for the Trier et al. (1996) case.

### IV.3 Hurricane experiments set up

Once the squall line simulations have been analyzed in detail, two sets of idealized hurricane-like vortex numerical simulations were performed in this study: the first set was called OCEAN and the second one was named LAND. Each of these experiments were carried out separately. The OCEAN experiment consisted of one simulation while the LAND case was composed of two simulations. The details behind each of these cases are described below.

Before describing the simulation procedure for each of these two experiments, it was important to mention that a separate hurricane test simulation at  $dx = dy = 2$  km, not shown in this study, was also carried out with LFO microphysics (instead of 10-ICE). The parameters and settings were identical than for the OCEAN case (described in the next paragraph). The results did not reveal as much differences in the simulated storm evolution and structure than for the squall line case, which suggests that the evolution of the hurricane-like storm in the simulation was more controlled by the dynamics rather than the microphysics. Nonetheless, the 10-ICE scheme was still necessary for our two sets of hurricane simulations because this more complex scheme provides a broader hydrometeor fall speed spectrum, which, as mentioned earlier, is indispensable for modeling charge separation with more accuracy.

The first TC experiment (OCEAN) consists of one simulation, which was carried out over an idealized, uniform warm ocean. The domain had 300 x 300 grid points in the horizontal with a horizontal grid spacing of 2 km and 46 vertical levels on an Arakawa C-grid. The lightning grid spacing was set to 1 km. The vertical grid stretched from 200 m

at the surface to a constant value of 600 m between 5.5 km and 17 km AGL. Above 17 km, the vertical grid stretched from 600 m to 1200 m. The model used a large time step ( $dt$ ) of 10 s, which, according to the CFL (Courant-Friedrich-Levy) criterion, would allow updraft speeds up to  $60 \text{ m s}^{-1}$  ( $dz_{top}/dt = 600 \text{ m} / 10 \text{ s}$ ) to be represented on the grid. Restrictions on the large time steps mainly arise from the vertical grid spacing because in a cloud model we usually have  $dx$  and  $dy > dz$ . Also, because we use explicit microphysics in the model, the large time step has to be small enough to allow more accurate calculations of the microphysics variables, thereby setting an upper bound for  $dt$ . To treat sound waves, the model uses a vertical explicit small time step solver with  $dt_2 = 0.5 \text{ s}$ . We chose this value for  $dt_2$  because it lies within the bounds of stability (i.e., WK78, their formula 3.5) of the solution.

For this experiment, landfall was not included, because the primary goal of this simulation was to provide a first quantitative description of the electrical and microphysical behavior of the storm.

The second TC experiment was intended to assess the impact of an idealized uniform, dry, flat land mass on the storm's microphysics and lightning (hereafter called LAND). Towards this goal, this experiment makes use of two additional (i.e., separate) simulations. As a first step, a control simulation was made without land parameterization similar to the simulation presented in the OCEAN case. Then, a second simulation was carried out with an idealized land mass, keeping all the kinematical, microphysical and electrical parameters identical. In this model, surface momentum fluxes were enhanced over land (by about a factor 10), while the surface sensible heat and moisture fluxes were set to zero: for momentum fluxes we set  $C_d$  to  $2 \times 10^{-2}$ , which is about one order of

magnitude greater than over water ( $1.14 \times 10^{-3}$ ). The land (or coast) was represented by a meridionally oriented slab moving towards the east at a constant translation speed of  $8 \text{ m s}^{-1}$ . In other words, we forced the coast to move towards the center of the domain where the center of circulation of the TC was located (see Fig. 4, land position shown for  $t = 1600 \text{ min}$  time at which the cross sections through the hurricane were taken). In the simulation, the land mass was introduced in the domain at  $t = 37000$  so that it would reach the TC eyewall only at maturity (which is near  $75000 \text{ sec}$ , see section V.3.2).

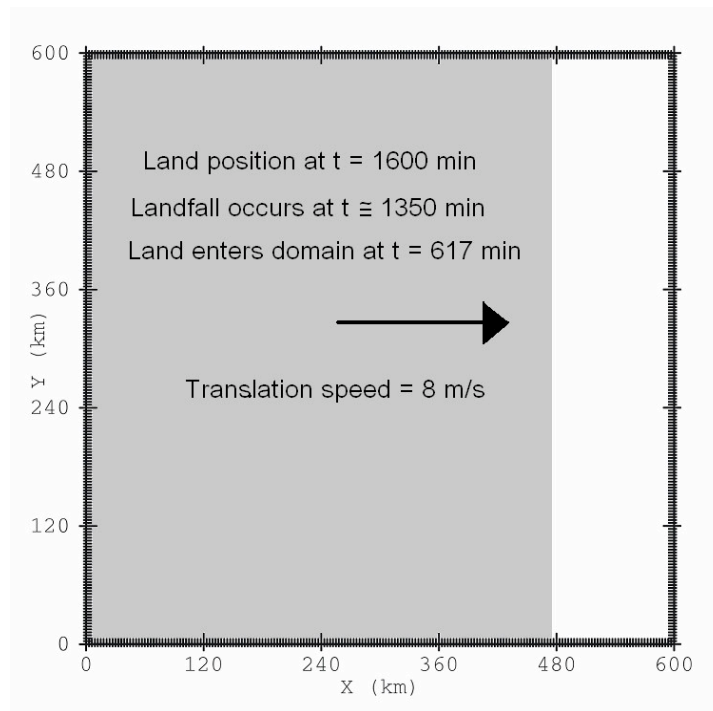
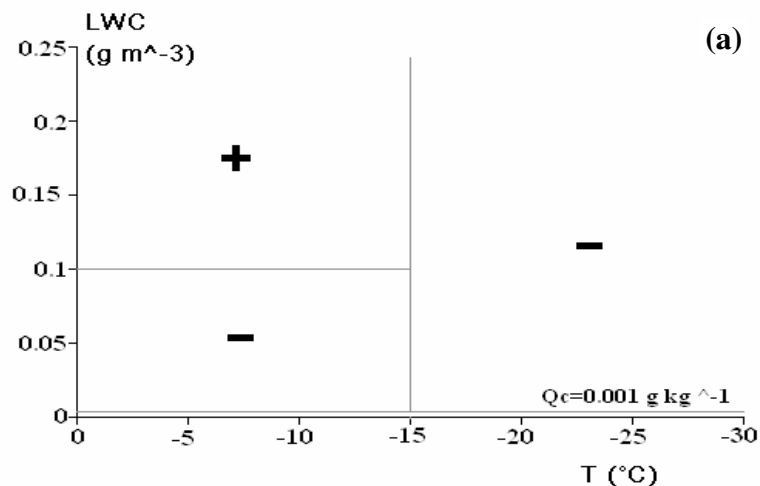


**Fig. 4.** Sketch of the land/coast position and orientation at  $t = 1600 \text{ min}$  for the second simulation of the LAND experiment.

Due to the very high cost of these numerical simulations and the relative small differences in microphysical and electrical behavior between horizontal grid spacings of  $2 \text{ km}$  and  $3 \text{ km}$ , the two numerical simulations in the LAND case were performed at  $dx = dy = 3 \text{ km}$ , while keeping the number of vertical levels, stretching factor and domain size identical. For the LAND case, the lightning grid spacing was set to  $1.5 \text{ km}$  (compared to

1 km for the OCEAN case). As for the OCEAN case, a large time step  $dt$  of 10 s was used for integrating the model equations.

As for the squall line simulations, the OCEAN experiment used the Saunders and Peck (1998, SP98, Fig. 5a) NI scheme. Brooks et al. (1997) transformed the Saunders et al. (1991) charging scheme to be in terms of the riming accretion rate (hereafter RAR) instead of LWC. The latter is defined as the effective liquid water content  $EW$  multiplied by the differential fall speed  $V$  between the droplet and the graupel.  $EW$  is defined as the portion of the cloud LWC that is captured by the rimer by virtue of its collection efficiency. Brooks et al. (1997) constructed a curve of critical RAR, which defined the upper and lower limit at which graupel acquired negative and positive charges, respectively. SP98 carried out further experiments at larger ranges of temperatures to better determine the RAR critical curve. In this study, the original SP98 curve was modified by Mansell et al. (2005) to be consistent with the fact that supercooled water can exist at temperature as low as -40 C and was thus translated towards that lower limit.



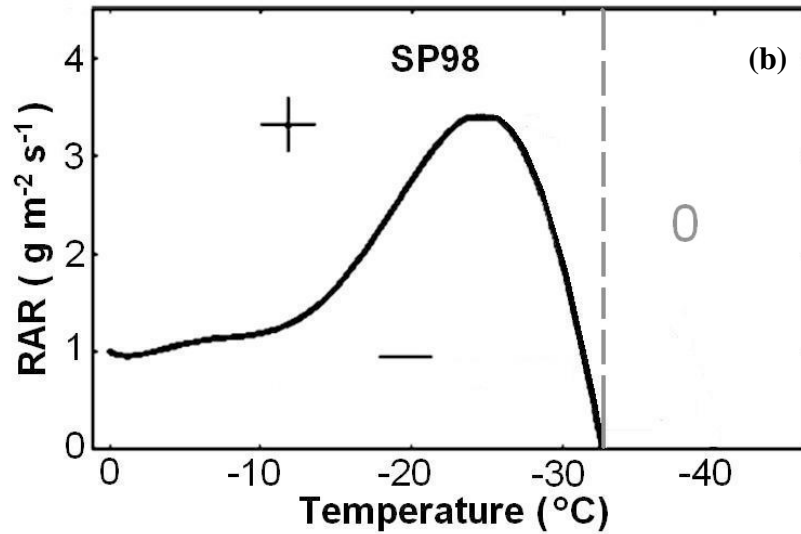


**Fig. 5.** (a) Gardiner et al (1985) NI scheme critical curve diagram adapted by Ziegler et al. (1991). The charging sign acquired by graupel particles colliding with ice crystals is shown by + and -, respectively. (b) Original Saunders and Peck (1998) For this scheme, there is no charging at temperature colder than  $-32.5\text{ }^{\circ}\text{C}$ , (indicated by the grey dashed line and the 0). In the Gardiner et al. scheme, graupel is not allowed to gain charges below the line of constant values of  $q_c = 0.001\text{ g kg}^{-1}$ .

The primary goal of the LAND experiment was to provide a qualitative description of the evolution of the storm electrical evolution at landfall. For this reason, the two simulations carried out in the LAND experiment used the Gardiner / Ziegler (1985, Fig 5b) NI charging scheme, where the magnitude of charge separated during individual graupel-ice collision can be modulated. The latter scheme is based on the Ziegler et al. (1991) adaptation of the Gardiner et al (1985) parameterization, which is based on the laboratory results of Jayaratne et al. (1983). Here, charging sign and rate is a function of  $q_v$  and  $T$ . This scheme uses a fixed charge reversal temperature  $T_r$ , which was set to  $-15\text{ }^{\circ}\text{C}$  for this simulation. Graupel and hail particles acquire negative charges at temperatures lower than  $T_r$  while gaining positive charges for collisions occurring at higher temperature. Additionally, the charging is negative at low CWC ( $< 0.1\text{ g m}^{-3}$ )

regardless of temperature. For cloud mixing ratio ( $q_c$ ) values less than  $10^{-3}$  g kg<sup>-1</sup>, charging was set to zero (Fig. 5b). To reduce the IC flash rate and computational costs, we chose to set the multiplier controlling the magnitude of charge separated during individual graupel-ice collisions to 0.0009. This procedure had, however, little influence on the total CG flash rate of the storm because the lowest charge layers (which control the CG flash rate and polarity) are also attributed to inductive charging (see later in this study).

For the same reason described earlier, the rebound efficiency  $R_{eff}$  controlling the inductive charging strength will be set to a smaller value in the LAND case (0.005) than in the OCEAN case (0.01). The impact of the land mass upon the storm microphysical evolution, however, will be described quantitatively, since the latter parameters are identical than in the OCEAN experiment.

The initial wind field was imposed as a modified Rankine-type vortex (from Kanak, 1990) in gradient wind balance, the strength of which could be modulated via changes in its radius and maximum relative vorticity (among other parameters). This modified Rankine vortex was cyclonic with decaying intensity in both horizontal and vertical directions, and the vertical vorticity  $\xi$ , is defined by

$$\xi = \begin{cases} \xi_{\max} & r = 0 \\ \xi_{\max} * e^{-\alpha r^4} & 0 < r < r_{\max} \\ 0 & r > r_{\max} \end{cases} \quad (8)$$

$$\alpha = -\ln(0.1) / (r_{\max})^4$$

In the vortex initialization, the vorticity values were normalized on the horizontal plane by summing the vorticity values of equation (8), which was then divided by the

sum of  $\sin(\pi r/r_{max})$ . The resulting ratio was then multiplied by each value of the sine function, which was then subtracted from each value of (8) in order to achieve a vorticity field with equal amount of positive and negative vorticity. The wind field was then computed using the streamfunctions  $\Phi$  defined as:

$$\begin{aligned}\nabla^2\Phi &= \xi \\ u &= A \frac{\partial\Phi}{\partial y} \\ v &= A \frac{\partial\Phi}{\partial x}\end{aligned}\tag{9}$$

Where  $A$  in (9) is a function which forces the winds to decrease exponentially in the vertical and is defined as:

$$A = \begin{cases} 1 & z \leq 15 \text{ km} \\ \text{Exp}\left(-\left(\frac{z-15}{2}\right)^2\right) & z \geq 15 \text{ km} \end{cases}\tag{10}$$

The maximum height of the vortex (i.e., above which the horizontal winds decrease exponentially to zero), is set in equation (10). In this study we chose this height to be 15 km.

An attractive feature of this vortex was its ability to remain stable and not to break down into several smaller vortices. In fact, several simulations with microphysics turned off, were carried out up to 50 h and showed that for a wide range of vortex sizes and strengths, the vortex maintained its initial shape and size, while slowly weakening under frictional effects.

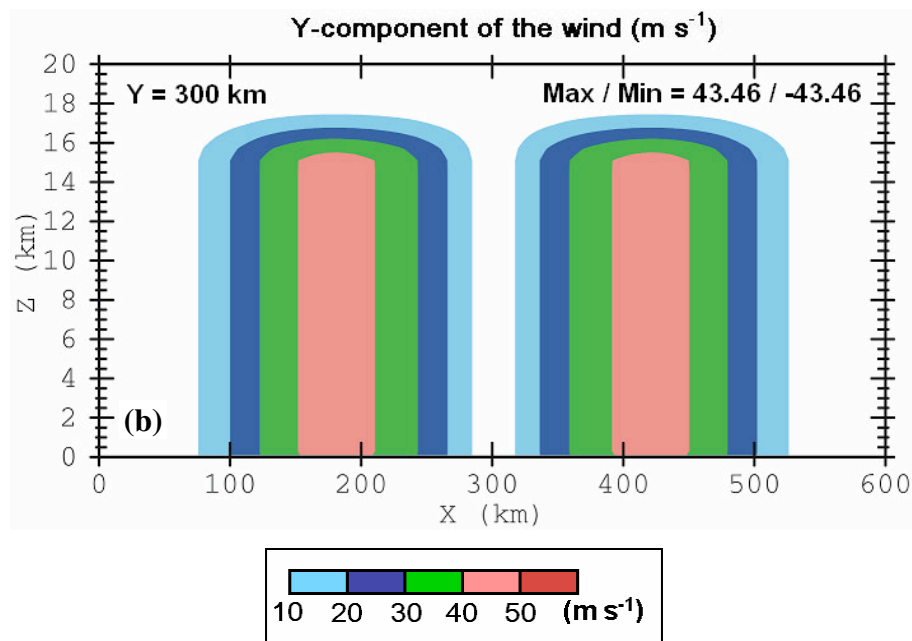
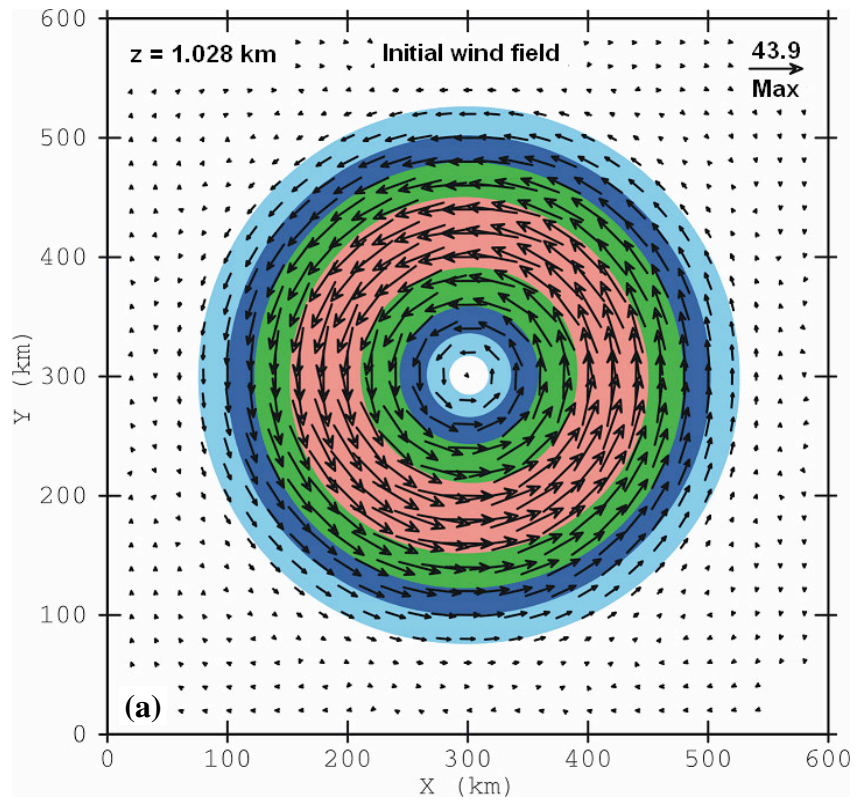


**Fig. 6.** (a) Horizontal cross section of the initial wind vector field overlaid by the initial wind speeds at  $z = 1.028$  km and (b) vertical cross section ( $X$ - $Z$ ) at  $Y = 300$  km of the initial wind speed. The wind speed scale is shown at the bottom of panel (b)

For our simulation we chose  $\xi_{max} = 13 \times 10^{-4} \text{ s}^{-1}$  and  $r_{max} = 280 \text{ km}$ . With these settings the maximum winds were about  $43.5 \text{ m s}^{-1}$  and were located at a distance of 180 km from the center (Fig. 6).

If the initial winds were to be weaker, a significant delay in the development of the convection by frictional convergence would occur, and in some cases, a hurricane-like vortex would fail to form. This procedure was mainly motivated because of the large amount of CPU needed for these hurricane simulations. On the other hand, for the same initial vortex radius, initial winds greater than about  $55 \text{ m s}^{-1}$  caused a rapid development of scattered convection the domain, which ultimately dominated that of the eyewall, resulting in an early decline of the storm.

The following simulation was carried out on an  $f$ -plane with Coriolis parameter set to  $3 \times 10^{-5} \text{ s}^{-1}$ . We did not consider latitudinal variations of  $f$ , because the  $\beta$ -effect mainly has an influence on the storm track (see section II.1.6) and not on the storm microphysical and electrical structure, which is the focus of this study.

Lower values of  $f$  (i.e.,  $< 2 \times 10^{-5} \text{ s}^{-1}$ ) gave similar results than for  $f = 0$ . Early test runs (using the same vortex size and strength shown above) revealed that setting  $f = 0$  resulted in intense convection developing progressively inward inside the vortex, leading to an unrealistic-looking solid disk of convection (i.e., with an eye of diameter  $< 10 \text{ km}$ ) with reflectivity values increasing rapidly towards the center. This small eye quickly dissipated (near 58000 s) and was immediately followed by the collapse of the vortex (rapid rise of the minimum surface pressure) and the development of sporadic convection in the entire domain. Most probably, the strong cold pool of the intense convection at the center of the disk ultimately dominated the lateral inflow causing a quick collapse of the

secondary circulation and hence, the vortex itself. As  $f$  increased, the diameter of the eyewall (and eye) increased as additional supply of planetary vorticity was constantly ingested into the storm, acting as an additional source of angular momentum. For instance, for a typical midlatitude values of  $f$  (i.e.,  $10^{-4} \text{ s}^{-1}$ ), the diameter of the eye at 45000 s was about 130 km compared to about 15 km for  $f = 0$  and about 40 km for  $f = 3 \times 10^{-5} \text{ s}^{-1}$  at the same time. Also, as  $f$  increased, progressively less convection developed outside the eyewall.

The surface pressure at sea level was 1011 mb everywhere across the domain. The sea surface temperature was set to  $28^\circ\text{C}$ , in order to enhance surface sensible heat fluxes (of Rotunno and Emanuel, 1987) at the lower boundary of the domain. Also, many studies showed that if the water temperature did not reach about  $26^\circ\text{C}$ , TCs generally did not develop (e.g., Palmen, 1948; Shay et al. 2000).

For both the LAND and OCEAN experiments, the initial environmental conditions were represented by a composite sounding of the 00 UTC Owen Roberts Airport, Grand Cayman Island sounding below  $z = 15 \text{ km}$  and the 00 UTC Kingston, Jamaica sounding of August 13<sup>th</sup> 2004 above that level (Fig 7, black thicker line). This was done because at that particular time, the Grand Cayman Island sounding had no data above 15 km. We chose the Kingston sounding for the composite because it was the closest station available around the Grand Cayman Island. At that time, Hurricane Charley passed over or near the islands (less than 100 miles) and was rated as a category 3 on the Saffir-Simpson scale (Simpson, 1974). As shown by the green lines in Fig. 5, the original composite sounding was modified in order to optimize the chances for a well defined hurricane-like vortex to form. The dry layer present between 300 and 500 mb

was likely a residual Saharan airmass (Dr. Jason Dunion, personal communication, 2006). Therefore, since this layer did not have a tropical/maritime origin, it was removed from the sounding. The sounding was also moistened between 500 and 800 mb in order to reduce evaporative cooling and hence downdraft strength at these levels. Also, between 700 and 850 mb, a capping inversion layer was added in order to prevent the convection within the bands from developing too rapidly at the beginning of the simulation. After these modifications, the sounding was nearly moist adiabatic, which is what is typically observed in the tropics over ocean away from land. The CAPE and CIN values of the model sounding (i.e., when interpolated to the model grid) were about 1473.6 and 99.2 J kg<sup>-1</sup>, respectively, compared to 1560 and 22.1 J kg<sup>-1</sup> in the original composite sounding.

It is noted that due to the idealized nature of the hurricane initialization in the model, the simulation presented in this study was not intended to reproduce Hurricane Charley (2004). Rather, the environmental conditions from this sounding are believed to offer an initial field that would favor hurricane development. That is, the sounding was assumed to be representative of typical conditions nearby intensifying or steady state hurricanes over ocean.

In order to keep the TC from moving away from the center of the domain the translation speed of the domain was set to constant values of  $u = -2.5 \text{ m s}^{-1}$  and  $v = 1.5 \text{ m s}^{-1}$  in all the 3 TC simulations presented herein.

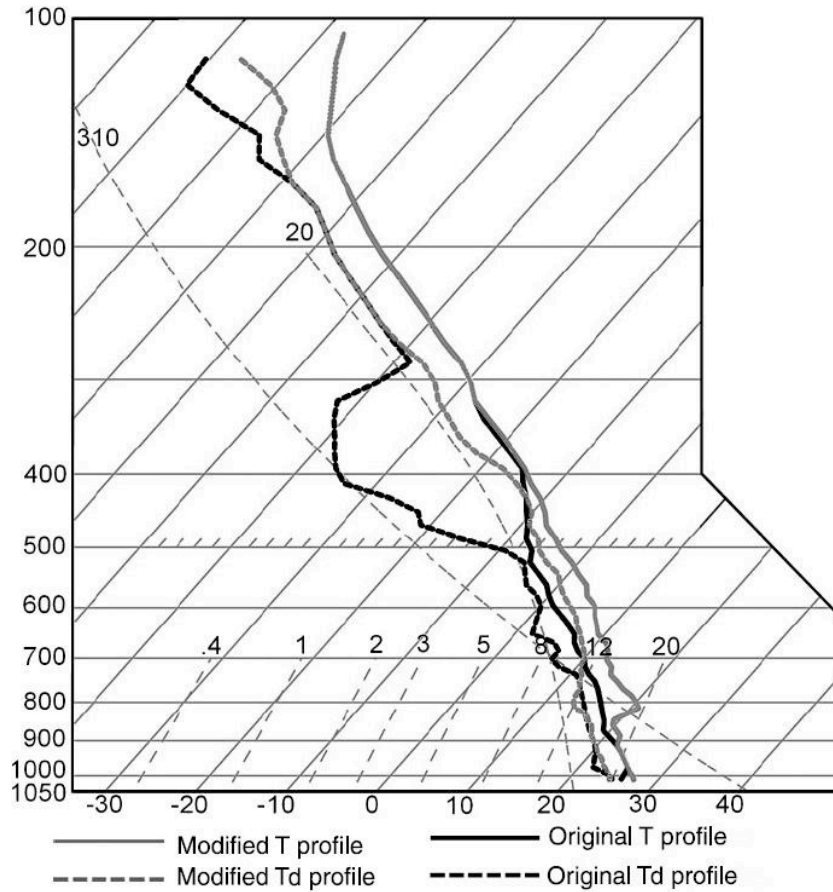


**Fig. 7.** Original (modified) composite Skew-T log-p diagrams (shown in thick black (green) lines for original (modified) sounding) of the 13<sup>th</sup> August 2004, 00 UTC Owen Roberts airport, Grand Caiman Island and 00 UTC Kingston, Jamaica.

For the three hurricane simulations presented in this study, convection in the vortex is triggered via local surface sensible heat fluxes. The surface layer parameterization makes use of velocity dependent, bulk aerodynamic formulae for sensible and latent heat fluxes, as well as for momentum fluxes following Rotunno and Emanuel (1987). The model also uses the surface dissipative heating parameterization of Bister and Emanuel (1998). The primary reasons for using these more simplistic bulk aerodynamic formulae (compared for example to the Louis (1979) surface layer parameterization) is that we use a rather coarse resolution in the vertical and also because these are also valid for high wind speeds. Furthermore, these simple formulae are very

easy to implement in a numerical model and have also been tested with success for hurricane simulations at somewhat coarse vertical resolution by Rotunno and Emanuel (1987). The drag coefficient ( $C_d$ ) for heat and moisture fluxes follows Deacon's formula (e.g., see formula (36) of Rotunno and Emanuel, 1987), where  $C_d$  increases with increasing wind speed, while for momentum flux  $C_d$  was set to a constant value of  $1.14 \times 10^{-3}$  (over water). The sea surface temperature was set to  $28^\circ\text{C}$  to enhance surface sensible heat fluxes at the lower boundary or first grid point above the ground of the domain.

## **V. Numerical simulations results**

### **V.1. Maritime tropical squall line simulation.**

#### **V.1.1. Introduction**

As mentioned earlier, the main motivations for this analysis were:

- The necessity to test the current model in a maritime tropical environment
- The need to determine quantitatively how sensitive the model simulated convection and associated dynamical, microphysical and electrical properties were to the horizontal grid spacing.

Improvements over Trier et al. (1996) work were the use of finer grid spacings, a far more sophisticated microphysical package and a three dimensional lightning module. Also, Trier et al. (1996) did not include lightning in their modeling / observational study. In a more recent study from Petersen et al. (1999), one of their squall lines which they referred as the “weak forcing” case, formed in similar environmental conditions than the Trier et al. (1996) “weak shear” case selected for this study. Both soundings had CAPE ranging between 1500 - 2000 J kg<sup>-1</sup> with almost no CIN (< 5 J kg<sup>-1</sup>). Moreover both vertical wind profiles exhibited a low level jet of about 20 knots near 850 mb and a similar curvature (i.e., directional shear) with height. All these environmental parameters being relatively similar, we believed that it was appropriate to also establish a comparison between our simulated microphysics fields with the Petersen et al. (1999) weak forcing observational case.

Petersen et al. (1999) also included lightning in their study. However, they only observed lightning in their strong forcing case, which cannot be *directly* compared to the Trier et al. (1996) case as the latter environment had stronger winds below 900 mb (by about  $5 \text{ m s}^{-1}$ ) and was also characterized by higher specific humidity above the mixed layer near 950 mb. Nonetheless, some qualitative aspects of the simulated lightning (e.g., CG polarity, CG strike location) will be compared to a first degree with Petersen et al. (1999) their strong forcing case because of the lack of such data.

### **V.1.2. Results of the 600 m squall line simulation**

After 2 h of simulation, the solid meridionally oriented line of convection started to resemble typical squall lines, with a well developed gust front at its leading edge (Fig. 8). The cold anomaly at the surface weakened after its initial collapse from a magnitude of -7 K to -2 K, but quickly regained strength once the downdrafts from the individual cells forming the convective line developed (not shown). The strong westerly jet present in the initial sounding at 850 mb caused the squall line to propagate in the X direction (Fig. 8).

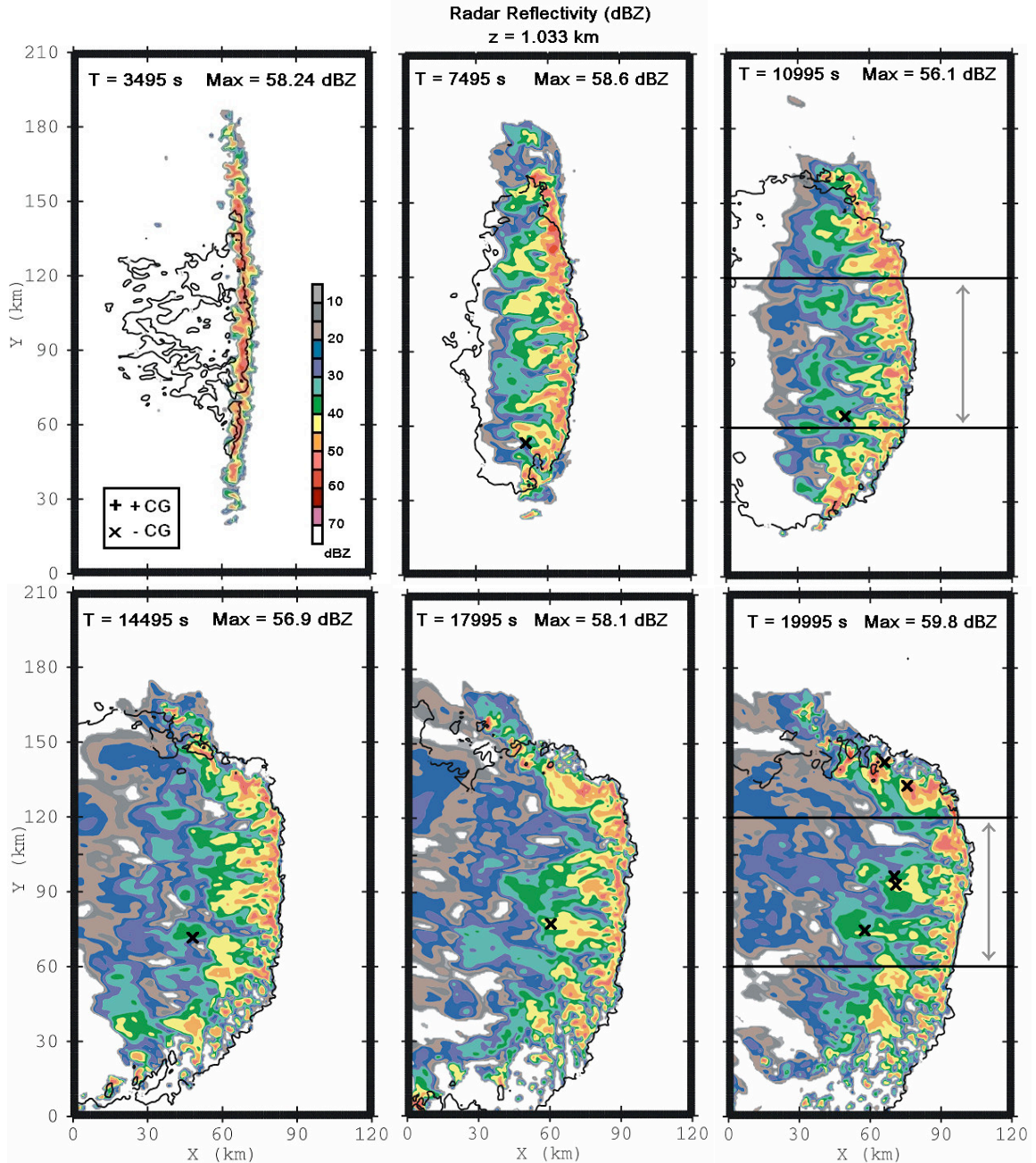


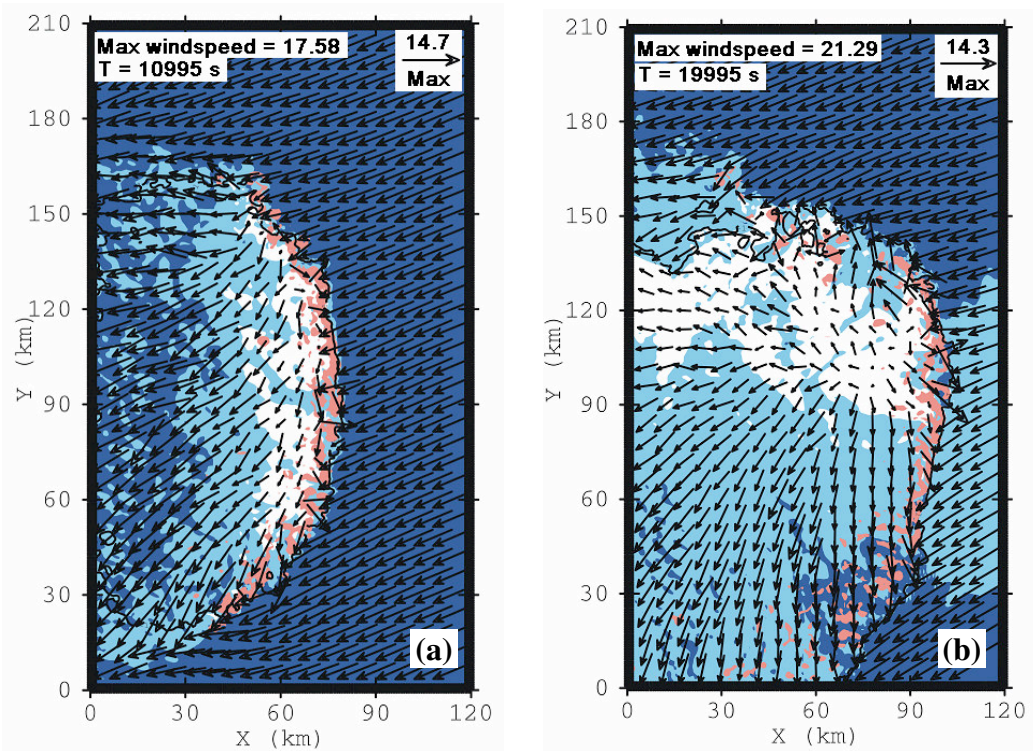
**Fig. 8.** Horizontal cross section of radar reflectivity (dBZ) at  $z = 1,033$  km AGL shown for each hour of the simulation. Contours are ranging from 5 dBZ to 75 dBZ by increments of 5 dBZ.. Locations of CG lightning strikes are also shown by a cross for –CG flashes and by a + for +CG flashes. The flash locations were plotted for a 30 min time interval until the cross section time. The black contour represents -1 K potential temperature perturbation at 50 m AGL, which depicts the cold pool near the surface. The horizontal thick black lines indicated by the grey arrows illustrate the location of the line averaging in Figs. 10c, d.

The surface winds possessed a storm relative westerly component normal to the gust front (Figs. 9a, b), which allowed the moist inflowing air to be forced upward the density current created by the storm's downdrafts ahead of the line. The surface storm relative winds also had a northerly component, which in turn was consistent with the stronger cells forming on the northern portion of the line (Fig. 8), in good agreement with Trier et al. (1996) model results. As time progressed, the convection at the leading edge of the squall line weakened (Fig. 8). In the next section we will show that this overall weakening of the squall line was attributed to relatively strong initial convective development, which caused the line to become progressively outflow dominated with time.

In good agreement with our results, observations showed maximum radar reflectivity of about 55 dBZ. The simulated squall line, however, exhibited a more linear reflectivity pattern than the observations did. We believed that this was because our initial environment was homogeneous and because we used a symmetric forcing to trigger convection.

After 4 h of simulations, a cyclonic and anticyclonic mesovortex developed on the line's northern side at about 4.5 km AGL. Meanwhile, this feature was not observed on the southern side of the line (Figs. 9b, c). Trier et al. (1996) simulation showed, however, both a cyclonic and anticyclonic mesovortex formed to the north and to the south of the line, respectively. This was probably because their simulation did not include the Coriolis terms in the equations of motions, which favor the development of a cyclonic mesovortex in detriment to an anticyclonic one (in the northern hemisphere). In our simulation two counter rotating mesovortices allowed the formation of a localized rear inflow jet on the

northern portion of the line at about 5 h 30 min (not shown). A separate test simulation carried out with  $f=0$  resulted in a weaker jet with wind speeds below  $10 \text{ m s}^{-1}$ . At 5 h 30 min, this jet was coincident with a rear inflow notch and weak reflectivity values at  $z = 1.033 \text{ km}$  (Fig. 8,  $X = 70 \text{ km}$ ,  $Y = 110 \text{ km}$ ). Except for this, the inclusion of the Coriolis force did not show any significant differences than with the same simulation carried out with  $f=0$ .



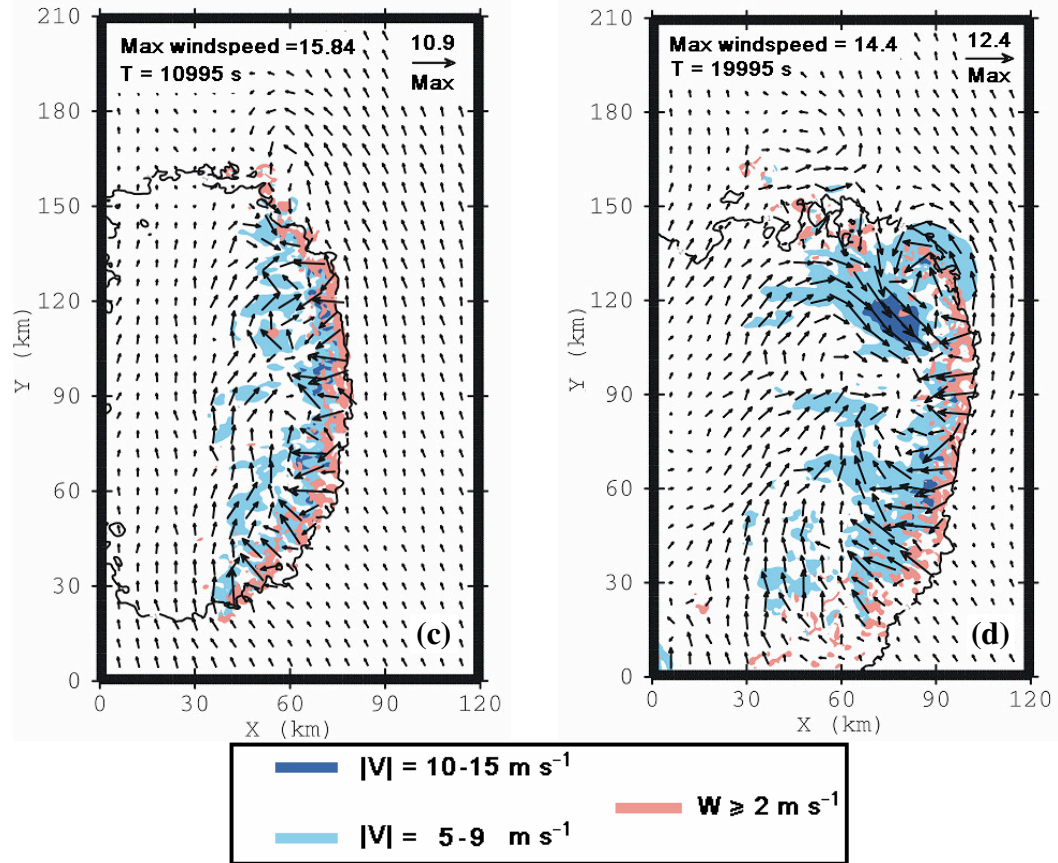


**Fig. 9.** Horizontal cross section of the storm relative wind vector field at  $z = 50$  m AGL (a) at  $t = 10995$  s and (b) at  $t = 19995$  s. Panels (c) and (d) are as in (a) and (b) at  $z = 3.2$  km. Light red filled contours show vertical winds exceeding  $2 \text{ m s}^{-1}$  at  $z = 2$  km AGL. Light (dark) blue filled contours show wind speeds exceeding  $5$  ( $10$ )  $\text{m s}^{-1}$ . Because the density of wind vector is 1 out of 10, the maximum wind speed shown in the upper left corner of the panel does not exactly match the maximum magnitude of the wind vector.

Overall, the squall line was composed of a succession of shallow narrow thunderstorm cells that developed at the leading edge of the gust front in a periodic fashion (Fig. 10). Consistent with observations, these newly formed cells progressively propagated towards the rear of the line (i.e., along the squall line motion vector) until they ultimately decayed to form a stratiform region characterized by small reflectivity values (Fig. 10a,  $X = 30$  km) and weak vertical motions (Fig. 11a,  $X = 30$  km). The cells reached their mature phase in what will be referred as the “mature zone”, which was the region located between the trailing stratiform region at the rear of the line (e.g., between

$X = 30$  km, Fig. 10a) and the leading edge of the line where cells formed (e.g.,  $X = 75$  km, Fig. 10a). Note that this region is different from the “transition zone” proposed by Biggerstaff and Houze (1991), who defined it as a region characterized by strong convective downdrafts between the strong convective cells just behind the gust front and the stratiform region further to the back of the line. We decided to use this different terminology because, in our simulated squall line, most of the action in terms of lightning activity, charging and CG activity occurs in that region (i.e., mature zone). Also, in our simulation, it was difficult to determine the presence of this transition zone, because of the many elevated updraft cores extending well behind the leading edge of the line (see later in this section).

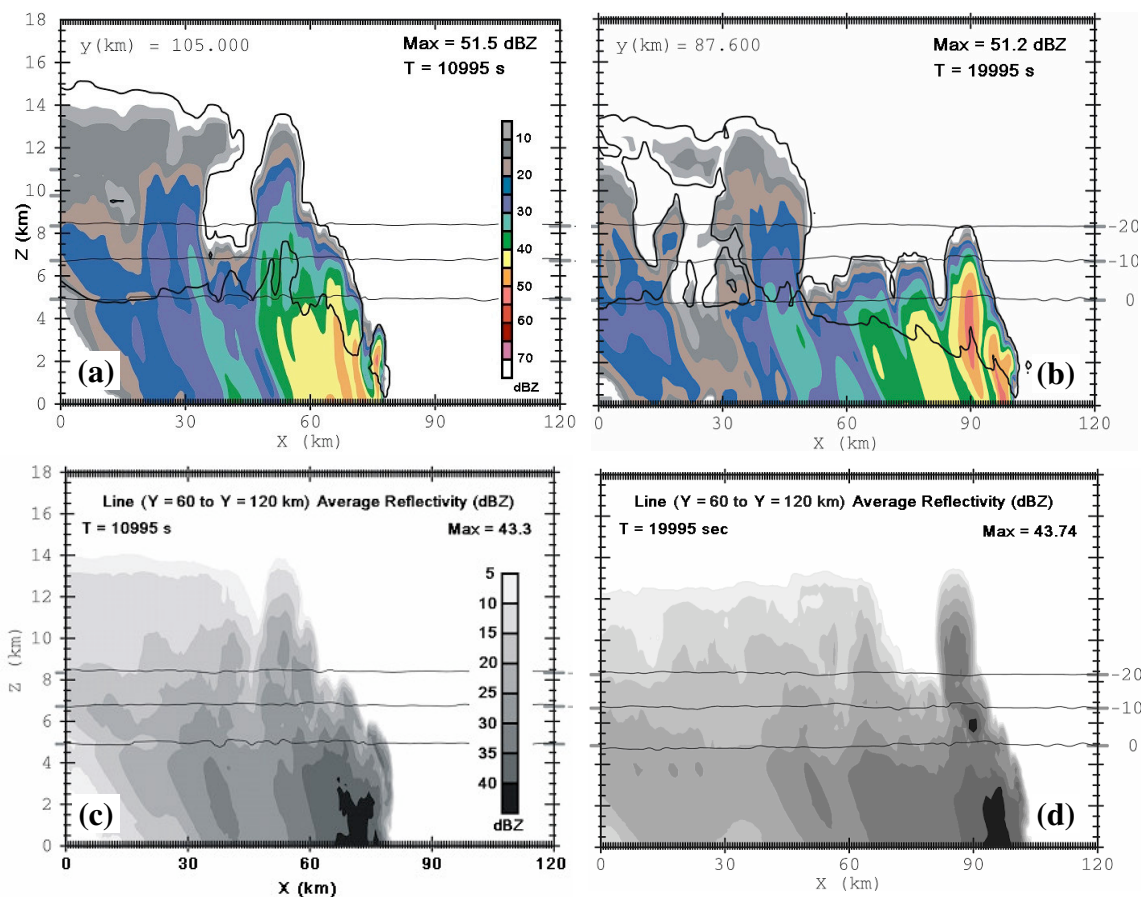


**Fig. 10.** Vertical cross section of radar reflectivity (in dBZ) at (a)  $Y = 105$  km at  $t = 10995$  s and (b)  $Y = 87.6$  km at  $t = 19995$  s. The quasi horizontal thin black lines in panels (a) and (b) show isotherms of 0, -10 and -20°C. The black contour depicts the cloud boundary ( $0.1 \text{ g kg}^{-1}$  which is the sum of cloud mixing ratio, snow mixing ratio, cloud ice mixing ratio and pristine ice mixing ratio). Similarly, line average reflectivity between  $Y = 60$  km and  $Y = 120$  km in the  $X$ - $Z$  plane are shown at (c)  $t = 10995$  s and (d)  $t = 19995$  s. This line averaging consists of adding all the reflectivity values greater than a minimum threshold value (here set to 1) along the  $X$  or  $Y$  axis and then divide this sum by the number of grid points along this  $X / Y$  axis where the reflectivity values are greater or equal than this threshold.

Overall, the 40 dBZ reflectivity contour almost never exceeded the top of the mixed phase region layer (or the -20°C isotherm, Fig. 10), which was consistent with overall weak updrafts seldom reaching  $5 \text{ m s}^{-1}$  at and above that level (Figs. 11c, d). This was also true for the 30 dBZ echo top, which rarely exceeded the -10°C level.

To offer a better view of some of the squall line's dynamical, microphysical and electrical properties, vertical cross sections of line-averaged quantities for a 60 km slab along the line (i.e., in the  $Y$  direction) were generated. The line-averaged values obtained with this method were somewhat lower than the ones obtained from individual cross sections. This is because the line average at each level was calculated by dividing the total sum of all the values of the quantity of interest within the slab along the  $X$  axis, by the sum of all the grid cells having values greater than a predetermined threshold value. For instance, the threshold value for reflectivity was set to 1 dBZ. For all plots, we chose a small threshold, always greater than zero because this will weight the sum towards slightly larger values and will smooth the presence of any local maxima during the averaging process without masking their presence. Note that for vertical velocities, the averaging of positive and negative values was carried out separately to avoid unwanted cancellation. For the electrical variables, however, we decided to show individual cross-sections (see the next subsection), because particle charging occurs in more specific,

discrete regions of the storm (i.e., cell-scale) that meet particular conditions (i.e., ambient temperature, sufficient amount of the particles involved in charge separation). Therefore, the gradients of these quantities can become large over very small distances, making the averaging process difficult and possibly uninformative.

In agreement with Trier et al. (1996) simulation, the line-averaged 30 dBZ reflectivity contour rarely exceeded the freezing level (Fig. 10). This in turn, was consistent with overall weak (line-averaged) updraft speeds seldom reaching  $5 \text{ m s}^{-1}$  at and above that level (Figs. 11a, b). Also consistent with Trier et al. modeling study, individual cross sections across the line, revealed updraft speeds locally exceeding  $8 \text{ m s}^{-1}$  (Figs. 11c, d). These strong updrafts were mainly observed near the gust front below 2 km. In some rare instances, however, isolated strong cells in the mature zone exhibited updraft speeds between  $5\text{-}8 \text{ m s}^{-1}$  above the freezing level (i.e., Fig. 11d at  $X = 60 \text{ km}$ ). Using observations based on Doppler wind retrieval methods, Trier et al. (1996) observations showed line-averaged updraft speeds greater than  $7 \text{ m s}^{-1}$  at upper levels (near 11 km AGL) in the mature zone. However, as in Trier et al., our simulation produced overall much weaker line-averaged updraft speeds at upper levels ( $w \sim 1\text{-}2 \text{ m s}^{-1}$  near 10 km) in the mature zone (Figs. 11a, b). As we will see later in this section, these isolated strong storm cells will account for most of the charge production (and thus lightning activity) of the squall line.

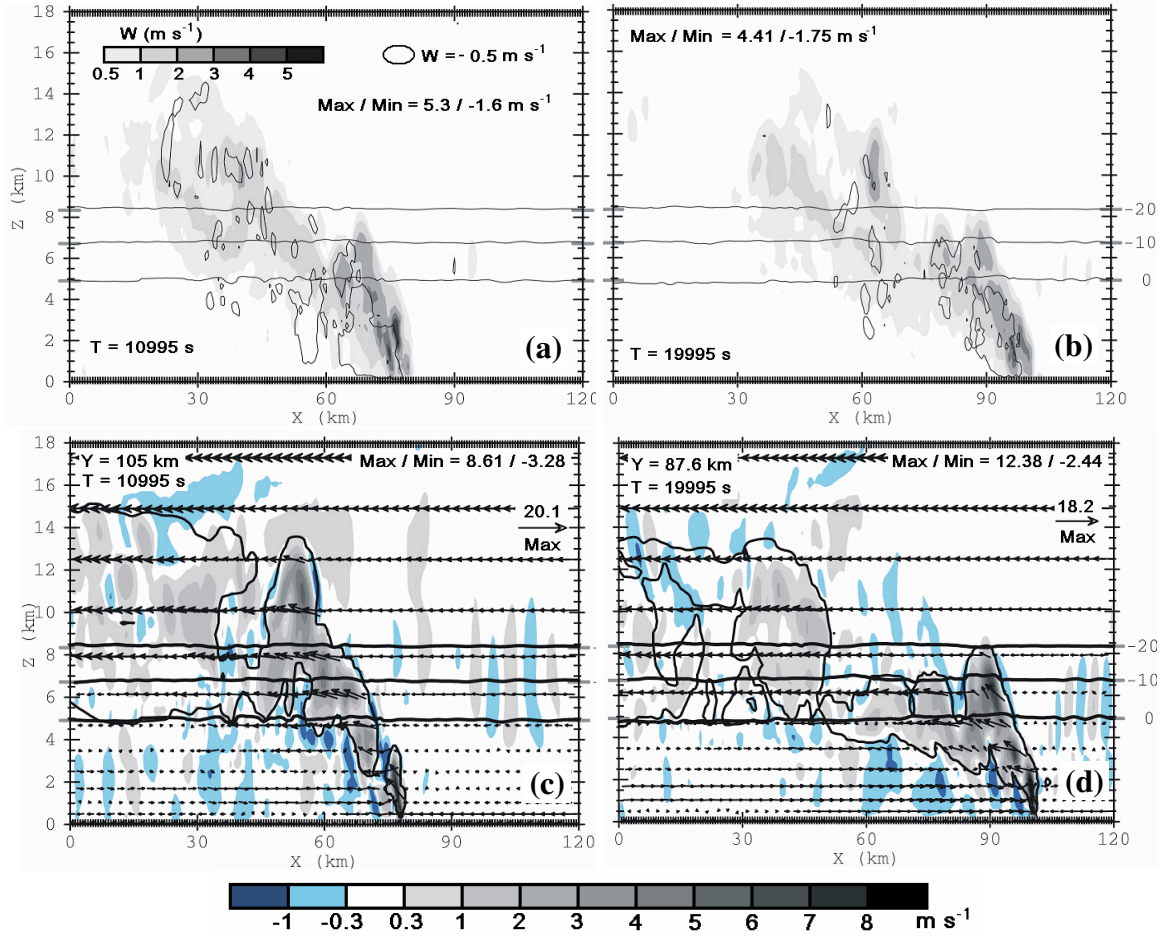
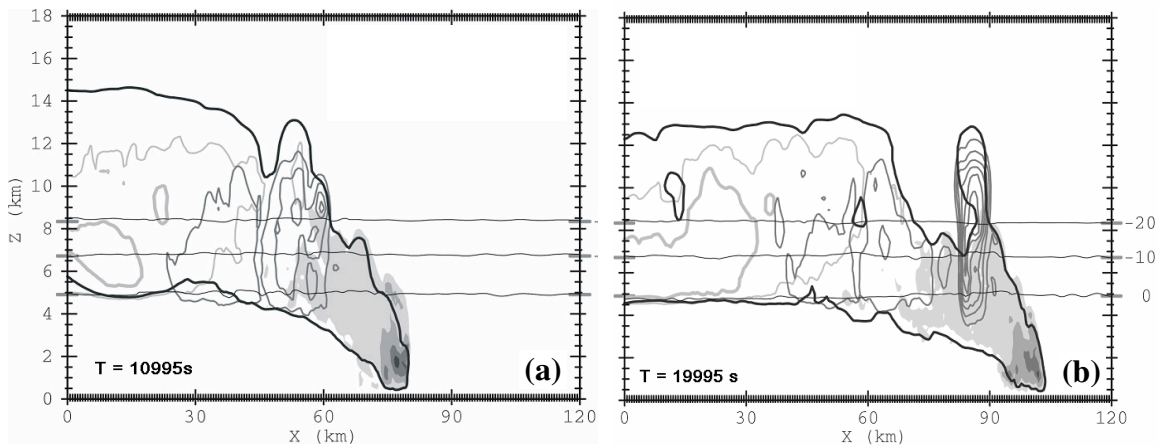


**Fig. 11.** Panels (a) and (b) are as in Figs. 10c and 10d for vertical wind in  $\text{m s}^{-1}$ . The threshold values for averaging the positive (negative) vertical velocities is  $0.1 \text{ m s}^{-1}$  ( $-0.1 \text{ m s}^{-1}$ ). Legends for shadings are shown in panel (a). The next to panels show vertical cross sections of vertical wind (in  $\text{m s}^{-1}$ ) and wind field vector (density of 1 out of 4) at (c)  $Y = 105 \text{ km}$  at  $t = 10995 \text{ s}$  and (d)  $Y = 87.6 \text{ km}$  at  $t = 19995 \text{ s}$ . Legend for vertical wind speed is shown below the panels and the scale for the wind vector is shown in the upper right corner of panel (c) and (d).

Rajopadhaya (1996) posited that these strong updraft speeds above the melting level in the mature zone were caused by a rapid depletion of liquid water drops below the melting level (water un-loading) due to enhanced warm rain processes in the convective region ahead of the line. Indeed, in our simulation, most of the liquid precipitation was found at the leading edge of the line (See orange and red contours in Figs. 12c, d). Trier et al. simulation also shows strong gradients of line-averaged rain mixing ratios at the

leading edge of the line below 5 km AGL, with maximum reaching  $3.3 \text{ g kg}^{-1}$ , which is slightly larger than our simulation ( $\sim 2.2 \text{ g kg}^{-1}$ , not shown). In another study from Trier et al. (1997), they also showed that these elevated updraft in the upper troposphere occurred when positively buoyant air parcels moved rearward, away from downward-directed pressure forces behind the gust front.

In summary, we found that strong updraft speeds (i.e.,  $> 5 \text{ m s}^{-1}$ ) were found below the melting level at the leading edge of the line, when the storm cell was in its early developing stage. Once the cell propagated rearward in the mature zone, its line-averaged updraft speed rarely exceeded  $3 \text{ m s}^{-1}$  below the melting level, consistent with most early studies of tropical convection (LeMone and Zipser 1980; Zipser and LeMone 1980; Jorgensen and LeMone 1989; Jorgensen et al. 1985; Lucas et al. 1994). A few of these cells, however, exhibited updraft speeds exceeding  $5 \text{ m s}^{-1}$  above the melting level, although observations clearly showed larger line-averaged updraft speeds. Further rearward in the stratiform region, the line-averaged updrafts velocities generally ranged between  $1$  and  $2 \text{ m s}^{-1}$ , consistent with observations (Trier et al. 1996; Petersen et al. 1999).



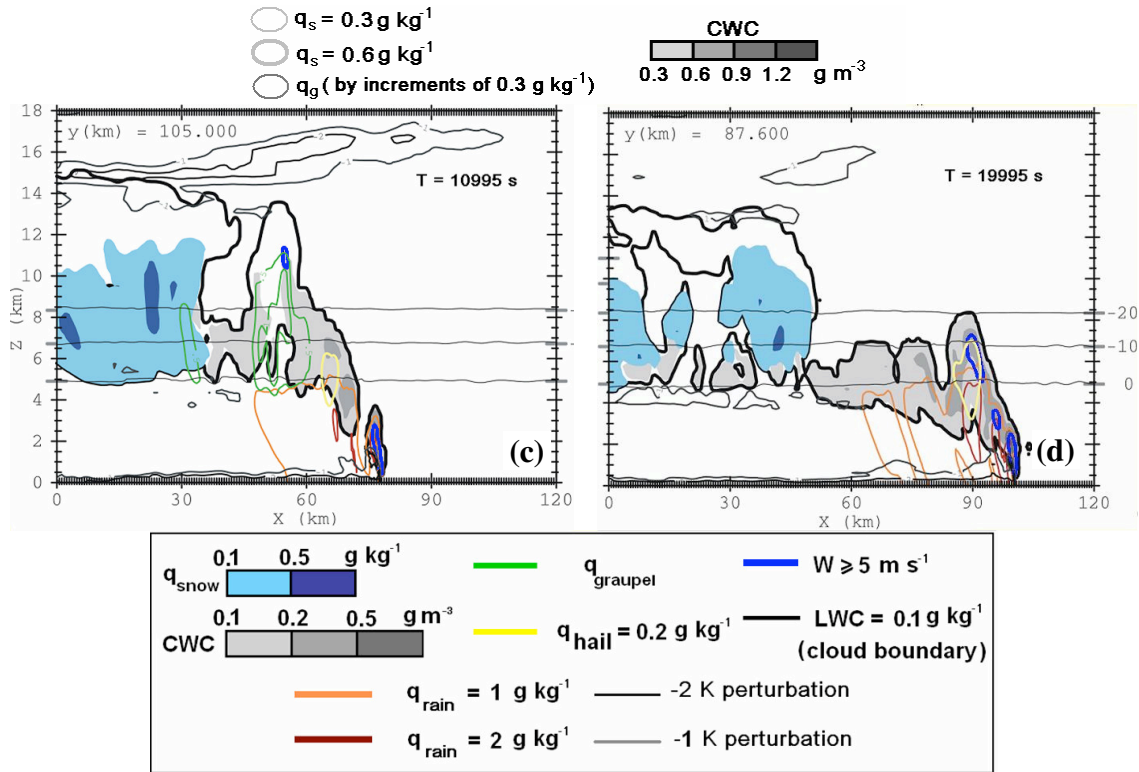


**Fig. 12.** Panels (a) and (b) are as in Figs. 11a and 11b except for the line-averaged total graupel (sum of three categories) mixing ratio ( $\text{g kg}^{-1}$ ), line-averaged snow mixing ratio ( $\text{g kg}^{-1}$ ), cloud water content (CWC) in  $\text{g m}^{-3}$ . See legends below panels (a) and (b) for contours and shadings. The threshold values for averaging the total graupel mixing ratio, CWC and snow mixing ratio are  $0.1 \text{ g kg}^{-1}$ ,  $0.05 \text{ g m}^{-3}$  and  $0.05 \text{ g kg}^{-1}$ , respectively. The line-averaged visible cloud contour (which is the sum of cloud mixing ratio, snow mixing ratio, cloud ice mixing ratio and pristine ice mixing ratio) of  $0.1 \text{ g kg}^{-1}$  is also shown. Panels (c) and (d) are as in Fig. 11c and 11d, except for snow mixing ratio ( $\text{g kg}^{-1}$ ), graupel mixing ratio ( $\text{g kg}^{-1}$ ), hail mixing ratio ( $\text{g kg}^{-1}$ ), rain mixing ratio ( $\text{g kg}^{-1}$ ) and potential temperature perturbation (K). The total graupel mixing ratio contours are plotted from  $0.5 \text{ g kg}^{-1}$  by increments of  $1 \text{ g kg}^{-1}$ .

Consistent with McFarquhar and Heymsfield (1996) and Stith et al. (2002), the trailing stratiform region of the line was mainly composed of snow particles and lighter ice crystals (Fig. 12) which accounted for the overall weak reflectivity values ( $< 30 \text{ dBZ}$ ) observed there at all altitudes. The line-averaged snow mixing ratio values in Fig. 12a and 12b are in agreement with Trier et al. who showed maximum snow mixing ratio of about  $1.0 \text{ g kg}^{-1}$  near 8 km AGL. The trailing stratiform region was also characterized by

even smaller line-averaged reflectivity values near the surface (i.e., < 25 dBZ, Fig. 5). This was probably because most of the snow particles and ice crystals melted and evaporated before reaching the surface (because of their small terminal fall velocity ranging between 1-2 m s<sup>-1</sup>, Straka and Mansell, 2005). Consequently, in this region, little charging and subsequent lightning activity occurred (see later in the section). However, right behind the leading edge of the line near the mature zone, some cells were able to loft their graupel particles within the mixed phase region (Figs. 12a-c). In fast moving squall lines, graupel pellets are only present within cell having a sufficiently high vertical depth (exceeding the -20°C isotherm or above the mixed phase region), the latter which takes a certain amount of time to develop. Once the storm cells started to decay as they propagated rearward in a more statically stable region, the whole cloud became completely glaciated (See blue shaded areas progressively replacing grey shaded areas in Figs. 10a and 10b), hence preventing further charge separation to occur there (not shown). This progressive complete glaciation of the cloud and subsequent hydrometeor unloading was also coincident with cloud top heights increasing relatively fast to the rear of the line.

As mentioned in the previous section, most of the charge present across the squall line was separated within the mature zone (not shown) where the cells reached their mature stage and contained a sufficient amount of graupel (i.e., > 0.5 g kg<sup>-1</sup>) and CWC (i.e., > 0.2 g m<sup>-3</sup>, Fig. 12) in the mixed phase region (defined as the layer between the freezing level and the -20°C isotherm). In the simulation, most of the graupel was found between 6 km and 10 km AGL with maximum line-averaged mixing ratios of about 1.0 g

$\text{kg}^{-1}$  (Figs. 12a, b). This results, again, are very similar than reported by Trier et al., who found mixing ratios near  $1.4 \text{ g kg}^{-1}$  near 8.5 km AGL in the mature zone.

Before continuing the analysis, it is important to mention that the line-averaged net space charge was computed by summing positive *and* negative space charge values along the line. The line-averaged charge structure across the squall line was overall more complex than simple normal dipoles (positive charge above negative charge) or normal tripoles (composed of a normal dipole with a lower positive charge) commonly found in the literature to describe thunderstorm charge structure (e.g., Williams, 1989). In some regions of the squall line, the charge polarity switched several times with height and was composed of many pockets of weaker (i.e.  $< 0.4 \text{ nCm}^{-3}$ ) charge density (Fig. 13). To facilitate the analysis we will, however, only consider the charge regions involved in lightning (i.e., regions with charge density  $> 0.4 \text{ nCm}^{-3}$ ).

At about 3 h, the SP98 scheme resulted in a normal tripole charge structure in the mature zone, while in the trailing stratiform region, a normal dipole was observed instead (Fig. 13a). At 5 h 30 min of simulation, however, the line-averaged net charge magnitudes in the mature zone are overall much weaker than in the stratiform region (again showing evidence of a normal dipole, Fig. 13b). Nonetheless, we notice that overall, the mature zone is characterized by a strong lower (midlevel) positive (negative) charge region, while instead, a strong positive (negative) charge region prevails in the stratiform region at low levels (midlevels). The strong lowest positive charge region in the mature zone, however, does not extend as far below as the lowest negative charge region observed in the stratiform region. As we will show later in this section, this will have important consequences on the CG lightning activity.

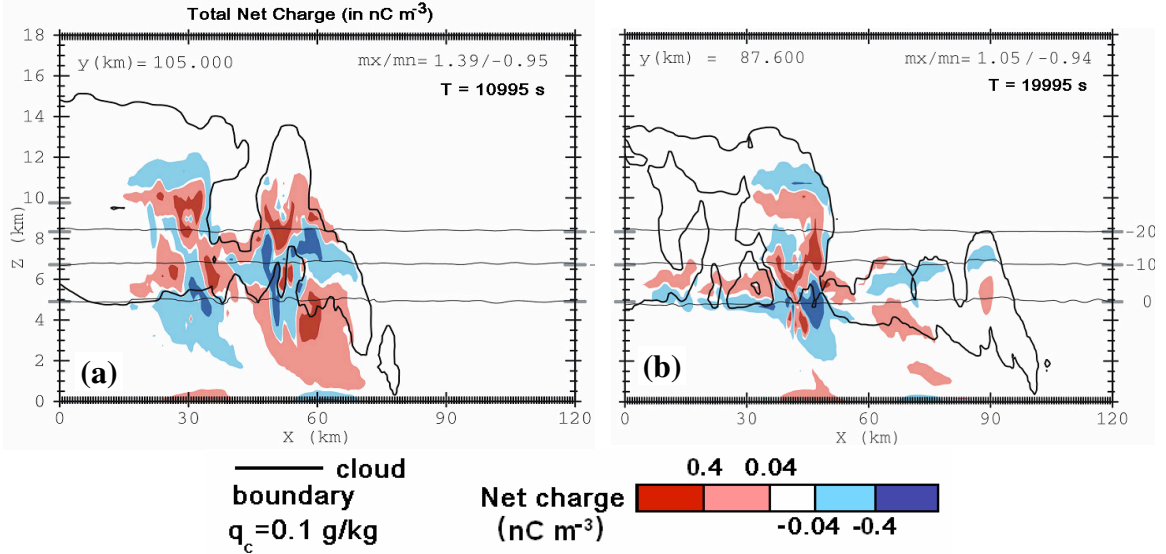


**Fig. 13.** Panels (a) and (b) are as in Figs. 9a and 9b but for the net amount of charge in  $\text{nC m}^{-3}$ . Legends for shadings and contours are shown below the figure.

In the mature zone, the graupel particles present in the mixed phase region gained negative charge via NI processes (not shown) and the lighter ice crystals carrying positive charge were lofted up and remained in the anvil cloud to form the upper positive charge region (Fig. 13). The lower positive charge region mainly present in the mature zone was a consequence of both inductive and NI charging mechanisms (not shown). Induction was particularly effective in this region of the line because the bulk of the liquid precipitation was found there. Indeed, this allowed graupel / hail to collide with liquid water droplets more frequently than anywhere else in the system.

Earlier in the section, we showed that the trailing stratiform region contained small amounts of CWC (i.e.,  $< 0.2 \text{ g m}^{-3}$ ) and graupel (i.e.,  $< 0.5 \text{ g kg}^{-1}$ ), which was consistent with weak charging occurring there (see later in the text). This graupel is believed to originate from the stronger isolated cells within mature zone that are later advected rearward in the stratiform zone. Most of the graupel present in those rearward moving cells will evaporate or melt before reaching the stratiform region. In the trailing

stratiform region, weak *in situ* NI charging occurred and was mainly confined within the mixed-phase region (not shown). This finding is in agreement with the hypotheses from Rutledge and Petersen (1994), who showed that in several Mesoscale Convective Systems (MCS) observed during the DUNDEE (Down Under Doppler and Electricity Experiment, Rutledge et al., 1992) field program, *in situ* NI charging was the process likely responsible for significant electrification in the trailing stratiform region. Additional cross-sections showed that the great majority of the regions of the stratiform cloud having net space charge density magnitude exceeding  $0.03 \text{ nC m}^{-3}$  were almost always coincident with weak (on the order of  $0.1 \text{ pC m}^{-3} \text{ s}^{-1}$ ) *in situ* NI charging. This suggests that the majority of the charge present in the trailing stratiform region was generated *in situ* and that the remaining charge originated further ahead, in the mature zone of the squall line. In continental squall lines, however, Rutledge and MacGorman (1988) and Schuur et al. (1991) proposed that the rearward advection of charged particles from the leading convective region of continental squall lines had a more important role in the origin of charge in the stratiform region. This is probably because in those stronger systems, more charge are being generated in the mature zone, which can then be transported rearward. For these continental squall lines, Schuur and Rutledge (2000) 2D modeling study showed that up to 70% of the charge in the stratiform region was generated by the NI mechanism *in situ*.

In our simulation, the midlevel negative charge region exhibited a downward sloping trend towards the rear of the line (Fig. 13a), which indicates that sedimentation of charged particles (mainly graupel) was occurring. In other words, the heavier particles in the cells within the mature zone slowly fell to lower levels (with a few of them eventually

reaching the ground), while the remaining lighter charged particles remained in the rearward propagating decaying cell which progressively became glaciated. During the rearward transport, most of these light charged particles remaining in the decaying cell kept most of their charge, thereby accounting for the charge layers observed in the trailing stratiform region. The lowest positive charge region was absent in the trailing stratiform region because most of the liquid precipitation occurred in the mature zone and at the leading edge of the line. The rearward advection of charged particles from the leading convective region of continental squall lines has already been documented by Rutledge and MacGorman (1988) and by Schuur, Smull, Rust and Marshall (1991).

As expected from the charge structure, the majority of the lightning flashes were found in the mature zone, where most of the charge resided (Fig. 14). All of the CG flashes produced by the squall line during the simulation lowered negative charge to ground (see next section) and were mainly located in the mature zone (Fig. 8). This result is consistent with Nielsen et al. (1994) who also found that in continental squall lines -CG flashes were often found near the leading edge of the line. The Petersen et al. (1999) “strong forcing” tropical squall line case also only produced -CG flashes. In our simulation, -CG flashes occurred in the mature zone because of the existence of a relatively strong and deep lower positive charge region (Figs. 13 and 14). The occurrence of lightning (IC or CG) flashes in the model was found primarily where the 30 dBZ echo top boundary (threshold value for significant hydrometeor mass) reached the -10°C level (Figs. 14a and 9a at  $X = 50$  km). This result again, was consistent with the tropical cases of Petersen et al. (1996; 1999) and continental cases of Nielsen et al. (1994).

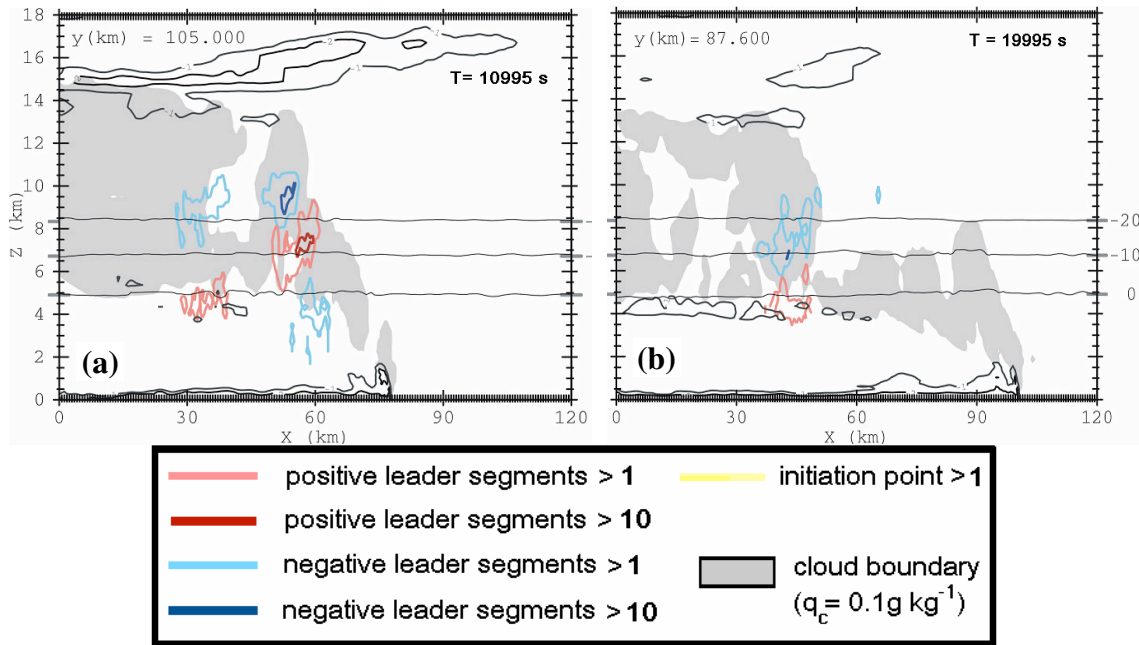


**Fig. 14.** As in Figs. 11a and 11b but for the total amount of positive and negative leader segments and lightning initiation locations. Light (dark) blue contour shows regions having more than 1 (10) negative leader segments. The same holds for the red contours. The leaders were summed for a time period of 10 min until the time of the cross section. The -1K (-2K) perturbation temperature contours are also shown in a dark grey (black) line.

The positive leaders propagating through the lower negative charge region in the stratiform region never reached ground (compare Figs. 13a and 14c). Additional horizontal cross-sections at low and midlevels (not shown here) through the entire squall line after 3 h, clearly indicated the existence of a bipolar lightning pattern. This result was encouraging as many investigators already showed that within continental squall lines, the stratiform region was characterized by the production of sparse, infrequent of +CG strikes (e.g., Orville et al., 1988; Nielsen et al. 1994). It is well established that convection in tropical maritime squall lines is overall weaker and shallower than their continental cousin. Therefore, we suspect that the stronger convection in the latter case would result in greater graupel (ice crystals / snow particles) concentration and volume at

low-to-mid (upper) levels in the stratiform regions. This greater graupel (ice crystals / snow particles) volume and low-to mid levels (upper levels) would result in a simultaneous enhancement of the lower negative and upper positive charge regions in the stratiform region and therefore would be more favorable for + CG flash production.

### **V.1.3. Conclusions**

Overall, the simulation results were consistent with observations of typical tropical oceanic squall lines (e.g., Trier et al. 1996; May and Rajopadhaya 1996; Petersen et al. 1999). The updraft speeds across the line seldom exceeded  $8 \text{ m s}^{-1}$  in turn consistent with relatively shallow 30 dBZ echo tops which rarely reached the top of the mixed phase layer ( $-20^{\circ}\text{C}$  isotherm near 8 km AGL). Similar to Trier et al. work, the simulated line-averaged updraft speeds at upper levels ( $\sim 10 \text{ km}$ ) were much smaller than the observed values by as much as  $5 \text{ m s}^{-1}$ .

Warm rain processes were found to be particularly efficient ahead of the line. This accounted for the overall small amount of supercooled water and graupel pellets above the melting level (Stith et al. 2002). Consistent with this, the total lightning activity across the line was generally weak.

The line-averaged snow, graupel and rain mixing ratio profiles across the line were similar than the ones simulated by Trier et al. This shows that the inclusion of a 10-ICE microphysics scheme did not result in significant differences in the simulated microphysics fields.

The stratiform region was mainly composed of light ice crystals and snow aggregates (MacFarquhar and Heymsfield, 1996), with discrete locations, however containing small amounts of graupel ( $\sim 0.1\text{-}0.3 \text{ g kg}^{-1}$ ), which were mainly medium to high density graupel particles. Most of the charge present in the line was generated within some storm cells in mature zones that had sufficiently strong updraft speeds near the melting level to carry graupel in the mixed phase region. The cells exhibiting the largest total flash rate were characterized by deeper 30 dBZ echo tops reaching the  $-10^{\circ}\text{C}$  level, consistent with observations (e.g., Petersen et al. 1999).

In these cells, NI charging was responsible for the creation of a mid-level negative charge region and an upper positive charge region. Also the heavier particles in these cells fell quickly to generate a lower positive charge region below 4 km AGL by both induction and NI charging process. The resulting normal tripole charge structure within these cells was consistent with the production of  $-CG$  flashes in the mature zone.

As these cells aged and became largely glaciated, they formed a trailing stratiform region, which was characterized by weak vertical velocities ( $< 2 \text{ m s}^{-1}$ ) and small reflectivity values at all levels ( $< 30 \text{ dBZ}$ ). Because of this, only weak charging was observed there. However, we found that almost all the charge present there was generated in situ non-inductively, with negative charge mainly on medium to high density graupel and positive charge on both snow aggregates and cloud ice. The remainder of this charge were on hydrometeor species that were advected from the mature zone, when the cell's updraft at the melting level was strong enough to carry the necessary amount of graupel and CWC in the mixed phase region. The gross charges structure in the trailing stratiform region resembled an inverted tripole. However, no  $+CG$  flash was produced in the trailing

stratiform region. This was probably because the lower negative charge region forming this inverted tripole did not extend sufficiently close to the ground to allow the positive leaders observed there to descend and reach ground.

We speculate that if the convection had been more intense in the mature zone, more charges would have been generated, particularly at upper and midlevels (along with a greater concentration of lighter hydrometeors). Once transported rearward, this would have resulted in a deeper and stronger normal dipole in the stratiform region that would have been more favorable for +CG flash production.

## **V.2. Dependence of the simulated squall line dynamics, microphysics and electrification on the horizontal grid spacing.**

### **V.2.1 Introduction**

The following section focused on analyzing the impact of the horizontal grid spacing on the squall line's dynamics, microphysics and electrification properties. Using the same kinematical, microphysical and electrical parameters, the squall line simulation presented in the previous section was reproduced at horizontal grid spacings of 1 and 2 km. In order to offer a wider spectrum of grid spacings simulations, a smaller version of this squall line was carried out at a fine horizontal grid spacing of 300 m. For computational purposes the 300 m simulation was carried out in a smaller domain up to 3 h of cloud time instead of 5 h 30 min for the remaining three simulations. We chose 300 m as a

lower bound hoping that it will give more insight on the turbulent flow across the line and on its resulting impacts on the storm's microphysical and electrical properties.

### **V.2.2. Results**

Horizontal cross section of radar reflectivity showed that overall, the 300 m and 600 m produced weaker squall lines than the two remaining cases. In particular, the 300 m squall line showed rapid signs of weakening only after 3 h of simulation. However, it is important to remind the reader that the 300 m squall line was initialized using a temperature anomaly three time smaller (in the *Y* direction) than the three remaining cases. Therefore, caution is warranted when attempting to establish a direct comparison with the other three cases of this study.

Probably the most striking difference was that the 2 km squall line was composed of two small bow echoes, while the three remaining squall line were part of only one large bow echo. Indeed, unlike the other cases, the convection in the 2 km run initially developed on the southern edge and on the northern edge of the line, while the center of the line was essentially devoid of strong convection. As time progressed, the convective activity at each tip of the line started to organize into two distinct larger storms. Later, these two large storms started to become outflow dominated, which led to two bow-shaped structures.

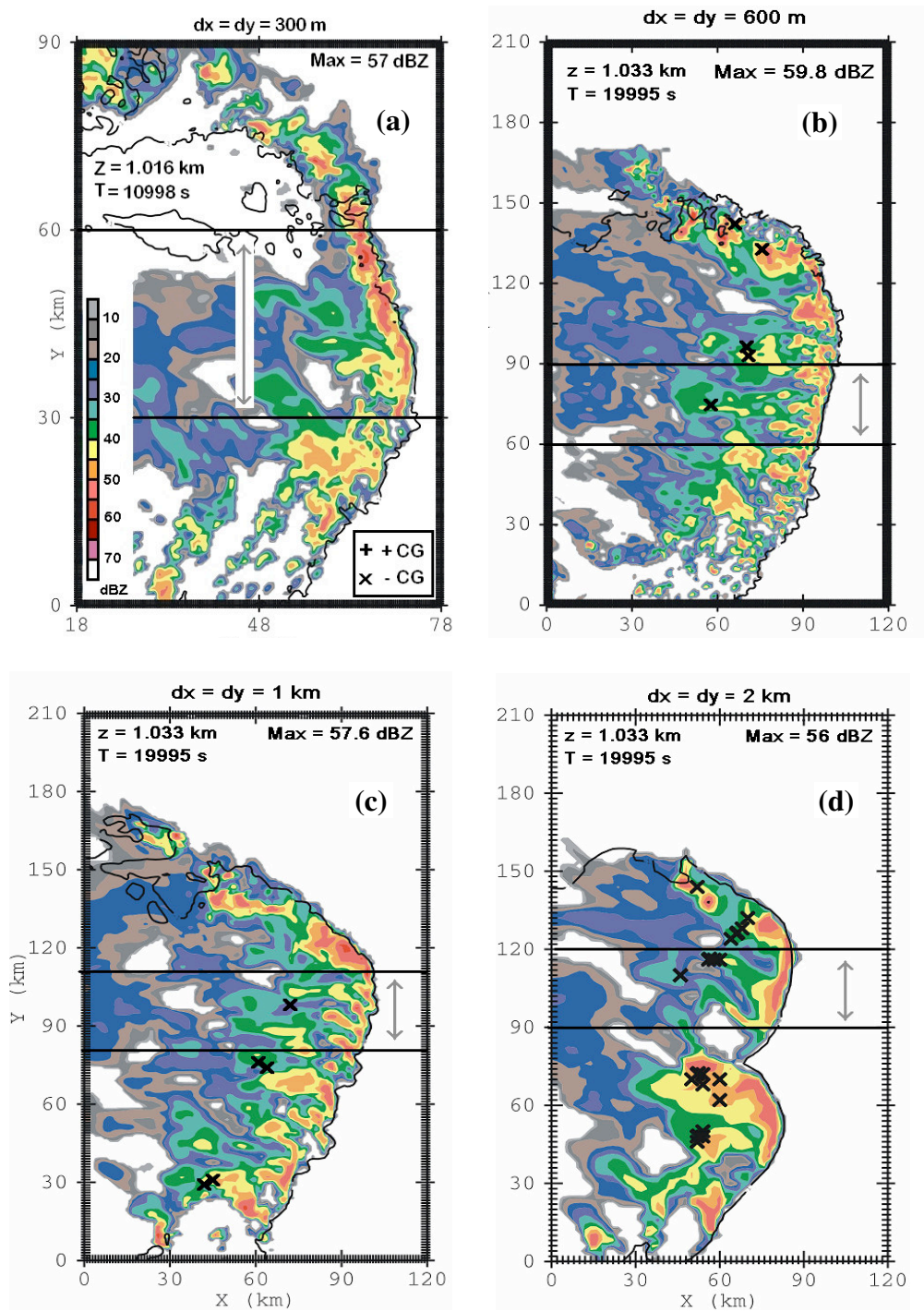


**Fig. 15.** As in Fig. 8 for (a) the 300 m run, (b) 600 m run, (c) 1 km run and (d) the 2 km run. Note that the cross section time in panels (b), (c) and (d) are shown for  $t = 19995$  s while in panel (a) it is shown for  $t = 10998$  s. The flash locations were plotted for a 30 min time interval prior the cross section time. The thick horizontal black lines and the grey arrows have the same meaning than in Fig. 8. Note that for all four panels, the longer thick marks on the  $X$  and  $Y$  axis represent a distance of 30 km.

The reflectivity notch located behind the northern tip of the bow in the 600 m case was still present (i.e., Fig.15b at  $X = 90\text{km}$  and  $Y = 120\text{ km}$ ), but less evident in the 1 km run (Fig. 15c). Consistent with this, the horizontal winds at  $z = 3.2\text{ km}$  AGL were qualitatively similar, with overall stronger winds near the notch for the 600 m run (not shown). This feature was, however, not observed in the 2 km simulation. We found that in the 600 m and 1 km case, this narrow rear inflow jet causing the formation of the reflectivity notch started to become evident only after about 5 h of simulation. Therefore, we cannot assert with certitude that this feature would not have been simulated in the 300 m case, since this simulation was only carried out for 3 h.

The southern portion of the 600 m and 300 m squall lines exhibited similar diffuse radar reflectivity pattern, which was associated with several small, weak cells. This particular aspect of the radar reflectivity pattern was, however, not observed in the two remaining cases (Fig. 15).

In all four cases the bulk of the CG lightning activity was generally located in the mature zone (Fig. 15). From the horizontal reflectivity plots in Fig. 15, it appeared, however, that the total CG flash production increased as the grid spacing increased (see later in the section). We speculate that the larger CG lightning flash rates at coarser resolution could be associated with overall larger individual storm cells across the line and resulting larger volume of radar reflectivity values exceeding 30-40 dBZ.

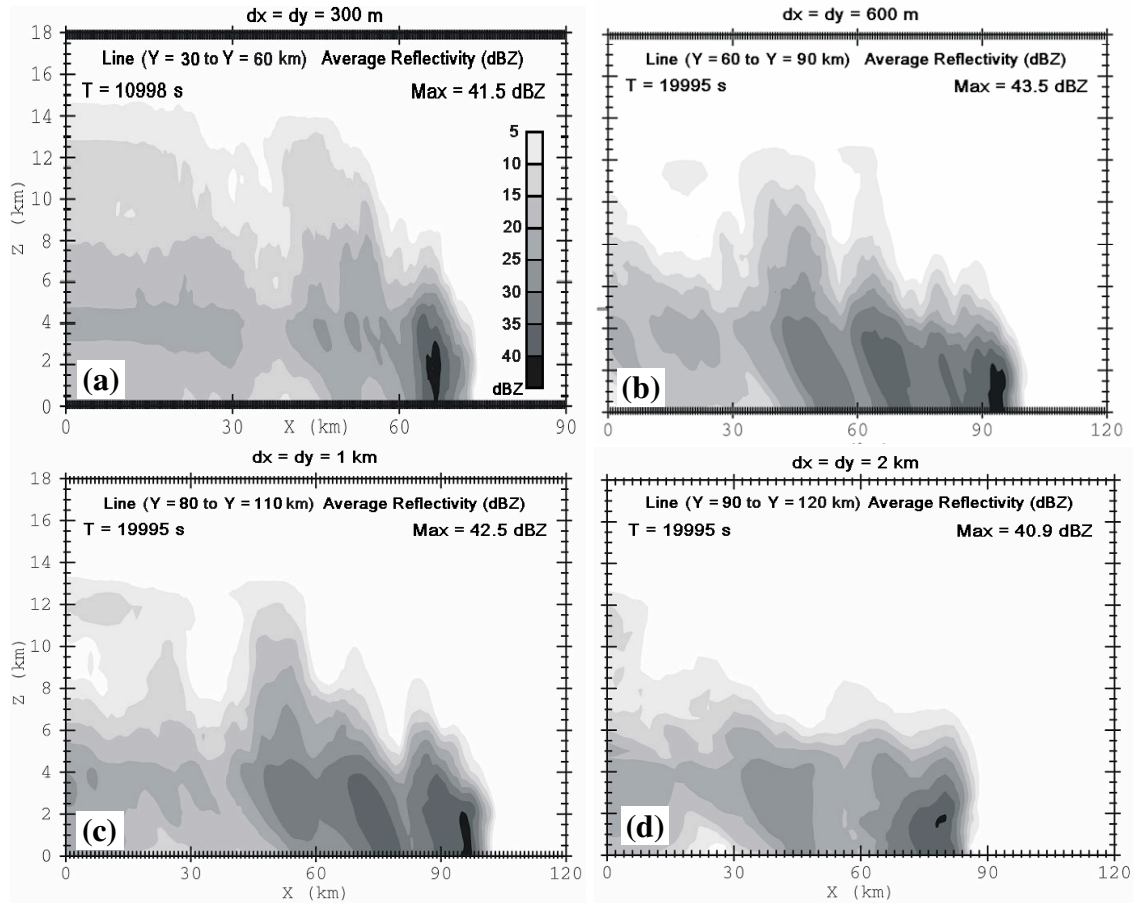


**Fig. 16.** As in Fig. 15 but for the line average of radar reflectivity (in dBZ) except with a threshold of 0 dBZ. This was done to eliminate the presence of isolated reflectivity maxima because, for the analysis in this section, we wish to establish a comparison of the main structure of squall line reflectivity profile. The averaging was performed in different portion of the line in a 30 km strip in the Y direction for all four cases. Details behind the averaging procedure are described in Fig. 10. For purpose of comparison, the thick marks in the Y axis represent a distance of 30 km for all cases.

Overall, the average vertical reflectivity profile across a 30 km section of the line was qualitatively similar in all four cases. The maximum in radar reflectivity, always exceeding 40 dBZ, was always located at the leading edge of the line. This maximum in reflectivity was associated with the rapid development of new cells by forced surface convergence at the gust front. Also, in all four cases, secondary maxima of about 30 dBZ were observed in the mature zone and even in the trailing stratiform region. These regions of relatively large reflectivity values were associated with decaying cells that

were advected to the rear of the line (Fig. 16). These secondary maxima, however, were less evident in the 300 m case at that time, because the horizontal radar reflectivity did not show any evidence of a well developed trailing stratiform region between  $Y = 50$  km and  $Y = 80$  km (Fig. 15). This was because we decided to run the 300 m case only up to 3 h of cloud time. Indeed in the 600 m case showed also a less extensive stratiform region at  $t = 3$  h than at  $t = 5$  h 30 min (Fig. 8). The homogeneous appearance of the average vertical reflectivity between  $Y = 0$  and  $Y = 20$  km was most likely due to the boundary being too close ( $\sim 35$  km) to the leading edge of the squall line during the restart of the simulation at 8000 s. Therefore the features located in this narrow strip of the domain were ignored in the analysis.

From Fig. 16, we notice that the 2 km and 3 km squall lines propagated much slower than the 600 and 1 km cases. As we will see later in this section, this was caused by a progressively increasing delay of the formation of the line as  $dx$  increases, because more work is required for the wider updrafts at coarser resolutions to develop.

In all four simulations, the extreme rear portion of the line at 5 h 30 min was overall characterized by small reflectivity values rarely exceeding 30 dBZ at all levels. In average, the reflectivity across the line for the 300 m, 600 m and 1 km cases were quantitatively similar, particularly ahead of the line. Nonetheless, the 2 km case showed overall shallower echo tops in the mature zone and in the trailing stratiform region (Fig. 16) despite generating the greatest amount of CG flashes (Fig. 15 and later in the section). As we will see later, it is not clear whether these shallow echo tops in the 2 km case arose from weaker vertical diffusion in the mature zone and the trailing stratiform region.

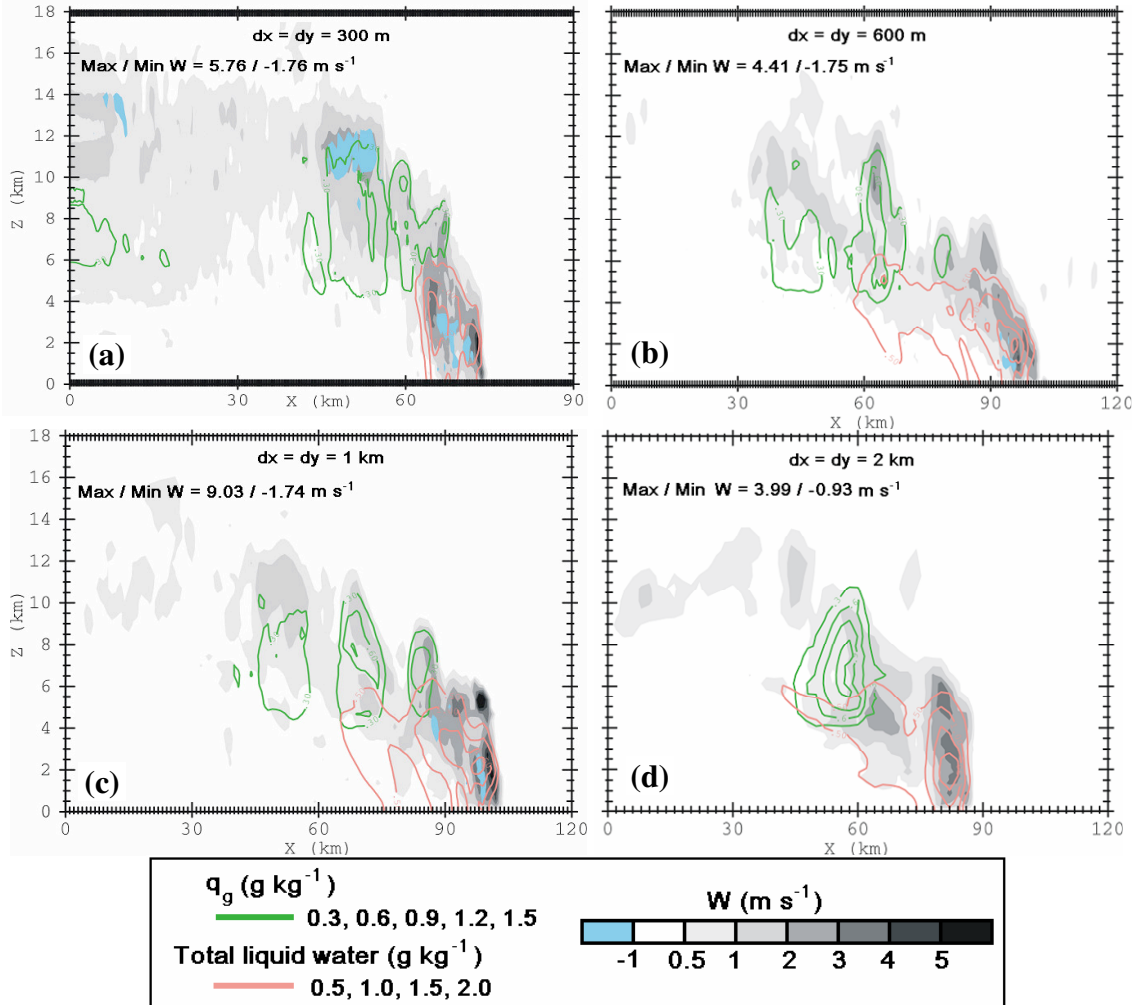


**Fig. 17.** As in Fig. 16, but for the total graupel mixing ratio ( $g kg^{-1}$ ), total liquid water ( $g kg^{-1}$ ) and vertical wind ( $m s^{-1}$ ). Shading and legends for the respective contours are shown at the bottom of the figure. The threshold value for the vertical wind and the graupel mixing ratio averaging was set to (+/-)  $0.1 m s^{-1}$  and  $0.1 g kg^{-1}$ , respectively. For the total liquid water mixing ratio, the averaging threshold was set to  $0 g kg^{-1}$ . Positive and negative values of vertical winds were summed separately in order to avoid unwanted cancellation.

The weaker reflectivity that was observed at all levels for the 2 km case was, however, consistent with overall weaker updrafts speeds across the line (Fig. 16). Despite this result, the 2 km squall line showed the greatest amount of graupel in the mature zone at the time of the figures (Fig. 17). This probably resulted from the presence of a strong

isolated updraft core within the cross section slab, although the latter would require further investigation.

Among all the four cases, the 300 m simulation seemed to exhibit the best looking stratiform region (Fig. 16) with showed evidences of mesoscale updrafts above the freezing level (Fig. 17a) in agreement with Bryan (2006). Nonetheless, the proximity of the western boundary in the 300 m case at the restart of the simulation was an important factor in enhancing convective rolls at midlevels in the stratiform region (not shown).

Overall, the vertical profiles of average vertical winds, total average graupel mixing ratio and average total liquid water across the line were qualitatively similar in all cases. The maximum in vertical winds and total liquid water were always located at the leading edge of the line (Fig. 17), consistent with the maximum in average reflectivity observed earlier (Fig. 15). This indicated that in all cases, the bulk of the liquid precipitation occurred at the leading edge of the line due to enhanced warm rain processes (i.e., compared to continental storms). This caused a rapid depletion of liquid water in the cloud as the cells were advected backwards. Also, in all cases, the greater amount of graupel was found between 6 and 10 km, within the mixed phase region in the mature zone.

In a recent study, Bryan and Rotunno (2005) showed using the Bryan and Fritsch (2002) numerical model, that updraft speeds magnitudes (and resulting reflectivity) are generally overestimated at larger scales (100 m and greater) because the largest eddies carrying the majority of vertical mass flux are too intense. For instance they found that the total surface rainfall decreased by a factor of 10 and the cloud top heights by a factor of two when horizontal resolution was changed from 250 m to 62.5 m. In all their cases,

however, the model reproduced consistency in the updraft speed and reflectivity profiles. Therefore, while our results could still provide a good overall representation of the updraft speeds, reflectivity and microphysics profile, these are likely to be overestimated by our model. Moreover, in order to determine if all the aforementioned consistent patterns (including for the lightning, as we will see later in this section) can be trusted, additional simulations should be carried out at even finer resolutions (i.e., 25 m or less).

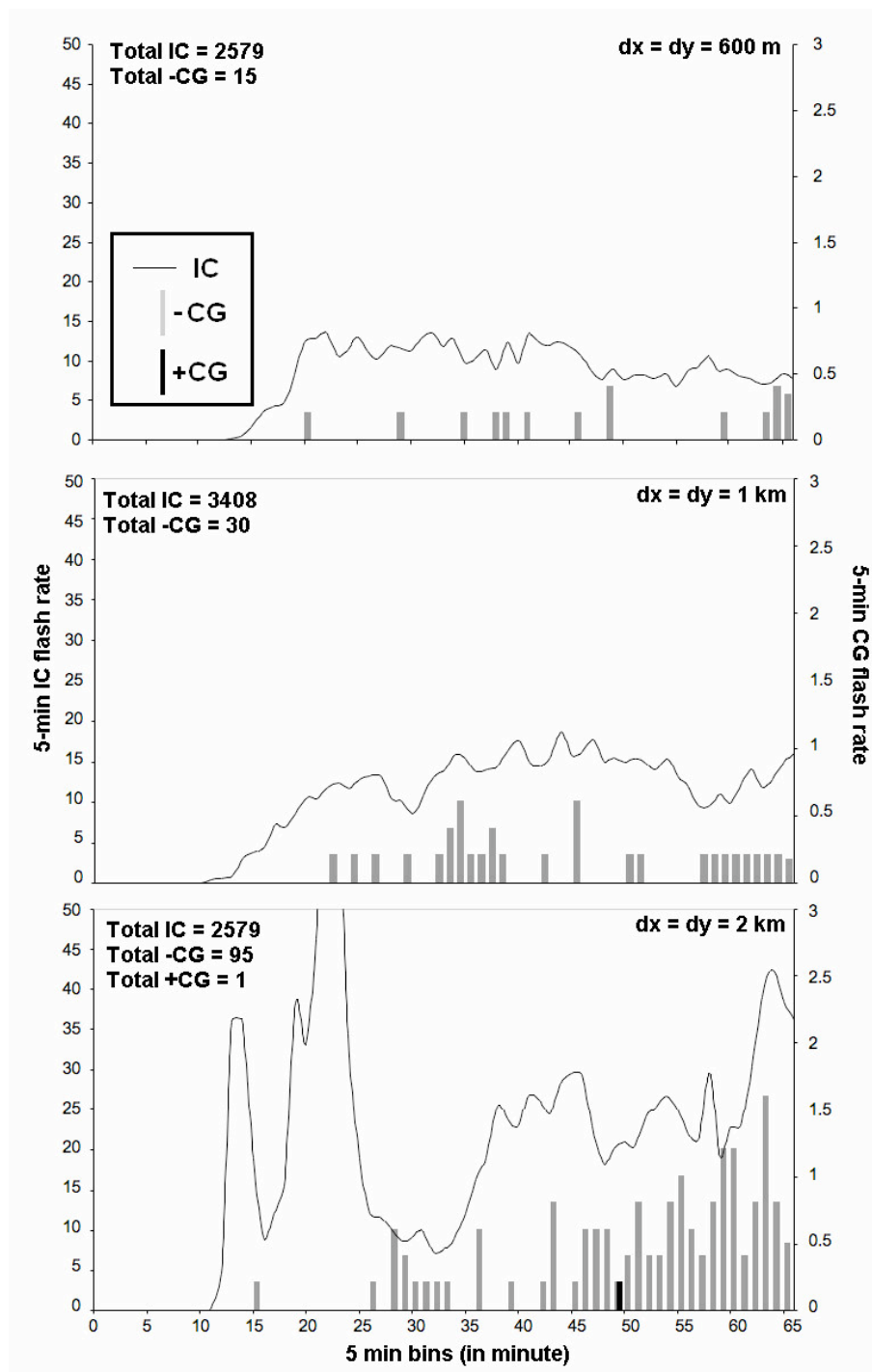
Because the 300 m simulation was carried out in a smaller domain, a direct comparison with the three remaining cases cannot be established and therefore, the time series of lightning was not included in the analysis. Nonetheless, it was worth mentioning that the 300 m simulation produced overall little lightning with IC flash rates rarely exceeding 5 per minute and hardly any CG flashes (two –CGs during the 3 h of simulation).

At the beginning of the simulation in all the four simulations, convection was triggered rapidly, causing a sharp quick rise in IC flash rate after 1 h (Fig. 17, not shown for the 300 m simulation). In all cases, the first flashes were IC flashes which was expected because in the model, charges are first produced by NI charging in the mixed phase region of the storm before they fall to lower levels. Once more, the 2 km simulation was qualitatively different from the three remaining cases: it was the only case that produced two peaks of large IC flash rate (exceeding 50 flashes per minute) at the beginning of the simulation. These two peaks in IC flash rate were associated with the existence of relatively strong updrafts exceeding  $20 \text{ m s}^{-1}$  during the first peak and with updrafts exceeding  $25 \text{ m s}^{-1}$  during the second peak (not shown). Similar updrafts speeds, however, were observed in the three other cases (not shown). Yet, these three cases did

not produce similar sharp peaks in IC flash activity (Fig. 18). The average amount of charge on the IC flashes occurring during the two sharp peaks in the 2 km case was smaller than 7 C (not shown), which indicates that the model was producing more IC flashes than needed to neutralize the excess of charge in the cloud at those particular times. In simple words, less IC flashes carrying 12-14 C (which is the average in the two other runs) would have been needed to produce the same work. Therefore, these two peaks should not be considered for the analysis of the lightning. These sharp peaks in the 2 km case were also associated with an exponential increase of the NI charging rate (NICR): for example the maximum negative NICR increased from about -2.5 to -50 pC m<sup>-3</sup> s<sup>-1</sup> between 50 min and 65 min of simulation, despite smaller graupel volume and total updraft mass flux than in the 600 m and 1 km case at those times (see later in the section). This suggests that possibly the lightning parameterization can in some rare instances have inherent issues at resolution greater or equal than 1 km (remember that the lightning horizontal grid spacing is set to half of that of horizontal grid spacing  $dx$  of the dynamic grid).

Overall, the 2 km case produced the greater amount of CG flashes and IC flashes: For instance, the amount of IC (-CG) flash that was produced in the 2 km run was two (three) times greater than for the 1 km run (Fig. 18). This result was surprising, provided that the 2 km squall line showed overall weaker updraft speeds (Fig. 17) and smaller if not similar reflectivity values at all levels (Fig. 16) than the 1 km run at 5 h 30 min. An additional time series plot (that includes an additional simulation carried out at  $dx = 3$  km) also clearly showed that overall, the maximum updraft speeds decreased as  $dx$  increased from 600 m to 3 km (with the 600 m and 1 km case being nearly similar), in

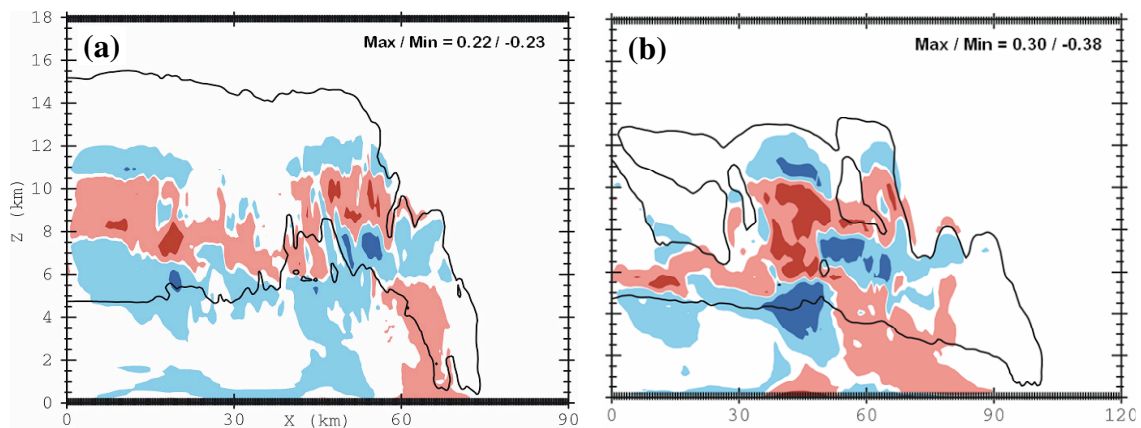
agreement with Bryan (2006). Despite this decrease of maximum updraft speed, our 2 km case produced the greatest average total graupel mixing ratio at 5 h 30 min, which in turn may explain why a greater amount of charge was generated in the 2 km case at that time (not shown). This is because in the model charging rate (and riming accretion rate) is proportional to mixing ratio. Bryan (2006) also found larger graupel mixing ratio values at  $dx = 1$  km compared to at  $dx = 125$  m. (Remember that for  $dx$  values ranging from 125 m and 1 km, they showed a progressive systematic increase in maximum updraft speed. Moreover, their 500 m and 1 km cases did not show significant difference in maximum updraft speed with time, which is in agreement with our results, not shown). After inspection, we noticed that the larger flash rates in the 2 km case (and larger graupel volume) after 4.5 h were coincident with larger (and deeper) updraft mass flux values (contours) at low levels (i.e., between  $z = 2$  and  $z = 4$  km, see later in this section). Therefore, while the updrafts were overall weaker and hence shallower in the 2 km case, they were likely wider than in the 1 km and 600 m case, which could explain why more graupel (and hence more charge and lightning) was produced in the 2 km case after 4.5 h. In other words, at about 5 h of simulation, the 2 km squall line became overall (i.e., in an average sense) more intense than the 1 km and 600 m case, which is in agreement with (Bryan 2006).

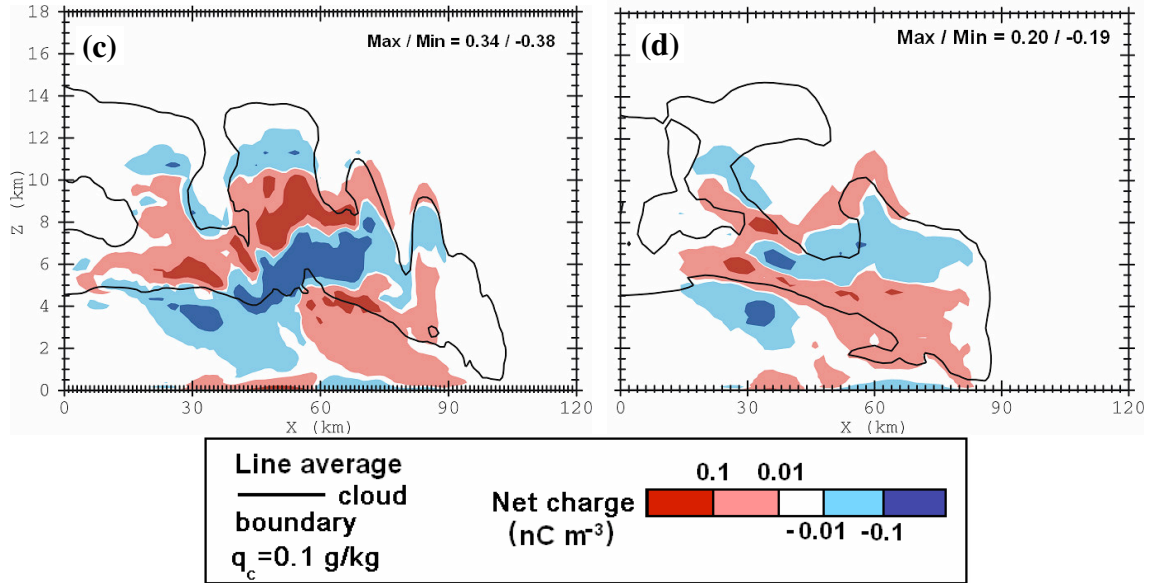


**Fig. 18.** Time series of 5-min IC and CG flash rate for the entire simulation for (a) the 600 m run, (b) 1 km run and (c) the 2 km run. The light gray (black) bars are for – (+) CG flashes, respectively and the thin black line for IC flashes.

These weaker reflectivity values in the 2 km run at 5 h 30 min were consistent with smaller values of total net space charge across the line (Fig. 19). In all cases, almost all ground flashes lowered negative charge to the surface, which were mainly observed in the mature zone. As shown in the previous section, the production of -CG flashes in the mature zone was attributed to the existence of a lower non-inductively and inductively generated positive charge region below 4 km AGL (charge shown in Fig. 19, but not charging).

Consistent with overall similar CG behavior, the average net space charge across the line showed remarkable similarities in all four cases at 5 h 30 min: the gross charge structure in the mature zone resembled a normal tripole (a main negative charge region at mid levels sandwiched between two positive charge regions) while instead, the stratiform region exhibited an inverted tripole (the opposite of a normal tripole, Fig. 19). This was an encouraging result given the somewhat large quantitative difference described earlier in the lightning behavior between all four cases.

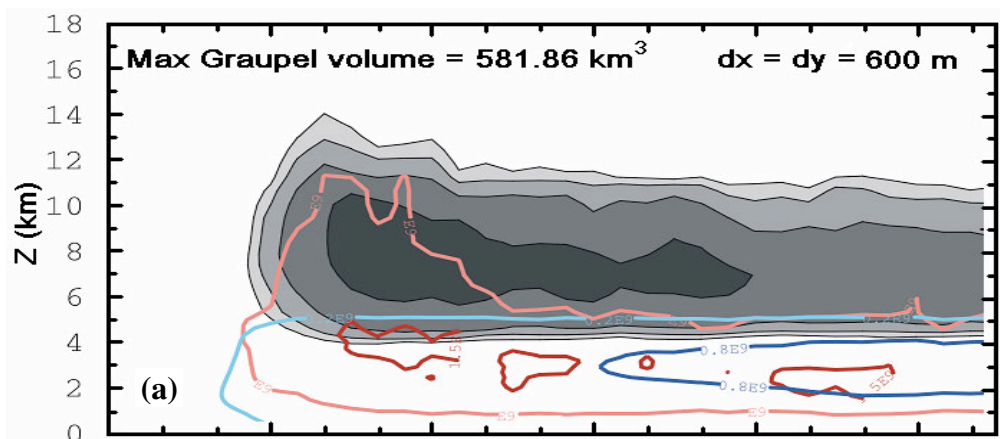




**Fig. 19.** As in Fig. 17, but for the line-averaged total net space charge (in  $\text{nC m}^{-3}$ ). Light (dark) red shaded area show where positive net space charge exceeds  $1 \times 10^{-2}$  ( $0.1 \text{ nC m}^{-3}$ ). Likewise, light (dark) blue shaded area show where negative net space charge exceeds  $1 \times 10^{-2}$  ( $0.1 \text{ nC m}^{-3}$ ), respectively. The positive and negative values of net space charge were summed along the  $Y$  axis regardless of the sign of charge. This was done in order to still obtain an average of the *net* amount of charge across the line. The thick black line represents the line average visible cloud mixing ratio of  $0.1 \text{ g kg}^{-1}$ .

In order to diagnose the squall line behavior in the 600 m, 1 km and 2 km simulations, time height plots of total updraft mass flux and total graupel volume were made. For the same reasons mentioned earlier, the time-height plot for the 300 m case was omitted from this analysis. That said, marked differences were observed between the three analyzed cases. For instances, the 600 m cases produced its largest graupel and updraft mass flux at the beginning of the simulation (Fig. 20a) rather than towards the end of the simulation as observed in the 2 km case (Fig. 20c). The 600 m run showed the largest updraft mass flux before 2 h, which was indicative of overall stronger convection generated at the beginning of the simulation. This was because all the three squall lines analyzed here were triggered with the same initial temperature perturbation. After 2 h, the

total updraft mass flux in the 600 m case remained fairly constant as the squall line convection increased in areal coverage. This indicated that after that time the overall convective strength across the 600 m squall line was progressively decreasing in intensity. This was also consistent with a general decreasing trend in total IC flash rate after 2 h for this case (Fig. 18b). Ignoring the too sharp peaks of IC flashes in the 2 km simulation for the reasons mentioned earlier, we can also note that, in all cases, the total graupel volume trend is coincident with the total IC flash rate evolution (consistent with Wiens et al. (2005) for continental supercells). In contrast to the 600 m run, the total graupel volume and total updraft mass flux in the 2 km case reached their maximum towards the end of the simulation. This was because, unlike the other three cases, the convection in the 2 km simulation did not develop in an even manner across the line and took more time to develop. In particular, the central portion of the line in the 2 km case was essentially devoid of strong convective activity. Later, at about 2.5 h, two relatively strong storm clusters started to develop on the northern and southern tip of the line, before bowing out (Fig. 15 d) and increasing in areal coverage in turn accounting for the rapid increase of total updraft mass flux and total graupel volume after 3 h.



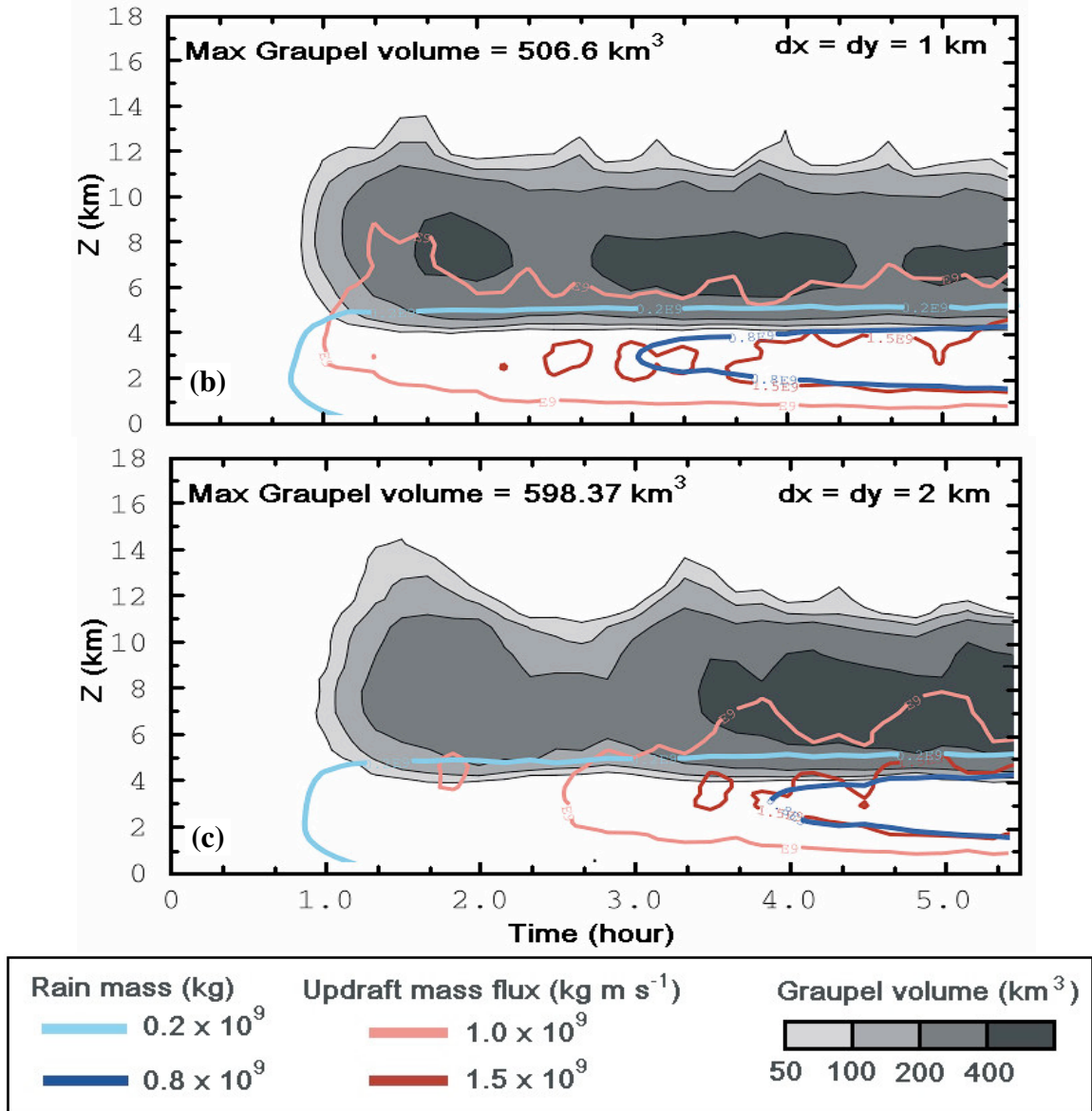


**Fig. 20.** Time-height contour plot across the entire domain of the total updraft mass flux ( $\text{kg m s}^{-1}$ , in red shown for  $10^9$  contour only), rain mass ( $\text{kg}$ , blue shown for  $10^{10}$  contour only) and total graupel volume ( $\text{km}^3$ , with the 50, 100, 200 and  $400 \text{ km}^3$  shown in light gray to darker gray) for (a) 600 m run, (b) 1 km run and (c) the 2 km run.

From its part, the 1 km case showed a relatively more steady evolution of total graupel volume than the 600 m and 2 km simulations. Also, the 1 km case exhibited an increasing trend of its total updraft mass flux, which was, however, less pronounced than

for the 2 km run (Fig. 20). Both of these trends likely indicated that as the convection increased in areal coverage in the 1 km run, it did not decrease in intensity as fast as it did in the 600 m case. The main cause for this difference in behavior between the 600 m and the 1 km case was because the initial stronger convective development (indicated by the  $10^9$  updraft mass flux contour exceeding the 10 km level, Fig. 20a) in the 600 m squall line generated much stronger and deeper cold pools than the 1 km case which ultimately lead to a progressive demise of the squall line in the 600 m case.

These results are in agreement with Bryan (2006), who also found that compared to horizontal grid spacings of about 500 m, the same squall line at  $dx = 2-3$  km developed much slower. Indeed, Fig. 19 shows that the  $1.5 \times 10^9$  updraft mass flux contour appeared progressively later in the simulation as the horizontal grid spacing was increased from 600 m to 3 km (not shown for the 3 km case). A separate time series plot of maximum updraft speeds also showed that, as  $dx$  increased from 600 m to 3 km, it took more time for these updrafts to develop. This is because the updraft cores are wider at coarser resolution and therefore more mass has to be lifted, which requires more work (i.e., for identical updraft speeds). This also explains why the updraft speeds at coarser resolution are generally weaker than at resolution of 500 m or 1 km. Below  $dx = 500$  m, however, entrainment of cooler, drier environmental air plays a dominant important role, which causes the updraft speeds to become weaker than at  $dx = 500$  m or 1 km (not shown). Therefore  $dx = 500$  m to 1 km seems to represent an optimal resolution at which the work done by buoyancy overcome the detrimental effects of entrainment.

We can also notice that after 4 h of simulation, the updraft mass flux, total rain mass and total graupel volume were much larger in the 2 km case, confirming that this

squall line became progressively stronger (i.e., in an average sense) than the two other cases, which was in turn consistent with the larger IC flash rate observed at those times (Fig. 18).

The supplementary 3 km case (not shown here) showed overall much smaller total graupel volume (max of 331 km<sup>3</sup>), updraft mass flux (smaller than  $1 \times 10^9$  kg m s<sup>-1</sup>) and maximum updraft speeds (by about 3-4 m s<sup>-1</sup>) than all the other cases and yet produced IC flash rates comparable to that of the 600 m case (i.e., about 15 flashes per min, Fig. 18). This case also exhibited CG flash rate comparable to that of the 2 km case (total of 96 -CGs and 4 +CGs, not shown). The maximum magnitude of negative NICR in the 3 km case was also overall smaller (by 50 to as much as 200 nC m<sup>-3</sup>) than the 600 m case. In other words, this additional simulation strongly suggests that the lightning production (IC and CG) in our model is *resolution dependant*.

The above result is important in the light of our next experiment (which was carried out at  $dx = 2$  km), particularly if one wished to determine quantitatively how IC flash production is related to convective burst intensity in the simulated hurricane eyewall. In other words, the result of this experiment strongly suggests that the qualitative rather than the quantitative aspect of the simulated lightning should be considered during the analysis of our idealized TC experiment. For the purpose of our study, however, this result is not of great concern as we mainly seek to acquire a better view of the qualitative aspect of the microphysics and lightning of the storm.

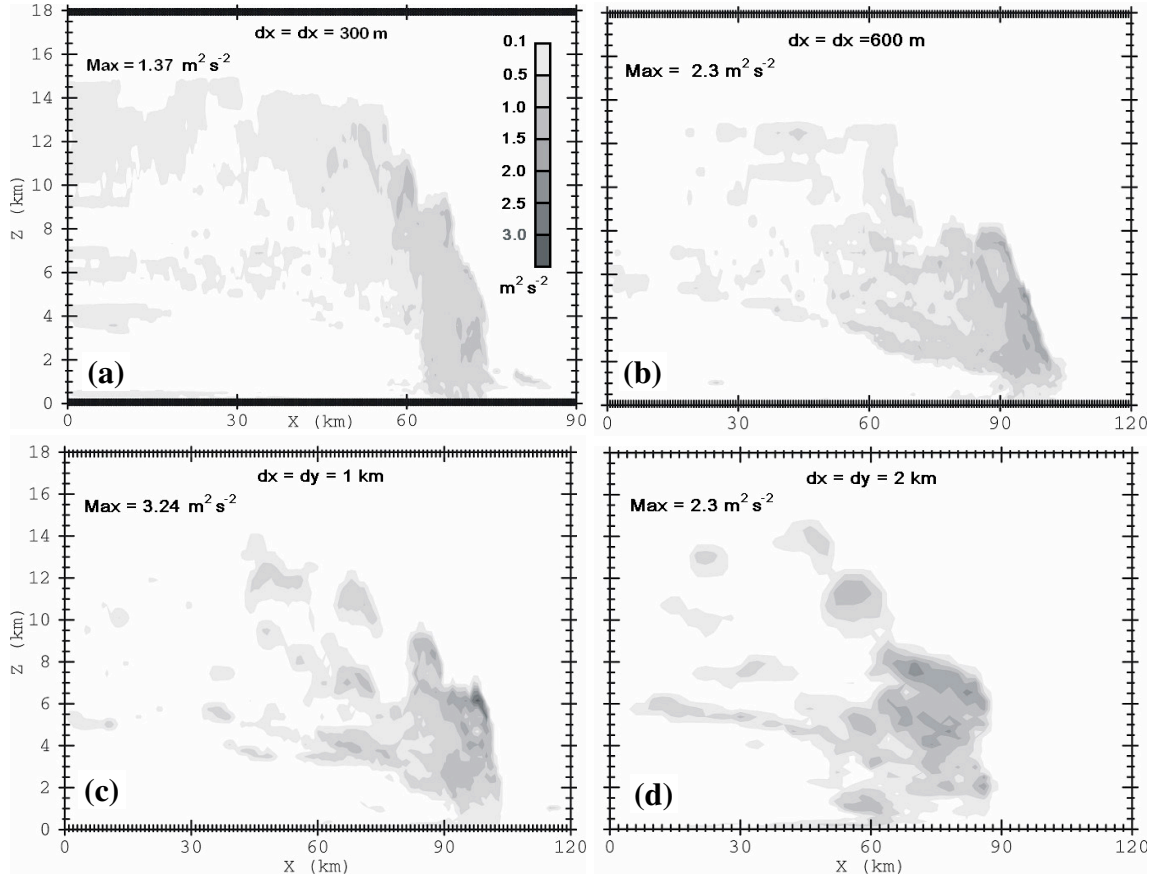


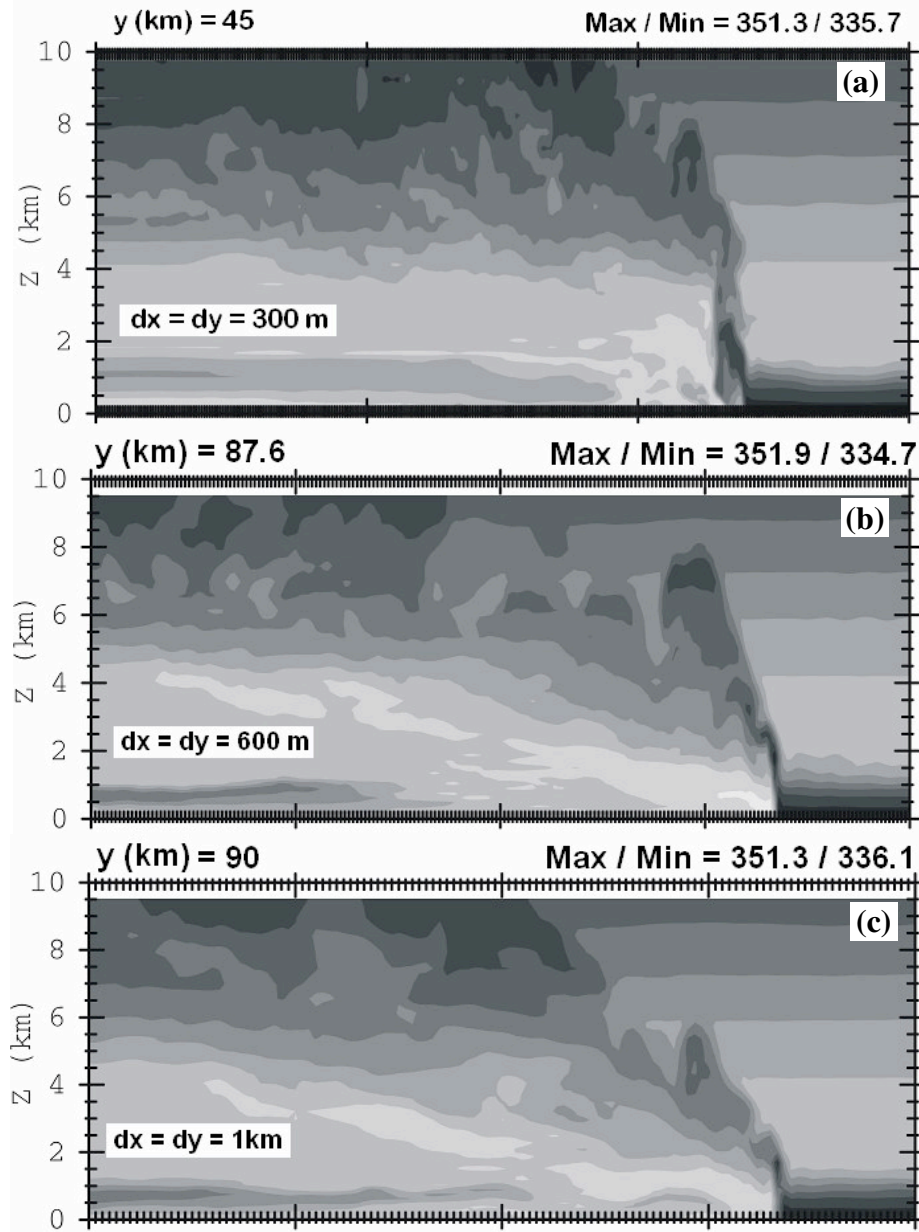
**Fig. 21.** As in Fig. 17 for the square root of the subgrid turbulence kinetic energy (TKE, in  $\text{m}^2 \text{s}^{-2}$ ). We plotted the square root of TKE, because as mentioned in section III.1, the model predicts the square root of TKE rather than TKE. Moreover, the qualitative aspect of these plots won't be affected by this scaling.

Consistent with Bryan et al. (2003), we found that the line average subgrid TKE increased as we increased the horizontal resolution from 300 m to 1 km (Fig. 21). The 2 km case, however, showed smaller values that would have been expected. Surprisingly, the areal extent of subgrid TKE values greater than zero did not decrease with increasing resolution as shown by Bryan et al. (2003). Except for the 2 km simulation, the maximum in subgrid TKE was generally observed at the leading edge of the line where the strongest shearing zones were found and then decreased progressively towards the rear of the line.

The consistently greater values of subgrid TKE as  $dx$  was increased from 125 m to 1 km in Bryan et al. (2003) work suggests that vertical diffusion (and thus updraft

strength and depth) was enhanced if not maximized at  $dx = 500$  m to 1 km. This is because TKE is proportional to the eddy diffusivity coefficient for momentum  $K_m$  (see formula (3) in section III.1). This formula also shows that when  $dx$  is multiplied by two,  $K_m$  increases by a factor  $4^{1/3}$ , which further confirms that vertical diffusion increased substantially in Bryan et al. (2003) work at  $dx = 500$  m to 1 km compared to 125 m. Indeed, in a similar more recent study with squall lines, Bryan (2006) found that the maximum updraft speed showed a progressive systematic increase as  $dx$  increased from 125 m to 1 km. This was consistent with overall taller clouds and larger graupel / hail mixing ratio at  $dx = 1$  km. Their 2 km simulation, however, had maximum updraft speeds about  $10 \text{ ms}^{-1}$  smaller than at  $dx = 1$  km (in agreement with our results), which should be consistent with shallower echo tops and possibly weaker vertical diffusion, although they did not perform this analysis.

From our results in Fig. 21 it is not clear, however, that the shallower echo tops observed in the mature zone and the trailing stratiform regions in the 2 km case at 5 h 30 min were attributed to weaker vertical diffusion. Nonetheless, ahead of the line, it seemed that our squall line exhibited larger  $K_m$  values when  $dx$  increased (Fig. 21 and formula 3) although the line-averaged updraft speeds ahead of the line did not show any clear increasing trend at that time (Fig. 17). Clearly, additional analysis of the data is necessary to elude the mysteries behind this apparent contradiction in the results herein.



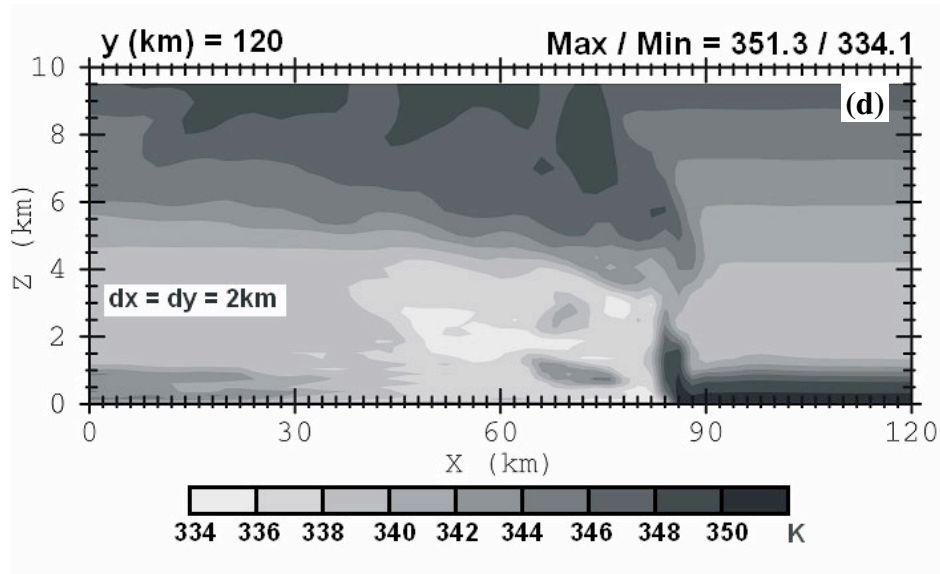


**Fig. 22.** Vertical cross section across the line in the X-Z plane of equivalent potential temperature ( $\theta_e$ ) at  $t = 10998$  s for (a) the 300 m run at  $Y = 45$  km, and at  $t = 19995$  s for (b) the 600 m run at  $Y = 87.6$  km, (c) the 1 km run at  $Y = 90$  km and (d) the 2 km run at  $Y = 120$  km.

Also worth mentioning, Bryan et al. (2003) showed that in their 1 km simulation, the  $\theta_e$  field of the air rising from the pre squall line boundary layer ahead of the gust front was relatively uniform. In our 1 km simulation, however, we start observing evidence of convective plumes (Fig. 22b at  $X = 90$  km). Nonetheless, at 2 km grid spacing, these plume structures were indeed inexistent as they were likely diffused away by the subgrid turbulence moisture and temperature fluxes. These plume-like structures became more visible as the grid spacing decreased, and as pointed out by Bryan et al. (2003). This was evidence that cloud entrainment processes became better resolved in our 300 m and 600 m simulations. Also, the 600 and 300 m cases displayed a more detailed flow structure than the two other cases in turn indicative of a more turbulent flow.

### V.2.3. Conclusions

This analysis revealed significant differences in some aspects of the simulated squall lines. For instance, the 600 m case produced the strongest updraft mass flux before 2 h, indicative of stronger updrafts and resulting stronger cold pools, which lead to a progressive weakening of this squall line after 2 h of simulation. In contrast, the 2 km case generated the strongest updraft mass flux towards the end of the simulation, which was coincident with the fast areal expansion of two bow echoes that formed on the northern and southern tip of the line. Consistent with recent studies, the 600 m squall line developed faster than the 1 km and the 2 km cases, and produced much larger total graupel volume, updraft mass flux and total rain mass at the beginning of the simulation, in contrast to the 1 km and particularly, the 2 km case. An additional simulation of the same squall line carried out at a horizontal grid spacing of 3 km confirmed this result as this squall line only started to exhibit comparable graupel volume and updraft mass flux values at about 6h.

Also in agreement with recent studies, the 600 m and 1 km squall line did not show much difference in their maximum updraft speeds, while the 2 km case exhibited the weakest maximum updraft speeds. The 3 km case mentioned earlier showed even weaker maximum updraft speeds (by about 3–4 m s<sup>-1</sup>), further confirming the above results.

It was also found that as the horizontal grid spacing increased, the total amount of lightning flashes (IC+CG) increased as well, warranting further caution in interpreting the qualitative aspects of the simulated lightning, particularly in our next experiment., which

was carried out at a similar coarse resolution. However, we found that the qualitative aspect of the lightning (i.e., dominant CG polarity, lightning distribution, charge structure, NICR and inductive charging rate profiles) was overall similar in all five cases.

Also, we found that the basic features of typical squall lines, such as a well developed gust front at its leading edge, a mature zone and a stratiform region with weak mesoscale updrafts/downdrafts at the rear of the line were reproduced with somewhat good consistency by the model in all cases. Also the graupel, snow mixing ratio and CWC profile was qualitatively similar in all four cases.

These results suggests that, at  $dx = 2$  km, useful information of the microphysics field and electrical behavior can still be acquired.

However, in order to assess whether these common patterns are reliable, additional simulations should be carried out at horizontal grid spacings ranging from 200 m to about 10's of meters to determine if the solution shows statistical convergence.

## **V. 3. OCEAN experiment**

### **V.3.1. Introduction**

The previous experiment showed that the model was able to reproduce maritime tropical convection with acceptable degree of trustworthiness. For a spectrum of horizontal grid spacings ranging from 300 m to 2 km, the simulated squall lines, however, showed non-negligible differences in their reflectivity patterns, total graupel volume and total updraft mass flux. The previous experiment also highlighted that the total amount of lightning flashes (IC+CG) generated by the model was quite sensitive to the horizontal grid spacing, which warrants caution if the quantitative aspect of the lightning is investigated.

Nonetheless, the overall flow structure, charge configuration and lightning distribution of the simulated squall line were all qualitatively similar. The latter also held for the microphysics profile across the line (mostly between the 300 m, 600 m and 1 km cases).

The results presented in the previous section suggested that when using a horizontal grid spacing of 2 km, caution should be exercised in interpreting the quantitative aspect of the simulated storms. In particular, while the reflectivity fields and updrafts could be generally shallower and weaker, the graupel and hail mixing ratios could be larger than expected from the same simulation carried out at horizontal grid rangings between 500 m and 1 km. It is also likely that most updrafts occurring in mature

TCs are smaller than 8 km in width, which is a rough estimate of the minimum updraft size that can be resolved at  $dx = dy = 2\text{km}$ .

However, the previous experiment also suggests that a hurricane simulation carried out at 2 km horizontal grid spacing could still provide useful qualitative insight on the simulated TC flow structure, microphysical and electrical properties. Moreover, such analyses are a necessary step in providing a base onto which investigators could make comparisons with future more detailed experiments carried out at lower resolutions.

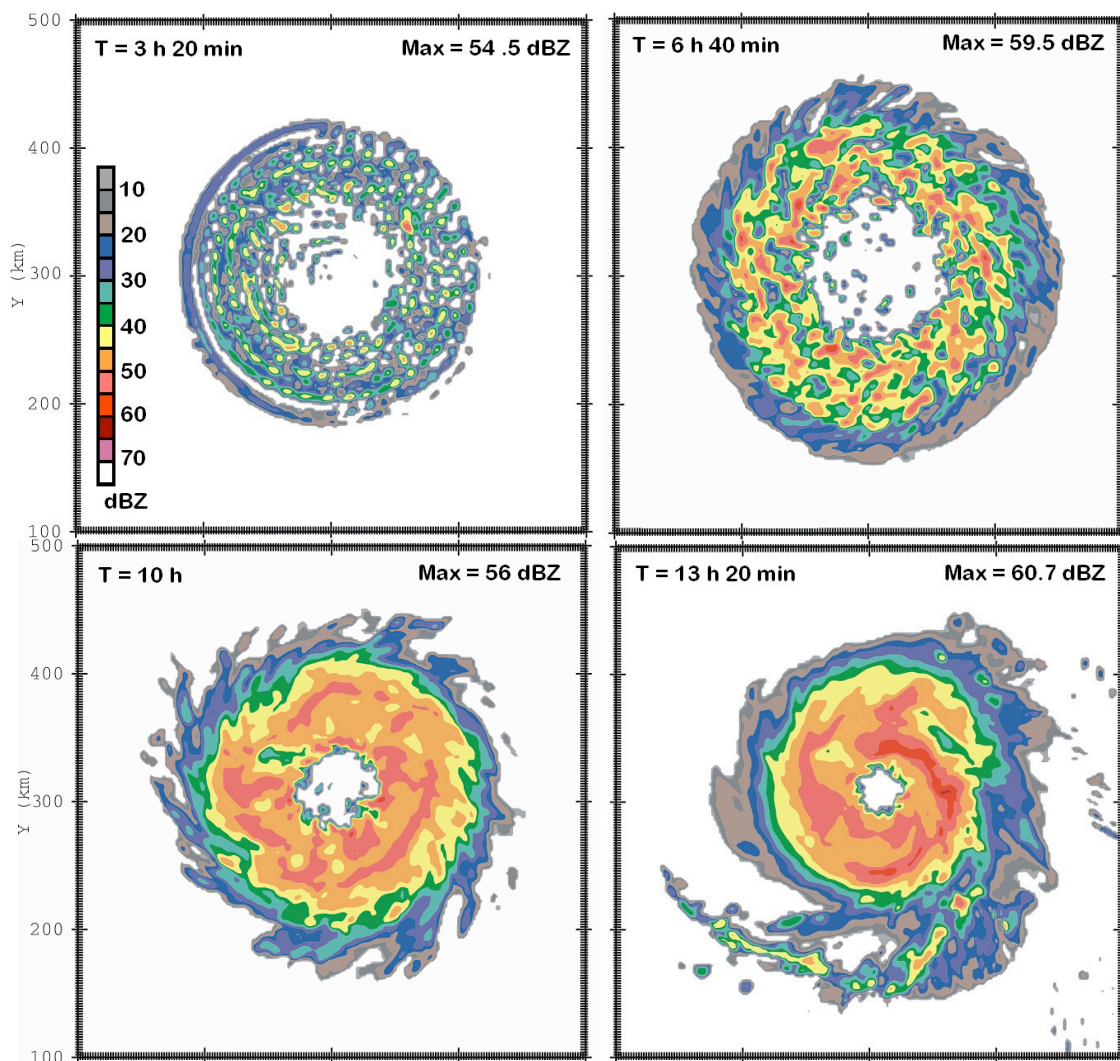
The first part of this analysis will describe the overall evolution of the formation of the TC in the model. Later for a common slice time, the microphysics and lightning activity of the simulated TC will be analyzed in detail.

### **V.3.2. Results**

The simulated vortex went through several phases; the first phase was the rapid development of convection in concentric rings around the center at about 3 h (Fig. 23) which was partly caused by using a homogeneous environment as the initial condition. As time progressed, the individual convective elements organized around the center to form a broad ill-defined eye around 9-10 h, coincident with a rapid increase of the areal coverage of the storm (e.g., in terms of the 40 dBZ reflectivity contour at 1 km AGL) and a progressive decrease in minimum surface pressure (Figs. 23, 24a). After about 10 h, the eyewall started to shrink progressively by advection of angular momentum and subsequent conservation of angular momentum from the induced secondary circulation. At about 19 h of simulation, the hurricane vortex reflectivity pattern started to exhibit

several features observed in mature hurricane in nature, namely a more solid, narrow strong ring of convection around the storm's center or eye and the formation of several spiral rainbands around the eyewall of the storm (Fig. 23). Clearly, the early development stage of the storm was very unrealistic, since we forced convection to occur via frictional convergence by using a quasi-symmetric Rankine type vortex already having category 1 hurricane force winds (Fig. 6) embedded in a homogeneous environment.

Moreover, the characteristic time scale for hurricane formation is in the order of 3-4 days, whereas in our simulations, a hurricane-like vortex became evident only after about 20 h. This procedure was mainly dictated by computational efficiency.



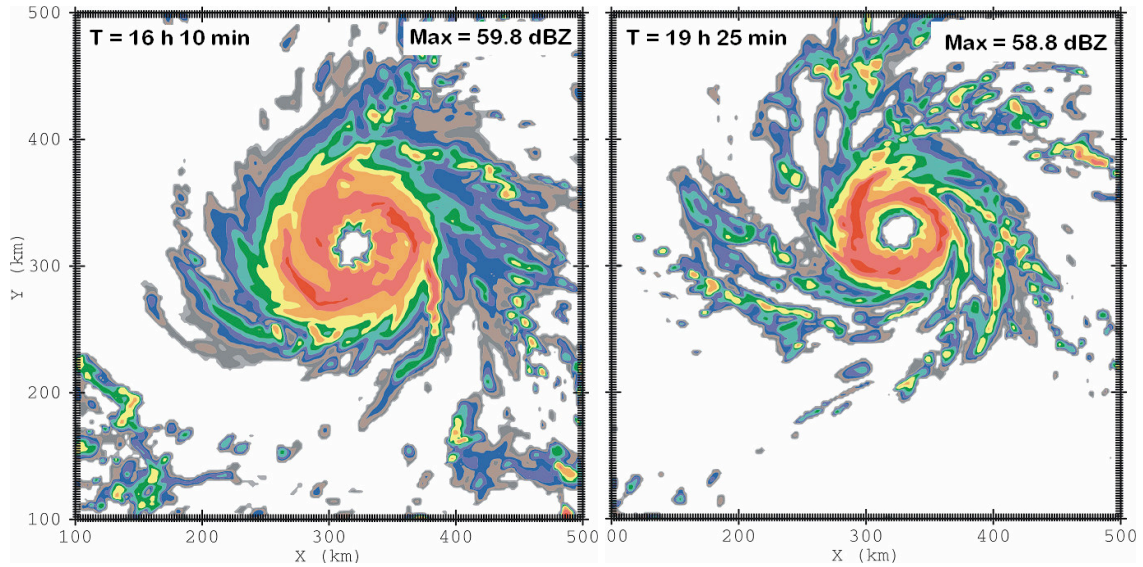


**Fig 23.** Horizontal cross sections of radar reflectivity at  $z = 1.028$  km AGL showing the time evolution of the TC in the model.

The storm experienced its sharpest drop in atmospheric pressure at 100 m between about 10 h and 17 h (Fig. 24a), which is a delayed (hydrostatic) response to stronger subsidence caused by the increasing upward mass flux around the vortex central axis of rotation about 4 h earlier.

The total simulated lightning activity, particularly the IC and –CG flash rate was correlated with the storm total 35-40 dBZ areal coverage (Figs. 23 and 24b). The area of 35 dBZ radar reflectivity reached a maximum radius of about 200 km at about 10 h of simulation (Fig. 23). Around that time, IC flash rate exceeded 1000 flashes per minute (Fig. 24b), which may be unrealistically high. Later on, however, as the intense ring of convection around the storm center shrank to more realistic sizes (10-15 km radius at about 20 h), the total IC flash rate decreased below 400 flashes per minute (Fig. 24b), which may be closer to actual values (although no reliable IC flash rate data are yet available for mature hurricane over ocean). The squall line sensitivity experiment, however, showed that these flash rates are likely to become smaller for grid spacings

ranging between 500 m and 1 km although the general trend should remain the same. Therefore, the flash rate values shown in Fig. 24b should only serve as an approximation of the storm total flash rate.

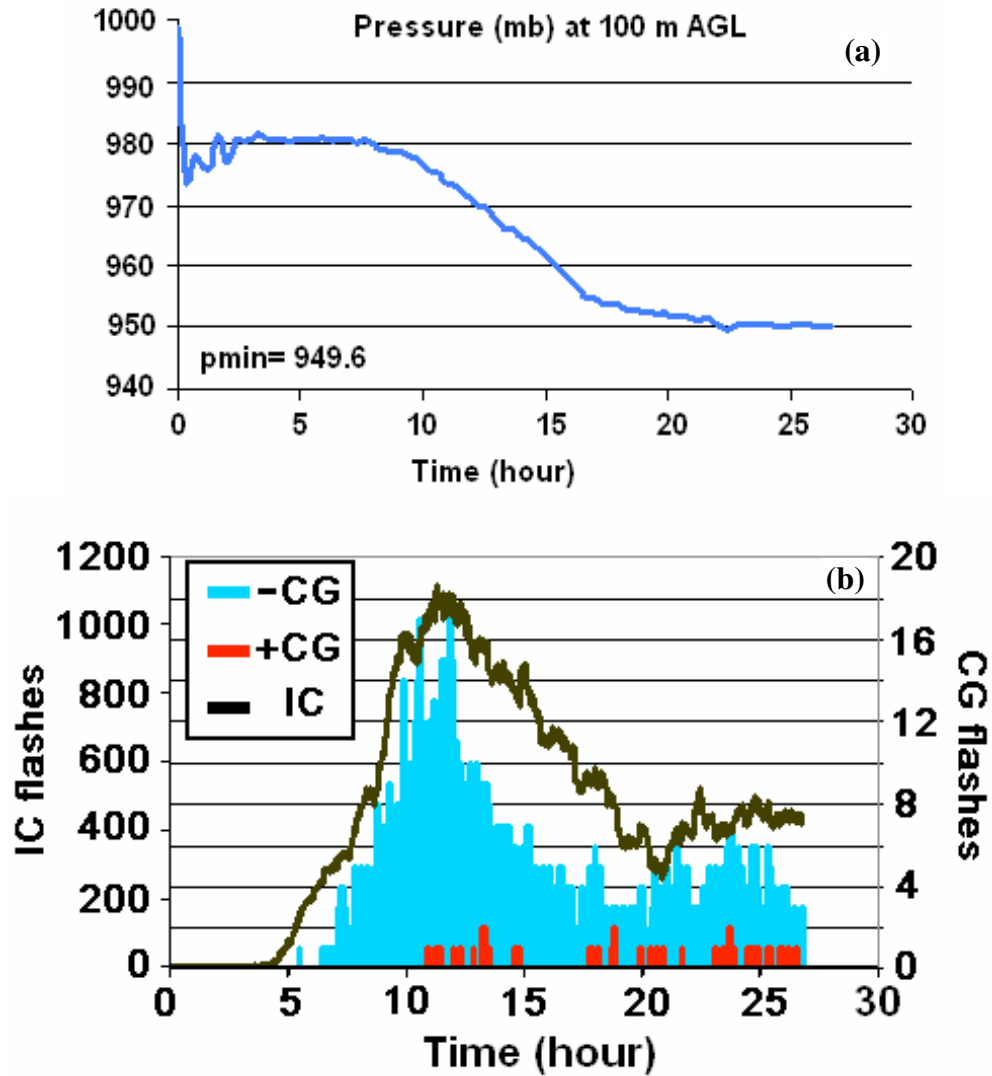


**Fig. 24.** Time series for the first 27 h of simulation of (a) pressure at  $z = 100$  m AGL and (b) for the 1-min +CG, -CG and IC flash rate across the whole domain.

At about 22 h, the TC experienced a temporary increase of total IC flash rate from about 400 to about 500 flashes per minute (Fig. 24b). This increase in IC flash rate was mainly caused by the formation of several strong cells north of the TC (not shown). Also

at about 22 h, a small burst of convection caused the eyewall to become asymmetric for about a 3 h period. The resulting intense precipitation core ( $> 55$  dBZ at 1 km AGL) spiraled around the eye. As this updraft core weakened and collapsed, the eyewall became again more symmetric. Between 20 and 24 h, the eyewall convection shrank further, and the updraft speeds just above the melting level ( $z = 6.1$  km AGL) experienced a general weakening trend (not shown). In contrast, during this period, the rainband convection gained strength and increased in areal coverage. Updraft speeds of  $5$   $\text{m s}^{-1}$  and greater were found all around the eyewall at about 24 h. Four hours later, at about 28 h, eyewall updrafts speeds rarely reached  $5$   $\text{m s}^{-1}$ , while the eastern portion of the eyewall was dominated by weak downdrafts ( $1$   $\text{m s}^{-1}$ ) at this level. The exact reasons for this rapid weakening of the eyewall updraft mass flux are not clear and will be addressed in the future work section in more detail.

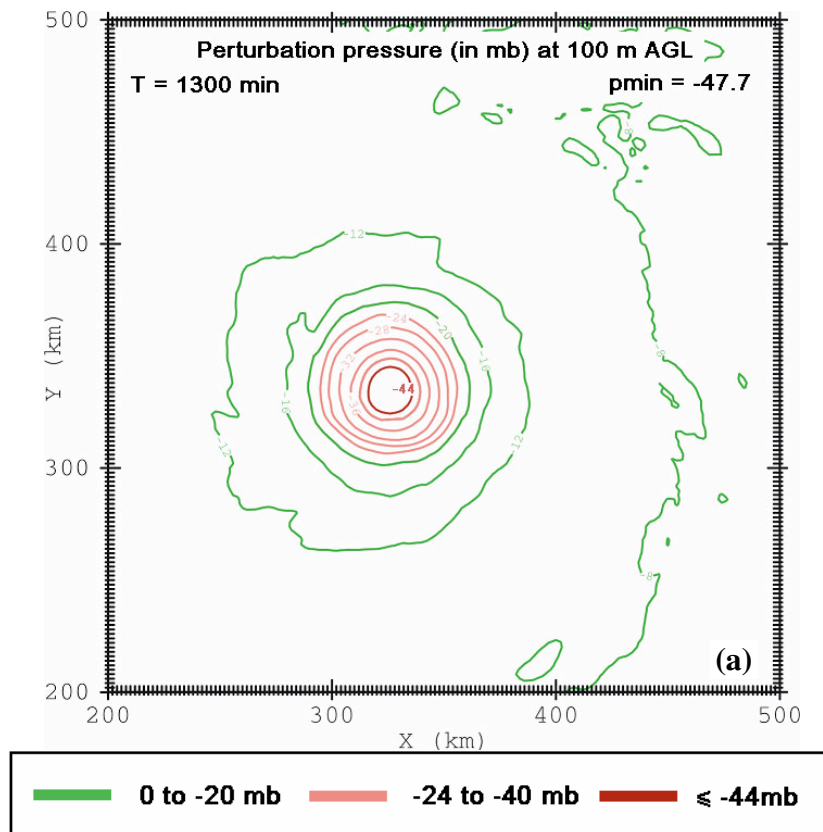
The sudden pressure drop from 999 mb to about 975 mb at the start of the simulation (Fig. 24) was likely caused by a rapid hydrostatic (geostrophic) adjustment response of the model to the Rankine vortex imposed as initial wind field. More precisely, the balance between centrifugal forces and pressure gradient forces (and Coriolis force) in a strong cyclonic (or anticyclonic) barotropic vortex caused the pressure at its center to drop. Hence the pressure field in the simulation domain dropped in response to re-establish equilibrium between the initial (cyclonic) Rankine vortex and the model base state environment.

As shown, the vortex experiences several phases and for this reason a common slice time was selected for analysis of the results. The vortex started to resemble a mature

hurricane near 20 h and therefore, a common slice time of 78000 sec (21 h 40 min) was chosen.

At that time, the lowest pressure was about 949 mb and as expected, was located near the storm center of rotation (Fig. 25a). This pressure drop was caused by the storm's cyclonic circulation at low levels and by the strong mid-tropospheric warming attributed to subsidence in the eye (Fig. 26a).

The maximum positive vertical vorticity values were found in the inner edge of the eyewall convective ring (Fig. 25b). This vorticity arose from conservation of positive angular momentum in the shrinking eye and also from the strong horizontal gradients of horizontal winds that exist between the eye and the eyewall. The exact reasons behind the presence of 2 concentric rings of maximum positive vertical vorticity were, however, unknown and will be the subject of future studies.



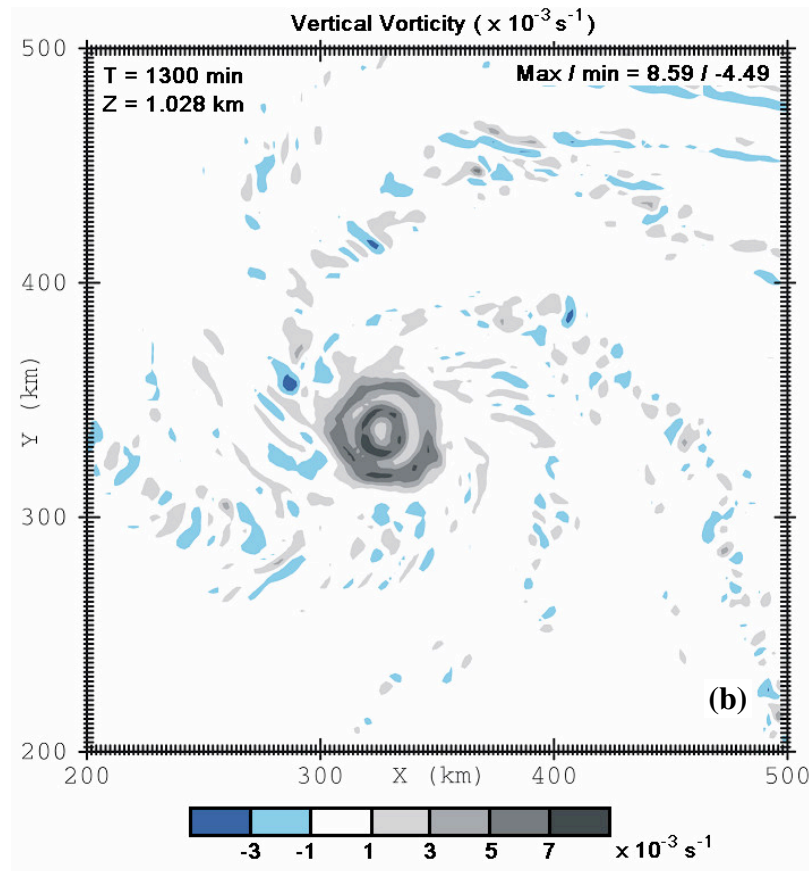


**Fig. 25.** Horizontal cross of (a) perturbation pressure in mb at 100 m AGL and (b) vertical vorticity ( $\times 1000 \text{ s}^{-1}$ ) at  $t = 1300 \text{ min}$ . In panel (a), green contours range from 0 to -20 mb by increments of 4 mb. In a similar manner, light (dark) red contours range from -24 to -40 (-44 mb) by increments of 4 mb. For panel (b), the legend for the vertical vorticity magnitude is shown below the X axis.

Above the storm's anvil, strong warming anomalies sometimes exceeding +20 K were observed in discrete locations (Fig. 26a). These unusually strong warm anomalies were likely attributed to gravity waves triggered by the strong penetrative updrafts (i.e.,  $> 10 \text{ m s}^{-1}$ , see later in the section) within the eyewall convection (e.g., Fovell et al. 1992). Since the tropopause level was characterized by strong static stability gradients and hence strong potential temperature gradients, strong anomalies were most likely to occur there. Strong cooling of about -20 K was also observed just atop the TC's central dense overcast. Also, outside the eyewall (at about  $X = 300\text{-}360 \text{ km}$ ), weak cooling (-1 K) was

observed between 2 and 3 km AGL. The strongest warming occurred near  $z = 13$  km AGL within the eye (Fig. 26a), which was expected in mature hurricanes having a well-defined eye at its center (e.g., Gray 1995).

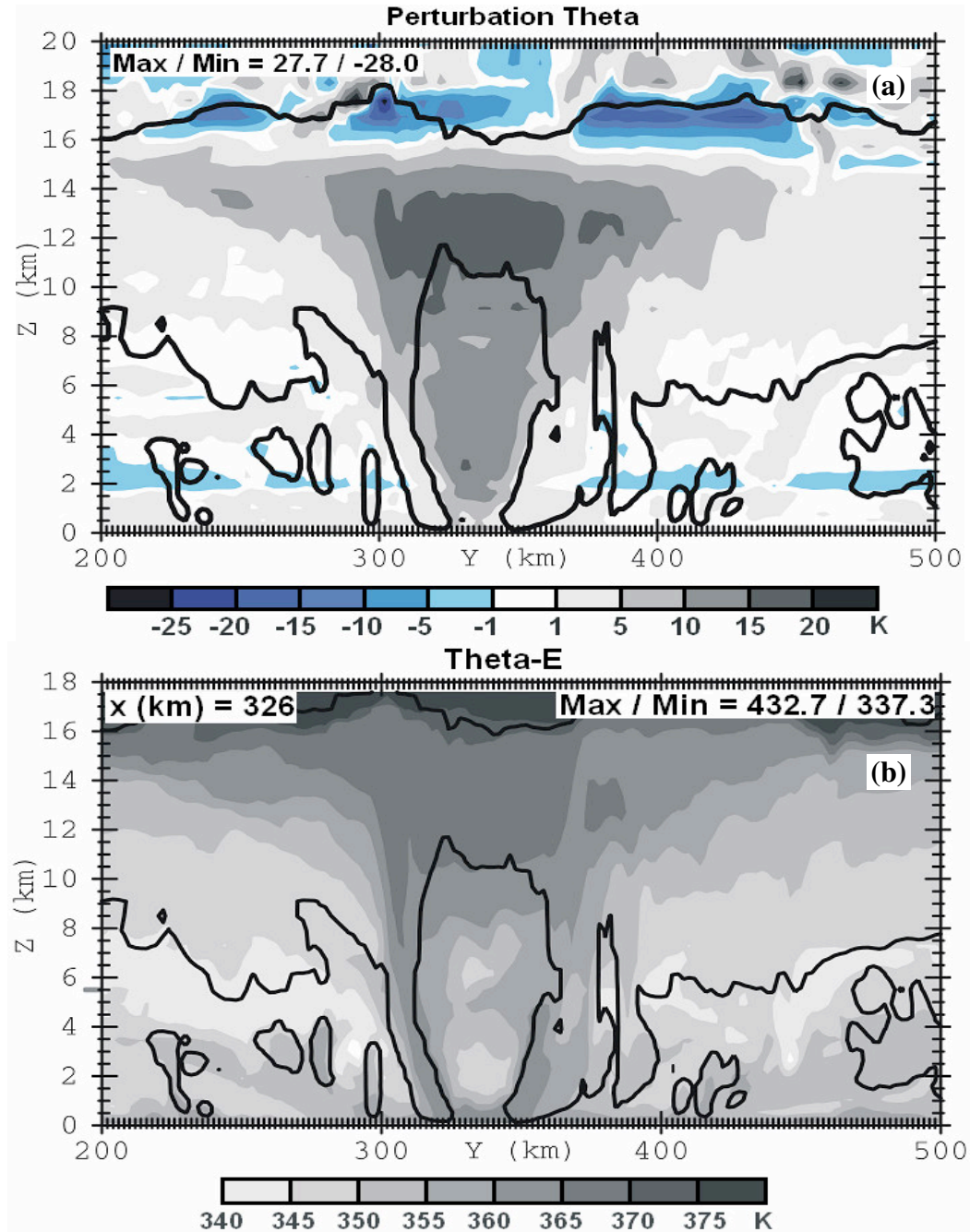


**Fig. 26.** (a) Vertical cross section in the  $Y$  direction at  $X = 326$  km of cloud mixing ratio ( $0.1 \text{ g kg}^{-1}$  contour in thick black line) and perturbation potential temperature (from initial base state). Panel (b) is as panel (a) for equivalent potential temperature

(indicated by shading). Note that the maximum altitude on the vertical axis goes until 18 km instead of 20 km for all the remaining model cross sections shown in this study.

The eyewall updraft was generally characterized by high equivalent potential temperatures ( $\theta_e$ ) of about 360 – 365 K (Fig. 26b), which are consistent with values observed within hurricane Isabel (2003) eyewall (Aberson et al. 2006). Similar  $\theta_e$  values were also found below 1 km AGL in the eye, while just above that level  $\theta_e$  is about 15 K lower. Similar to observations made by Willoughby (1998), this sharp  $\theta_e$  gradient in the eye was associated with an inversion separating the more humid, warm air in the boundary layer caused by moist air inflow and surface fluxes and the drier, subsiding air from aloft that has been trapped by the TC circulation. However, Willoughby (1998) found that this inversion was generally located at higher levels between 850 and 500 mb. Also, as mentioned earlier, observations made within three recent category five hurricanes showed that  $\theta_e$  could reach 380 K in the eye at low levels, which in some instances can become mixed into the eyewall updraft by small, shallow mesovortices forming on the inner edge of the eyewall, thereby providing further heat energy to the eyewall (providing convective instability, Kossin et al. 2004; Aberson et al. 2006).

Above 8 km in the eye,  $\theta_e$  steadily increased to values ranging between 365 and 370 K near 13 km AGL (Fig. 26b), due to adiabatic compression, and hence warming (Fig. 26a), of the subsiding air.

The eyewall convection and resulting radar reflectivity exhibited numerous asymmetries (Fig. 27), as is often the case for mature hurricanes in nature. Tangential wind speeds exceeded  $60 \text{ m s}^{-1}$  (Fig. 28c), with the highest gusts just within the boundary layer above the surface (Fig. 28a). Thus, the simulation corresponded to a mature high-end category 3 storm at this time.

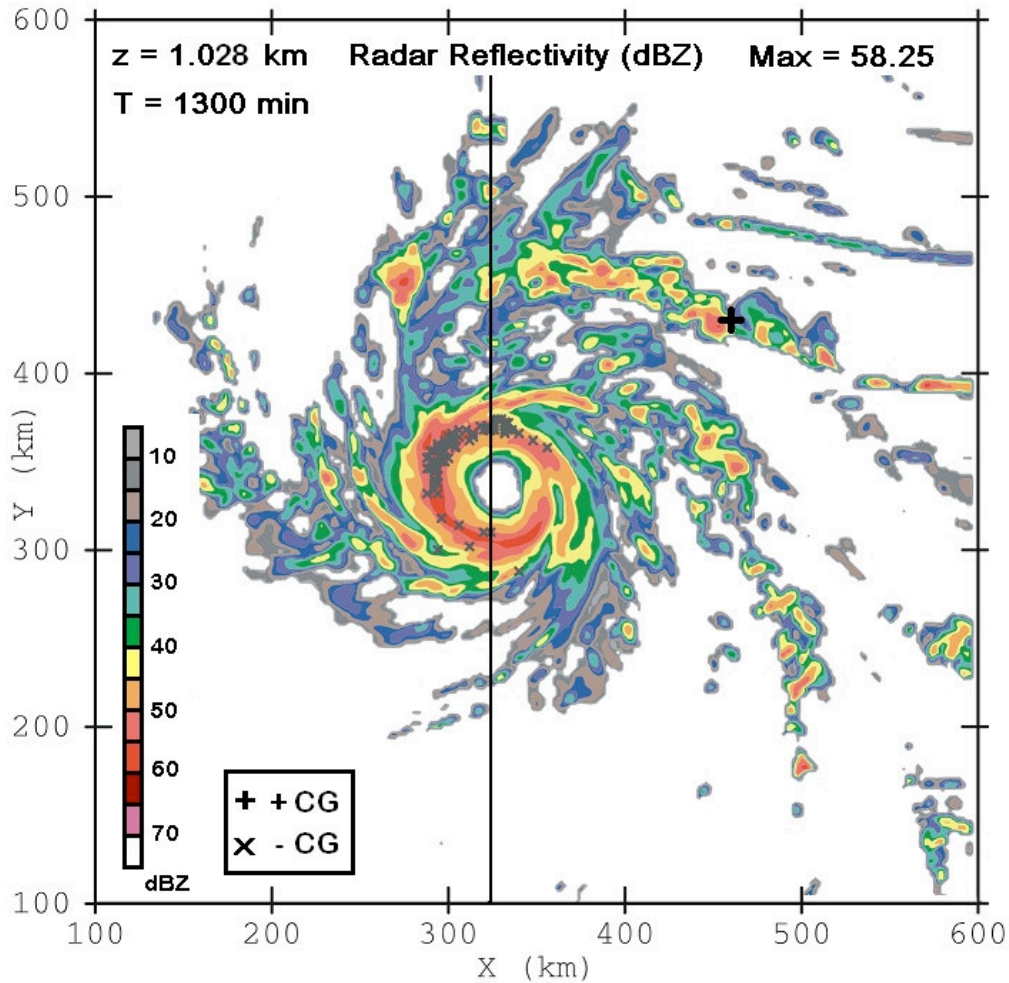
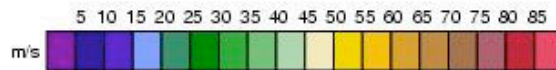
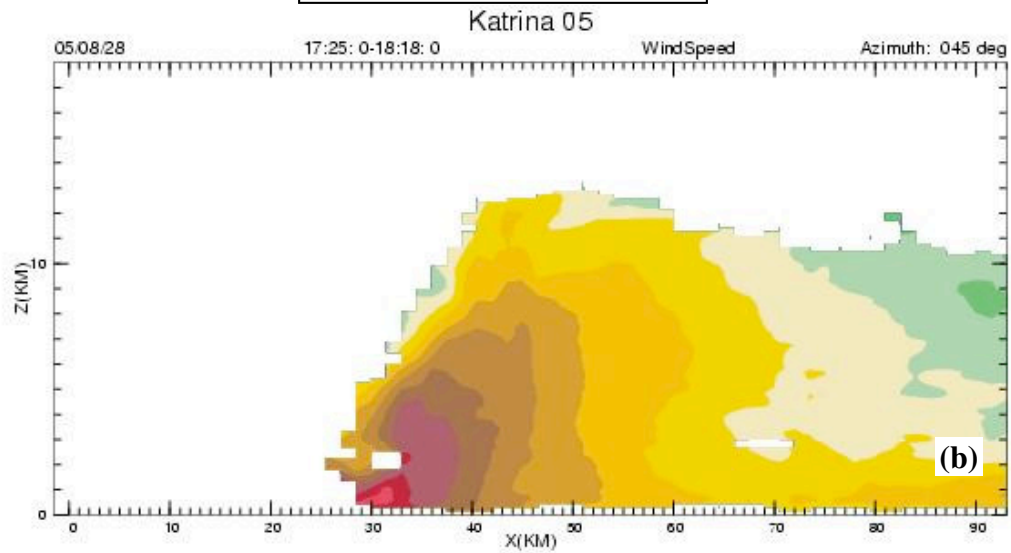
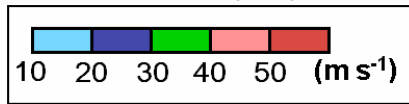
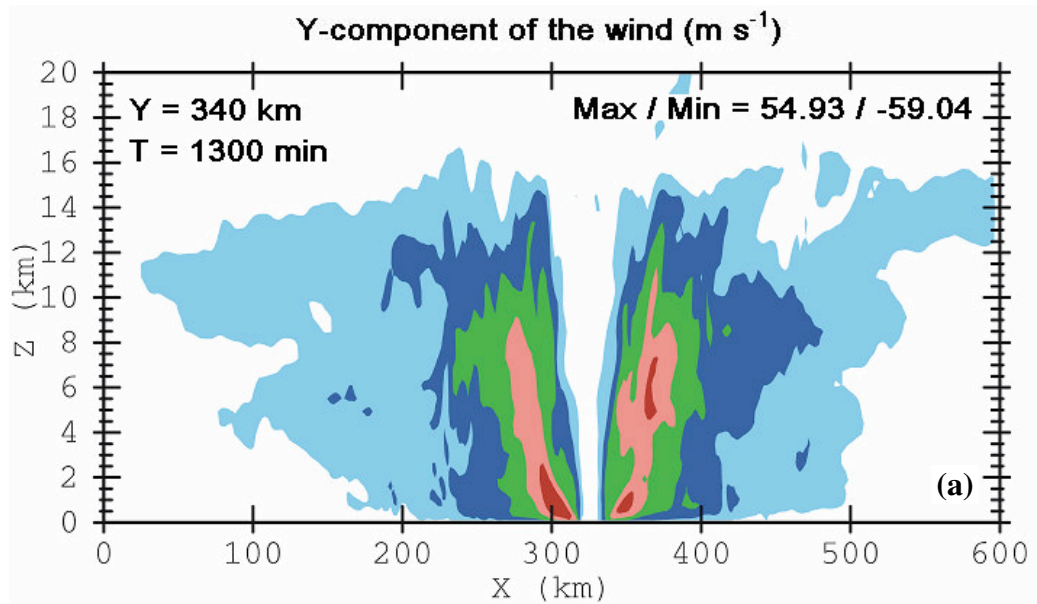


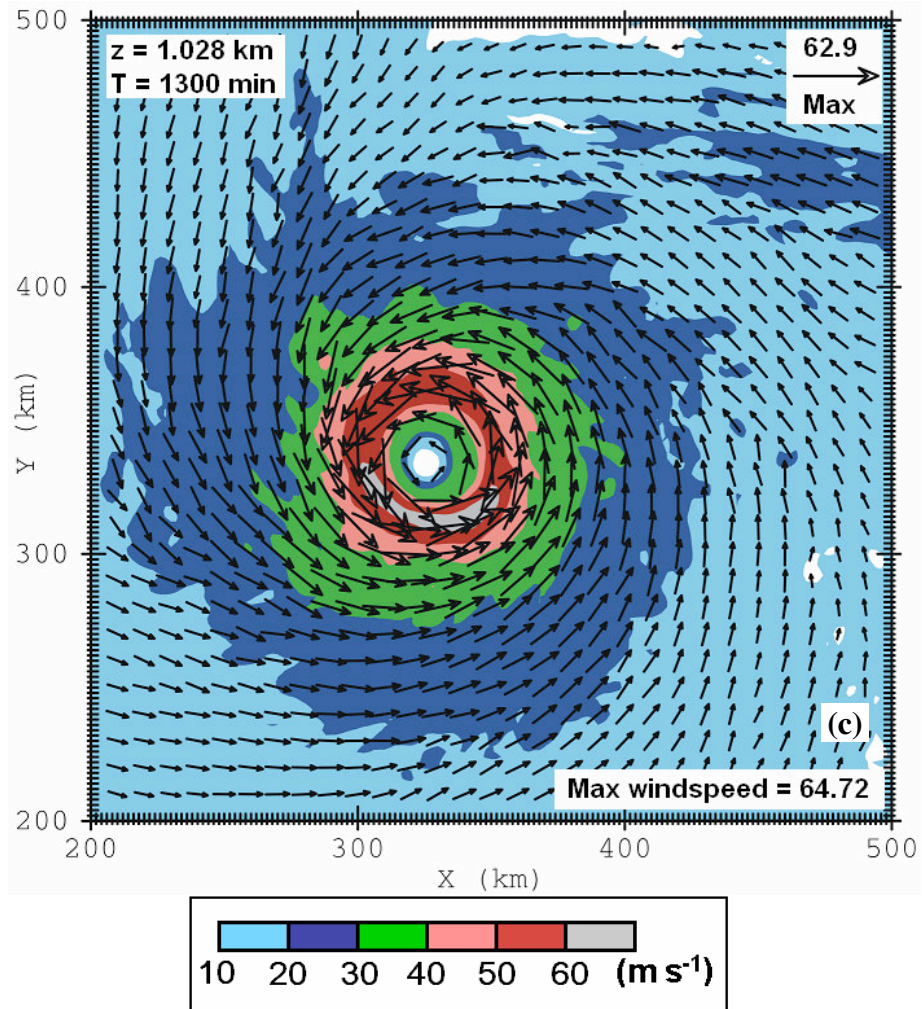
**Fig. 27.** Horizontal cross section of radar reflectivity (dBZ) at  $t = 1300$  min and  $z = 1.028$  km. Shading indicates reflectivity in 5 dBZ increments from 5 dBZ to 75 dBZ. Locations of CG lightning strikes are also shown by a cross for  $-CG$  flashes and by a + for  $+CG$  flashes. The flash locations were plotted for a 30 minutes interval up to the cross section time. A black line shows the location of the vertical cross section of the majority of the plots shown in this study.

Consistent with many *in situ* aircraft observations, the simulated TC eyewall tangential winds exhibited an outward tilt with height (Fig. 28), also seen in the vertical reflectivity profile (Fig. 29a). Between the eyewall and rainband convection, a stratiform region with weak reflectivity values was also evident (e.g., see Fig. 29a at  $Y = 390$  km). Secondary weak bands below the outer core stratiform region of the eyewall were also found on the western and eastern flanks of the storm (see Figs. 29a at  $Y = 400$  km). The

heaviest rainfall rates were found in the vicinity of the eyewall, with a secondary maximum in the outer rainband (Fig. 29a).



CONTOUR: S  
LATITUDE: 28 DEG 20 MIN 0 SEC LONGITUDE: -88 DEG -39 MIN 0 SEC



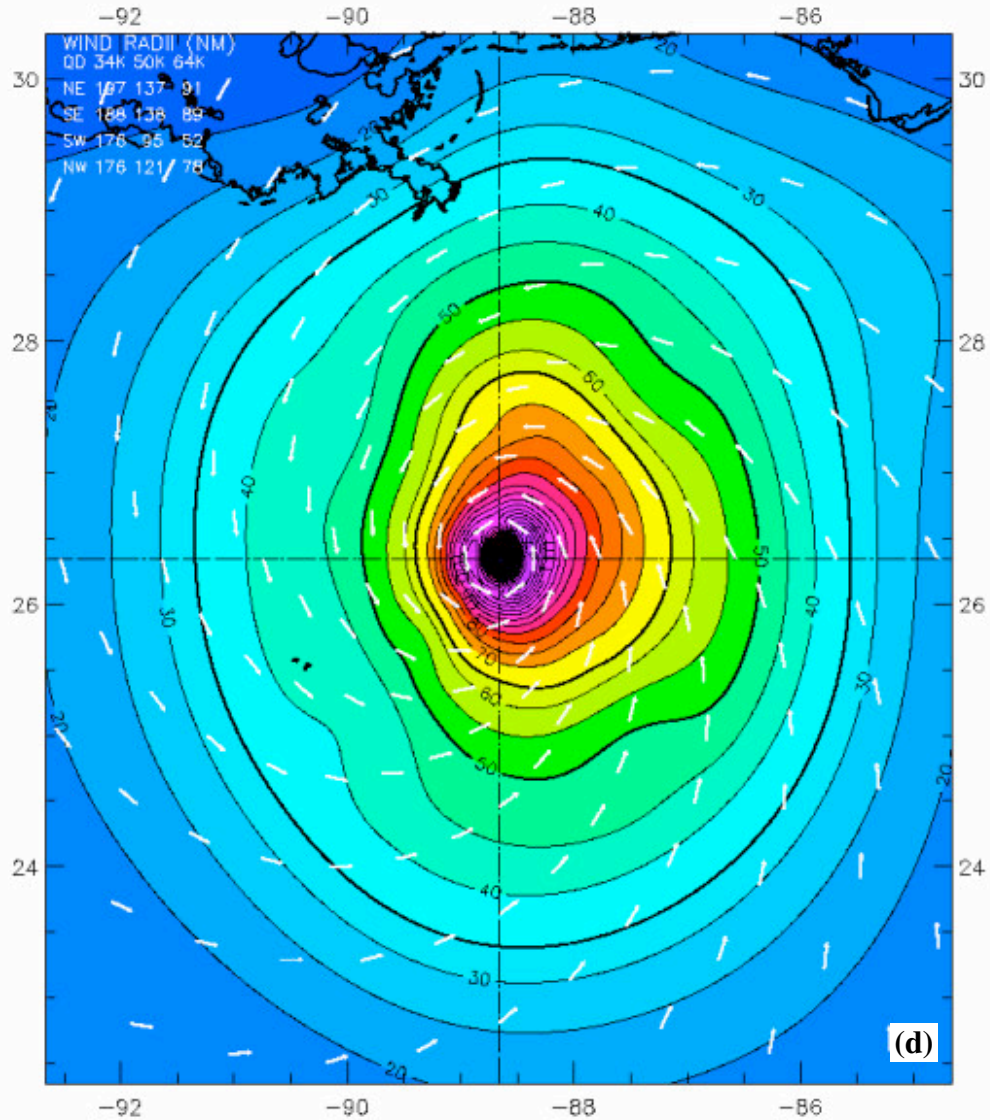
## Hurricane Katrina 1800 UTC 28 AUG 2005

Max 1-min sustained surface winds (kt)

Valid for marine exposure over water, open terrain exposure over land

Analysis based on AFREC from 0907 - 1459 z; SFMR43 from 1622 - 2100 z;  
 CMAN from 1500 - 2100 z; FCMP\_TOWER from 1510 - 2055 z;  
 ASOS from 1500 - 2056 z; BACKGROUND\_FIELD from 1800 - 1800 z;  
 SHIP from 1612 - 1818 z; GPSSONDE\_WL150 from 1503 - 2041 z;  
 METAR from 1500 - 2059 z; MOORED\_BUOY from 1509 - 2100 z;  
 TAIL\_DOPPLER43 from 1755 - 2038 z; GOES from 1602 - 1902 z;  
 MESONET from 1500 - 2058 z;

1800 z position interpolated from 1755 Army Corps; mslp = 902.0 mb



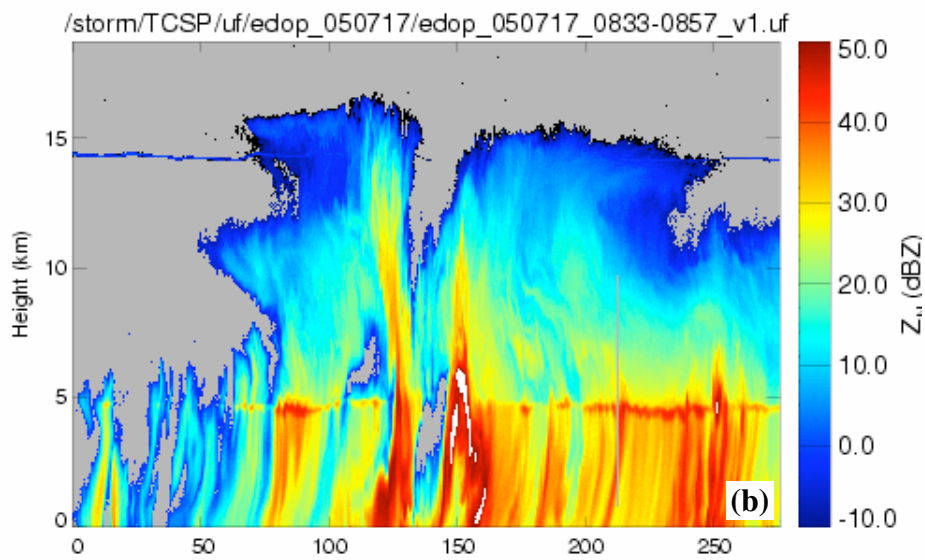
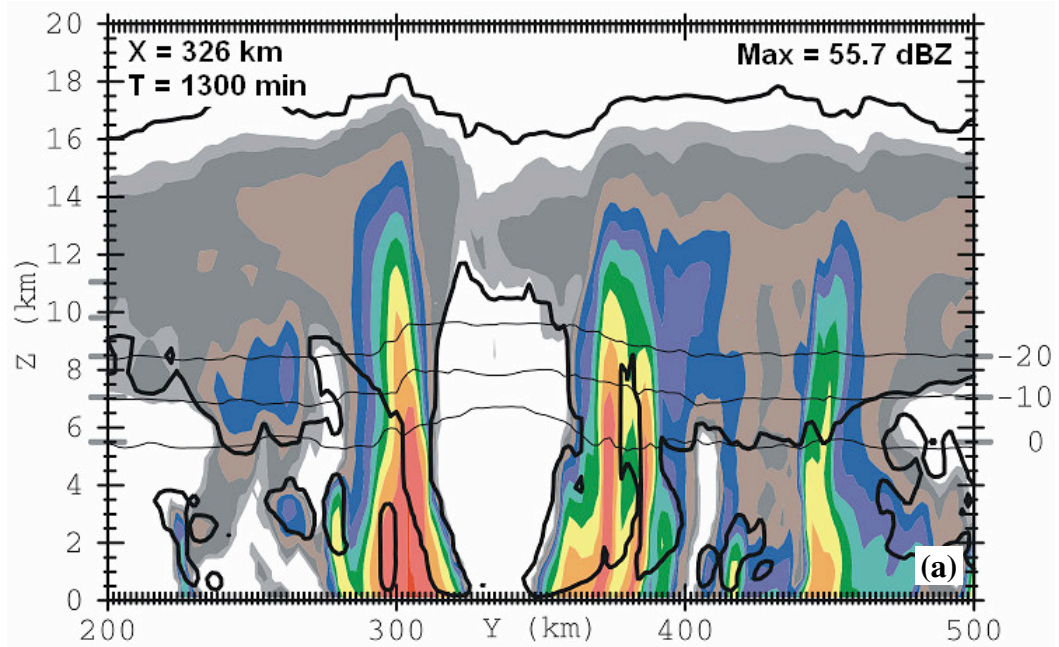
Observed Max. Surface Wind: 138 kts, 16 nm NE of center based on 1744 z SFMR43 sfc measurement  
 Analyzed Max. Wind: 138 kts, 18 nm NE of center

**Fig. 28.** (a) Vertical cross section at  $Y = 340$  km of and (c) horizontal cross section at  $z = 1.028$  km of the  $Y$ -component of the wind. Both panels (a) and (b) are shown for  $t = 1300$  min. As in Fig. 9, the maximum vector magnitude is smaller than the

maximum windspeed because the density of the vector field is 1 out of 10. Panels (b) shows a cross section of the tangential winds (in  $\text{m s}^{-1}$ ) from a P-3 aircraft reconnaissance of Hurricane Katrina (2005) near 1800 Z and panel (d) shows interpolated horizontal winds (in knots) at the surface from various data sources. Images in panel (b) and (d) are courtesy of <http://www.aoml.noaa.gov/hrd>.

The 0 C and -20 C isotherms were found at higher altitude inside the eye (e.g.,

Fig. 29a), which was consistent with hurricane being warm cored lows.



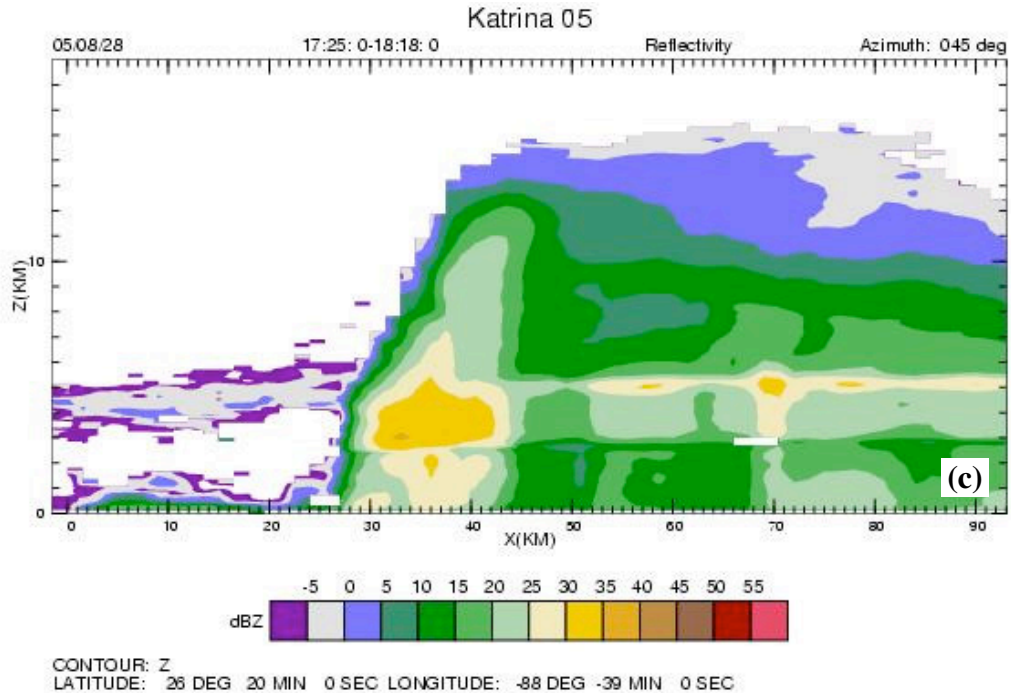


**Fig. 29.** (a) Radar reflectivity in the vertical cross section across the eyewall in at  $X = 326$  km. Shading are as in Fig. 27. Panel (a) only shows a section of the total  $Y$  domain distance from 200 km to 500 km The quasi-horizontal thin black lines represent isotherms at 0, -10 and  $-20^{\circ}\text{C}$ , which depicts part of the mixed-phase region in which most of NI charging occurs. The thick black contours are for cloud mixing ratio of  $0.1 \text{ g kg}^{-1}$  which depicts the cloud boundary. Panel (b) shows radar reflectivity from a NASA ER-2 Doppler Radar (EDOP) overflight of Hurricane Emily on the 17<sup>th</sup> of July 2005 between 8h33-8h57 Z when the hurricane was a category 4. The data were collected by the EDOP during the Tropical Cloud Systems and Processes (TCSP) field program in 2005. Panel (c) shows another cross section of radar reflectivity from P-3 aircraft reconnaissance of Hurricane Katrina (2005) near 1800 Z. Image courtesy of <http://www.aoml.noaa.gov/hrd>. The flight level was near 3 km AGL, and hence reflectivity values below that level are considerably attenuated, while above that level an offset of 8 dBZ needs to be added to the computed reflectivity values (Dr. John Gamache, personal communication, 2006).

It is well-established from satellite observations that hurricanes tend to exhibit considerable variations in their size and shape. The overall eyewall vertical reflectivity profile of intense hurricanes (i.e., category 3 or greater), however, do exhibit more consistent similarity. Therefore, a comparison of the simulation with *in situ* aircraft measurements of Hurricane Emily in 2005 (category 4 at the time of the scan) can be made. The NASA ER-2 Doppler radar (EDOP, Heymsfield et al. 1996) aircraft

observations from the Tropical Cloud Systems and Processes (TCSP, Halverson et al. 2006) field program shows some favorable similarities in the eyewall convection with the simulated TC. For instance, the 35 dBZ contour reaches up to about 10 km in the observation and to about 11-12 km in the simulation (Figs. 29a, b). However, Hurricane Emily (2005) was extreme in terms of convective and electrical activity; electric fields as large as  $9 \text{ kV m}^{-1}$  were measured above that storm. This is the highest value ever recorded above a TC (Dr. Blackslee, personal communication, 2006). To highlight the rarity of such deep high-reflectivity echo tops (i.e.,  $> 30 \text{ dBZ}$ ) in TC eyewalls, the reflectivity profile across the eyewall of Hurricane Katrina (2005) reveals that the 33 dBZ echo top hardly reached 7 km in the eyewall Fig. 29c). Another more contrasting example is Hurricane Isabel (2003), also category 5, which showed even weaker reflectivity values in its eyewall (Dr. J. Gamache, personal communication, 2006). The weaker reflectivity values which may explain why, unlike Katrina, Isabel was overall devoid of lightning activity in its eyewall during its steady state period as a category 5 storm (Molinari et al. 1999, Demetriades and Holle 2005). These observations suggest weak, if any, relationship between surface wind speed and lightning/higher reflectivity above the freezing level. This is because in TCs, the surface wind speed is mainly proportional to the tangential component of the wind vector and not to the inflow winds or radial wind component, which is the component that is related to the updraft mass flux and thereby the reflectivity/lightning in the eyewall.

For both this simulation and for Hurricane Emily (2005), the maximum height of detectable reflectivity values lies near  $z = 16 \text{ km}$  (Fig. 29a). In the simulation, however, no clear evidence of a well-defined inner band (Cecil et al. 2002a) stratiform region was

found between the outer rainbands and the eyewall. The reflectivity values there were overall small (i.e., < 30 dBZ) below the melting level compared to the reflectivity values of Hurricane Emily (Fig. 29a  $X = 420$  km and Fig. 29b at  $X = 170$  km). In the model, the aggregates and light ice crystals were all assumed to fall at velocities ranging between 1 and  $1.5 \text{ m s}^{-1}$  for a given mixing ratio. Therefore, these melted and evaporated quickly before reaching the ground in turn accounting for the weak reflectivity values below the melting level in the inner band region of the simulated TC.

In the model reflectivity calculation, it is assumed that the ice particles are dry, which explains why no bright band is visible in the simulated reflectivity profile (Fig. 29a). The bright band of Hurricane Emily (2005, Fig. 29b) tended to indicate that the melting level was located near 5 km, which was in good agreement with the temperature profile of our simulation (melting level located near 5.5 km, Fig. 29a).

Overall, our simulation tended to produce larger reflectivity values than the observed cases by about 10-15 dBZ. Such differences were also noted by Rogers et al. (2007) in their high resolution (1.67 km) numerical simulation of Hurricane Bonnie (1998) and Floyd (1999), using the MM5 numerical model. Their composite analysis of reflectivity data from 34 passes over 18 TCs and tail Doppler radar data from 233 legs across 9 TCs revealed that the eyewall reflectivity rarely exceeded 40 dBZ below the 5 km level, while their model tended to produce reflectivity values exceeding 55 dBZ there. They hypothesized that this was likely caused by differences in the way the data were processed/calculated in the model and the observations: Such difference include inadequate reflectivity-mass (Z-M) relationships in the calculation of reflectivity in the model, uncertainties in the assumption of the hydrometeor fall speeds used to compute

the vertical motion of the air, and possible differences in resolution between observational and model data. Another important source for these large reflectivities values in simulated TCs could come from the formulation of the size distribution in the microphysics.

Based on the squall line sensitivity experiment, it is possible that if the simulation was carried out at a horizontal grid spacing of 500 m or even 1 km, the resulting reflectivity profiles could have been overestimated even further by the model although the overall profile and structure are still expected to remain similar.

Just above the melting level at about 6.1 km, updrafts speed in the simulated eyewall rarely exceeded  $10 \text{ m s}^{-1}$ , while updraft magnitudes exceeding  $5 \text{ m s}^{-1}$ , however, were fairly common in the simulated eyewall within the mixed phase region (defined as the layer between the  $0^\circ\text{C}$  and  $-20^\circ\text{C}$  isotherm between about 5 and 7 km, Fig. 30a, b), which should be adequate for sufficient electrification to occur (Black and Hallett 1999, Petersen et al. 1999). Updraft magnitudes exceeding  $5 \text{ m s}^{-1}$  were also found at higher levels near 9 km in the simulation (not shown), and this further supports the likelihood of significant electrification occurring there. The same is true within some of the individual cells forming the rainbands, where isolated updrafts sometimes exceeded  $15 \text{ m s}^{-1}$ . The eastern portion of the eyewall was dominated by downdrafts and weak reflectivity values (Figs. 30a and 27). Overall, the eyewall was dominated by updrafts, consistent with Jorgensen et al. (1985) and Rogers et al. (2006a). The presence of downdrafts on the outer edges of the eyewall updrafts was also consistent with observations (Fig. 29b).

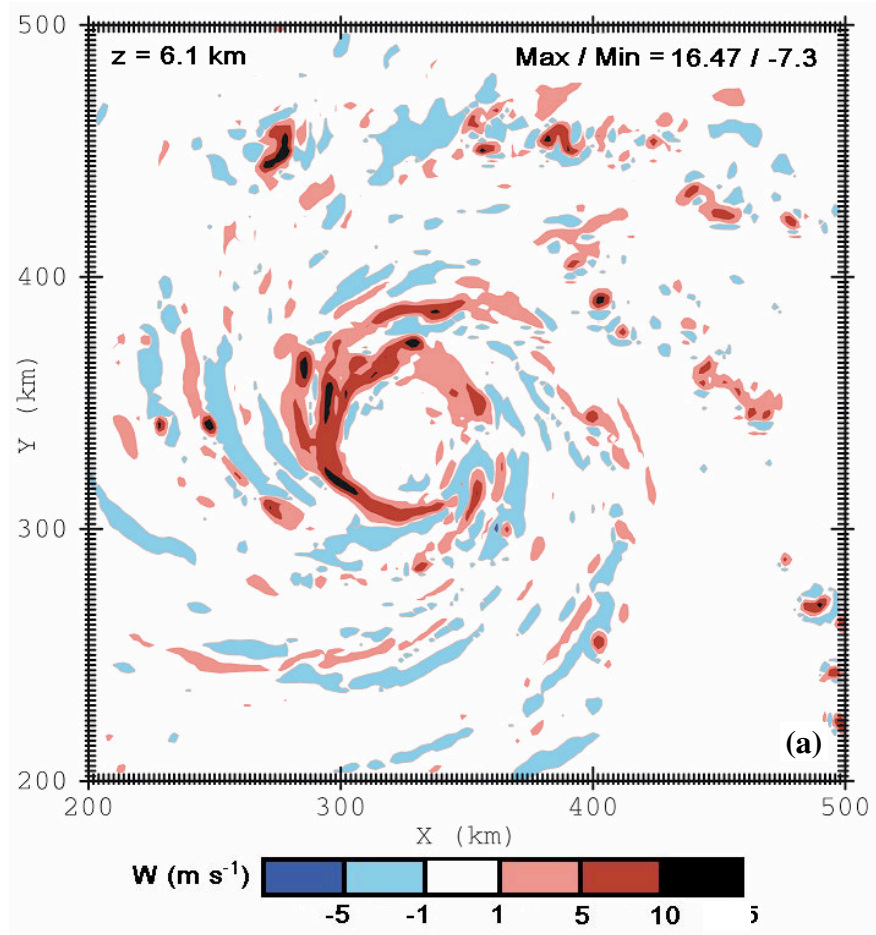
Overall, however, the updrafts speeds shown in Fig. 30b are generally greater than those observed in real hurricanes: Rogers et al. (2006a), showed that vertical

velocities obtained from vertical incidence tail doppler radar data from 233 radial legs from nine different TCs were generally weak ( $|w| < 2 \text{ m s}^{-1}$ ) with only 1-2% of these exceeding a magnitude of  $6 \text{ m s}^{-1}$  (with extreme localized events reaching  $12 \text{ m s}^{-1}$ ). These extreme events were observed in Hurricane Katrina (not shown) and Hurricane Emily (1987, Black et al. 1994). Updrafts speeds exceeding  $8 \text{ m s}^{-1}$  ( $6 \text{ m s}^{-1}$ ) were found at 4 km (12 km AGL) in Hurricane Katrina's eyewall as it reached category 5 status on 28 August 2005 near 1800 Z (Fig. 30c).

This tendency of the model to generate updraft speeds larger than observed is expected to persist and possibly to become more pronounced for horizontal grid spacings ranging between 500 m and 1 km. However, as mentioned earlier, for horizontal grid spacings  $< 100 \text{ m}$ , Bryan and Rotunno (2005) study suggests that the simulated updrafts speeds should become smaller and therefore maybe more realistic in the context of this TC simulation.

After about 15 h of simulation, the updraft speeds in the eyewall experienced a general weakening trend until the eyewall convection started to dissipate after 35 h of simulation time. This weakening of the eyewall convection will be discussed later in this section. Similar cross sections across the eye at later times (e.g., 25 h), showed more realistic, weaker vertical winds in the eyewall along with smaller (and maybe more realistic) mixing ratios of heavier hydrometeor species, such as graupel (not shown). This in turn resulted in overall weaker reflectivity values at all levels and weaker total lightning activity in the eyewall. Despite the results being quantitatively different between 21 h and 25 h, the qualitative aspects of the storm remain unchanged and thus,

any detailed analysis of the storm's dynamical, microphysical and electrical properties carried out in this time window ought to be similar.



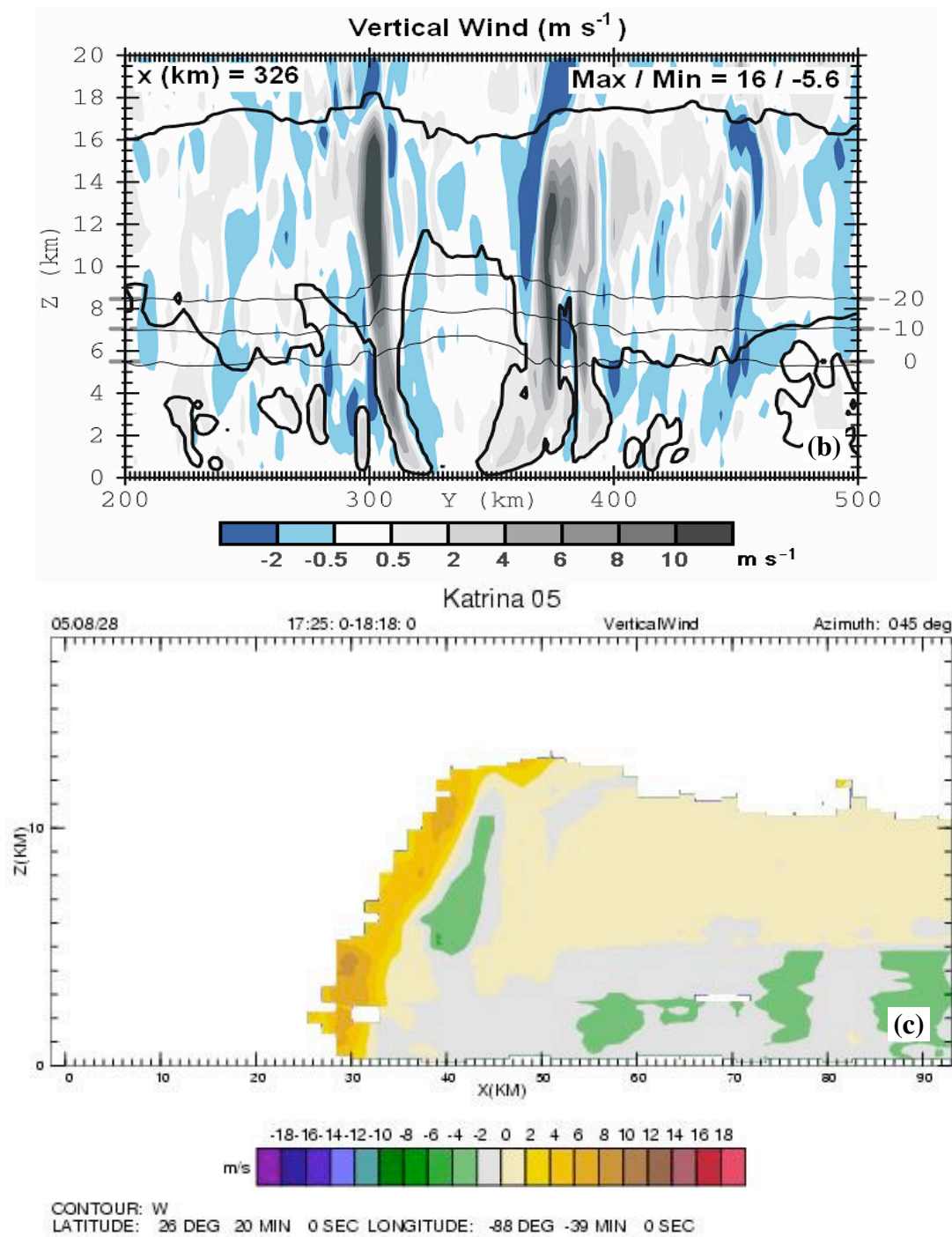


**Fig. 30.** (a) Vertical winds indicated by shading in a horizontal cross section at  $z = 6.1$  km just above the melting level, and (b) a vertical cross section through the eye at the same location as in Fig. 29a. The thick black contours and thin black lines in panel (a) have the same meaning as in Fig. 29a. Panel (c) shows P-3 aircraft vertical wind observations across one side of the eyewall of Hurricane Katrina (2005) taken on the 28<sup>th</sup> of August 2005 near 1800 Z. Image courtesy of <http://www.aoml.noaa.gov/hrd>. Legends for vertical winds magnitude are shown below each panel.

Across the storm, the environment was generally conditionally stable (with respect to vertical displacements), except in the eye at mid-to-upper levels ( $\sim 10$  km), where the environment was nearly neutral (not shown). As a result, parcels originating from outside the eyewall in the boundary layer that later rose in the eyewall must have acquired significant amount of heat near the surface (i.e., below 1 km AGL) via sensible and moisture heat flux. In a MM5 high resolution ( $dx = dy = 1.3$  km in the finer mesh) of Hurricane Bob (1991), Braun (2002) showed that the parcels in the eyewall were first accelerated upward by pressure gradient forces until the boundary layer level, where they further accelerated via convective instability. They showed that along the outward sloped path of the parcels, the environment was characterized by conditional symmetric instability, but because these parcels were displaced horizontally by the low level outflow above the boundary layer, they became unstable with respect to vertical displacements. In order to confirm the latter in the current model, a complete parcel history of a family of parcels originating from outside the eyewall in the boundary layer and later rising in the eyewall must be performed. Additional work will be designed in the future to address this question in further detail.

The two regions dominated by updrafts, namely the eyewall and the connecting rainbands (Figs. 30), were coincident with regions of strong horizontal convergence at 1 km AGL (Figs. 31). On the other hand, the eye was characterized by diverging flow. Another interesting observation was the presence of large scale gravity waves (BL rolls) near the axis of the outer rainbands (compare Fig. 31 and Fig. 27). Similar cross sections taken at different times at the same level tended to indicate that the strongest waves

preceded the formation of the TC outer rainbands. This could suggest the possible importance of low-level gravity waves in the development of TC outer rainbands.

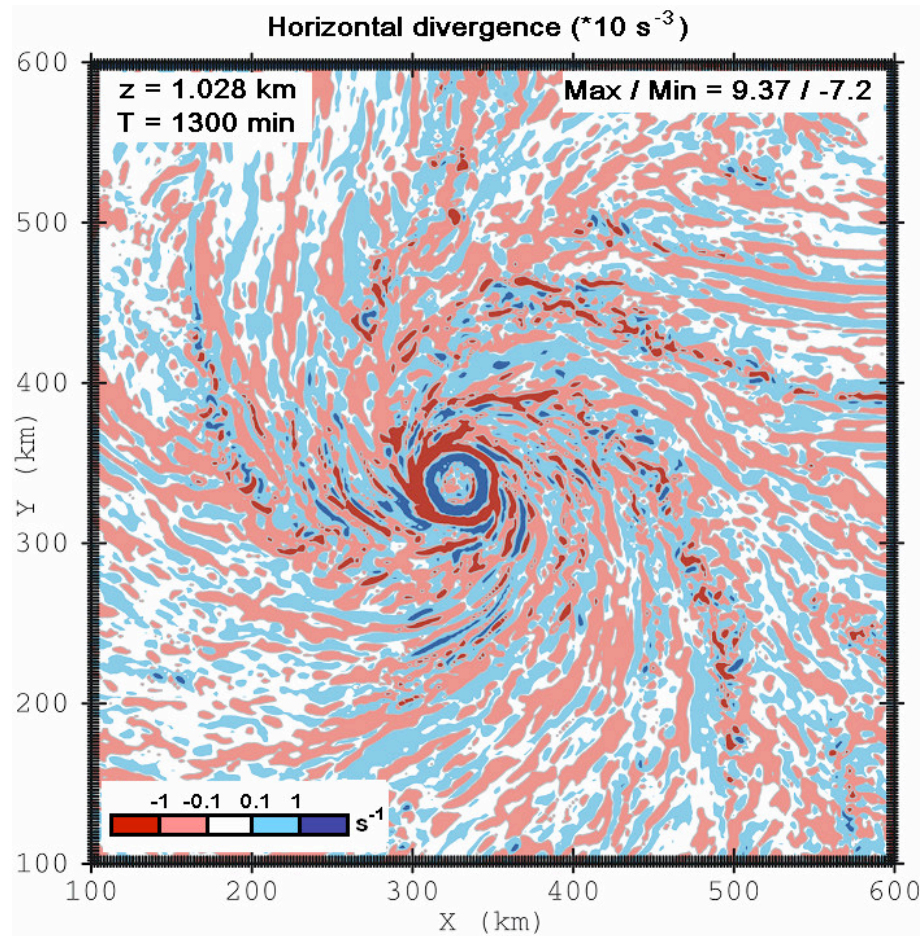


**Fig. 31.** Horizontal cross-section at  $z = 1.028$  km AGL of horizontal convergence (red) and horizontal divergence (blue) at  $t = 1300$  min.

In the next section, emphasis will be directed towards the storm's microphysical evolution and its relationship to the TC electrification and lightning activity.

Moderate total hail ( $\geq 0.2$  g  $kg^{-1}$ ) and total graupel ( $\geq 0.5$  g  $kg^{-1}$ ) mixing ratios were found primarily within the eyewall and within the individual convective cells forming the outer rainbands (Fig. 32). The lighter ice crystals and snow aggregate particles nucleating inside the eyewall were advected radially outward by the TC strong circulation to form a large anvil cloud (Fig. 32 at  $X = 390$  km). Hail particles were found

near the 0°C and -10°C isotherms (Fig. 32), while the majority of the smaller, lighter graupel pellets were located further aloft in the eyewall updraft between the -10°C and -20°C isotherm (Fig. 32). The majority (> 90%) of the graupel present there consisted of moderate and high density graupel, while low density graupel particles were rare and were found mainly at higher altitude near 12 km (not shown). As expected, these hydrometeors were located near moderate to strong updrafts (Figs. 29b, 32) which were also associated with larger cloud water content (CWC) due to enhanced condensational heating.

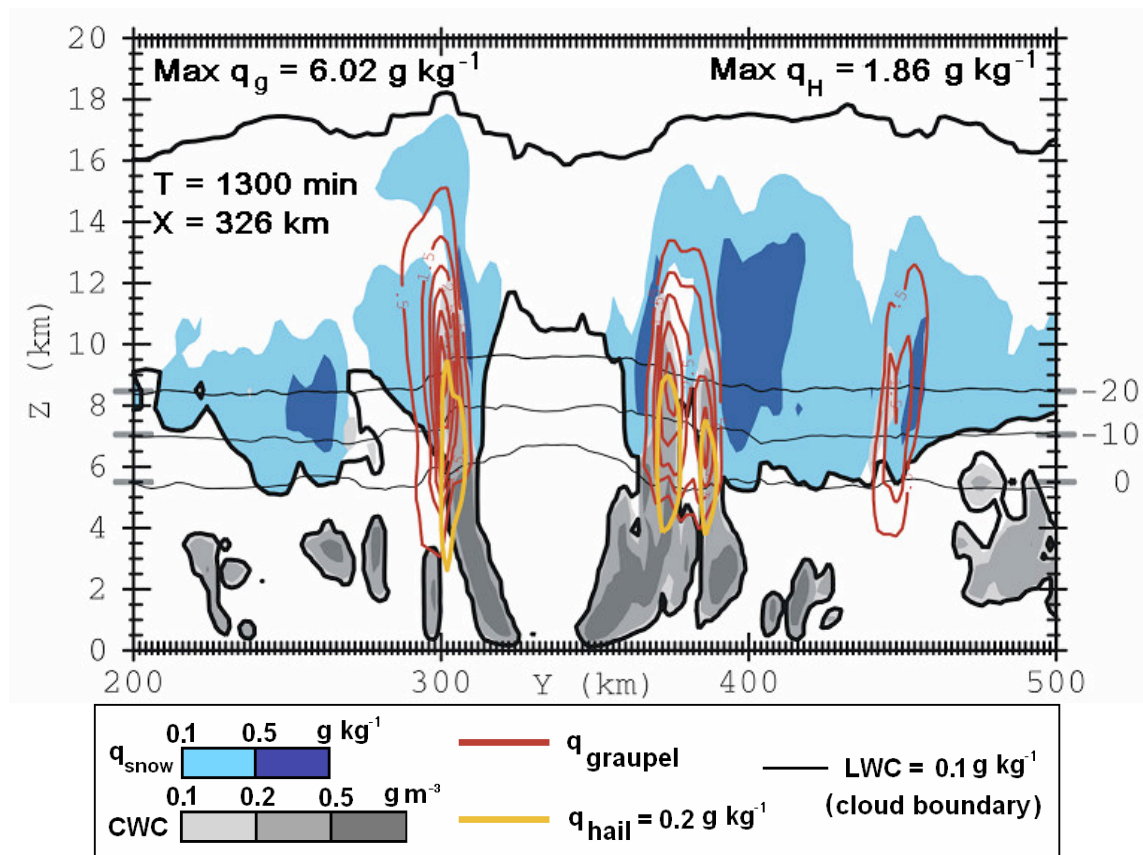


**Fig. 32.** Vertical cross sections in the Y direction at X = 326 km and t = 1300 min for snow mixing ratio, total hail mixing ratio, total graupel mixing ratio and cloud water content (CWC in  $\text{g m}^{-3}$ ). Total mixing ratios are the sum of the mixing ratios of all the graupel (low, medium, and heavy density) and hail (small, large) categories. The thick black line depicts the cloud boundary ( $0.1 \text{ g kg}^{-1}$  cloud mixing ratio). The scale of shading for CWC is shown in the legend below the figure. Red (orange) contours show

regions of the storm where the total graupel (hail) mixing ratio exceeds  $0.5 \text{ g kg}^{-1}$  in increments of  $1 \text{ g kg}^{-1}$  ( $0.2 \text{ g kg}^{-1}$ ). Light (dark) blue-filled shading shows snow mixing ratios greater than  $0.1 \text{ g kg}^{-1}$  ( $0.5 \text{ g kg}^{-1}$ ).

The simulated graupel and hail mixing ratios are larger than the ones generally observed by radiosondes in mature hurricanes during aircraft penetration (Dr. R. Black, personal communication, 2005). The squall line sensitivity experiment, however, suggest that these values could become smaller at grid spacings ranging between 500 m and 1 km. The latter, nonetheless, remains to be tested. In particular, if larger updraft speeds are reproduced at these resolutions (as in the squall line case), these could result in enhanced production of graupel particles.

Because the eyewall and the strongest cells forming the rainbands contained the largest mixing ratios of graupel ( $\geq 0.5 \text{ g kg}^{-1}$ ) and the larger CWC ( $\geq 0.2 \text{ g m}^{-3}$ ) and updrafts, these regions were more conducive for collision NI charging processes to operate between graupel/hail and the lighter ice crystals. Consequently, these regions also produced the largest flash rates in the TC (compare Figs. 32 and 33). At the time shown in Fig. 32, the IC flash rate of the entire storm system was about 300 per minute (not shown). However, based on Figs. 33 and 34 alone, it was not possible to distinguish which fraction of this total lightning activity occurred within the eyewall and within the outer rainbands of the storm. A simple analysis of horizontal and vertical cross sections at  $t = 21 \text{ h } 40 \text{ min}$  (i.e., Figs. 27 and 12) or a few hours prior and after that time (i.e., between  $t = 19 \text{ h}$  and  $t = 25 \text{ h}$ , not shown), however, indicated that in general, the majority of the total lightning flashes (IC + CG) in the mature phase of the hurricane-like vortex was found in the eyewall. The majority ( $> 75 \%$ ) of these lightning flashes in the eyewall were found to initiate in two distinct layers, approximately between 6 km and 8

km and between 9 km and 11 km (Fig. 33). These layers coincided with the interfaces between regions of net positive charge and negative charge (Figs. 33 and 34), where the electric field magnitude was largest.

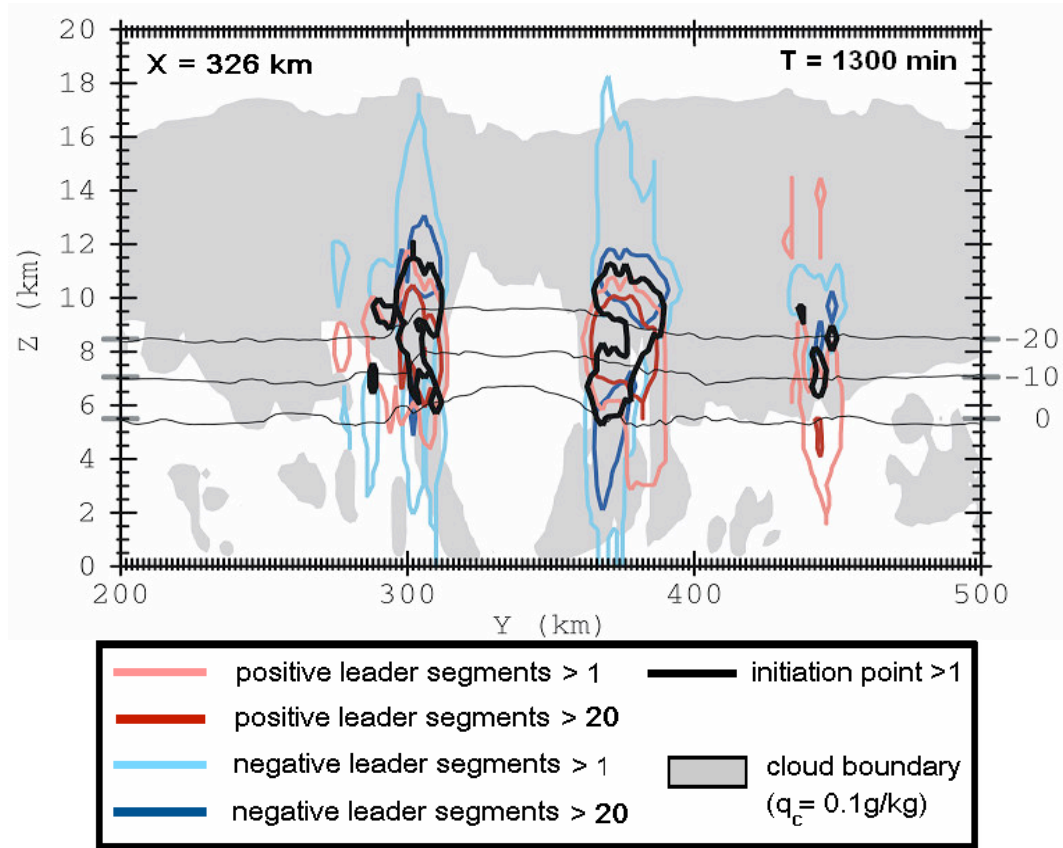


**Fig. 33.** As in Fig. 32 but for cloud mixing ratio  $> 0.1 \text{ g kg}^{-1}$  (grey shaded area) and positive (negative) leader segments in red (blue) contours. Light (dark) blue contours show regions having more than 1 (20) negative leader segments. The same convention holds for red contours and positive leader segments. Thick black contours show locations having more than one flash initiation. Total flashes are plotted for a period of 30 minutes prior to the cross section time.

Several vertical cross sections taken in slightly different locations / orientation across the eyewall revealed small to moderate differences in charge structure and magnitudes. The overall charge structure in the eyewall was complex, with the charge polarity switching several times as one ascends vertically. However, if one considers only the charge regions involved in lightning, i.e., regions with charge density  $> 0.4 \text{ nC m}^{-3}$ ,

the SP98 scheme resulted in a gross normal tripole charge structure, which is composed of a normal dipole (positive charge above negative charge) with a lower positive charge (Fig. 34). Simple normal dipole charge structures also occur in some of the storm cells forming the rainbands (see Fig. 34 at  $X = 450$  km). The squall line experiment showed that despite some slight differences in net charge magnitudes, the overall charge structure was preserved as  $dx$  was varied from 300 m to 2 km. Therefore the charge structures obtained herein are likely to be similar at a horizontal resolution of 500 m.

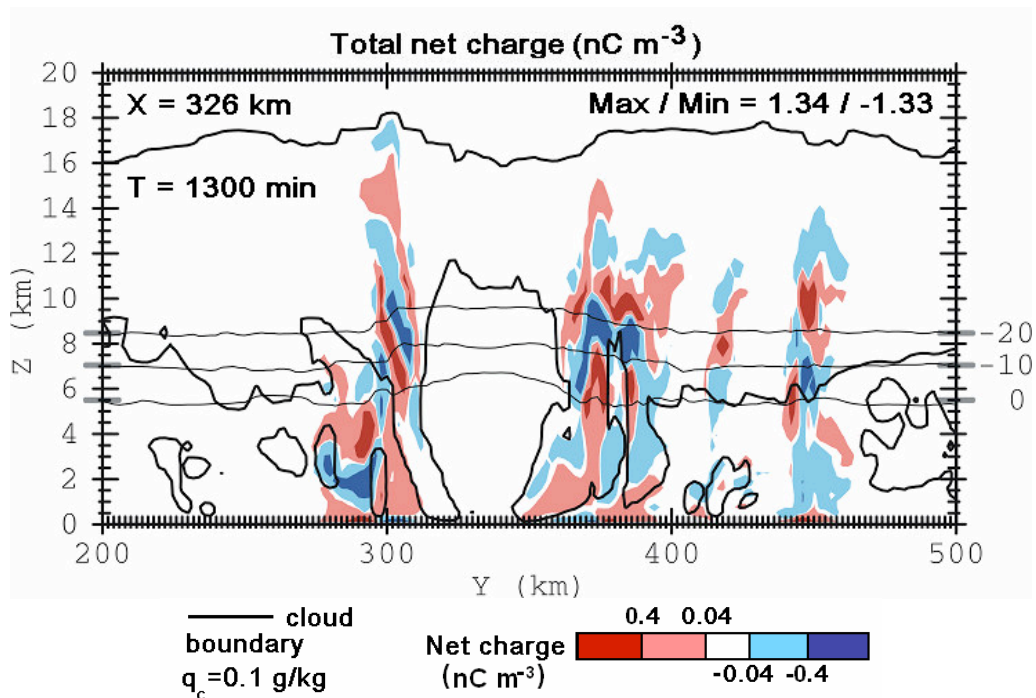


**Fig. 34.** As in Fig. 32 but for the net total amount of net charge in  $\text{nC m}^{-3}$ . Light (dark) red filled contours show region where net charge exceeds  $4 \times 10^{-2}$  ( $0.4 \text{ nC m}^{-3}$ ). Likewise light (dark) blue filled contours shows where negative net charge magnitudes exceed  $4 \times 10^{-2}$  ( $0.4 \text{ nC m}^{-3}$ ).

Almost all of the CG flashes produced in the eyewall of the storm were  $-CG$  flashes (i.e., they lowered negative charges to the ocean surface). The majority of the  $-CG$  flashes were found radially outside the eyewall on the northwestern side (Fig. 27).

Note that the rainbands were essentially devoid of CG flashes, with the exception of one lone +CG flash. In Fig. 27, the –CG flashes in the eyewall near the vertical cross section shown in Fig. 34, were coincident with a region of larger positive charge density below 6 km. The lone +CG flash in the outer band, however, was coincident with a region of larger negative charge density below 6 km.

From the squall line experiment, we suspect that although the number of simulated lightning flashes is likely to be smaller at smaller grid spacings (i.e., between 500 m and 1 km), we don't expect the overall CG /IC flash pattern and polarity to differ from to one observed herein. The same holds for the simulated NI and inductive charging rate profiles.

Of interest here is how (qualitatively) the NI and inductive charging processes account for the charge structure within the TC inner core region, rainbands and outer core region (dominated by weak updraft and anvil clouds). Also, emphasis will also be given in how these charge structures within, and below cloudbase are related to CG and IC flash initiation, respectively.

In order to investigate the origins of the charge regions in the storm in more detail, a single cross section at a particular time was selected for the analysis. (Similar cross sections across the eyewall were made a few grid points away and revealed little qualitative difference in the charge and charging structure of the storm at that time). The lower positive charge region (below 7 km) closer to the center of the eyewall (near  $Y = 300$  and  $Y = 375$  km, Fig. 34) was mainly attributed to positive charging of graupel by both NI and inductive mechanisms (Figs. 35a, b). The main negative charge region

located at mid-levels near 8-9 km and the upper positive charge region (near 10 km) were mainly a consequence of NI charging (Figs. 34, 35a, b).

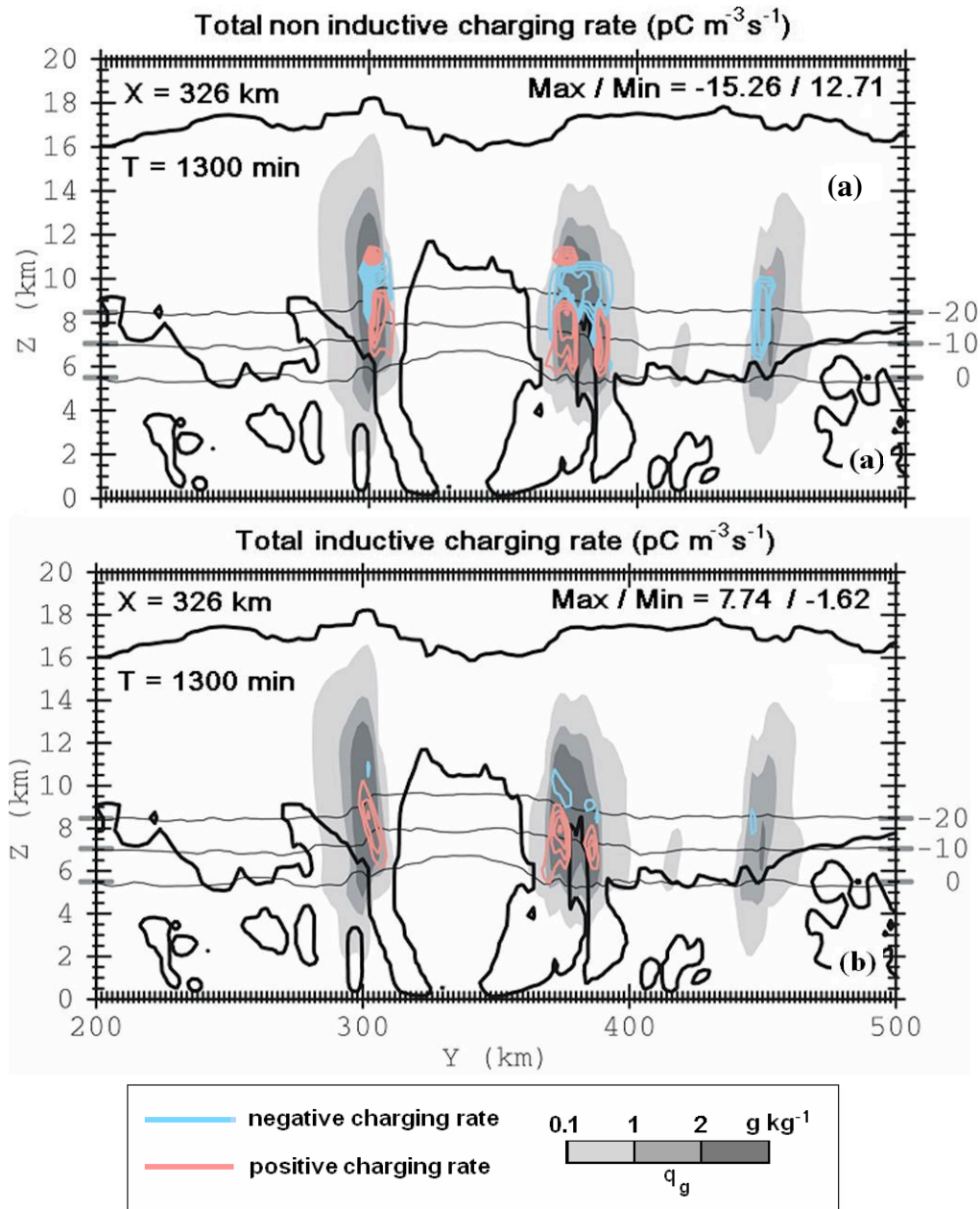


**Fig. 35.** As in Fig. 32 but for (a) total non-inductive and (b) total inductive charging rate in  $\text{pC m}^{-3} \text{s}^{-1}$ . Positive (negative) contours are shown by the red (blue) contours in increments of  $2 \text{ pC m}^{-3} \text{s}^{-1}$  starting at  $1 \text{ pC m}^{-3} \text{s}^{-1}$ . Light to darker grey filled contours shows total graupel mixing ratio (see legend).

Between the outer rainbands and the eyewall updrafts, almost no charging was occurring (e.g., Fig. 35,  $Y = 390$  km), because this region of the TC had negligible amounts of CWC and graupel (Fig. 32). This lack of CWC and graupel between the outer rainbands and the eyewall updrafts was consistent with overall weak updraft speeds ( $< 1$  m s<sup>-1</sup> in Fig. 30b). Moreover, this stratiform cloud was essentially glaciated as it was composed almost exclusively of snow aggregates (Fig. 32). As a result, most of the charges that are observed in these regions of the storm were likely produced initially in the eyewall convection and then advected radially outward by the storm's strong circulation. As they were advected they fell to lower levels while keeping the polarity of charge gained in the eyewall (see downward slope of the main negative charge region and the upper positive charge region with radial distance away from the eyewall in Fig. 34 between  $Y = 360$  km and  $Y = 390$  km). In Fig. 34, the three charge layers forming the normal tripole in the eyewall ended at roughly the same radius from the eyewall, but in some vertical cross sections at earlier times (not shown), the two upper charges regions forming this tripole extended farther into the inner band stratiform region than the lower did. In this situation, the resulting charge distribution could be described as a normal dipole. The reason for this charge configuration in the inner band region was probably that heavier charged precipitation particles fell out of the lower regions and the remaining mix of hydrometeor types lacked the necessary ingredients for both inductive and NI charging (i.e., there were no or too little amount of graupel and ice crystals).

The analysis of both the tropical squall line and the hurricane simulations revealed that the electrical and microphysical properties of the eyewall of TCs bore some remarkable resemblance with that of the mature zone of squall lines. The same was true

between the inner band region of the TC and the trailing stratiform region of the squall line. This was causal because, some regions of the simulated TCs showed similar kinematical and microphysical behaviors than particular regions of the simulated squall lines. For instance, both the eyewall and transition zone of squall lines were characterized by strong updrafts associated with moderate-to-large total graupel mixing ratio and CWC, where most of the charging occurred. On the other hand, the inner band region of the TC and rearward stratiform region of the squall line were both characterized by very weak updrafts and were mainly composed of snow aggregates, which resulted in weak to almost inexistent charging there. Consistent with this, we also found that the charges present in both of these stratiform regions were advected from the convectively active regions of the storm, namely, the eyewall or the mature zone.

Additional analysis of the charge structure and lightning location at earlier times (not shown) revealed that the maximum in lightning activity in the eyewall was not always near the region of maximum charging (not shown). At first, this result may appear counterintuitive. However, while charges must be generated in a region of the eyewall that is more conducive for the NI charging process (because it has a larger CWC and larger total graupel mixing ratio), the advection of these charges by the storm strong circulation can cause the onset of lightning to occur further downwind (similar to the hypotheses of Corbosiero, 1999). In other words, the advection (and sedimentation) of charges was likely one important factor in determining the lightning distribution in the simulated eyewall.

### V.3.3. Conclusions

Using a numerical model featuring a complex 12-class microphysics scheme and a three dimensional lightning module, a high-resolution simulation of a hurricane-like vortex was carried out with success. At about 22 h of simulation, the model reproduced many of the features observed in TCs in nature. One feature was a well-defined eye and eyewall with several connecting rainbands. Also, the vertical reflectivity and wind profile showed an outward tilt with height that was consistent with a strong mid-level warming aloft caused by adiabatic compression of subsiding air in the eye. This in turn was partly responsible for the rapid pressure drop at the storm's center via hydrostatic balance. Relatively higher  $\theta_e$  values were found in the sloping eyewall and in the lowest kilometer inside the eye, which generally agreed with observations.

The largest updraft speeds and resulting total graupel mixing ratios, CWC, and lightning flash rates were found in the eyewall, and within some isolated stronger convective cells forming the outer rainbands. The updraft speeds at that time were somewhat stronger and deeper than typically observed within mature TCs, which led to more graupel and hail than is observed, mainly in the eyewall. This tendency for larger updraft speeds is expected to be more pronounced at grid spacings ranging between 500 m and 1 km.

The outer eyewall stratiform region was mainly composed of lighter ice crystals and snow aggregates that were ejected from the eyewall convection, a pattern which was consistent with observations and also with a dearth of lightning activity there.

The gross charge structure in the eyewall resembled a normal tripole, while in

some of the strongest cells in the rainbands and in some portion of the outer eyewall stratiform region a normal dipole was observed instead. As for the squall line simulations, the mid-level negative and upper positive charge layers were mainly a consequence of NI charging while the lowest positive charge region was attributed to both induction and NI charging. This charge configuration across the storm was consistent with almost all ground flashes lowering negative charge to the surface, as in most continental storms.

It is important to mention that, in this highly idealized simulation, the model did not reproduce the changes in intensification that occur in nature in mature TCs which are occasionally accompanied by lightning bursts in the eyewall. In contrast, the simulated storm (i.e., after its mature stage at  $t = 19\text{h}$ ) experienced a steady deepening trend throughout the whole simulation while exhibiting a rather steady production of CGs and IC flashes in the eyewall. Therefore, one main question relating the TC change in intensity and lightning burst in the eyewall still remains to be answered. Nonetheless, good insight on how lightning would occur in the eyewall during these lightning bursts has been gained.

## **V. 4. LAND experiment**

### **V.4.1. Introduction**

The OCEAN experiment demonstrated that the model was also able to reproduce a hurricane-like vortex that exhibited many features observed in real hurricanes at about 20

h of simulation. This allowed a first detailed analysis of electrification processes and lightning activity within such storms. This experiment being successful to some degree (details in section V.5), we wished as a next step, to explore how the TC microphysical and electrical properties would change when the latter interacts and weakens over a flat, dry landmass. We assumed that over land, sensible and moisture fluxes were turned off, while the momentum fluxes were enhanced. We decided to make these two changes simultaneously over land, because these are believed to be the most simplistic and most important differences between oceanic and continental surface having a direct effect on TC intensity at landfall.

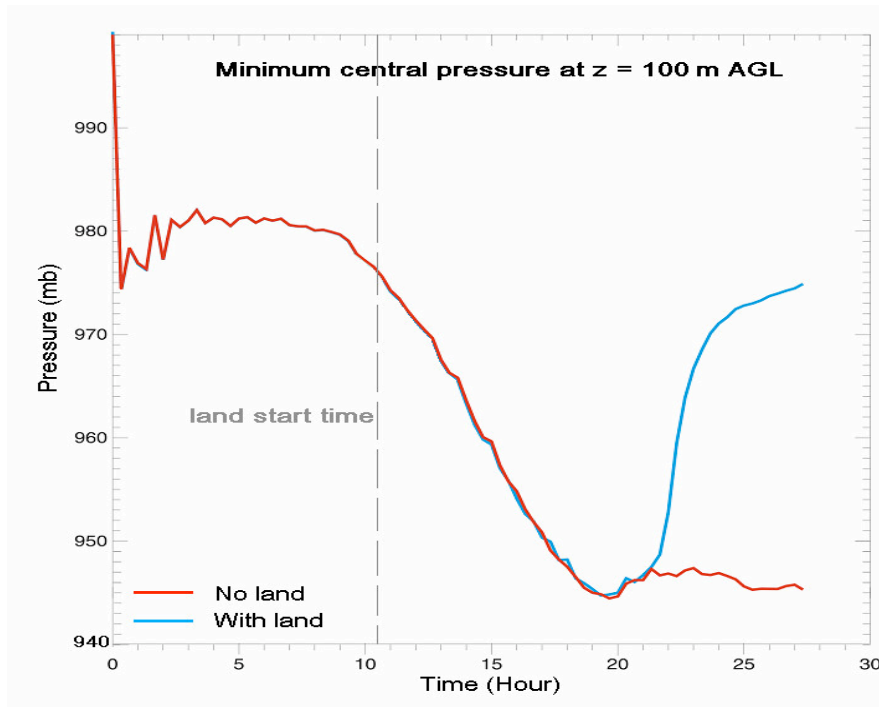
In order to determine quantitatively the individual effects of zero sensible / heat fluxes versus increased momentum fluxes (or drag coefficient) on the weakening of the simulated TC, an additional simulation was carried out where the momentum fluxes were left unchanged over land (i.e., same as over water). The results are consistent with Chan and Liang (2003) and showed that setting zero sensible / heat flux did have a negligible impact on the storm weakening about 6 h after landfall (occurring at about 70000 s and defined as half or more of the eye being over land) compared to that of increased momentum flux (or enhanced surface drag). Indeed, at about 90000 s of simulation, the minimum pressure at 100 m AGL for the simulation having both momentum and sensible heat fluxes altered over land is about 974 mb compared to about 954 mb for the run having only sensible /heat fluxes set to zero over land. When the storm evolves over water (i.e., does not make landfall), the minimum surface pressure at 100 m at 90000 s is about 945.5 mb. Therefore, increasing the surface drag over land accounts for about 70 %

of the pressure rise of the storm at 90000 s (with values within 5% one hour before and after 86400 s).

#### **V.4.2 Results**

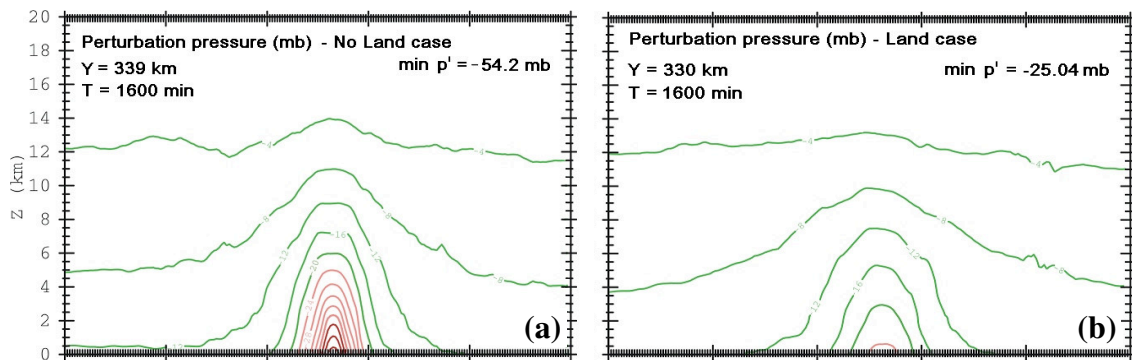
As in the OCEAN experiment, the minimum central pressure at 100 m AGL started to drop progressively after 8 h of simulation and reached a minimum of about 945 mb at about 19.5 h (Fig. 36). As the landmass started to interact with the TC eyewall near 19.5 h, the 100 m minimum central pressure experienced a sharp and fast increase, which was coincident with a rapid decay and weakening of the storm. The difference in minimum surface pressure between the landfalling case and the control run reached about 30 mb at about 26 h of simulation (Fig. 36). As shown earlier, about 30 % of this rapid pressure rise was associated with the suppression over land of the sensible and latent heat fluxes from the underlying warm ocean surface, while the remaining 70 % was associated with increased surface drag (or enhanced momentum fluxes).

This weakening of the storm was associated with overall weaker updrafts in the eyewall and hence, smaller total updraft mass flux there (described later in the section). The smaller updraft mass flux in the eyewall was consistent with a weaker inward mass flux at low-to-mid levels, which lead to smaller positive temperature anomalies at mid-to-upper levels in the eye (not shown).



**Fig. 36.** As in Fig. 24. The blue (red) line represents the land (no-land) case.

As in the OCEAN experiment, the isobars at 100 m AGL exhibited a well defined concentric pattern around the storm center (Figs. 37c, 37d). Once the storm was over land, the main difference in the pressure field was observed near the center and below 8 km (Figs. 37a, b).



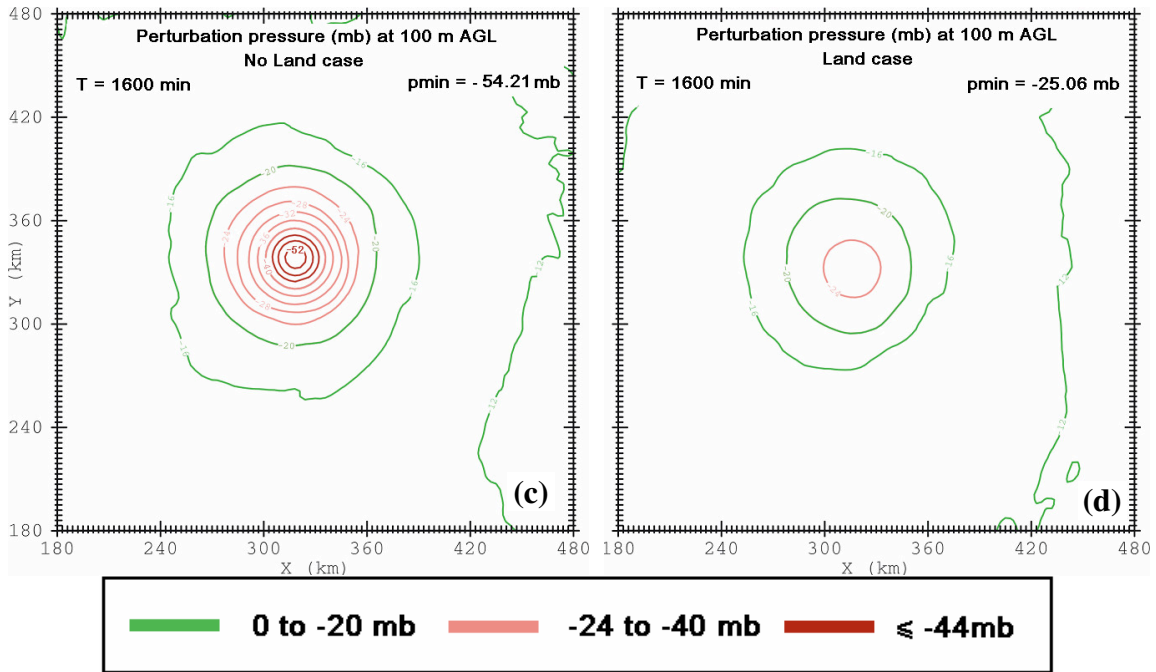


**Fig. 37.** Vertical cross section (in X-Z direction) at  $t = 1600$  min of perturbation pressure (in mb) for (a) the no-land and (b) land case. Panels (c) and (d) show the same field as in panels (a) and (b), except in the X-Y direction. Green contours range from 0 to -20 mb by increments of 4 mb. Likewise, light (dark) red contours range from -24 to -40 (-44 to -52 mb) by increments of 4 mb.

This weakening of the TC after landfall was also evident for instance in the tangential winds profile (compare Figs. 38a and 38b), with maximum exceeding  $50 \text{ m s}^{-1}$  in the control run (i.e., no land case), while barely reaching  $40 \text{ m s}^{-1}$  in the land case at the same time. Consistent with the vertical pressure profiles shown earlier, the greatest difference in wind speed was also observed near the surface below 2 km in the boundary layer, (compare Figs. 38b and 38c). This difference exceeded  $10 \text{ m s}^{-1}$ . Note also that the depth of the wind speed contours exhibited notable differences: for instance, in the control run, the  $30 \text{ m s}^{-1}$  contour spanned almost the whole depth of the eyewall sometimes exceeding the 10 km level. On the other hand, for the landfalling storm, the  $30 \text{ m s}^{-1}$  contour barely reached 6 km AGL and spanned a much smaller volume of the

eyewall. The vertical tangential wind profile in both cases exhibited an outward tilt with height (Figs. 38a, b).

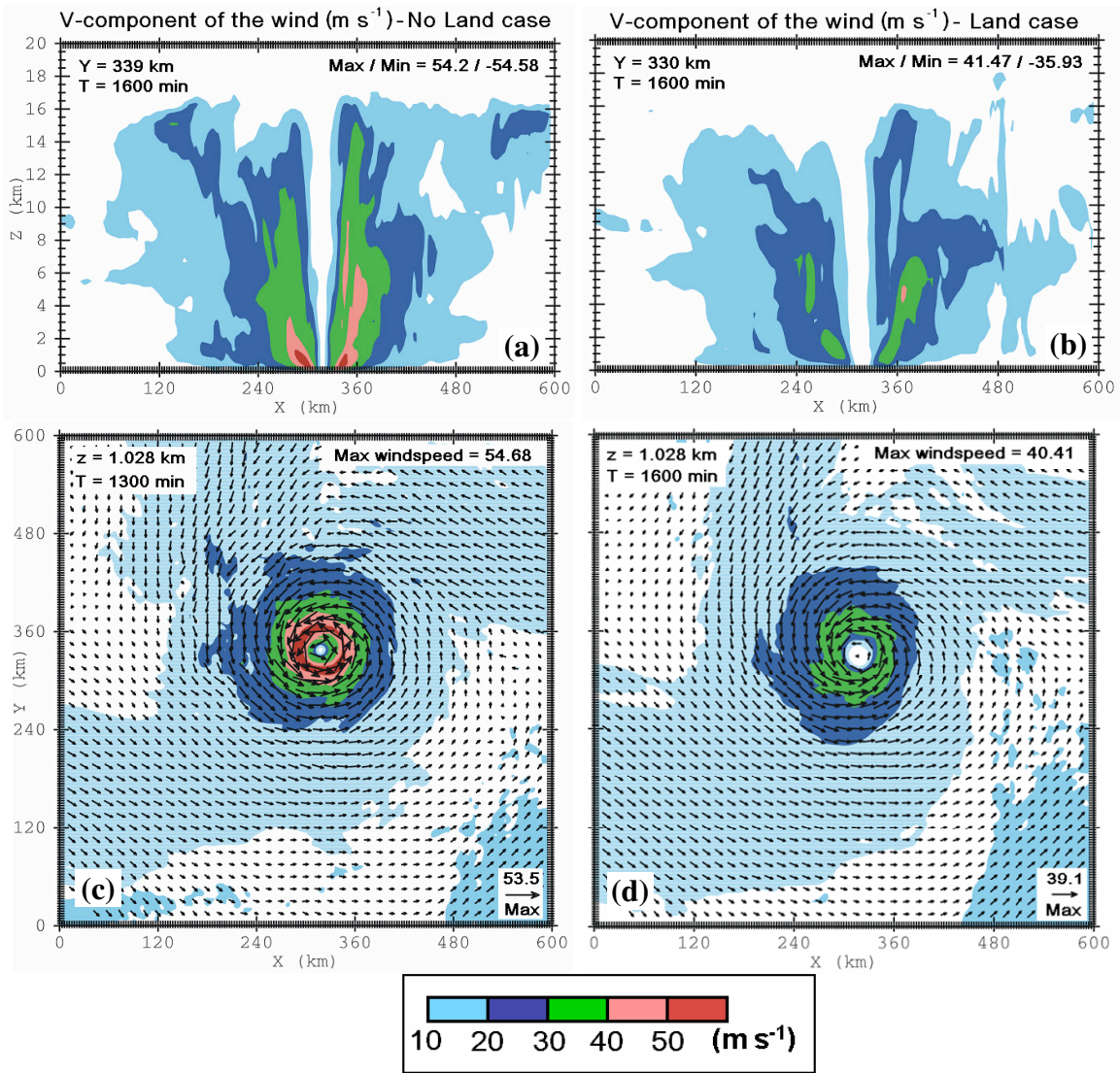
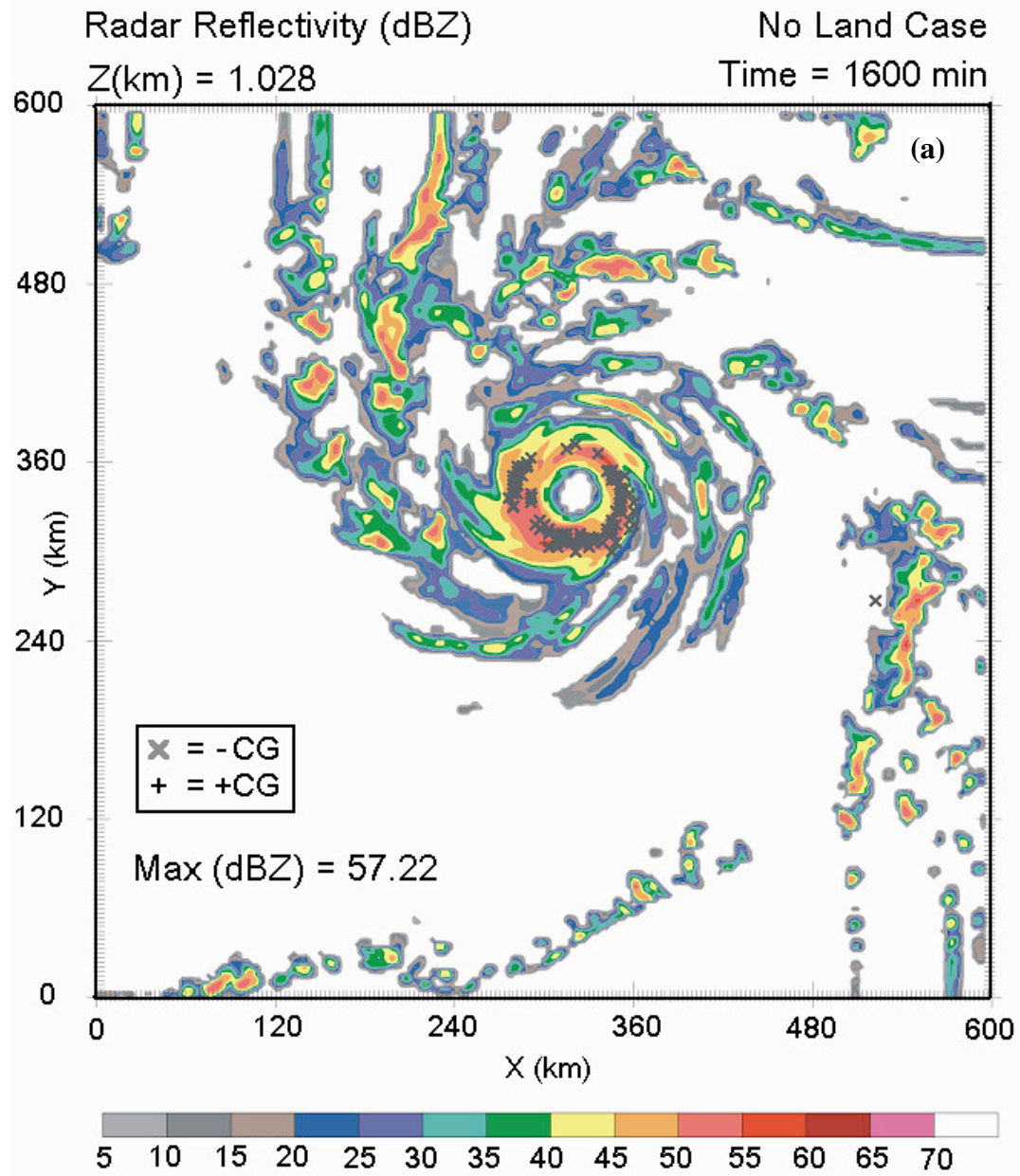


**Fig. 38.** Vertical cross sections at  $Y = 339$  km of the V-component of the wind (in  $m s^{-1}$ ) for (a) the no-land case and (b) the land case. Panels (c) and (d) are as in panels (a) and (b), except in the  $X$ - $Y$  plane at  $z = 1.028$  km AGL. Shading legend for the wind speed scale is shown below.

The horizontal and vertical reflectivity profile of the simulated TC after landfall showed many features consistent with *in situ* observations; namely, weaker reflectivity in and around the eyewall, the absence of a closed circular eyewall and eye near the storm's

center (Figs. 39b and 40b) and a generally asymmetric structure (e.g., Chan et al. 2003; Kimball, 2004). The convection within in the rainbands became more sporadic over land.

As expected from these differences in the storm structure after landfall, the distribution of CG lightning flashes in the eyewall was also different. During the time period of Fig. 33, the TC of the control run produced exclusively –CG flashes, which were distributed in a relatively even manner around the eyewall. The landfalling storm, however, mainly produced CG flashes in the southern portion of its ill-defined eyewall (Figs. 40a, b). Most importantly, the landfalling case also produced a non negligible amount of +CG flashes there, the origin of which will be explained latter in this section.



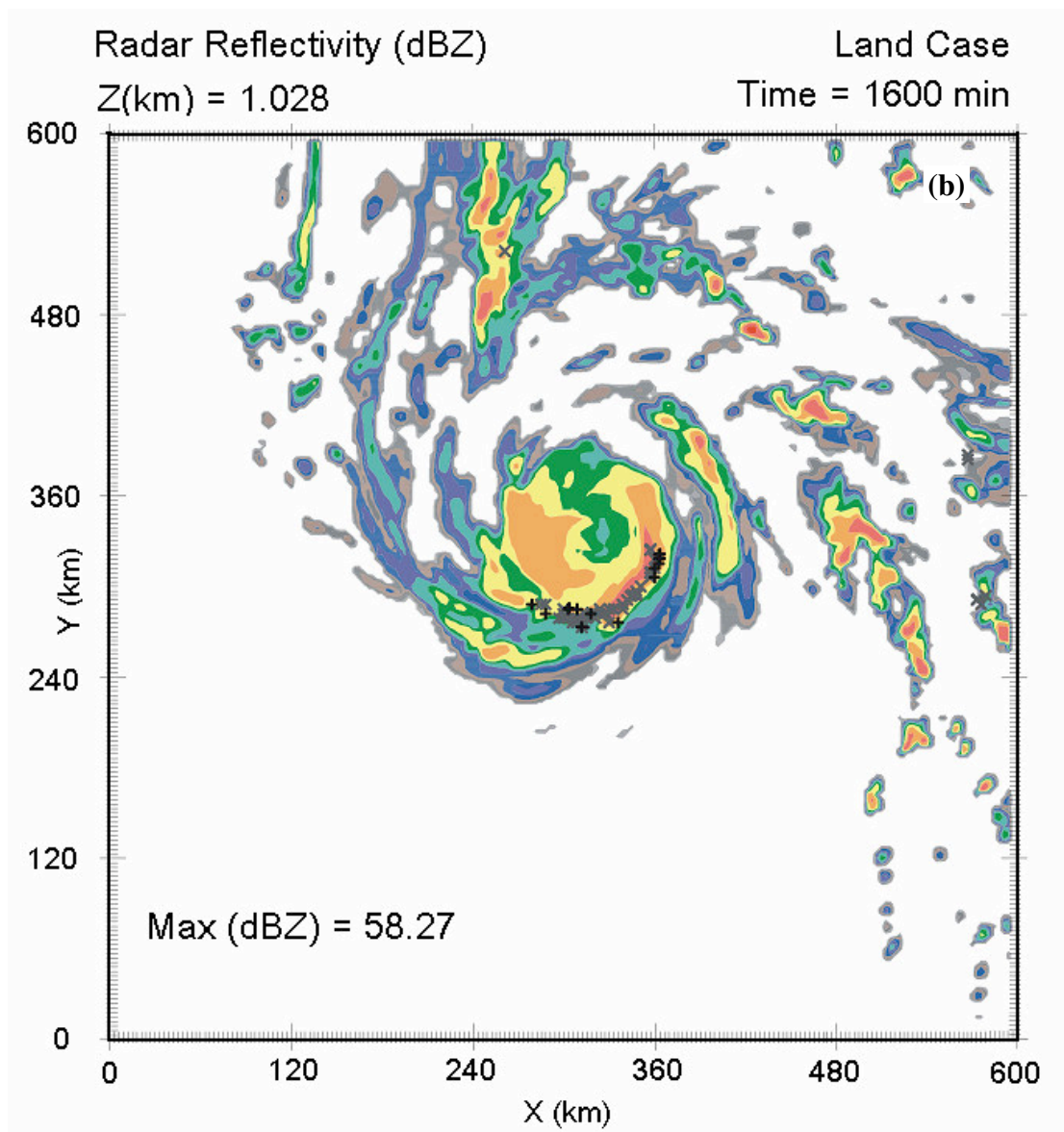


**Fig. 39.** As in Fig. 27 at  $t = 1600$  min for (a) the no-land case and (b) the land case. The flash locations were plotted for a 1 h 40 min time interval from the figure's cross section time.

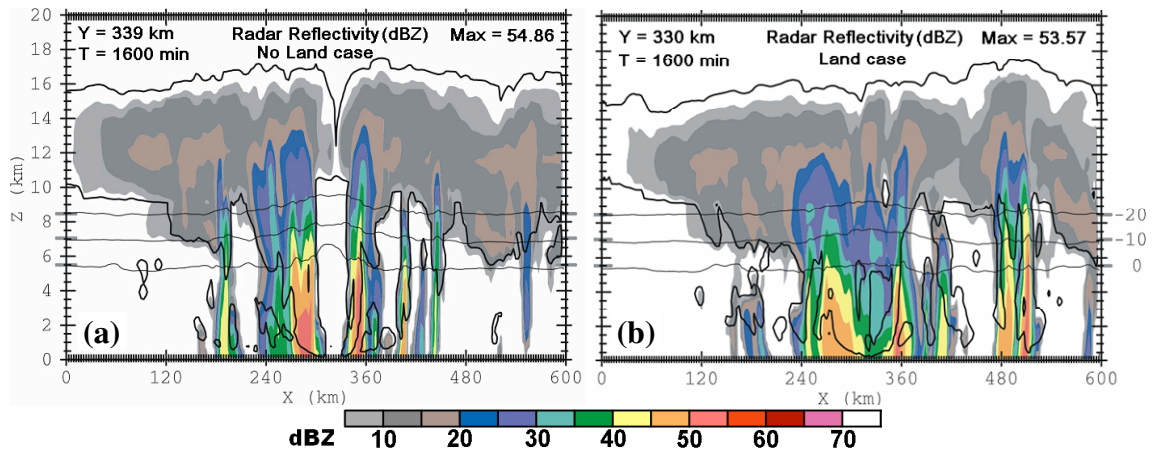


**Fig. 40.** As in Fig. 29a at  $t = 1600$  min for (a) the no-land case and (b) land case.

After landfall, the entire eye became filled with hydrometeor particles (Fig. 40b and 41b, Jordan 1961; Kimball 2004). This was a direct consequence of weaker updraft mass flux and resulting overall weaker convection in the eyewall (Fig. 41). The weaker convection in the eyewall accounted for the overall smaller cloud top heights and shallower reflectivity contours in the eyewall, while, however, deeper convection was found in the outer rainband adjacent cells (Fig. 40b). The 40-45 dBZ contour barely reached the melting level in the landfalling case while attaining 8 km in the control run (Figs. 40a, b).

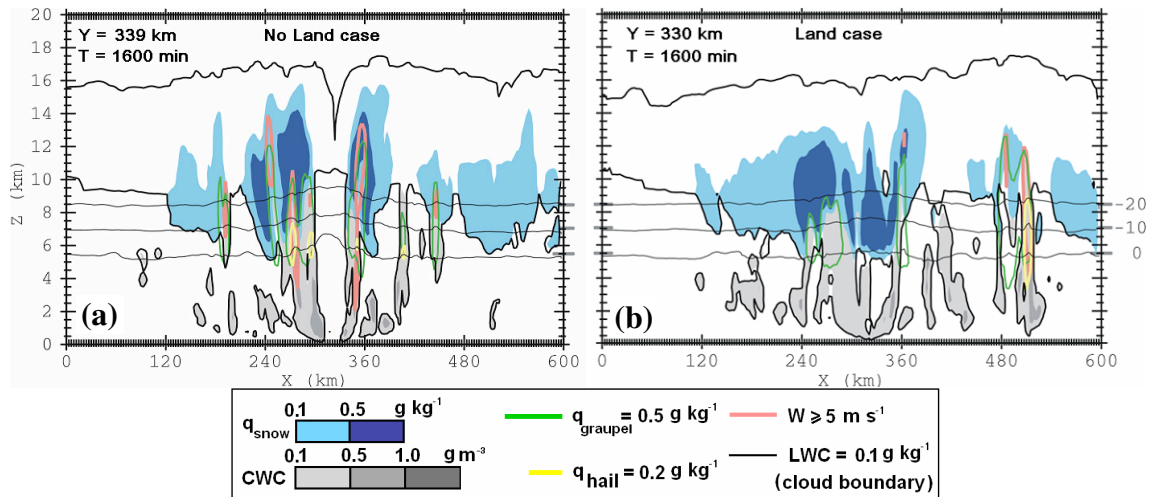


**Fig. 41.** As in Figs. 38a and 38b but for CWC ( $\text{g m}^{-3}$ ), snow mixing ratio, total hail mixing ratio and total graupel mixing ratio. CWC is shown in grey shading with corresponding scale shown by the legend below the panel. Green (yellow) contours depict regions of the storm where the total graupel (hail) mixing ratio exceeds  $0.5 \text{ g kg}^{-1}$  ( $0.2 \text{ g kg}^{-1}$ ). Light (dark) blue-filled area shows snow mixing ratios greater than  $0.1 \text{ g kg}^{-1}$  ( $0.5 \text{ g kg}^{-1}$ ).

After landfall, the updrafts in the eyewall above the melting levels at 6.1 km AGL in the southern strongest portion of the eyewall rarely reached  $5 \text{ m s}^{-1}$  (not shown). Moreover, such updraft speeds were almost inexistent on the eastern and western flanks of the storm after landfall (Fig. 41b). Because of overall weaker updrafts in the eyewall in the land case, smaller amount of graupel and hail were found in the mixed phase region of the eyewall compared to the control run (Fig. 41). The presence of more graupel in the control run was in turn consistent with more charge and more lightning production in the eyewall (Figs. 42 and 43).

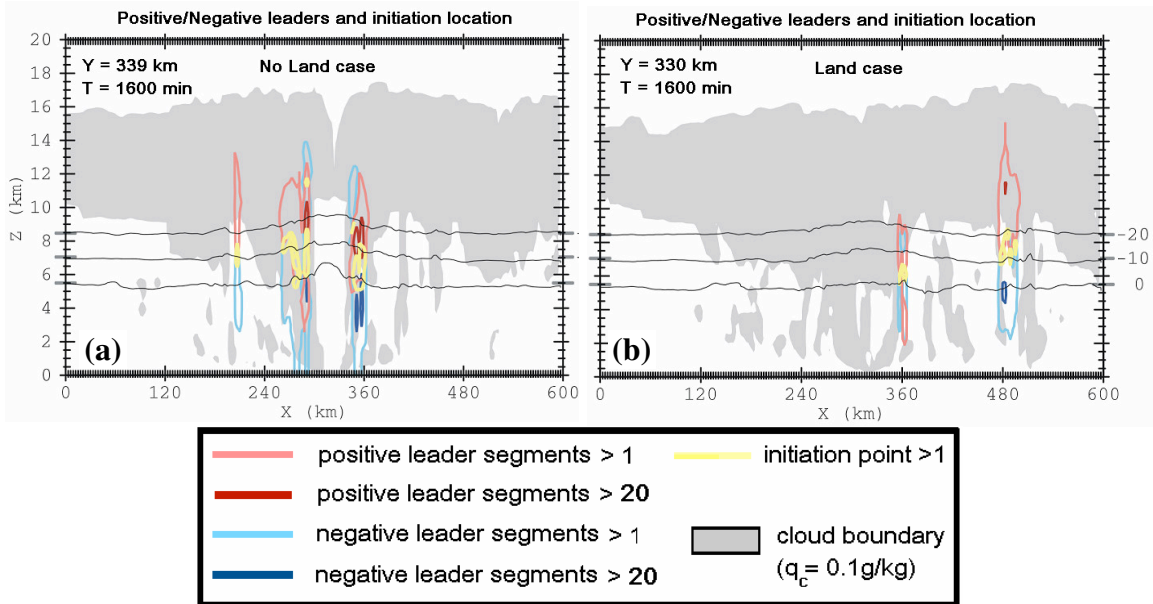


**Fig. 42.** As in Figs. 38a and 38b but for the cloud mixing ratio ( $\text{g kg}^{-1}$  grey shaded area) and positive (negative) leader segments in red (blue) contours. The leader contours starts at 1 by increments of 10. Yellow contours show flash initiation locations greater than 1. The leader contours represent the total amount of for a time period of 1 h 40 min until the cross section time. This explains why a few leader contours are found outside the cloudy region.

Before carrying out an analysis of the charge structure, it was relevant to remind the reader that for this simulation the magnitude of charge separated non-inductively by individual graupel-ice collision was reduced by a factor of about 1000 (the NI charging multiplier coefficient was set to 0.0009). This procedure principally reduced the amount of charges at upper levels of the storm (above 9 km) and hence the amount of IC flashes generated there. Previous simulations using the Gardiner NI scheme and a multiplier of 0.1 produced IC flash rates exceeding 500 per minute (not shown) and therefore, highlighted the extreme sensitive nature of the IC flash rate generated in the model to the NI multiplier chosen in this NI scheme. Decreasing the NI charging magnitude, however, did not have as much impact on the low-level charging (below  $z = 5\text{km}$ ) because the latter was also a consequence of induction (see later in the section).

That said, the Gardiner scheme tended to support a gross normal tripole charge structure (two positive charge layers enclosing a negative one, Fig. 43). Note that in the control run, the western portion of the eyewall of the TC exhibited an inverted tripole instead. The latter charge structure is also observed in the southern portion of the eyewall of the landfalling storm. Since the advection of charges was shown to be important in the eyewall, a complete parcel history would be necessary to explain the origins of this charge structure in the eyewall.

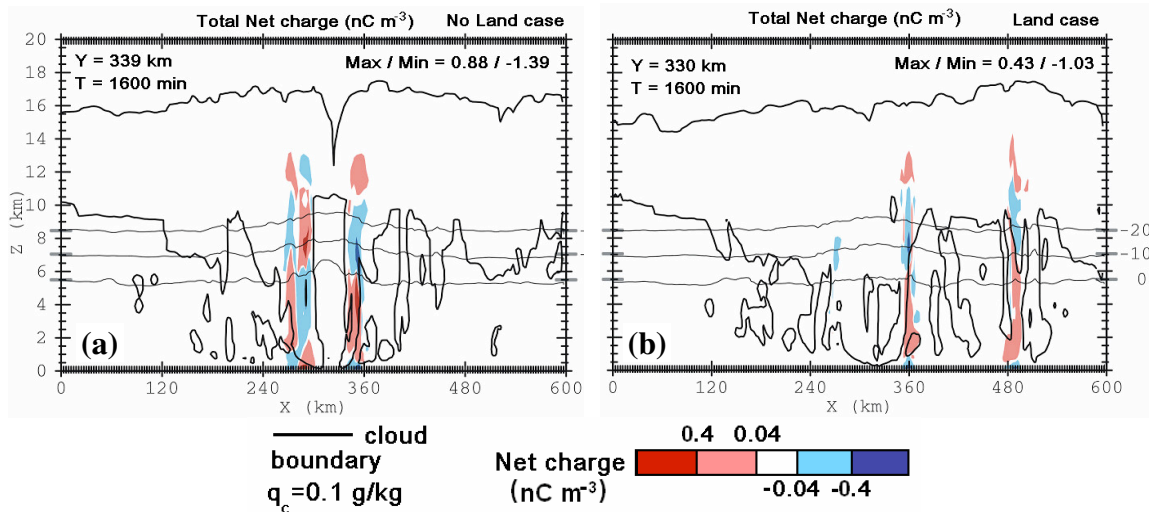
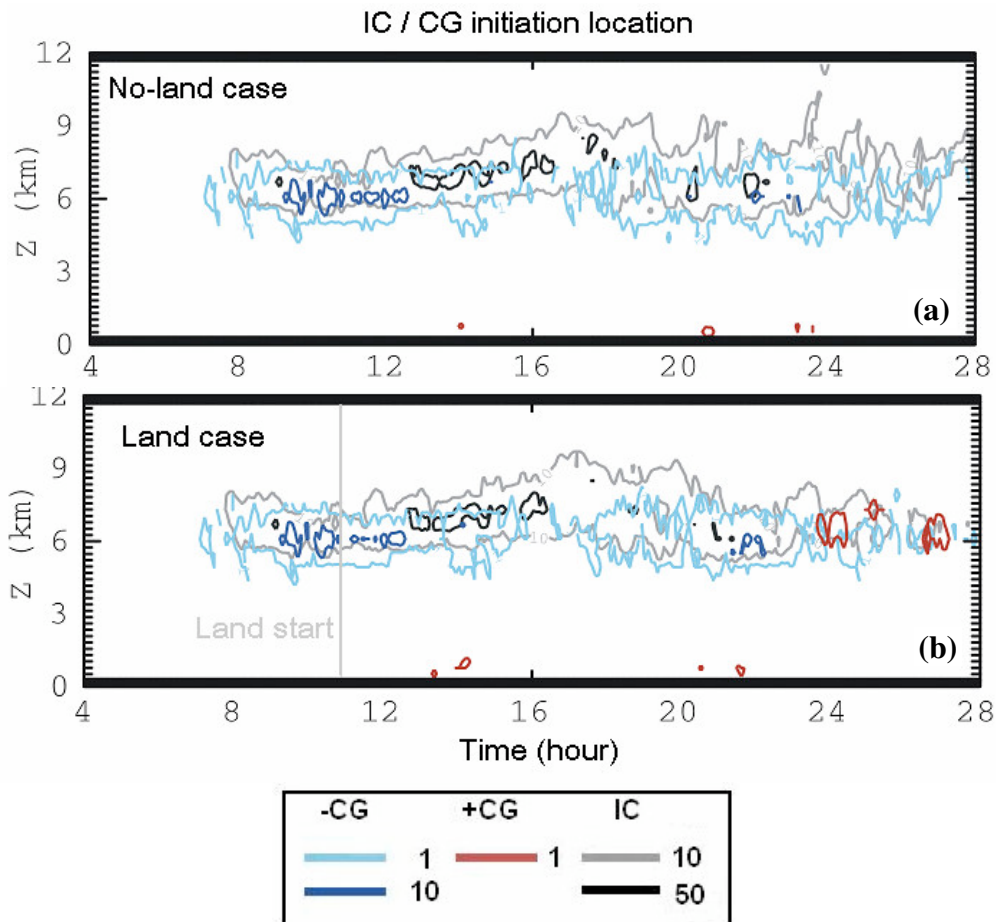


**Fig. 43.** As in Fig. 34 for (a) the no-land case and (b) the land case.

Because we significantly reduced the magnitude of charge separated by NI processes, it was not surprising to find that all the charge regions within the TC mainly owed their existence to induction (not shown). At that particular time and location of the storm, the positive (negative) inductive charging rate maximum is about 30 (8) times that of NI charging (not shown). If the NI charging rate multiplier was set to 1 instead of 0.0009, stronger negative (positive) NI charging rates would have occurred at midlevels (upper levels), possibly promoting a general positive tripole charge configuration across

the storm's eyewall. Therefore, it is possible that the +CG flashes observed after landfall in the eyewall could have been a consequence of weak NI charging settings, although the latter would need further investigation.

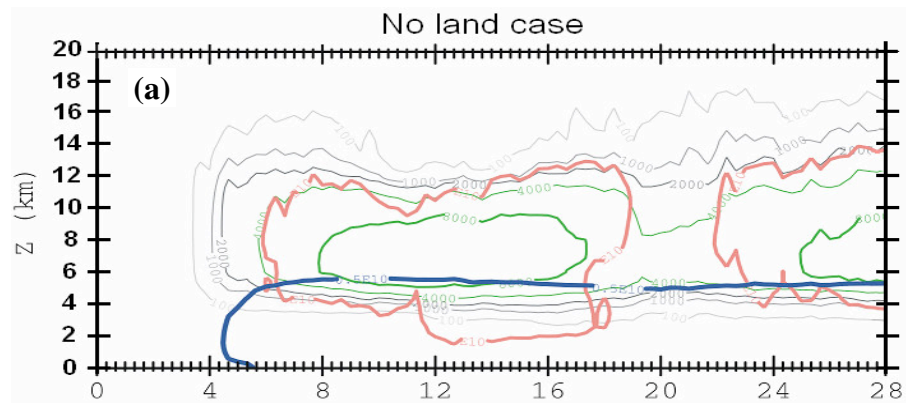
As the storm matures, the IC (CG) flash rate (through the whole domain) rarely exceeded 50 (10) flashes per minutes in both cases. Note that due to our weak NI settings, almost no IC flashes were found above 9 km (Fig. 44).



**Fig. 44.** Time-height plot of the horizontally integrated IC and +/-CG flashes across the entire domain for the first 28 h of simulation for (a) the no-land case and (b) the land case. The time at which the landmass starts to enter the domain is indicated by a vertical light grey line in panel (b).

The few +CG flashes that were observed below 2 km in Fig. 44 were the result of corona or point discharge from the ground. As mentioned earlier, after 24 h, the landfalling storm produced several +CG flashes in the southern portion of the eyewall, which was not the case for the control run (Fig. 44). Additional cross sections not shown here revealed that these +CG flashes were coincident with a general inverted tripole charge structure (a main positive charge region amidst two negative ones). In the cells forming the southern eyewall, relatively strong negative charge magnitude (i.e.  $> 10^{-1} \text{ nC m}^{-3}$ ) extended all the way to the ground and were collocated with positive leaders propagating all the way to the ground (not shown).

The model result seemed to support Wolff (2000) findings who showed that landfalling TCs could have different CG flash behavior once they made landfall. They found, however, that the relative percentage of strikes either negative or positive exhibited great variation from storm to storm and that therefore, it was not possible to generalize the TC CG flash behavior before and after landfall.



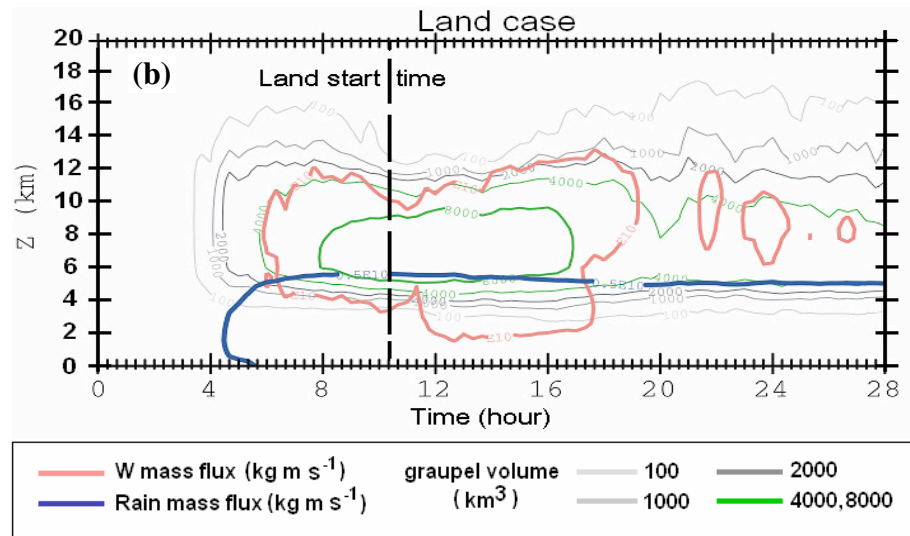


**Fig. 45.** As in Fig. 44 for the total updraft mass flux (in  $\text{kg m s}^{-1}$ , in red shown for  $10^{10}$  contour only), rain mass (in  $\text{kg}$ , blue shown for  $10^{10}$  contour only) and total graupel volume (in  $\text{km}^3$ , see legend below panel b). Note that the  $8000 \text{ km}^3$  graupel volume contour is shown in a thicker green contour than for  $4000 \text{ km}^3$ . The thick dotted black line in panel (b) has the same meaning than the grey line in Fig. 44b.

As the TC convection evolved, its microphysical state exhibited noticeable phases, which were in turn coincident with phases in the overall lightning behavior of storm (e.g., MacGorman et al. 1989; Lang et al. 2002; Wiens et al. 2005). For instance, the 1000 and 2000 graupel volume contours at upper levels showed a rising trend after about 14 h of simulation, which coincided in time with an upward movement of the updraft mass flux contour and an increase of updraft mass flux below 4 km (Fig. 45). This suggested that during this period, most of the charges carried by graupel (and also lighter ice crystals), relocated higher in the storm, which was consistent with a temporal weakening of the total lightning activity at lower levels and a simultaneous increase of the IC flash rate aloft (Fig. 44).

The differences between both simulations became more evident after the storm made landfall near 22 h. After that time, the land case showed overall much weaker total

updraft mass flux, which contour spanned a smaller depth than the control case (Fig. 45). This weaker total updraft mass flux after landfall was also correlated with smaller total graupel volume (Fig. 45). Consequently, less total charge will be separated in the TC, leading to a progressive decrease in the total lightning activity across the storm after landfall (Fig. 44).

### **V.4.3. Conclusions**

Overall, the simulation gave satisfactory results consistent with observations. As expected, the landfalling storm was much weaker and less organized than the storm evolving over ocean. After landfall, the surface pressure experienced a sharp quick rise, in turn leading to a rapid weakening of the storm's secondary circulation and to a fast decrease of the tangential winds, particularly at the lowest levels. This disruption of the storm circulation caused the eye to become partially filled with light ice crystals and snow aggregates. This weakening of the storm was also associated with a substantial decrease in the eyewall total updraft mass flux, shallower echo tops (particularly 30 dBZ and greater), smaller total graupel volume aloft and therefore, weaker total lightning activity.

Perhaps the most interesting finding of this study was the tendency for the simulated TC to produce several +CG flashes after landfall, which was not observed in the control case. Although, weak NI charging settings were chosen for this analysis, this result strongly suggested that there exists a qualitative difference in the storm electrical

behavior over land versus over ocean, which as we showed, was directly linked to its change in kinematical and microphysical fields.

## **V.5 Major issues raised by the simulations.**

Currently, two major issues need to be considered. The first problem was related to the storm internal dynamics and kinematics: once a well-defined eyewall and outer rainbands started to form, the TC started to lose its definition near 30 h of simulation. In some parts of the domain, the outer rainbands convection expanded to form several small storm clusters. Later, at about 35 h, the convection in the vicinity of the eyewall had completely dissipated while the storm clusters progressively propagated away from the eyewall. In the same time, the eyewall has lost its closed circular pattern, which was coincident with a progressive decrease in the eyewall total updraft mass flux.

We speculate that the detrimental effect of the low  $\theta_e$  air from the cold pools generated by the outer storm clusters were not the primary cause for the progressive weakening of the eyewall convection. Indeed, further analysis showed that the regions around the eyewall void of convective activity at the LCL (between 1 and 1.7 km) were characterized by warm temperature anomalies exceeding 2-3 K which were not observed about 5 h earlier. This generalized stabilization of the atmosphere at the LCL was apparently not caused by large scale subsidence across the domain. It is possible that the inclusion of radiative cooling (e.g., Newtonian cooling parameterization) could have helped in reducing this generalized warming of the atmosphere as radiative cooling acts on the same time scale as the simulated warming.

Surprisingly, even though the eyewall convection weakened and became more ill-defined, the TC was still undergoing slow progressive deepening. Additional cross sections revealed that the strong warm anomaly caused by subsidence in the eye (and responsible for the pressure fall near the surface in the eye) persisted for several hours after the convection in the eyewall had significantly weakened (not shown). The exact reasons behind this behavior remain the subject of future investigation.

The second major problem was, on the other hand, related to the storm microphysics and electrification parameterizations used in the model. One major caveat of the current microphysics is the lack of predicted ice particle concentration. This diagnostic method may overestimate the total ice particle concentration in the TC and lead to unrealistically high total (horizontally integrated) IC flash rate ( $> 800$  per minute) above 9 km. This method could result in too few ice crystals at temperature ranging between 0 to  $-15^{\circ}\text{C}$ . That is why, in the future, an improved version of the code featuring explicit prediction of ice particle concentration rather than an arbitrary diagnosis would improve in reproducing lower and maybe more realistic ice particles profiles in the storm, although the 2-moment parameterization still has its own issues, which remain beyond the scope of this study.

In general, observed particle size distributions do not fit a single analytical function and are also not constant with time and space (Giaiotti et al. 2001; Bringi et al. 2002; Brandes et al. 2004a, b) as assumed in the current model. Allowing for time-varying and/or space-varying particle size distribution in a numerical model, however, remains extremely difficult, not to say almost unfeasible.

Other improvements on the microphysics not mentioned earlier would be

allowing collection efficiencies to vary with particle diameter for each hydrometeor specie.

Before mentioning some possible improvements that could be made in the electrification, it is important to point out that many of the electrical properties of a storm are hard if not impossible to measure (e.g., inductive or NI charging rate of individual species), which makes parameterizations of such phenomena very difficult. That is also why, some of the parameterizations in the lightning model rely on laboratory experiments and not observations.

For the charging parameterizations possible improvements include the addition of more parameters known to influence the sign of charge acquired by the rimer during collision such as the relative diffusional growth rates (Baker et al. 1987; Mitzeva et al. 2003), water vapor supersaturation (Saunders et al. 2001, 2003), and the cloud droplet size distribution (e.g., Avila et al. 1999). Other improvements that could impact the results include the allowance of inductive processes during meltwater shedding from hail/graupel below cloud base and allowing corona from ice particles. Also, although expected to have a lesser impact, other model improvements might include the effects of electrical forces on collection efficiencies and other microphysics variables.

Finally, apart from the way that electrification, lightning, and microphysics are parameterized in the model, the environmental conditions might be initialized in a more sophisticated way in future studies (e.g., using data assimilation).

## VI. Future work

The model results presented before were based upon sensitivity testing carried out a coarser grid spacing ( $> 5$  km). In particular, the optimal vortex size, strength and Coriolis parameters were determined by analyzing the storm evolution in several numerical simulations carried out at grid spacing greater than 5 km. Therefore, this experiment should be repeated for grid spacings ranging between 1 and 2 km using a broader spectrum of vortex size, vortex strength (controlled by the maximum vertical vorticity for a given vortex radius) and vortex depth (which was set to about 15 km.) These experiments should be also all repeated for various Coriolis parameters ranging between 0 to midlatitude values (e.g.,  $1 \times 10^{-4} \text{ s}^{-1}$ ) and SST values ranging between  $24^{\circ}\text{C}$  (i.e., below SST threshold value for hurricane formation) and  $31^{\circ}\text{C}$  (representative of the extreme SST values).

Also the above experiment should be repeated with different soundings representative of various cases in order to determine quantitatively how the initial environment influences on the hurricane formation in the model. In particular, which types of maritime/tropical soundings would fail in spinning up a well defined hurricane-like vortex in the model and in turn how are these results consistent with observations?

Also important would be to test different bogus vortex parameterizations (e.g., from Leslie and Holland, 1995) to determine if the one used in this study gives optimal results for an idealized TC simulation. Indeed, Leslie and Holland (1995) showed that TC track and intensity was very sensitive to the bogus vortex initial location, size and intensity. Consequently, great caution was warranted in choosing such vortex by

determining accurate vertical structure, asymmetries, diabatic heating distribution and nearby environmental synoptic features (such as troughs, ridges, front, etc). Zehnder (2001) and Prater (2004) further showed that overall TC intensity and evolution was very sensitive to the cumulus parameterization used in the model, warranting additional caution.

In order to further support the robustness and validity of the results shown hitherto, additional simulation should be carried out at finer grid spacings (with and without land), keeping as many electrical and kinematical parameters constant. A similar analysis than from Brian et al. (2003) should also be undertaken for the hurricane simulation, since squall lines behave differently than hurricanes, particularly in terms of their dynamics.

Another important test would be to evaluate the resolution dependence of the microphysics parameterizations used in the model. This is a relevant problem as a copious amount of studies ranging from hurricanes to continental supercells have been published and thus far, no one really knows whether these microphysical parameterization behave differently or not at very small grid spacings (i.e. of the order of ten's of meters). The Marshall and Palmer (MP, 1948) inverse exponential size distribution has been developed in the late 1940's and yet, no studies in the current literature have addressed the possible impact the horizontal (as well as vertical) grid spacing could have on the simulated microphysics fields. Akin to LES schemes, it is critical to determine whether or not these bulk microphysics schemes (MP or Gamma distribution) were *designed* to work at grid spacings of the order of 1 km, as it remains clear that at these relatively coarse resolutions, one assumes a grid box of the order of 1

km X 1 km X 500 m to have the same mixing ratios values for all the species present in this box, which highly unrealistic and could have non negligible impacts on the storm latent heating vertical (and horizontal) profile, and in turn on the storm structure and evolution. The main difficulty in carrying out such experiment, however, is that it will be difficult to *isolate* the effect of horizontal resolution from the effect of the resulting changes in the dynamics of the storm. This is particularly true at finer grid spacings as Bryan et al. (2003) showed that at scales of about 10's of meters, the dynamics of their simulated storms behaved differently than at 1 km as turbulent processes were allowed to be explicitly reproduced at these small scales. As a result, these finer scale features could be important in modulating the transport and distribution of the different hydrometeor species in the storm.

Apart from resolution dependence, the adequacy of the 12-class bulk microphysical scheme used in this study needs to be tested within the TC framework. For instance, McFarquhar and Black (2004) proposed that different microphysical parameterizations should be used in convective and stratiform regions within TCs. However, at present, applying this idea to numerical models remains very difficult and maybe unfeasible.

As mentioned earlier, the drag coefficient  $C_d$ , which controls the magnitudes of the surfaces fluxes, is assumed to increase with increasing wind speed. However, we highlighted that recent studies (e.g., Ginis et al. 2004) suggested that  $C_d$  was actually decreasing for wind speeds over  $30 \text{ m s}^{-1}$  (which is close to a category 1 storm), because at these wind speeds the sea surface becomes progressively covered with foam, which offers less resistance to the wind than water. Therefore, the use of Deacon's formula for

heat and moisture fluxes could overestimate these fluxes underneath the eyewall, where the tangential winds are likely to exceed  $30 \text{ m s}^{-1}$  and in turn could lead to large errors in the computation of the budget of the boundary layer moist entropy of the storm's eyewall. Therefore, additional simulations should be carried out in the future using a parameterization of  $C_d$  that accounts for this decrease of  $C_d$  at large wind speeds.

Once the kinematical and microphysical behavior of the storm has been analyzed in more details, one can focus on the lightning and electrification processes that are included in the model. In particular, different NI charging schemes should be tested for identical microphysical and kinematical settings to see to what extent to lightning behavior (polarity, amount, and distribution) is affected.

For the landfalling experiment, different surface wetness, roughness, and land surface temperature should also be tested in order to determine how the final intensity of the landfalling TC is affected by these parameters (excluding the influence of orography). For instance, Wang and Holland (1999) showed that the land temperature did have a great influence on the landfalling TC final intensity. Also Kimball (2004), showed that the larger the roughness length, the weaker the winds at the surface.

The rainfall amounts and distribution over land is strongly affected by the presence of higher terrain (e.g., Lin et al. 2002b). For instance, mountainous regions such as the island of Haiti, Taiwan or the Western Mexican Coast are more subject to devastating mud slides when a TC makes landfall, because the flow of the TC is forced up the escarpment, leading to enhanced and more persistent convective activity there (e.g. Chang, 1982). The stronger convection arising from orographic forcing could be associated with larger hail or graupel mass aloft (e.g., Black and Hallett, 1995; Lang et al.

2002; Wiens et al. 2005). Hence, it would be important to describe in a quantitatively and qualitatively manner how the simulated hydrometeor field, and hence reflectivity profile, evolves as the primary circulation of a TC interacts with topography (in an idealized sense). In particular, it would be important to determine to what extent the rainfall amount (and hence the flooding potential), is enhanced by orography and in turn which areas in the vicinity of the mountains will be more impacted.

Apart from orography, some investigators showed that the angle of impact at landfall (e.g., Zehnder and Reeder, 1997) could have non-negligible effect on the storm rainfall distribution and evolution, which in turn can seriously affect the amount of damage caused over land.

## **VII. Appendix A: Recent results from simulations of the weakly electrified 9 February 1993 TOGA COARE squall line.**

### **VII.1 Introduction**

The only comprehensive observational study of *both* the dynamics and electrification of a tropical squall line appears to have been carried out by Petersen et al. (1999, referred to as P99). In February 1993, several oceanic tropical squall lines were well sampled by the TOGA COARE field program. In particular, on 9 February 1993, two maritime tropical squall lines were also sampled electrically. The cloud-to-ground (CG) lightning flashes in this squall line were detected using the Advanced Lightning Direction Finder network (ALDF; Petersen et al., 1996). Because intracloud (IC) flashes have weaker electromagnetic radiation than CG flashes (e.g., MacGorman and Rust, 1998), they were not detected by the ALDF network. A field mill measured surface electric fields and could detect transients from both IC and CG lightning.

Many numerical simulation studies of TOGA COARE (e.g., Trier et al., 1996; Montmerle et al., 2000) and other tropical squall line cases (e.g., Nicholls, 1987) have been carried out since then. However, until present, no numerical study focusing on the electrical nature and characteristics of these systems has been performed.

In this appendix, we present a simulation of the 9 February 1993 squall line that was sampled just east of the New Ireland island in Papua New Guinea, by the *John V. Vickers* (Massachusetts Institute of Technology, MIT radar) and the *Xiang Hang Hong 5* (NOAA TOGA radar) research vessels (P99). No -CG flashes were detected during the

entire lifetime of this squall line, which was about 5 hours, and no lightning was seen by eye (system evolved during nighttime).

This simulation was carried out using the same numerical model as in the previous experiments (described in section III). With that model we expect to obtain greater insight into the simulated electrical and microphysical properties of these weakly electrified maritime systems. Initially, particular focus will be on the reflectivity profiles evolution, the depth of the convection, and the precipitation structure and intensity. Later, we will determine how the latter parameters are related to the simulated charging rates, IC and CG flash rate in different regions of the storm.

## **VII.2 Description of the initialization procedures**

As for all the other cases shown earlier in this work, we chose the SP98 NI scheme. The numerical simulation presented in this appendix was carried out to 4 h 30 min in a 132 km x 210 km x 22 km domain. The horizontal grid spacing in the  $X$  and  $Y$  direction was set to 600 m with an average grid spacing of 400 m in the vertical, resulting in a total of 220 x 350 x 60 grid points. The vertical grid stretched from  $dz = 100$  m near the surface to  $dz = 600$  m at and above 7 km AGL. The lightning grid spacing was set to half the horizontal grid spacing (i.e., 300 m).

For this simulation, the surface moisture and sensible heat fluxes (parameterized as in Rotunno and Emanuel, 1987) were turned on and a homogeneous sea surface temperature of 29°C was chosen, because this value is close to the average observed temperatures at this time of the year in the region. The Coriolis force was set to zero,

because at these latitudes ( $\sim 2^\circ$  S), it has a negligible impact on simulated squall lines as they last only a few hours.

The initial environmental conditions were assumed to be homogeneous and were represented by the sounding taken aboard the R/V *Vickers* at 0600 UTC (Fig. A1). This sounding has moderate convective available potential energy (CAPE) of about  $1710 \text{ J kg}^{-1}$  and a convective inhibition (CIN) of about  $10 \text{ J kg}^{-1}$ . A low-level jet of about  $12 \text{ m s}^{-1}$  is located between 830 and 760 mb.

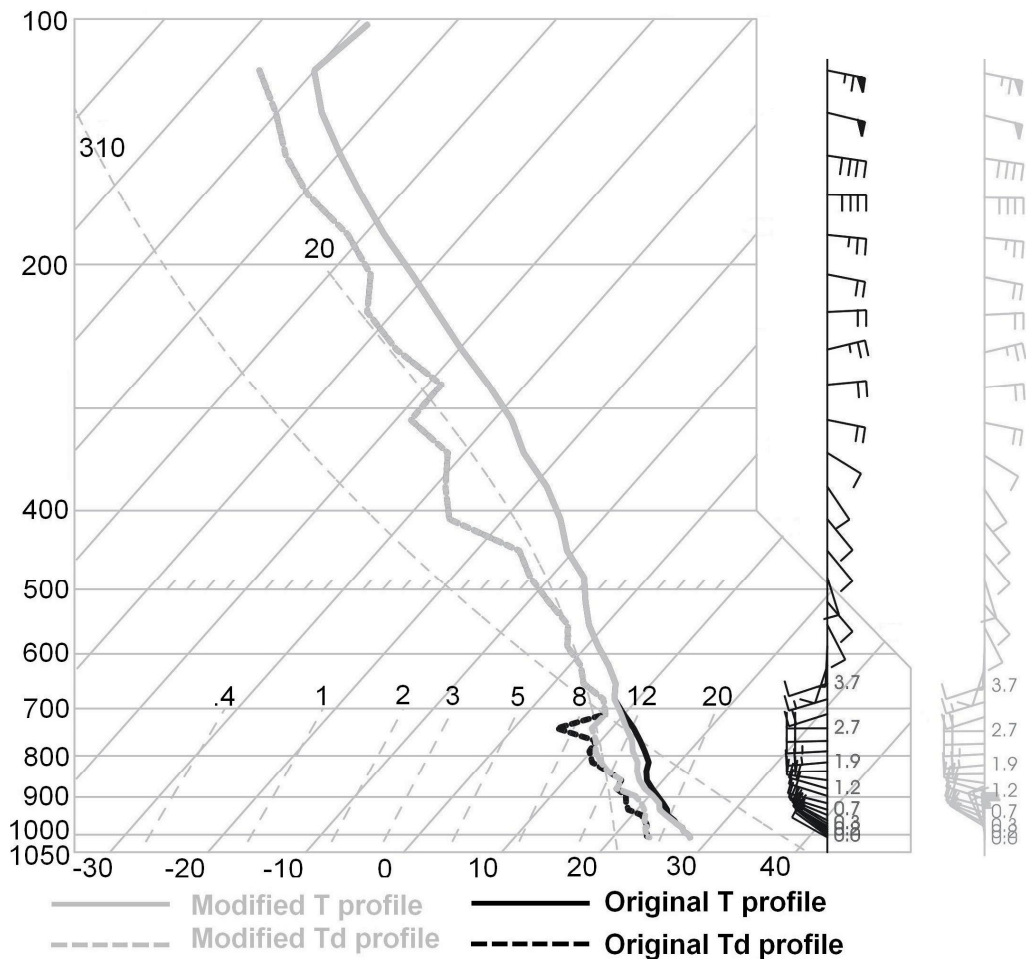


**Fig. A1.** Original (modified) Skew-T log-p diagrams of the 9 February 1993 R/V *Vickers* squall line case shown in the black (grey) thick line. Sounding data courtesy of the Earth Observing Laboratory, National Center of Atmospheric Research (NCAR).

Since this sounding has almost no CAPE between 900 and 850 mb, which is just above the Lifting Condensation Level (LCL), the initial convection in a preliminary simulation carried out with this sounding quickly dissipated after about one hour. For this reason, we made several minor modifications to the original R/V *Vickers* sounding. First, the temperatures between 920 and 850 mb were slightly decreased to enhance convective instability near and above the LCL (Fig. A1). This change resulted in a sounding having a total CAPE value of about  $1753 \text{ J kg}^{-1}$ . Second, the low level winds between the surface (1007 mb) and 975 mb were rotated in a clockwise fashion from a NW direction to a more Northerly direction in order to increase the storm relative inflow at these levels. Last, the vapor mixing ratio values were increased slightly between 950 and 850 mb. Without including all these minor changes, the model failed to generate a squall line that lasted more than 3 hours.

To trigger convection in the model, we used, as before, a  $-7^\circ\text{K}$  temperature anomaly with dimensions of  $20 \times 130 \times 2 \text{ km}$  centered at  $z = 1500 \text{ m}$ , which was placed at  $X = 105 \text{ km}$  and  $Y = 54 \text{ km}$ . In order to preserve the observed squall line orientation, the winds at all levels were rotated clockwise by 50 degrees. For the display in the horizontal plane, the domain will be rotated in counterclockwise manner by 90 degrees. With both of these changes our simulated north-south oriented squall line will be equivalent to a squall line oriented with a constant angle of  $-40$  degrees (relative to the zonal axis, that is, nearly NW-SE). In our simulation, we did not consider the latitudinal variation of the Coriolis force (or beta effect), so the aforementioned rotation of the winds (and of the domain) will not affect the results of the simulation.

Our idealized initialization resulted in the development of convection along a quasi NW-SE oriented line (see next section). The gravity current caused by the collapse of the initial cold anomaly allowed this convection to persist along its leading edge, mimicking observed squall lines. The magnitude of the cold anomaly rapidly decreased from -7 K to about -2 K due to mixing at and near the surface (i.e., lowest 100 m).

## **VII.3 Results**

### **VII.3.1 Kinematic and microphysics evolution**

At the beginning of the simulation, near 1 h 30 min, the simulated squall line exhibited a solid linear reflectivity pattern (Fig. A2a), consistent with observations (P99, their Fig. 3). Around that time, however, the reflectivity values near 1 km AGL were larger than the observations by about 10-15 dBZ, probably because the initial environment was homogeneous and because we used a symmetric forcing to trigger convection. After about 2 h 30 min of simulation, the solid NW-SE oriented line of convection began to resemble a typical squall line, with a well-developed gust front at its leading edge (Fig. A2b, thick black line). The cold anomaly at the surface weakened, after its initial collapse, from a magnitude of -7 K to -2 K, but quickly recovered once the downdrafts from the individual cells forming the convective line developed. The squall line propagated toward the Northeast (Fig. A2) at a ground-relative speed of about 10 m s<sup>-1</sup>.

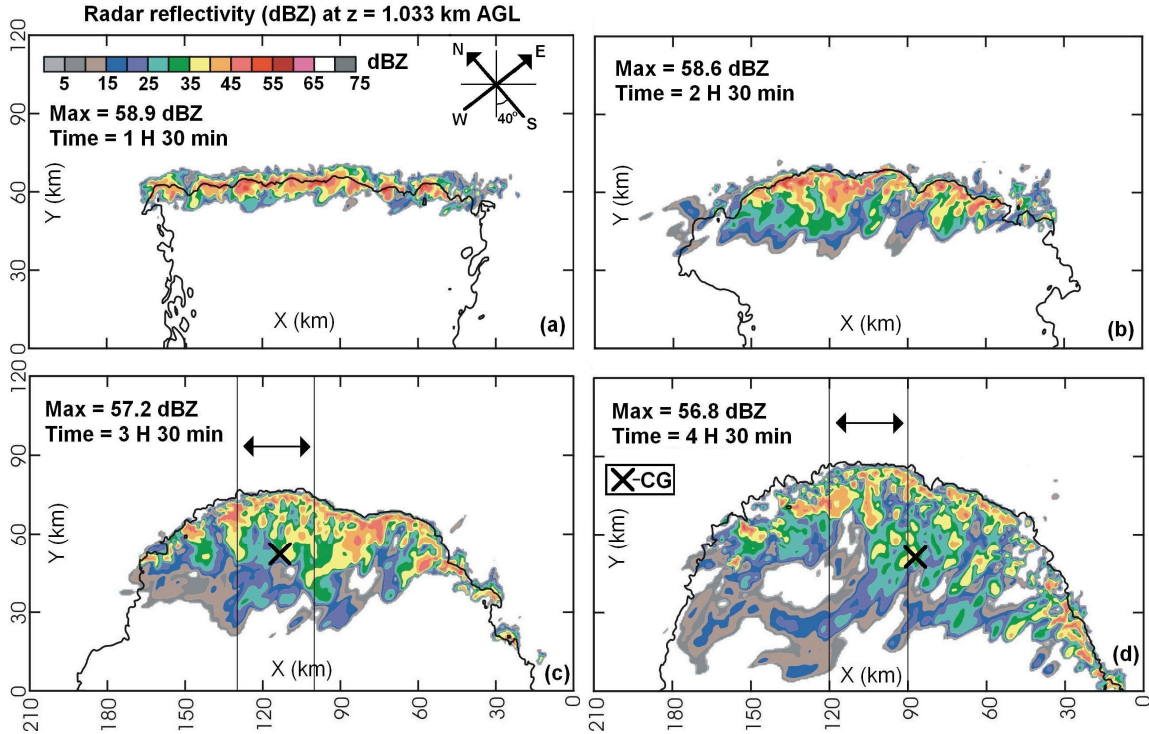


**Fig. A2.** Horizontal cross section of radar reflectivity (dBZ) at  $z = 1,033$  km AGL shown for (a)  $t = 1$  h 30 min, (b) 2 h 30 min, (c) 3 h 30 min and (d) 4 h 30 min. Contours range from 5 dBZ to 75 dBZ by increments of 5 dBZ. The flash locations were plotted for a 20 min time interval until the cross section time. Locations of -CG lightning strikes are also shown by a cross (Note that no +CG flashes were produced in the time frame for each plots). The black contour represents -1 K potential temperature perturbation at the ground, which depicts the cold pool at the surface. A compass indicates the orientation of the domain and the two thin black lines denoted by a double arrow indicates the region of the line averaging in Figs. A3-A5.

The modified surface winds possessed a storm-relative component normal to the gust front (Figs. A1 and A2), which allowed the moist inflowing air to be forced upward and over the density current created from the storm's downdrafts at the leading edge of the line. As time progressed, particularly after 3 h, the convection at the leading edge of the squall line weakened and started to exhibit reflectivity values closer to observations (maximum near 40 dBZ, Fig. A2c-d). The simulated squall line lost its definition and started to dissipate about 5 hours after its formation, which is close to the lifetime of the

observed squall line. During the weakening stage, the simulated squall line expanded in areal coverage and a well-defined stratiform region became evident, mostly after about 4 h (Fig. A2d, near  $Y = 30$  km).

As before, to provide a clearer view of the squall line's *dynamical* and *microphysical* properties, vertical cross sections of line-averaged quantities across a 30 km slab along the line (i.e., in the  $X$  direction of Fig. A2) were generated at 3 h 30 min ( $X = 100$  km to  $X = 130$  km) and 4 h 30 min ( $X = 90$  to  $X = 120$  km) of simulation time. In many instances, individual cross sections (not shown) were also made to further support the results. We selected these two times, based on similarities between the observed and the simulated horizontal reflectivity values and patterns. We also wished to highlight the possible relevant differences and commonalities in the squall line dynamical, microphysical and electrical behavior between those two particular times.

Individual cross-sections revealed that, the squall line was composed of a succession of shallow narrow thunderstorm cells that developed along the leading edge of the gust front in a periodic fashion. These newly formed cells progressively propagated to the rear of the line (along the squall line motion vector) until they ultimately decayed to form a stratiform region (mostly evident after 4 h) characterized by small reflectivity values generally smaller than 30 dBZ (e.g., Fig. A3b,  $Y = 30$  km) and weak vertical motions on the order of  $1 \text{ m s}^{-1}$  (Fig. A4b,  $Y = 30$  km).

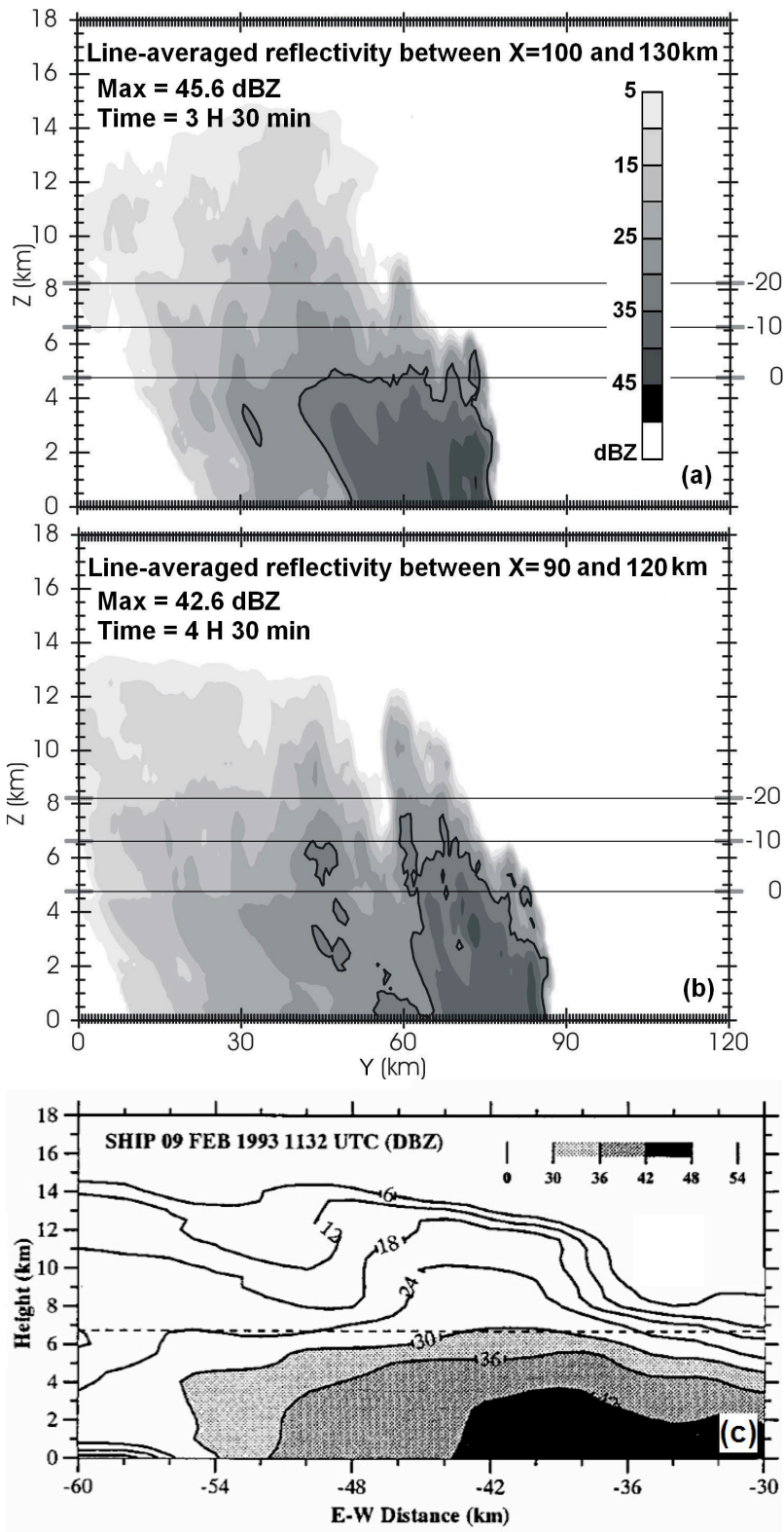


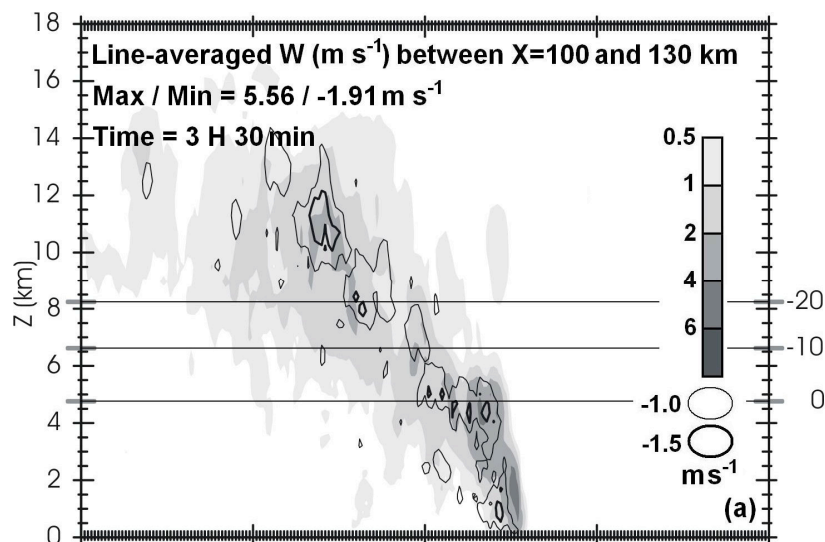
**Fig. A3.** Vertical cross section of line-averaged radar reflectivity (in dBZ) between (a)  $X = 90$  km and  $X = 120$  km at  $t = 3$  h 30 min and (b) between  $X = 100$  and  $X = 130$  km at  $t = 4$  h 30 min. Legend for reflectivity is shown in panel (a). The line

averaging consists of adding all the reflectivity values greater than a minimum threshold value (here set to 1 dBZ) along the  $X$  or  $Y$  axis and then divide this sum by the number of grid points along this  $X / Y$  axis where the reflectivity values are greater or equal than this threshold. The horizontal thin black lines show the average locations of the 0, -10 and -20°C isotherms. The 30 dBZ contour has been highlighted in a thicker black line. Panel (c) shows ship cross sections (1132UTC) of composite maximum radar reflectivity through the observed squall line within a box of dimensions  $(x ; y) = (30,10)$  km. Reflectivity values are displayed in increments of 6 dBZ, with reflectivity values greater than 30 dBZ shaded. The dashed line indicates approximate location of the -10°C isotherm. Panel (c) from Petersen et al. (1999), used with permission.

As before, the cells reached their mature phase and maximum updraft speeds in the “mature zone”, which in this simulation is located in between the trailing stratiform region at the rear of the line at about  $Y = 30$  km (Fig. A3b) and the leading edge of the line or gust front where cells formed between  $Y = 70$  and  $Y = 80$  km (Fig. A3b).

At 3 h 30 min, the line-averaged 30 dBZ reflectivity contour almost never exceeded the freezing level (Fig. A3a), whereas at 4 h 30 min, the line-averaged 30 dBZ contour reached the -10 C isotherm level (Fig. A3b). The deeper 30 dBZ echo tops at 4 h 30 min, was associated with larger line-averaged updraft speeds above the freezing level of about  $2\text{-}4 \text{ m s}^{-1}$  (Fig. A4b) compared to about  $1\text{-}2 \text{ m s}^{-1}$  at 3 h 30 min (Fig. A4a). However, individual cross-sections across the line, revealed updraft speeds locally exceeding  $8 \text{ m s}^{-1}$ , mainly in two locations. The first region of stronger updraft cores was near the gust front below 2 km, which was a consistent feature across the line. The persistence of these stronger updrafts at the gust front in turn, accounted for the generally larger values of line-averaged updraft speeds there (i.e.,  $> 5 \text{ m s}^{-1}$ ) than everywhere else in the system (Fig. A4). The second location where relatively stronger updrafts were present was within a few isolated strong cells in the mature zone. In this region, local, narrow ( $< 3$  km) updrafts speeds greater than  $10 \text{ m s}^{-1}$  above the -20 C level between  $z =$

10 and 12 km AGL were present (not shown). These stronger isolated elevated updraft cores in the mature zones account for the secondary (smaller) maximum of line-averaged updraft speed observed there, generally ranging between 2-4  $\text{m s}^{-1}$  (Fig. A4). These results agreed closely with the ship dual-Doppler observations of P99: They showed that along-line-averaged updraft speeds greater than 7  $\text{m s}^{-1}$  existed at upper levels (near 11 km AGL) in the mature zone in one of the strongest cells of the line 2.5-3 h min after its formation (Fig. A4c), which were consistent with line-averaged 30 dBZ echo tops reaching the -10 C, without exceeding that level (Fig. A3c). Therefore, as in the observations, we expect our simulated squall line to produce overall weak total lightning activity (CG + IC flashes). Zipser and Lutz (1994) argued that in tropical oceanic convection, strong electrification required the existence of average updraft cores of about 6-7  $\text{m s}^{-1}$ , 2-3 km wide within the mixed-phase region (defined as the layer between the freezing level and the -20 C isotherm). These thresholds were barely reached in the simulation and in the next section, we will show that these elevated updraft core near 11 km AGL, are not associated with significant charging (i.e., greater than 0.1  $\text{pC m}^{-3} \text{ s}^{-1}$ ), because at these high levels, CWC are generally very low (i.e.,  $\ll 0.1 \text{ g m}^{-3}$ ).



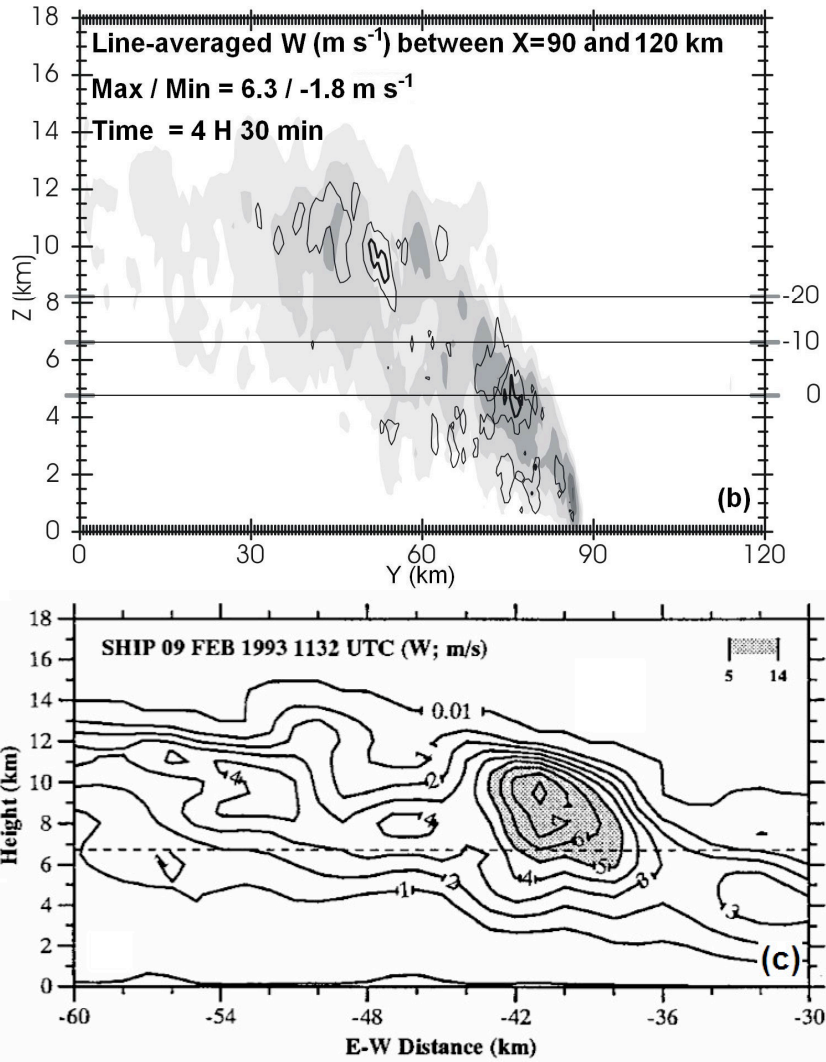
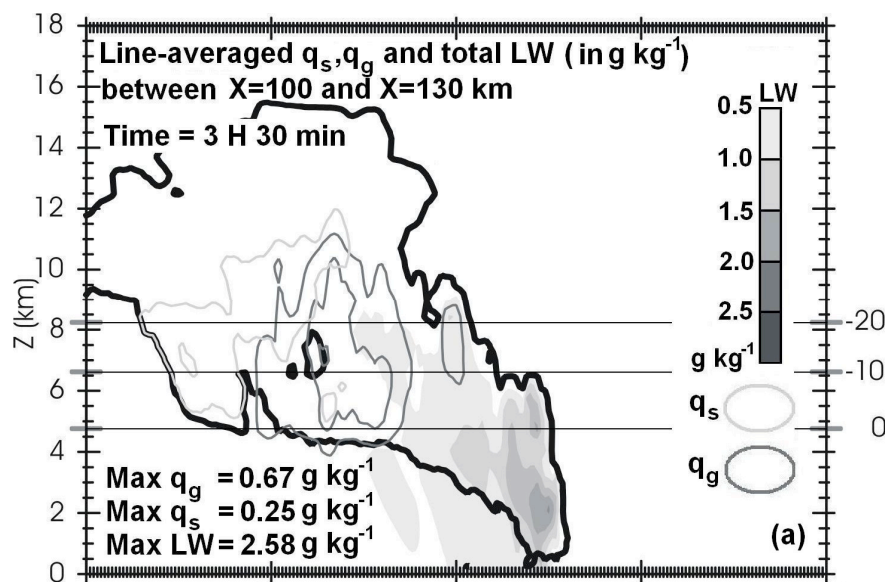


**Fig. A4.** As in Fig. A3, for the vertical wind component in  $\text{m s}^{-1}$ . The threshold value for the averaging of the positive (negative) vertical velocities is  $0.01 \text{ m s}^{-1}$  ( $-0.01 \text{ m s}^{-1}$ ). In Panel (c), velocities are contoured every  $1 \text{ m s}^{-1}$  with values  $\geq 5 \text{ m s}^{-1}$  shaded. The  $0.01 \text{ m s}^{-1}$  contour is also shown. Panel (c) from Petersen et al. (1999), used with permission.

In the mature zone, the line-averaged updraft speed rarely exceeded  $3 \text{ m s}^{-1}$  below the melting level (Fig. 5), consistent with early studies of tropical convection (LeMone and Zipser 1980; Zipser and LeMone 1980; Jorgensen and LeMone 1989; Lucas et al. 1994). Further to the rear, in the stratiform region (i.e., near  $Y = 30 \text{ km}$  at  $t = 3 \text{ h } 30 \text{ min}$

and 4 h 30 min), the line-averaged updrafts velocity magnitudes generally did not exceed  $1 \text{ m s}^{-1}$  (Fig. A4).

As we will see later in this section, these isolated strong storm cells in the mature zone account for most of the charge production (and thus lightning activity) of the squall line. May and Rajopadhaya (1996) posited that these larger updraft speeds above the melting level in the mature zone were partly caused by a rapid depletion of liquid water drops below the melting level (i.e., water unloading) due to enhanced warm rain processes in the convective region at the leading edge of the line, below 4 km AGL. Indeed, in our simulation most of the liquid precipitation was found at the leading edge of the line, while little or almost no liquid water (LW) was present above the melting level and in the mature zone (Fig. A5). These small amounts of LW at upper levels also results from freezing (e.g., P99). In another study by Trier et al. (1997), they showed that these elevated updrafts in the upper troposphere occurred when positively buoyant air parcels moved rearward, away from downward-directed pressure forces behind the gust front.



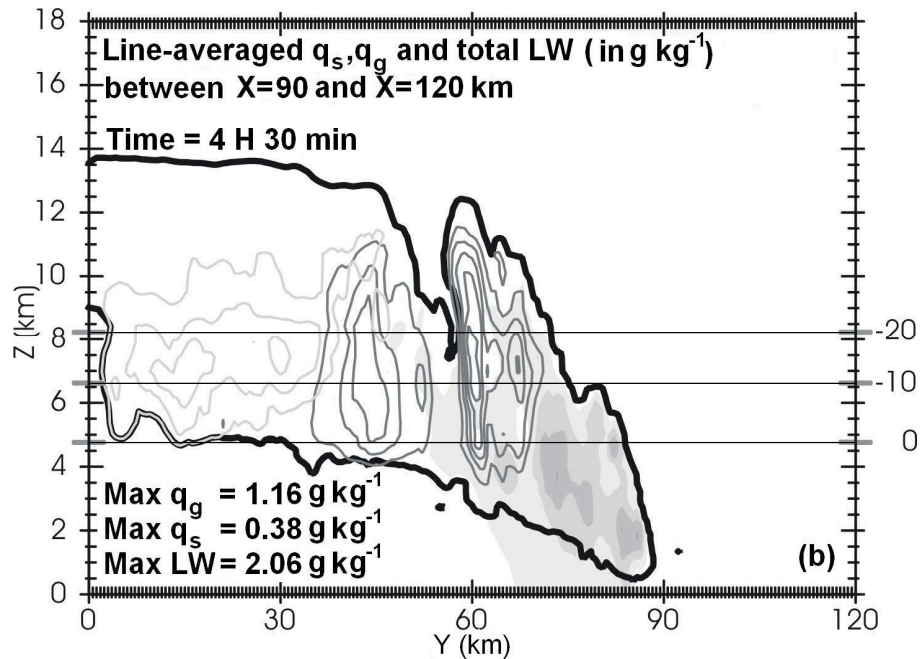


**Fig. A5.** As in Fig. A3 for line-averaged total graupel (sum of the three categories), mixing ratio ( $\text{g kg}^{-1}$ ), line-averaged snow mixing ratio ( $\text{g kg}^{-1}$ ), and total liquid water (LW) in ( $\text{g kg}^{-1}$ ). See legends in panel (a) for contours and shadings. The threshold value for averaging the total graupel mixing ratio, LW and snow mixing ratio is  $0.01 \text{ g kg}^{-1}$ . The line-averaged visible cloud contour (which is the sum of cloud mixing ratio, snow mixing ratio, cloud ice mixing ratio and pristine ice mixing ratio) of  $0.1 \text{ g kg}^{-1}$  is also shown in a thick black line.

Consistent with McFarquhar and Heymsfield (1996) and Stith et al. (2002), the trailing stratiform region of the squall line was composed mainly of snow particles (Fig. A5) and lighter ice crystals (see next section) which accounted for overall small line-averaged reflectivity values ( $< 30 \text{ dBZ}$ ) at all altitudes. In other words, once these storm cells in the mature zone started to decay as they propagated rearward in a more statically stable environment, the whole cloud became largely glaciated. In some discrete regions of this stratiform region, however, small amounts of graupel were still found (Fig. A5,  $Y = 30\text{-}40 \text{ km}$ , and Fig. A8 in the next subsection), which were mainly medium and high density graupel (not shown). This graupel is believed to originate from the stronger isolated cells within the mature zone that are later advected rearward in the stratiform region. Most of the graupel present in the rearward moving cells will evaporate, melt or

fall out before reaching the stratiform region (i.e.,  $Y = 30$  km in Fig. A3). As we will show later, the presence of this graupel will result in weak *in situ* charging in the stratiform region. The trailing stratiform region also was characterized by even smaller line-averaged reflectivity values near the surface (i.e.,  $< 25$  dBZ, Fig. A3). This was because most of the snow particles and ice crystals melted and evaporated before reaching the surface (because of their small terminal fall velocity which is of the order of  $1\text{-}2\text{ m s}^{-1}$ , Straka and Mansell, 2005).

In contrast, in the mature zone, a few cells showed evidence of moderate graupel (i.e.,  $> 0.3\text{ g kg}^{-1}$ ) and CWC (i.e.,  $> 0.1\text{ g m}^{-3}$ , see next subsection) in the mixed-phase region. Therefore, we expect most of the charging and lightning activity to occur there (see next subsection).

The simulated squall line experienced a general strengthening phase between 3 and 4 h, which was indicated by a simultaneous increase of the total graupel volume and an increase of the total updraft mass flux, especially near 4 km AGL (Fig. A6), which is about 1 km below the melting level (e.g., see Fig. A4). During this time, the stratiform region and the 40 dBZ contour at 1 km AGL also expanded in areal coverage (Fig. A3). Thus, the total lightning activity would be expected to peak during this time period (e.g., Carey and Rutledge, 2000; Wiens et al., 2005, see next subsection).

### **VII.3.2 Lightning activity and charge structure**

As mentioned in the previous subsection, for the analysis of the electrical properties, we chose to display individual cross-sections instead of line-averaging

quantities, because in-cloud charging and lightning activity are cell-scale phenomena. These cross-sections were made at the same two times, namely,  $t = 3$  h 30 min and 4 h 30 min. The location of the cross section was chosen to be the location or grid point at which a negative cloud-to-ground (-CG flash) occurred within 20 minutes of the cross-section time (i.e.,  $X = 114$  km and  $X = 87$  km, respectively). There were three main reasons for this choice: First, this will show under what particular conditions the model generates -CG flashes in the simulated squall line. Second, several additional cross-sections were made a *few* grid points away from the point of interest and only revealed small differences in the fields shown in this subsection (i.e., charge density, lightning channel polarity, NI and inductive charging rates). Last, we will be able to determine quantitatively how the electrical properties of the system change as the simulated squall line evolves from its overall strongest phase ( $t = 3$  h 30 min), characterized by moderate lightning flash rates, to its weakening stage, characterized by weak electrical activity ( $t = 4$  h 30 min, Fig. A6).

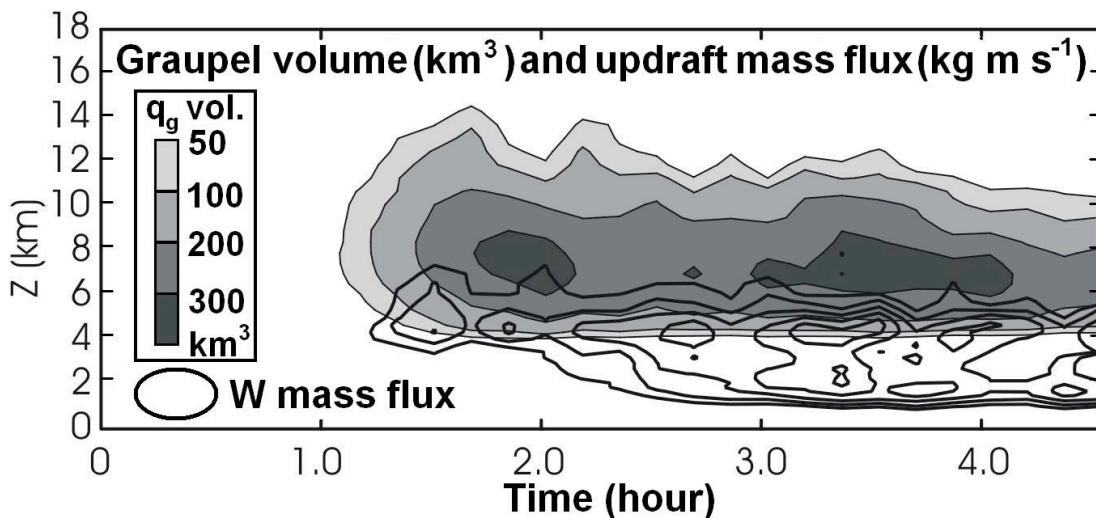


**Fig. A6.** Time-height contour plot across the entire domain of the total updraft mass flux (in  $\text{kg m s}^{-1}$ , in black shown from  $10^9$  until  $1.5 \times 10^9$  in increments of  $10^8$ ) and

total graupel volume (in  $\text{km}^3$ , with the 50, 100, 200 and  $300 \text{ km}^3$  shown in light gray to darker gray in the legend).

The charge structure across the simulated squall line was overall more complex than normal dipoles (positive charge above negative charge) or normal tripoles (composed of a normal dipole with a lower positive charge) commonly found in the literature to describe thunderstorm charge structure (e.g., Williams, 1989), although more recent observational studies have shown more complex charge structures (i.e., more layers) as summarized in Stolzenburg et al. (1998). In some regions of the squall line, the charge polarity switched several times with height and included many pockets of weaker (i.e.  $<0.3 \text{ nC m}^{-3}$ ) charge density (Figs. A7a-b). To facilitate the analysis we will, however, only consider the charge regions involved in lightning propagation or initiation (i.e., regions with charge density  $> 0.3 \text{ nC m}^{-3}$ ; compare Figs. A7a-b and Figs. A7c-d).

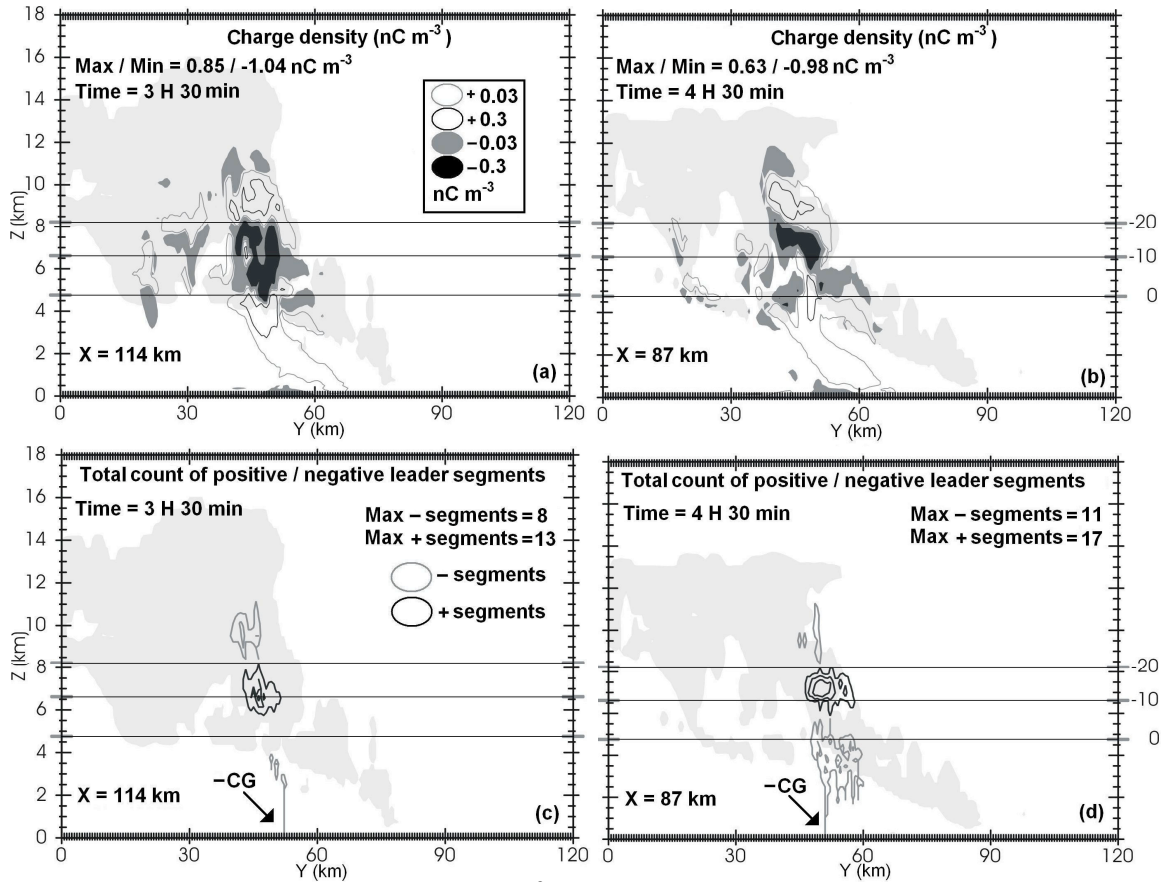


**Fig. A7.** Charge density in  $\text{nC m}^{-3}$  for (a)  $t = 3 \text{ h } 30 \text{ min}$  at  $X = 114 \text{ km}$  and (b)  $t = 4 \text{ h } 30 \text{ min}$  at  $X = 87 \text{ km}$ . Panels (c) and (d) are as in panels (a) and (b) show the total count of positive (black) and negative (darker grey) leader segments for a 20 min time interval prior the time of the figure. The 1, 5 and 10 contours for the total number of leaders are shown. The lighter grey shaded area depicts the cloud mixing ratio of  $0.01 \text{ g kg}^{-1}$ . See legends in panels (a) and (c) for the meaning of the remaining contours and shadings.

As expected from the results of the previous subsection, the stronger charge regions able to support lightning activity are present in the mature zone, because of the simultaneous presence of moderate amounts of graupel ( $> 0.3 \text{ g kg}^{-1}$ , Fig. A5) and CWC ( $> 0.1 \text{ g m}^{-3}$ , see later in the subsection). At 3 h 30 min and 4 h 30 min, the SP98 scheme resulted in a normal tripole charge structure in the mature zone (Figs. A7a-b,  $Y = 50 \text{ km}$ ). The trailing stratiform region, however, was characterized by overall little charge (e.g.,  $< 0.3 \text{ nC m}^{-3}$ , Fig. A7a,  $Y = 30 \text{ km}$ ), because of the general small amounts of CWC (i.e.,  $<$

0.1 g m<sup>-3</sup>, see later in the subsection) and graupel pellets (< 0.3 g kg<sup>-1</sup>, Fig. A5 at  $Y = 30$  km). Nevertheless, it is relevant to note that the polarity of the lowest charge region switched from positive in the mature zone (Figs. A7a-b) to negative in some discrete parts of the trailing stratiform region (Fig. A7a at  $Y = 30$  km, but is more evident (~0.3 nC m<sup>-3</sup>) in cross-sections made for instance at  $X = 95$ -100 km at 4 h 30 min). As we will discuss later in more detail, this reversal of polarity of the lowest charge region could have important consequences for the lightning activity pattern.

In the mature zone, the graupel particles present in the mixed-phase region at midlevels gained negative charge mainly from the NI charging mechanism (compare Figs. A8a-b and Figs. A8c-d). The lighter ice crystals (i.e., rimed, columns and plates), carrying the opposite polarity of charge after colliding non-inductively with those graupel pellets, were lofted up in the anvil cloud to form an upper positive charge region (Figs. 10a-b). Most of the negative charge at midlevels was on medium and low density graupel and rimed cloud ice particles, while the positive charge at low levels was mainly on the heavier species, namely, medium and high density graupel (Fig. A9, not shown for individual species but shown for total cloud ice and total graupel). The magnitude of charge carried by hail stones, all in the small hail category, was about 20 to about a 100 times smaller than the charge carried by each of the three graupel categories, which was on the order of 0.2 nC m<sup>-3</sup> (not shown). Inductive charging at midlevels accounted only for about 10-20% of the total charge there (compare Figs. A8a-b and Figs. A8c-d). On the other hand, the lowest positive charge region present in the mature zone resulted from both inductive and NI charging (Fig. A8). Induction was particularly effective at the lowest levels because liquid precipitation mostly was found there (Fig. A7) and hence,

allowed graupel (or hail) to collide with liquid water droplets more frequently than elsewhere in the system. A separate simulation was carried out with inductive charging turned off. As mentioned earlier, the electrification in the model does not feed back to the microphysics and therefore, the simulated squall line remained identical. The results showed that the maximum net charge density magnitudes are smaller by as much as 25%, at midlevels and particularly at low levels (not shown). As demonstrated later, this has non-negligible impacts on the resulting total lightning activity.

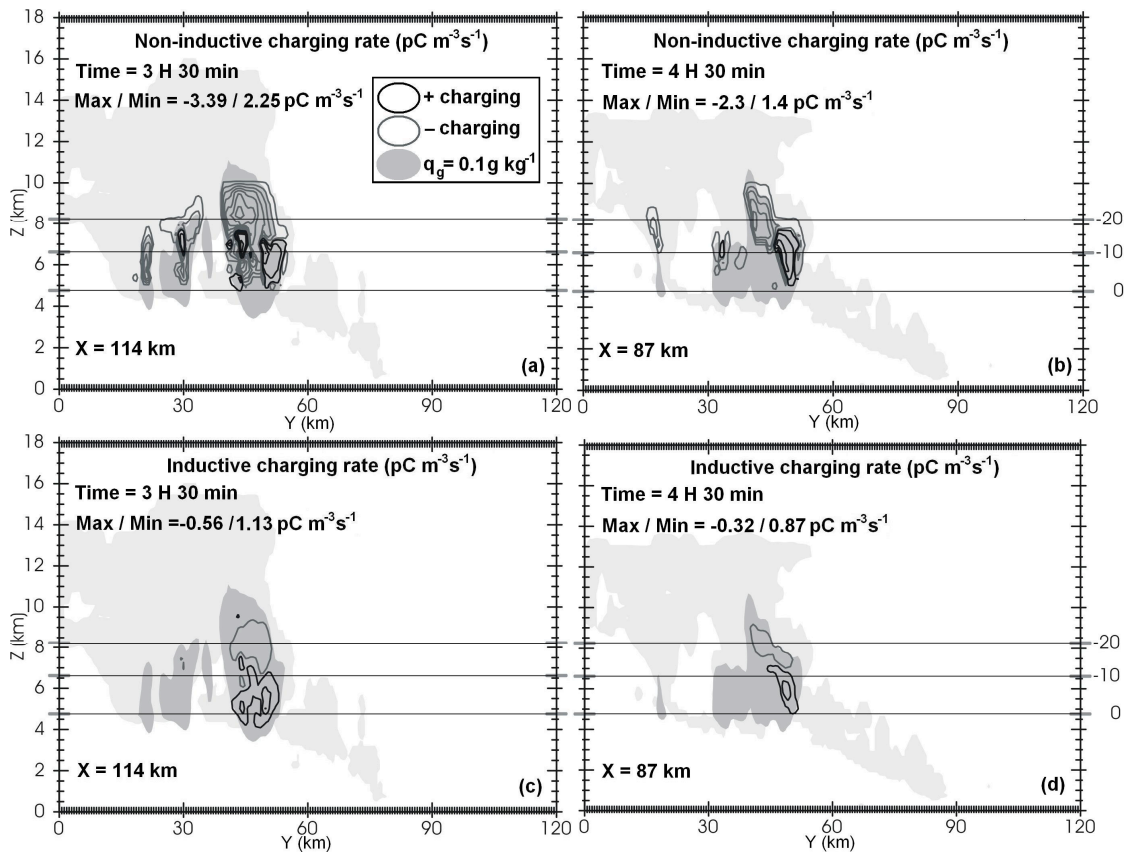


**Fig. A8.** As in Fig. A7, for total (i.e., all ice species) non-inductive charging rate (NICR) at (a)  $t = 3 \text{ h } 30 \text{ min}$  and (b)  $t = 4 \text{ h } 30 \text{ min}$  and for total inductive charging rate at (c)  $t = 3 \text{ h } 30 \text{ min}$  and (d)  $t = 4 \text{ h } 30 \text{ min}$  (in  $\text{pC m}^{-3} \text{ s}^{-1}$ ). The contours start at  $0.1 \text{ pC m}^{-3} \text{ s}^{-1}$  and increase by increments of  $0.5 \text{ pC m}^{-3} \text{ s}^{-1}$ . Contours and shadings are indicated by the legends in panel (a).

It is relevant to note that in general, little or negligible charging occurred in the elevated updraft core located near 10-12 km AGL in the mature zone (Figs. A4 and A8). This is primarily because at these levels, CWC is usually very low ( $\ll 0.1 \text{ g m}^{-3}$ , Figs. A9c-d), which prevents the already little amount of graupel present there (Fig. A5) to separate charge non-inductively (Figs. A8a-b) and inductively (Figs. A8c-d). The positive charge present near 10-12 km AGL (Figs. A7a-b) on ice crystals and snow particles (Figs. A9a-b) originates from lower levels, near the upper layer of the mixed-phase region (i.e.,  $-20 \text{ C}$  isotherm near 8 km AGL), where, after being left with an excess of positive charge during NI collisional charging with graupel (which carries the excess of negative charge, Figs. A8a-b), they were carried upward by the accelerating updraft.

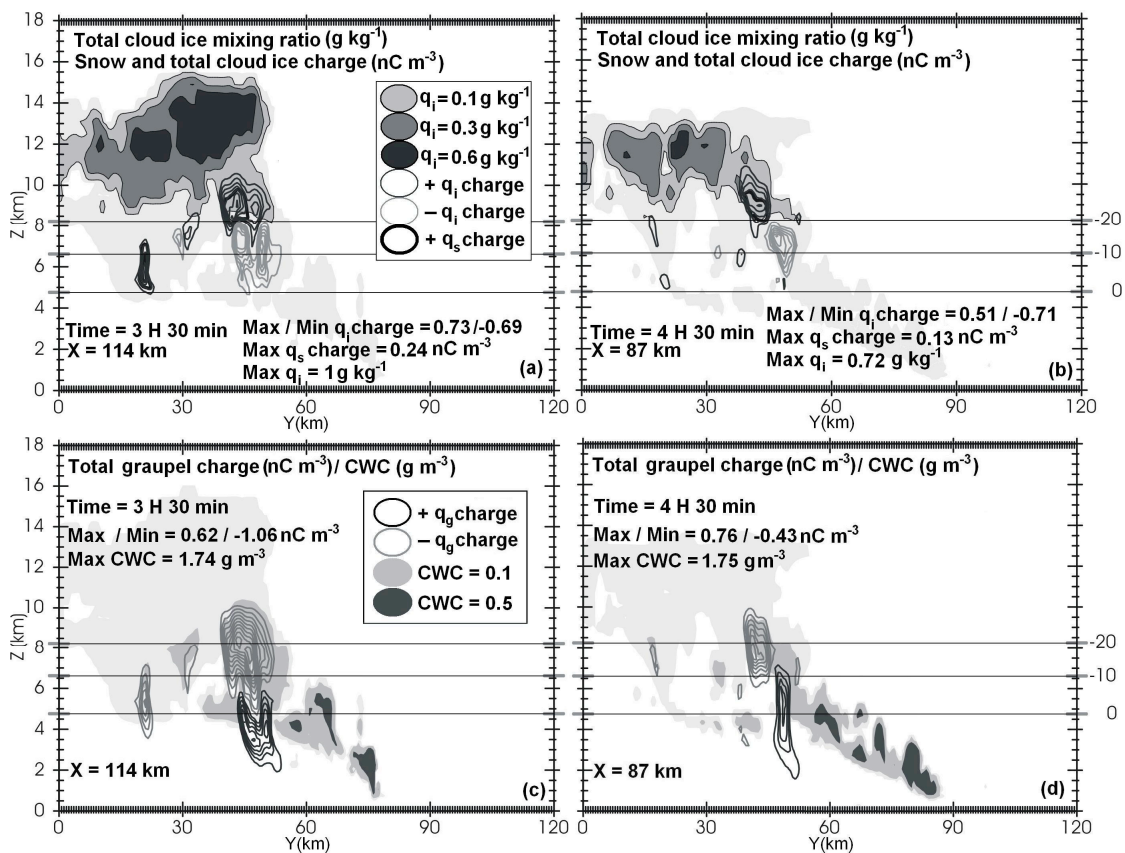


**Fig. A9.** As in Fig. A7, for total cloud ice mixing ratio (i.e., sum of columns, plates and rimed ice particles, in  $\text{g kg}^{-1}$ ), total cloud ice charge and snow particles charge (in  $\text{nC m}^{-3}$ ) at (a)  $t = 3 \text{ h } 30 \text{ min}$  at  $X = 114 \text{ km}$  and (b)  $t = 4 \text{ h } 30 \text{ min}$  at  $X = 87 \text{ km}$ .

Panels (c) and (d) are as in panels (a) and (b) for total graupel charge (i.e., the sum of low, medium and high density graupel species,  $\text{nC m}^{-3}$ ) and cloud water content (CWC, in  $\text{g m}^{-3}$ ). The meaning for contour and shadings are shown in the legends in panels (a) and (c). The cloud ice charge, snow charge and graupel charge are shown by increments of  $0.1 \text{ nC m}^{-3}$  starting at  $0.1 \text{ nC m}^{-3}$ .

In the trailing stratiform region, weak *in situ* NI charging occurred and was confined mainly within the mixed-phase region (e.g., Fig. A8a,  $Y = 20\text{-}30 \text{ km}$ ). This finding is in agreement with the hypotheses from Rutledge and Petersen (1994), who showed that in several Mesoscale Convective Systems (MCS) observed during the DUNDEE (Down Under Doppler and Electricity Experiment, Rutledge et al., 1992) field program, *in situ* NI charging was the process likely responsible for significant electrification in the trailing stratiform region. Additional cross-sections showed that the great majority of the regions of the stratiform cloud having net space charge density magnitude exceeding  $0.03 \text{ nC m}^{-3}$  were almost always coincident with weak (on the order of  $0.1 \text{ pC m}^{-3} \text{ s}^{-1}$ ) *in situ* NI charging. This suggests that *in situ* NI charging is a plausible cause for the majority of the charge present in the trailing stratiform region and that likely, the remaining charge originated further ahead, in the mature zone of the squall line. In continental squall lines, however, Rutledge and MacGorman (1988) and Schuur et al. (1991) proposed that the rearward advection of charged particles from the leading convective region of continental squall lines had a larger role in the origin of charge in the stratiform region. This is probably because in those stronger systems, more charge is separated in the mature zone, which then can be transported rearward. We note that, in general, negative NI charging prevailed in the mixed-phase region of the stratiform region (Figs. A8a-b), because in this region of the storm, the rime accretion rate (RAR) was small (i.e.  $< 1 \text{ g m}^{-2} \text{ s}^{-1}$ , Fig. 5) due to small graupel and CWC ( $< 0.1 \text{ g m}^{-3}$ , Figs. A5

and 10c-d at  $Y = 30$  km). For the same reason, only negligible inductive charging rates (i.e.,  $\ll 0.1 \text{ pC m}^{-3} \text{ s}^{-1}$ , Figs. A8c-d) occurred there. These two factors combined result in a lowest charge region having opposite polarity of charge in the stratiform region (negative) than in the mature zone (positive, Fig. 5). In the stratiform region, the negative charge was mainly on medium and in some areas on high density graupel, while the positive charge was both on ice crystals and snow particles (Fig. A9). Schuur and Rutledge (2000) found that NI charging of non-graupel particles could play a major role in the electrification of stratiform region in thunderstorms. Nonetheless, we found that in general, the simulated magnitudes of NI charging rates involving non-graupel particles collisions (i.e., snow-ice), were overall much smaller, by about 10-100-fold than for graupel-ice or graupel-snow collisions, because differential fall speeds (and therefore RAR) between ice and snow particles are small ( $< 0.1 \text{ m s}^{-1}$ ) and ambient CWC is low ( $\ll 0.1 \text{ g m}^{-3}$ ).

As expected from the charge structure, the majority of the lightning flashes were found in the mature zone (Figs. A7c-d), where most of the charge resides (Figs. A7a-b). The three CG flashes produced by the squall line during the simulation lowered negative charge to ground and were located mainly in the mature zone where the line-averaged 25 dBZ and 30 dBZ echo tops reached their maximum height, mainly between the 0 C and -10 C isotherm without, however, exceeding the -20 C isotherm level (Figs. A3 and Fig. A10). Note that the P99 “weak” forcing squall line case observed by the instruments aboard the R/V *Vickers* research vessel did not produce any CG lightning flash, which is remarkably close to our results. The P99 “strong forcing” tropical squall line case, however, did produce CG lightning flashes that were *only* -CG flashes. These mainly

were clustered just behind the leading edge of the line, where the radar echo tops reached 18 km and where the 30 dBZ echo top extended into the mixed-phase region, consistent with our results. In our simulated squall line, all three  $-CG$  flashes were coincident with storm cells exhibiting a relatively strong ( $0.03\text{-}0.1\text{ nC m}^{-3}$ ) and deep (extending below 2 km AGL) lower positive charge region (Figs. A8a-b). Mansell et al. (2002) showed that the polarity of charge in which a lightning channel propagated, must be opposite to that of the CG flash (compare Figs. A7a and A7c), in order to remove charge and locally reduce the electric field.

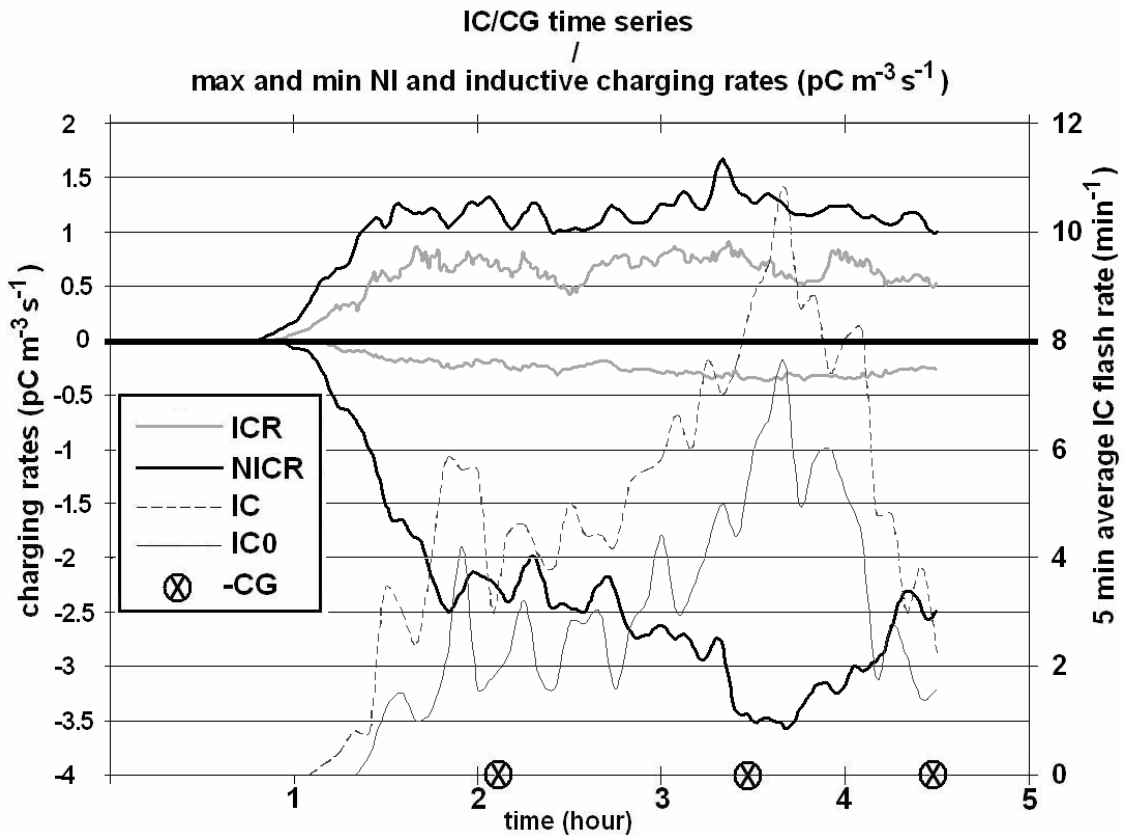


**Fig. A10.** Time series of maximum and minimum non-inductive charging rate (NICR) and inductive charging rate (ICR) overlaid by a time series of CG flash rate and 5-minute average IC flash rate. All time series are for the entire domain. The meaning behind each curve is shown in the legend. The circles filled with a cross indicates the time at which a  $-CG$  flash occurred (note, again, that no  $+CG$  flash was generated in the simulation). The label “IC0” in the legend means it is the 5 min average IC flash rate for the simulation carried out with inductive charging turned off.

The great majority of the IC flashes were also found to occur within these stronger cells in the mature zone having 25-30 dBZ echo tops extending into the layer between the 0 C and -10 C isotherms. These IC flashes were found to initiate at two distinct locations, namely near 8.5 km AGL and roughly at about 5 km AGL (not shown). These two regions coincided with the interface of regions of strong ( $> 0.3 \text{ nC m}^{-3}$ ) net positive charge and strong net negative charges (Figs. A7a-b). In those particular regions of the storm, the magnitude of the electric field is greatest, because the electric field is inversely proportional to the distance separating two elements of charge. Therefore, the electric field will be more likely to exceed the breakdown electric field value required for flash initiation in those regions of the cloud. The great majority of these IC flashes (more than 90%) initiate at upper levels, near 8.5 km AGL (e.g., Fig.A7a), because the breakeven electric field decreases exponentially with height, making initiation more likely at upper levels compared to lower levels for the same electric field magnitude. When inductive charging was turned off, no CG flashes were generated by the squall line and the total number of IC flashes decreased (Fig. A10) by about 43% (total of 1050 flashes compared to 603 flashes). Despite this large reduction in total flashes, the simulated total lightning rate (particularly IC flash rate) was still larger than observed. The midlevel and particularly the lowest level charge regions were weaker, so lightning was less likely to initiate at the interface located at 5 km AGL, resulting to a dearth of CG flashes there. In the same time, fewer IC flashes occurred at the upper interface (at 8.5 km) due to weaker midlevel charge region, causing the total IC flash rate of the system to decrease.

In the model, the production rate of IC flashes was directly related to the magnitude of the negative NI charging rate (Fig. A10), which was, as expected, directly related to the total volume of graupel (Fig. A8), particularly within the mixed-phase region. In our simulations with this model, the magnitude of the (stronger) main midlevel charge region (and in turn of the upper level charge region) was always controlled by the NI charging rate, which is proportional to the graupel volume within the mixed-phase region (as in Carey and Rutledge, 2000; Wiens et al. 2005. Compare figs. A6 and A10). Overall, the total mean IC flash rate during a 5 min time interval rarely exceeded 10 flashes per minute. When inductive charging was turned off, the mean IC flash rate did not exceed 8 flashes per minute (Fig. A10). However, these IC flash rates were still greater than observed: Only 1 IC transient was observed by the field mill aboard the R/V *Vickers* and no lightning was seen by eye (P99, system evolved at nighttime). Nevertheless, using the same numerical model and the SP98 NI charging scheme, these average IC flash rates remain well below the IC flash rates simulated in continental supercells by as much as a factor 10 (Fierro et al. 2006, Kuhlman et al. 2006) and by as much as a factor 50 for simulated hurricanes (see section V.3.2).

Generally, little lightning occurred or propagated into the trailing stratiform region, because the charge densities there were usually small (i.e., on the order of  $0.01 \text{ nC m}^{-3}$ , Figs. A7a-b). Sufficient NI charging (i.e.,  $> 0.1 \text{ pC m}^{-3} \text{ s}^{-1}$ ) did occur in some discrete regions of the stratiform region after 3 h, which resulted in the formation of a local normal dipole charge structure (positive charge atop a negative charge region, not shown). In those particular discrete regions of the stratiform region, a few flashes were able to initiate, resulting in positive leader propagation into the lower negative charge

region of this dipole. Most of these positive leaders were found below 3 km AGL without, however, reaching the ground (not shown). Horizontal cross-sections of positive and negative leaders across the level of the lowest charge regions, at 4.5 km AGL, showed evidence of a “bipolar” lightning pattern (Fig. A11), which has been documented by many investigators for mid-latitude continental MCSs and squall lines (e.g., Orville et al., 1988; Rutledge and MacGorman, 1988).

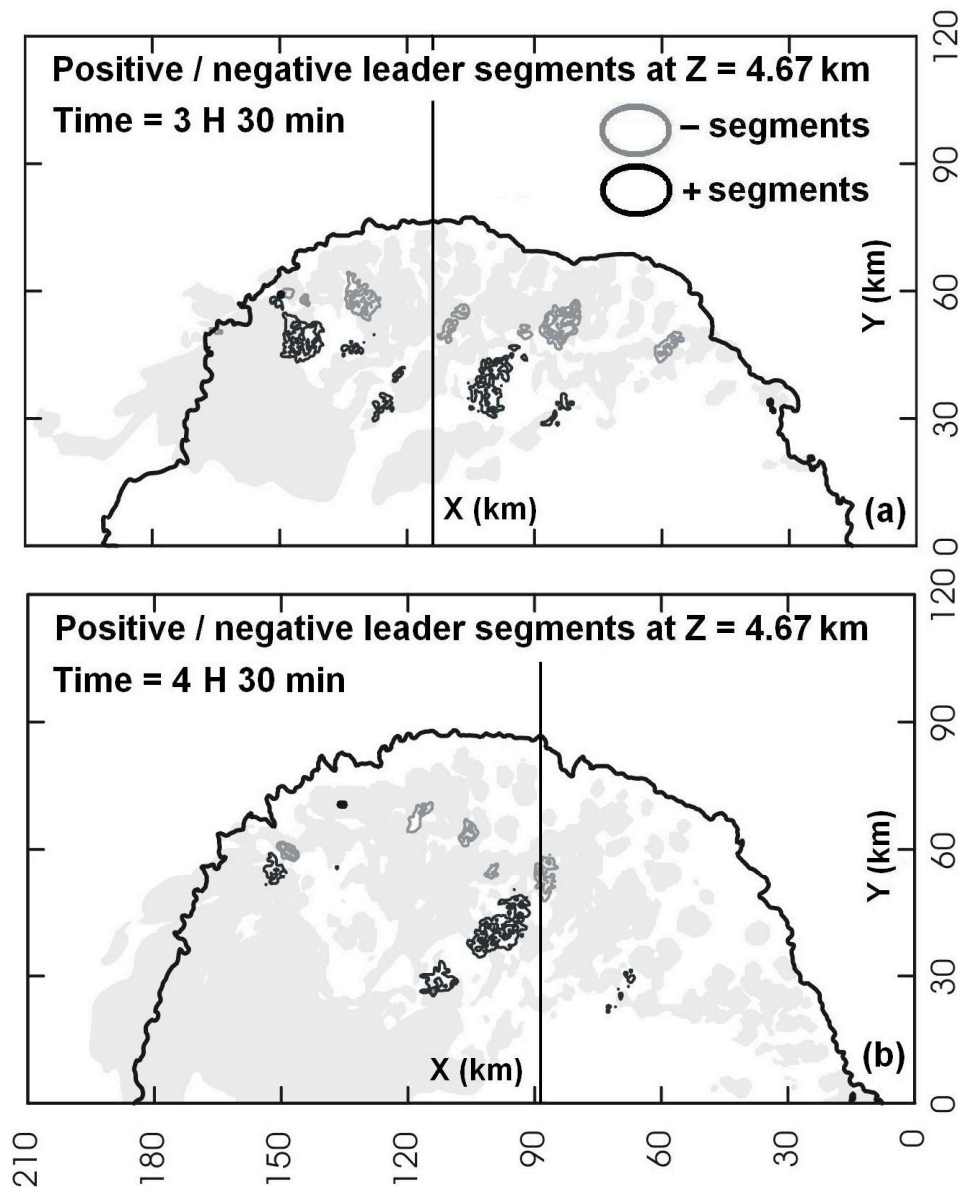


**Fig. A11.** Horizontal cross sections of positive and negative leaders segments as  $z = 4.67$  km AGL at (a)  $t = 3$  h 30 min and (b)  $t = 4$  h 30 min. The thick black curves line showed the location of the gust front ( $-1$  K perturbation temperature). The light grey shaded area shows cloud mixing ratio of  $0.01 \text{ g kg}^{-1}$ , and the horizontal black line shows the location of the vertical cross sections of Figs. A7-A9. Legends for leaders are as in Figs. 8c-d.

In the simulation, most (i.e.,  $> 90\%$ ) of the lightning leaders in the stratiform region at low levels (near 4.5 km AGL) were positive, while in the mature zone these leaders were mostly negative (Fig. A11). This bipolar lightning pattern was reversed at midlevels near 7 km AGL, with positive channels propagating in the mature zone (Figs. A7c-d) and negative channels propagating into more discrete regions within the stratiform region (not shown). This was concordant with a midlevel negative charge region present in the mature zone (Figs. A7a-b) and with, locally, a midlevel positive charge region in the trailing stratiform region.

## VII.4 Conclusions

The simulated squall line exhibited many features that were consistent with the squall line observations made on 9 February 1993. In particular, the updraft speeds across the line seldom exceeded  $10 \text{ m s}^{-1}$ , in turn resulting in relatively shallow 30 dBZ echo tops which rarely exceeded the top of the mixed-phase layer (i.e.,  $-20^\circ\text{C}$  isotherm). The maximum line-averaged updraft speeds were found mainly in two regions; immediately behind the gust front, below 2 km AGL, and in the upper levels near 10 km AGL, in the mature zone, where isolated convective cells exhibited deeper 25-30 dBZ echo tops (sometimes reaching the  $-15^\circ\text{C}$  isotherm) and the taller cloud tops (about 14-16 km). The

elevated updraft cores near the troposphere in the mature zone were likely caused by water unloading at low levels (< 4 km AGL) right behind the gust front and also because these positively buoyant air parcels were able to move away from behind the gust front, which generally features a downward-directed pressure force which inhibits updraft cores development.

Enhanced warm rain processes caused most of the liquid water (LW) to precipitate at the leading edge of the line below 4 km AGL, resulting in rapid depletion of LW, particularly above the freezing level towards the rear of the line. This accounted for the small amount of supercooled water and graupel pellets present above the melting level. Consistent with this, the total lightning activity across the line generally was small compared with continental tropical systems, with IC flash rates rarely exceeding 10 flashes per minute. However, these flash rates were still much greater than inferred in the observed case (1 IC flash within the range of the field mill that was aboard the R/V *Vickers* and no lightning seen by eye). When inductive charging was turned off, no CG flashes were produced and the total number of IC flashes decreased by 43 %, which was still more lightning than observed.

In general, the cells having the largest total flash rate (the sum of all IC and CG flashes) were those characterized by deeper 30 dBZ echo tops in the mature zones. For the charge regions involved in lightning, the general charge structure in these cells resembled a normal tripole. We found that NI charging was the main mechanism responsible for the formation of the mid-level negative charge region and the upper positive charge region of this tripole. The lower positive charge region of this tripole, located below 5 km AGL, was attributed to both inductive and NI charging. Most of the

negative charge residing at midlevels was on low and medium density graupel, while the positive charge at upper levels (i.e., above 8 km AGL) was mainly carried by cloud ice particles (columns, plates and rimed) with a small amount ( $< 30\%$ ) of this charge carried by snow particles. At low-levels, on the other hand, heavier particles carried the great majority of the (positive) charge, namely, medium and high density graupel pellets, with a negligible ( $< 5\%$ ) contribution from small hail stones. This normal tripole charge structure within these cells was in turn consistent with the production of (only three) –CG flashes there.

As the convective cells present in the mature zone aged and became largely glaciated, they formed a trailing stratiform region, composed mainly of lighter ice crystals and snow particles, with a few discrete regions having small total graupel mixing ratio of about  $0.1\text{-}0.3 \text{ g kg}^{-1}$ . This region of the storm was characterized by weak vertical velocities ( $< 1 \text{ m s}^{-1}$ ) and by small reflectivity values at all levels ( $< 30 \text{ dBZ}$ ). Therefore, little charge separation, and thus lightning activity, occurred in this region of the storm. Consistent with previous hypotheses, we found that *in situ* NI charging mechanism is a plausible source for the generation of the majority of the charge present in the stratiform region. The remainder of the charge likely originated from the storm cells in mature zones that exhibited sufficiently strong updraft speeds near the melting level to carry moderate amounts of graupel (i.e.  $> 0.5 \text{ g kg}^{-1}$ ) in the mixed-phase region. NI charging in the stratiform cloud always occurred within those discrete regions exhibiting small graupel mixing ratios ( $\sim 0.1\text{-}0.3 \text{ g kg}^{-1}$ ). The negative charge there was mainly on medium and high density graupel, while both cloud ice and snow particles carried most ( $> 90\%$ ) of the positive charge gained non-inductively.

A bipolar lightning pattern was found in our simulated squall line at low levels (4.5 km AGL ) across the lowest charge regions, and at midlevels (7 km) across the midlevel charge region. At low levels, the great majority (> 90%) of the lightning leaders were positive in the stratiform region and negative in the mature zone. The opposite lightning polarity pattern was present at midlevels with negative (positive) leaders mainly found in the stratiform (mature) zone. Because lightning channels in the model always propagate into a region of opposite polarity of charge, we found a reversed bipolar pattern in the charge polarity at mid and low levels. In the stratiform (mature) zone the charge polarity changed from negative (positive) at low levels to positive (negative) at midlevels. This resulted in a normal dipole in some discrete regions of the stratiform regions, and a more consistent, tripole charge structure in the mature zone.

## VIII. References

Aberson, B. D., M. T. Montgomery, M. Bell and M. Black, 2003: Hurricane Isabel (2003): New Insights into the Physics of Intense Storms. Part II: Extreme Localized Wind. *Bull. Amer. Meteor. Soc.*, **187**, 1349-1354.

Anderson, J. R., K. K. Droegemeier and R. B. Wilhelmson, 1985: Simulation of the thunderstorm subcloud environment. Preprints, *14th Conference on Severe Local Storms, American Meteorological Society*, Indianapolis, IN, 147-150.

Avila, E. E., R. G. Pereyra, G. G. A. Varela, and G. M. Caranti, 1999: The effect of the cloud-droplet spectrum on electrical-charge transfer during individual ice-ice collisions, *Q. J. R. Meteor. Soc.*, **125**, 1669–1679.

Baker, M. B., E. R. Jayaratne, J. Latham, and C. P. R. Saunders, 1987: The influence of diffusional growth rates on the charges transfer accompanying rebounding collisions between ice crystals and soft hailstones. *Quart. J. Roy. Meteor. Soc.*, **113**, 1193–1215.

Bansmer A. R., A. J. Heymsfield and P. T. Willis, 2002: *In situ* measurements of particle size distributions in Hurricane Humberto. Preprints, *25th Conference on Hurricanes and Tropical Meteorology, American Meteorological Society*, San Diego, CA, 4 pp.

Bedrick M. and W. Burgett, 1999: A tropical oceanic cloud-to-ground lightning study. Preprints, *23rd Conference on Hurricanes and Tropical Meteorology, American Meteorological Society*, Dallas, TX, 243-245.

Bell M. M., M. T. Montgomery, M. L. Black and S. D. Aberson, 2004: Observed vortex and thermodynamic structure of hurricane Isabel at maximum intensity. Preprints, *26th Conference on Hurricanes and Tropical Meteorology, American Meteorological Society*, Miami, FL, 2 pp.

Bender, M., R. Tuleya, and Y. Kurihara, 1987: A numerical study of the effect of island terrain on tropical cyclones. *Mon. Wea. Rev.*, **115**, 130-155.

Biggerstaff, M.I., and R.A. Houze, Jr., 1991: Kinematic and precipitation structure of the 10-11 June 1985 squall line. *Mon. Wea. Rev.*, **119**, 3034-3065.

Bister M. and K. A. Emanuel, 1998: Dissipative heating and hurricane intensity. *Meteor. Atmos. Phys.*, **65**, 233–240.

Black, R. A., 1984: Distribution of particles types above 6.0 km in two Atlantic hurricanes. Preprints, *16th Conference on Hurricanes and Tropical Meteorology, American Meteorological Society*, San Diego, CA, 537-541.

Black, P. G., and G. J. Holland, 1995: The Boundary Layer of Tropical Cyclone Kerry (1979). *Mon. Wea. Rev.*, **123**, 2007–2028.

Black, R.A., Hallett, J. 1986: Observations of the distribution of ice in hurricanes. *J. Atmos. Sci.*, **43**, 802–822.

Black, P. G., R. A. Black, J. Hallett, and W. A. Lyons, 1986: Electrical activity of the hurricane. Preprints, *23d Conf. on Radar Meteorology, American Meteorological Society*, Snowmass, CO, J277–J280.

Black, R. A. and J. Hallett, 1990: Electric field and microphysical measurements in vigorous hurricane eyewalls. Preprints, Preprints, *Conference on Cloud Physics, American Meteorological Society*, San Francisco, CA, 662-665.

Black, R. A., J. Hallett, and C. P. R. Saunders, 1993: Aircraft studies of precipitation and electrification in hurricanes. Preprints, *17'th Conference on Severe Local Storms and Conference on Atmospheric Electricity, American Meteorological Society*, St. Louis, MO, J20-J25.

Black, R. A., H. B. Bluestein and M. L. Black. 1994: Unusually strong vertical motions in a caribbean hurricane. *Mon. Wea. Rev.*, **122**, 2722–2739.

Black RA, Hallett J, Willis P (1995) Aircraft measurements of ice and electrical evolution in regions of vertical shear in convective cloud. 21<sup>st</sup> General Assembly of IUGG, Boulder, Colorado.

Black, M. L., R. W. Burpee and F. D. Marks 1996: Vertical motion characteristics of tropical cyclones determined with airborne doppler radial velocities. *J. Atmos. Sci.*, **53**, 1887–1909.

Black, R. A. and J. Hallett, June 1999: Electrification of the hurricane. *J. Atmos Sci*, **56**, 2004-2028.

Black, R. A. and G. M. Heymsfield and J. Hallett, 2003: Extra large particle image at 12 km in a hurricane eyewall: Evidence of high altitude supercooled water ?. *Geophys. Res. Lett.*, **30**, NO 21, 2124, doi:10.1029/2003GL017864.

Blakslee R. J., D. M. Mach, M. G. Bateman and J. F. Bailey, 2006: Electric field and lightning observations in the core of category 4 Hurricane Emily. *Poster, Conference on Meteorological Application of Lightning Data, American meteorological society, Atlanta, GA*, P2.13.

Blackwell, K. G., 2000: The evolution of hurricane Danny (1997) at landfall: Doppler-observed eyewall replacement, vortex contraction/intensification and low-level wind maxima. *Mon. Wea. Rev.*, **128**, 4002-4016.

Boccippio D. J., Kenneth L. Cummins, H. J. Christian and S. J. Goodman. 2001: Combined Satellite- and Surface-Based Estimation of the Intracloud–Cloud-to-Ground Lightning Ratio over the Continental United States. *Mon. Wea. Rev.*, **129**, 108–122.

Brandes E. A., G. Zhang, and J. Vivekanandan, 2004a: Drop size distribution retrieval with polarimetric radar: Model and application. *J. Appl. Meteor.*, **43**, 461–475

Brandes E. A., G. Zhang, and J. Vivekanandan, 2004b: Comparison of polarimetric radar drop size distribution retrieval algorithms. *J. Atmos. Oceanic Technol.*, **21**, 584–598

Braun S. A., 2002: A Cloud-Resolving Simulation of Hurricane Bob (1991): Storm structure and eyewall buoyancy. *Mon. Wea. Rev.*, **130**, 1573–1592.

Bringi V. N., G.-J. Huang, V. Chandrasekar, and E. Gorgucci, 2002: A methodology for estimating the parameters of a gamma raindrop size distribution model from polarimetric radar data: Application to a squall-line event from the TRMM/Brazil campaign. *J. Atmos. Oceanic Technol.*, **19**, 633–645.

Bryan, G. H., and M. J. Fritsch, 2002: A benchmark simulation. for moist nonhydrostatic numerical models. *Mon. Wea. Rev.*, **130**. 2917–2928.

Bryan, G. H., J. C. Wyngaard and J. M. Fritsch. 2003: Resolution requirements for the simulation of deep moist convection. *Mon. Wea. Rev.*, **131**, 2394–2416.

Bryan, G. H., and R. Rotunno, 2005: Statistical convergence in simulated moist absolutely unstable layers. *Preprints, 11th Conf. on Mesoscale Processes, American Meteorological Society*, Albuquerque, CD-ROM, 1M.6.

Bryan, G. H., 2006: The dynamics of the trailing stratiform region of squall lines: Presentation at North Carolina State University, Raleigh, NC: 16 October 2006

Camp J. P., and M. T. Montgomery, 2000: Hurricane maximum intensity: past and present. . Preprints, *24th Conference on Hurricanes and Tropical Meteorology, American Meteorological Society*, Ft. Lauderdale, FL, 230-231.

Carey, L. D. and S. A. Rutledge, 1998: Electrical and multiparameter radar observations of a severe hailstorm. *J. Geophys. Res.*, **103**, 13979-14000.

Carey, L.D., and S.A. Rutledge, 2000: The Relationship between Precipitation and Lightning in Tropical Island Convection: A C-Band Polarimetric Radar Study. *Mon. Wea. Rev.*, **128**, 2687–2710.

Carpenter, R. L., K. K. Droegemeier, and A. M. Blyth, 1998: Entrainment and detrainment in numerically simulated cumulus congestus clouds. Part I: general results. *J. Atmos. Sci.*, **55**, 3417-3432.

Cecil, D. J. and E. J. Zipser, 1999: Relationships between Tropical Cyclone Intensity and Satellite-Based Indicators of Inner Core Convection: 85-GHz Ice-Scattering Signature and Lightning. *Mon. Wea. Rev.*, **127**, 103–123.

Cecil, D. J., E. J. Zipser, and S. W. Nesbitt, 2002a: Reflectivity, ice scattering, and lightning characteristics of hurricane eyewalls and rainbands. Part I: quantitative description. *Mon. Wea. Rev.*, **130**, 769-784.

Cecil, D. J., E. J. Zipser, 2002b: Reflectivity, ice scattering, and lightning characteristics of hurricane eyewalls and rainbands. Part II: intercomparison of observations. *Mon. Wea. Rev.*, **130**, 785-801.

Chan J. C. L., 1982: On the physical processes responsible for tropical cyclone motion. Department of Atmospheric Science Pap. 358, Colorado State University, 200 pp.

Chan, J. C. L., F. M. F. Ko and Y. M. Lei, 2002: Relationship between potential vorticity tendency and tropical cyclone motion. *J. Atmos. Sci.*, **59**, 1317-1336.

Chan, J. C. L., and X. Liang, 2003: Convective asymmetries associated with tropical cyclone landfall. Part I: *f*-plane simulations. *J. Atmos. Sci.*, **60**, 1560-1576.

Chang, S.W., 1982: The orographic effects induced by an island mountain range on propagating tropical cyclones. *Mon. Wea. Rev.*, **110**, 1255-1270.

Chang, C.-P., T.-C. Yeh, and J.M. Chen, 1993: Effects of Terrain on the Surface Structure of Typhoons over Taiwan. *Mon. Wea. Rev.*, **121**, 734-752

Chao W. C., Chen B., and Wei-Kuo, 2002: Sensitivities of modeled tropical cyclones to surface friction and the Coriolis parameter. Preprints, *25th Conference on Hurricanes and Tropical Meteorology, American Meteorological Society*, San Diego, CA, 2 pp.

Cheng H. J., Wu C. C. and Y. Wang, 2004: The eyewall evolution and intensity change in a landfalling typhoon. Preprints, *26th Conference on Hurricanes and Tropical Meteorology, American Meteorological Society*, Miami, FL, 451-452.

Chiu, C.-S 1978: Numerical study of cloud electrification in an axisymmetric, time-dependent cloud model. *J. Geophys. Res.*, **81**, 5025–5049.

Chorin, A. J., 1967: A numerical method for solving incompressible viscous problems. *J. Comput. Phys.*, **2**, 12-26.

Chronis T. and Anagnostou E., 2006a (*in press*): Evaluation of a Long-Range Lightning Detection Network with Receivers in Europe and Africa, *IEEE Transaction on Geosciences and Remote Sensing*.

Chronis T., Williams E., Anagnostou E. and W. A Petersen, 2006b (*to be submitted*): Lightning as an indicator of tropical cyclogenesis in African easterly waves.

Corbosiero K. L., 1999: Lightning in hurricanes. Preprints, *23th Conference on Hurricanes and Tropical Meteorology, American Meteorological Society*, Dallas, TX, 66-67.

Cotton W.R. and R.A. Anthes, 1989: Storm and Cloud Dynamics, *Academic Press*, 883 pp.

Curry J. A., Webster P. J., and G. J. Holland, 2006: Mixing politics and science in testing the hypothesis that greenhouse warming is causing a global increase in hurricane intensity. *Bull. Amer. Meteor. Soc.*, **87**, 1025-1037.

Deardroff, J. W., 1980: Stratocumulus-capped mixed layers derived from a three-dimensional model. *Bound.-Layer Meteor.* **18**, 495-527.

DeMaria, M., 1996: The effect of vertical shear on tropical cyclone intensity change. *J. Atmos. Sci.*, **53**, 2076–2087.

Demetriades, N.W.S., and R.L. Holle, 2005: Long-range lightning applications for hurricane intensity and precipitation nowcasting. *Preprints, Conference on Meteorological Application of Lightning Data, American Meteorological Society, San Diego, CA, 9 pp.*

Demetriades, N.W.S., and R.L. Holle, 2006: Long-range lightning nowcasting applications for tropical cyclones. *Conference on Meteorological Application of Lightning Data, American Meteorological Society, Atlanta, GA, 9 pp.*

Dudhia, J., 1989: Numerical study of convection observed during the winter monsoon experiment using a mesoscale two-dimensional model. *J. Atmos. Sci.*, **46**, 3077–3107.

Emanuel, K. A., 1986: An air-sea interaction theory for tropical cyclone. Part I: steady state maintenance. *J. Atmos. Sci.*, **43**, 585-604.

Emanuel, K. A., 1988: The maximum intensity of hurricanes. *J. Atmos. Sci.*, **45**, 1143-1155.

Emanuel, K. A., 1991: The theory of hurricanes. *Annu. Rev. Fluid. Mech.*, **23**, 179-196.

Emanuel, K. A., 2004: Tropical Cyclone Energetics and Structure. Program in Atmospheres, Oceans, and Climate Massachusetts Institute of Technology

Emanuel, K. A., 2005: Increasing destructiveness of tropical cyclones over the past 30 years. *Nature*, **436**, 686-688.

Elsberry, R. L., 1987: Tropical cyclone motion. Chapter 4, A Global View of Tropical Cyclones, Office of Naval Research, 91-131.

Farfan, L. M., and J. A. Zehnder, 2001: An analysis of the landfall of Hurricane Nora (1997) *Mon. Wea. Rev.* **129**, 2073-2088.

Fletcher, N. H., 1962: The physics of rain clouds. *Cambridge University Press*, 390 pp.

Fiorino, M., and R. L. Elsberry, 1989: Some aspects of vortex structure related to tropical cyclone motion. *J. Atmos. Sci.*, **46**, 975–990.

Fierro, A. O., M. S. Gilmore, E. R. Mansell, L. J. Wicker, J. M. Straka, and E. N. Rasmussen, 2006: Electrification and lightning in an idealized boundary-crossing supercell simulation of 2 June 1995. *Mon. Wea. Rev.*, **134**, 3149–3172.

Fovell R., D. Durran and J. R. Holton, 1992: Numerical simulations of convectively generated stratospheric gravity waves. *J. Atmos. Sci.*, **49**, 1427–1442.

Frank W. M. and E. A. Ritchie, 1999: Environmental effects on hurricane core structure. Preprints, *23<sup>rd</sup> Conference on Hurricanes and Tropical Meteorology*, American Meteorological Society, Dallas, TX, 680-681.

Frank, W. M., and P. E. Roundy, 2006: The relationship between tropical waves and tropical cyclogenesis. *Mon. Wea. Rev.*, **134**, 2397-2417.

Franklin J. L., R. J. Pasch, L. A. Avila, J. L. Beven II, M. B. Lawrence, S. R. Stewart, and E. S. Blake, 2006: Atlantic Hurricane Season of 2004. *Mon. Wea. Rev.*, **134**, 981–1025.

Fujita, T. T., 1971: A proposed characterization of tornadoes and hurricanes by area and intensity. SMRP Paper 91, 42 pp., Univ. of Chicago.

Gallacher, P. C., R. Rotunno, and K. A. Emanuel, 1989: Tropical cyclogenesis in a coupled ocean–atmosphere model. Preprints, *18th Conference on Hurricanes and Tropical Meteorology*, American Meteorological Society, San Diego, CA, 121–122

Gardiner, B., D. Lamb, R. L. Pitter, J. Hallet, and C. P. R. Saunders, 1985: Measurements of initial potential gradient and particles charges in a Montana thunderstorm, *J. Geophys. Res.*, **90**, 6079–6086.

Geerts, B., G. Heymsfield, L. Tian, and J. Halverson, 2000: Hurricane George Landfall in the Dominican Republic: Detailed Airborne Doppler Radar Imagery, *Bull. Amer. Meteor. Soc.*, **81**(5), 999-1018.

Geizler, D. A. and J.A. Zehnder, 2000: Barotropic vortex motion near large-scale mountain ranges: Case studies of Hurricane Gilbert (1988) and Tropical Storm Hermine (1980). *Met.Atmos.Phys.* **73**, 61-76.

George, J. E., and W. M. Gray, 1976: Tropical cyclone motion and surrounding parameter relationships. *J. Appl. Meteor.*, **15**, 1252-1264.

Giaiotti D., E. Giancesini, and F. Stel, 2001: Heuristic considerations pertaining to hailstone size distributions in the plain of Friuli-Venezia Giulia. *Atmos. Res.*, **57**, 269–288.

Gilmore M. S., J. M. Straka and E. N. Rasmussen. 2004a: Precipitation uncertainty due to variations in precipitation particle parameters within a simple microphysics scheme. *Mon. Wea Rev.*, **132**, 2610–2627.

Ginis I., Moon J., B. Thomas and T. Hara, 2004: Effect of ocean breaking waves on air-sea momentum fluxes and hurricane intensity. Preprints, *26th Conference on Hurricanes and Tropical Meteorology, American Meteorological Society*, Miami, FL, 2 pp.

Goodman, S.J., and D. R. MacGorman, 1986: Cloud-to-ground lightning activity in mesoscale convective complexes. *Mon. Wea. Rev.*, **114**, 2320–2328.

Gray, W.M., 1968: Global view of the origin of tropical disturbances and storms. *Mon. Wea. Rev.*, **96**, 669-697.

Gray, W. M, 1995: Tropical cyclones. Colorado State University, *Report, World Meteorological Society*, 163 pp.

Gray, W. M., 1997: The tropical cyclone maximum potential intensity (MPI). Preprints, *22nd Conference on Hurricanes and Tropical Meteorology, American Meteorological Society*, Ft. Collins, CO, 288-289.

Gray, W.M., 1998: The formation of tropical cyclones. *Meteor. Atmos. Phys.* **67**, 37-69.

Halverson J, Azofeifa PL, Black M, Braun S, Cecil D, Goodman M, Heymsfield A, Heymsfield G, Hood R, Krishnamurti T, McFarquhar G, Molinari J, Rogers R, Turk J, Velden C, Zhang DL, Zipser E, Kakar R (2006) NASA's Tropical Cloud Systems and Processes (TCSP) Experiment: Investigating Tropical Cyclogenesis and Hurricane Intensity Change. Submitted to Bull Amer Meteor Soc.

Hanley D. E., 1999: The effect of trough interactions on tropical cyclone intensity change. Preprints, 23<sup>rd</sup> Conference on Hurricanes and Tropical Meteorology, American Meteorological Society, Dallas, TX, 987-988.

Hawkins, H. F., and D. T. Rubsam, 1968: Hurricane Hilda, 1964, II. Structure and budgets of the hurricane on October 1 1964. *Mon. Wea. Rev.*, **96**, 617–636.

Helsdon, J. H., Jr., 1980: Chaff seeding effects in a dynamical-electrical cloud model. *J. Appl. Meteor.*, **19**, 1101-1125.

Helsdon, J.H., 1980: Chaff Seeding Effects in a Dynamical-Electrical Cloud Model. *J. Appl. Meteor.*, **19**, 1101–1125.

Helsdon, J. H., Jr., W. A. Wojcik, and R. D. Farley, 2001: An examination of thunderstorm-charging mechanisms using a two-dimensional storm electrification model. *J. Geophys. Res.*, 106, 1165–1192.

Henshaw W. D. and H.-O. Kreiss, 1995: Analysis of a difference approximation for the incompressible Navier-Stokes equations. Research Report LA--UR--95--3536, Los Alamos National Laboratory.

Heymsfield GM., Bidwell S, Caylor IJ, Ameen S, Nicholson S, Boncyk W, Miller L, Vandemark D, Racette PE, Dod LR (1996) The EDOP radar system on the high-altitude NASA ER-2 aircraft. *J Atmos Oceanic Tech* 13: 795-809.

Holland, G.J., 1993: "Ready Reckoner" - Chapter 9, Global Guide to Tropical Cyclone Forecasting, WMO/TC-No. 560, Report No. TCP-31, World Meteorological Organization; Geneva, Switzerland.

Holle, A. I. Watson, R. E. López, D. R. MacGorman, R. Ortiz, and W. D. Otto, 1994: The life cycle of lightning and severe weather in a 3–4 June 1985 PRE-STORM mesoscale convective system. *Mon. Wea. Rev.*, **122**, 1798–1808.

Hoyos, C.D., Agudelo, P.A., Webster, P.J. and J.A. Curry, 2006: Deconvolution of the factors contributing to the increase in global hurricane intensity. *Science*, **312**, 94-97.

Johnson R. L. and S. J. Goodman, 1984: Atmospheric electrical activity associated with hurricane Alicia. Preprints. *7th International Conference on Atmospheric Electricity, American Meteorological Society*, Albany, NY, 295-298.

Jones, R. W., 1987: Simulation of hurricane landfall with a numerical model featuring latent heating by the resolvable scales. *Mon. Wea. Rev.*, **115**, 2279-2297.

Jones S. C. and E. A. Ritchie, 2002: The development of asymmetric vertical motion in idealized tropical cyclones under the influence of vertical shear. Preprints, *25th Conference on Hurricanes and Tropical Meteorology, American Meteorological Society, San Diego, CA*, 2 pp.

Jordan, C. L., 1961: Marked changes in the characteristics of the eye of intense typhoons between the deepening and filling stages. *J. Meteor.*, **18**, 779–789.

Jorgensen, D. P., E. J. Zipser, and M. A. LeMone, 1985: Vertical motions in intense hurricanes. *J. Atmos. Sci.*, **42**, 839–856.

Jorgensen, D., and M. LeMone, 1989: Vertical velocity characteristics of oceanic convection. *J. Atmos. Sci.*, **46**, 621–640.

Kakar, R, M. Goodman, R. Hood, A. Guillory, 2006: Overview of the Convection And Moisture Experiment, *J. Atmos. Sci.*, **63**, 5-18

Kanak, K.M., 1990: Three-dimensional, non-hydrostatic, numerical simulation of a developing tropical cyclone. M.S. Thesis, University of Wisconsin, 130 pp.

Kelley, O. A., J. Stout, and J. B. Halverson, 2004: Tall precipitation cells in tropical cyclone eyewalls are associated with tropical cyclone intensification. *Geophys. Res. Lett.*, **31**, L24112-L24115.

Kessler, E., 1969: *On the Distribution and Continuity of Water Substance in Atmospheric Circulation. Meteor. Monogr.*, No. 32, Amer. Meteor. Soc., 84 pp.

Kim, J.-H., C.-H. Ho, and C.-H. Sui, 2005: Circulation features associated with the record-breaking typhoon landfall on Japan in 2004, *Geophys. Res. Lett.*, **32**, L14713, doi:10.1029/2005GL022494.

Kimball, S. A., 2004: A modeling study of the sensitivity of landfalling hurricanes to surface evaporation and surface roughness. Preprints, *26th Conference on Hurricanes and Tropical Meteorology, American Meteorological Society*, Miami, FL, 2 pp.

Knabb R. D., Rhome J. R., and D. P. Brown, 2005: Tropical Cyclone Report. Hurricane Katrina. 23-30 August 2005. National Hurricane Center (NOAA), Miami, USA.

Knaff J. A. and R. M. Zehr, 1999: Convective asymmetries in mature tropical cyclones associated with motion and vertical shear. Preprints, *23th Conference on Hurricanes and Tropical Meteorology, American Meteorological Society*, Dallas, TX, 464-467.

Kong J. and S. T. Soong, 1997: A numerical study of orographic effects on typhoons. Preprints, *22nd Conference on Hurricanes and Tropical Meteorology, American meteorological society*, Ft. Collins, CO, 246-247.

Kossin J. P., W. H. Schubert, C. Velden, M. Black, P. Black, R. Zehr, S. Aberson and J. Dunion, 2004: Mesovortices in hurricane Isabel (2003). Preprints, *26th Conference on Hurricanes and Tropical Meteorology, American Meteorological Society*, Miami, FL, 2 pp.

Kuhlman, K.M., C.L. Ziegler, E.R. Mansell, D.R. MacGorman, and J.M. Straka, 2006: Numerically Simulated Electrification and Lightning of the 29 June 2000 STEPS Supercell Storm. *Mon. Wea. Rev.*, **134**, 2734–2757.

Landsea, C.W. 2005. Hurricanes and global warming. *Nature* 438 (22 December 2005) doi:10.1038/nature04477.

Lang T. J., Rutledge S.A., 2002: Relationships between convective storm kinematics, precipitation, and lightning. *Mon. Wea. Rev.*, **130**, 2492–2506.

Lawrence M. B. and H. D. Cobb, 2005: Tropical Cyclone Report. Hurricane Jeanne. 13-28 September 2004. National Hurricane Center (NOAA), Miami, USA.

Lei Y. M. and J. C. Chan, 1999: Relationship between asymmetric convection and tropical cyclone motion. *23<sup>rd</sup> Conference on Hurricanes and Tropical Meteorology, American Meteorological Society*, Dallas, TX, 305-307.

LeMone, M., and E. Zipser, 1980: Cumulonimbus vertical velocity events in GATE. Part I: Diameter, intensity and mass flux. *J. Atmos. Sci.*, **37**, 2444–2457.

Leonard, B. P., 1991: The ULTIMATE conservative difference scheme applied to unsteady one-dimensional advection. *Comput. Methods Appl. Mech. Eng.*, **88**, 17-74.

Leslie, L.M., and G.J. Holland, 1995: On the bogussing of tropical cyclones in numerical models: a comparison of vortex profiles. *Meteor. and Atmos. Phys.*, **56**, 101-110.

Lin, Y.-L., R. D. Farley, and H. D. Orville, 1983: Bulk parameterization of the snow field in a cloud model. *J. Climate Appl. Meteor.*, **22**, 1065–1092.

Lin, Y. L., N. C. Witcraft and S. Y. Chen, 2002a: Modeling track deflection for tropical cyclones passing over a mesoscale mountain and its potential application to track prediction. Preprints, *25th Conference on Hurricanes and Tropical Meteorology*, American Meteorological Society, San Diego, CA

Lin, Y. L., D. B. Ensley, S. Chiao, and C. Y. Huang, 2002b: Orographic influences on rainfall and track deflection associated with the passage of a tropical cyclone. *Mon. Wea. Rev.*, **130**, 2929-2950.

Louis J. F., 1979: A parametric model of vertical eddy fluxes in the atmosphere. *Bound.-Layer Meteor.*, **17**, 187–202.

Lucas, C., E. Zipser, and M. LeMone, 1994: Vertical velocity in oceanic convection off tropical Australia. *J. Atmos. Sci.*, **51**, 3183–3193.

Lyons, W.A., M.G. Venne, P.G. Black and R.C. Gentry, 1989: Hurricane lightning: A new diagnostic tool for tropical storm forecasting ? Preprints, 18<sup>th</sup> *Conf. on Hurricanes and Tropical Meteorology, San Diego, American Meteorological Society*, 113-114.

Lyons, W.A., and C.S. Keen, 1994: Observations of lightning in convective supercells within tropical storms and hurricanes. *Mon. Wea. Rev.*, **122**, 1897-1916.

MacCaul, W.W. Jr. and M.L. Weisman, 1996: Simulations of shallow supercell storms in landfalling hurricane environments. *Mon. Wea. Rev.*, **124**, 408-429.

MacGorman, D. R., D. W. Burgess, V. Mazur, W. D. Rust, W. L. Taylor and B. C. Johnson, 1989: Lightning rates relative to tornadic storm evolution on 22 May 1981. *J. Atmos. Sci.*, **46**, 221-250.

MacGorman, D. R., Rust W. D., 1998: *The Electrical Nature of Storms*. Oxford University Press, New York, 422 pp.

Mackerras D., M. Darveniza, R. E. Orville, E. R. Williams and S. Goodman, 1998: Global lightning total, cloud and ground flash estimates. *J. Geophys. Res.*, **103**, D16, August 27, 19791-19809.

Maddox, R. A., 1980: Mesoscale convective complexes. *Bull. Amer. Meteor. Soc.*, **61**, 1374–1387.

Mansell, E. R., D. R. MacGorman, C. L. Ziegler and J. M. Straka, 2002: Simulated three-dimensional branched lightning in a numerical thunderstorm model. *J. Geophys. Res.*, **107**, No. D9, 10.1029/2000JD000244.

Mansell, E. R., D. R. MacGorman, C. L. Ziegler and J. M. Straka, 2005: Charge structure and lightning sensitivity in a simulated multicell storm. *J. Geophys. Res.*, **110**, D12101, doi:10.1029/2004JD005287.

Marshall, J. and W. Palmer (1948). The distribution of raindrops with size. *J. of Meteor.*, **5**, 165-166.

May, P. T., and D. K. Rajopadhyaya, 1996: Wind profiler observations of vertical motion and precipitation microphysics of a tropical squall line. *Mon. Wea. Rev.*, **124**, 807–815.

May, P.T. and G.J. Holland, 1999: The role of potential vorticity generation in tropical cyclone rainbands, *J. Atmos. Sci.*, **56**, 1224-1228.

McCumber, M., W.-K. Tao, and J. Simpson, 1991: Comparison of ice-phase microphysical parameterization schemes using numerical simulation of tropical convection. *J. Appl. Meteor.*, **30**, 985–1004.

McFarquhar, G. M., and A. J. Heymsfield, 1996: Microphysical characteristics of three anvils sampled during the central equatorial pacific experiment. *J. Atmos. Sci.*, **53**, 2401–2423.

McFarquhar, G., M., R.A. Black, 2004: Observations of particle size and phase in tropical cyclones: implications for mesoscale modeling of microphysical processes. *J. Atmos. Sci.*, **61**, 422-439.

McFarquhar, G., M, H. Zhang, G. Heymsfield, J. Dudhia, J. B. Halverson, R. E. Hood and F. Marks, 2004: A modeling study of the impacts of microphysical processes on the evolution of hurricane Erin 2001. Preprints, *26th Conference on Hurricanes and Tropical Meteorology, American Meteorological Society*, Miami, FL, 2 pp.

Medlin J. J. and K. G. Blackwell, 1999: A persistent supercell associated with prolonged excessive rainfall within hurricane Danny's eyewall over Mobile Bay. Preprints, *23th Conference on Hurricanes and Tropical Meteorology, American Meteorological Society*, Dallas, TX, 196-199.

Meyers, M. P., P. J. DeMott, and W. R. Cotton, 1992: New primary ice-nucleation parameterization in an explicit cloud model. *J. Appl. Meteor.*, **31**, 708-721.

Mitzeva, R. P., B. Tsenova, and C. P. R. Saunders, 2003: A modeling study of the effect of cloud supersaturation on NI charge transfer in thunderstorm electrification. *Preprints, International Conference on Atmospheric Electricity*, Versailles, France. Vol II, pp 235–239.

Molinari, J., P.K. Moore, V.P. Idone, R.W. Henderson, and A.B. Saljoughy, 1994: Cloud-to-ground lightning in Hurricane Andrew. *J. Geophys. Res.-Atmos.*, **99**, 16665-16676.

Molinari, J., P. Moore, V. Idone, April 1999: Convective structure of hurricanes as revealed by lightning locations. *Mon. Wea. Rev.*, **127**, 520 - 534.

Molinari, J., N.W.S. Demetriades, and R.L. Holle and D. Vallaro 2006: Applications of long-range lightning data to hurricane formation and intensification. *Preprints, Conf. On Meteor. Appl. of Lightning Data, American meteorological society*, Atlanta, GA, 2 pp.

Montgomery, M. T., and R. J. Kallenbach, 1997: A theory for vortex Rossby waves and its application to spiral bands and intensity changes in hurricanes. *Quart. J. Roy. Meteor. Soc.*, **123**, 435-465.

Morales C. A. and J. S. Kriz, 1997: The evolution of sferics around hurricane Lilli-1996. Preprints, *22nd Conference on Hurricanes and Tropical Meteorology*, American Meteorological Society, Ft. Collins, CO, 127-128.

Montmerle, T., J.-P. Lafore and J.-L. Redelsperger, 2000: A tropical squall line observed during TOGA COARE: Extended comparisons between simulations and Doppler radar data and the role of midlevel wind shear. *Mon. Wea. Rev.*, **128**, 3709–3730.

Neumann, C.J., 1993: "Global Overview" - Chapter 1" *Global Guide to Tropical Cyclone Forecasting*, WMO/TC-No. 560, Report No. TCP-31, World Meteorological Organization; Geneva, Switzerland.

Ngan, K. W., and J. C. L. Chan, 1995: Tropical cyclone motion—Steering vs. propagation. Preprints, *21st Conf. on Hurricane Tropical Meteorology*, Miami, FL, Amer. Meteor. Soc., 23–25.

Nielsen, K. E., R. A. Maddox, and S. V. Vasiloff, 1994: The evolution of cloud-to-ground lightning within a portion of the 10-11 June 1985 squall line. *Mon. Wea. Rev.*, **122**, 1809-1817.

Nicholls, M., 1987: A comparison of the results of a two-dimensional numerical simulation of a tropical squall line with observations. *Mon. Wea. Rev.*, **115**, 3055–3077.

Nolan, David S., and Michael T. Montgomery, 2002: From asymmetric heating to axisymmetric intensification. Preprints, *25th Conference on Hurricanes and Tropical Meteorology, American Meteorological Society, San Diego, CA, 2 pp*

Orville R. E. and J. M. Coyne, 1999: Cloud-to-ground lightning in tropical cyclones (1986-1996). Preprints, *23rd Conference on Hurricanes and Tropical Meteorology, American Meteorological Society, Dallas, TX, 194. .*

Orville, R. E., R. W. Henderson, and L. F. Bosart, 1988: Bipole patterns revealed by lightning locations in mesoscale storm systems, *Geophys. Res. Lett.*, **15**, 129–132.

Palmén, E., 1948: On the formation and structure of tropical hurricanes. *Geophysica*, **3**, 26–38.

Persing, J. and Michael T. Montgomery 2002: Comparison of hurricane intensity as realized in an axisymmetric model with MPI theory. Preprints, *25th Conference on Hurricanes and Tropical Meteorology, American Meteorological Society, San Diego, CA, 2 pp.*

Petersen, W.A., R. Cifelli, S.A. Rutledge and B.F. Smull, 1995: Cloud-to-ground lightning and the related kinematic structures of two tropical oceanic MCS's: Contrasting cases. Preprints, *Conference on Cloud Physics, American Meteorological Society, Dallas, TX.*

Petersen, Walter A., Rutledge, Steven A., Orville, Richard E. 1996: Cloud-to-ground lightning observations from TOGA COARE: selected results and lightning location algorithms. *Mon. Wea. Rev.*, **124**, 602–620.

Petersen, W. A., R. C. Cifelli , S. A. Rutledge , B. S. Ferrier , and B. F. Smull, 1999: Shipborne dual-doppler operations and observations during TOGA COARE., *Bull. Amer. Meteor. Soc.*, **80**, 81-97.

Powell, M.D., 1987: Changes in the low-level kinematic and thermodynamic structure of Hurricane Alicia (1983) at landfall. *Mon. Weather Rev.*, **115** , 75-99

Powell, M. D., 1990a: Boundary layer structure and dynamics in outer hurricane rainbands. Part I: mesoscale rainfall and kinematic structure. *Mon. Wea. Rev.*, **118**, 891-917.

Powell, M. D., 1990b: Boundary layer structure and dynamics in outer hurricane rainbands. Part II: downdraft modification and mixed layer recovery. *Mon. Wea. Rev.*, **118**, 918-938.

Pudov, V. D., 1992: The ocean's response to the cyclone's influence and its possible role in their track formations. *Proc. ICSU/WMO Int. Symp. on Tropical Cyclone Disasters*, Beijing, China, WMO, 367–376.

Reap R. M. and D. R. MacGorman, 1989: Cloud-to-ground lightning: Climatological characteristics and relationships to model fields, radar observations, and severe local storms. *Mon. Wea. Rev.*, **117**, 518-535.

Reisner, J., R. T. Brientjes, and R. M. Rasmussen, 1993: Preliminary comparisons between MM5 NCAR/Penn State model generated icing forecasts and observations, Preprints, *5th International Conference on Aviation Weather Systems*, American Meteorological Society, Vienna, VA, 65-59

Reisner, J., R. M. Rasmussen, and R. T. Brientjes, 1998: Explicit forecasting of supercooled liquid water in winter storms using the MM5 mesoscale model. *Quart. J. Roy. Meteor. Soc.*, **124**, 1071-1107.

Rodgers E., J. Weinman, H. Pierce and W. Olson, 2000: Tropical cyclone lightning distribution and its relationship to convection and intensity change. Preprints, *24th Conference on Hurricanes and Tropical Meteorology*, American Meteorological Society, Ft. Lauderdale, FL, 537-541.

Rogers, D. P., J. W. Telford, and S. K. Chai, 1985: Entrainment and the temporal development of the microphysics of convective clouds. *J. Atmos. Sci.*, **42**, 1846-1858.

Rogers, R. F., 2003: The relationship between vertical shear, storm motion, and rainfall patterns produced from numerical simulations of tropical cyclones. Preprints, *10th Conference on Mesoscale Processes, American Meteorological Society*, Portland, OR.

Rogers, R., M. Black, F. Marks, K. Valde and S. S. Chen, 2006a: A comparison of tropical cyclone hydrometeor profiles from TRMM, airborne radar, and high resolution simulations. Preprints, *27th Conference on Hurricanes and Tropical Meteorology, American Meteorological Society*, Monterey, CA. 3 pp.

Rogers, R., M. Black, P. Willis, R. Black, A. Heymsfield, A. Bansemer, and G. Heymsfield, 2006b: An evaluation of the microphysics fields of Hurricane Dennis (2005) at different stage of its lifecycle. Preprints, *27th Conference on Hurricanes and Tropical Meteorology, American Meteorological Society*, Monterey, CA, 4 pp.

Rogers, R.F., M.L. Black, S.S. Chen, and R.A. Black, 2007: An Evaluation of Microphysics Fields from Mesoscale Model Simulations of Tropical Cyclones. Part I: Comparisons with Observations. *J. Atmos. Sci.*, **64**, 1811–1834.

Rogers, R. R. and M. K. Yau, 1989: A short course in cloud physics. 3<sup>rd</sup> edition, Pergamon Press, New York, 293 pp.

Rotunno R. and K. A. Emanuel. 1987: An air–sea interaction theory for tropical cyclones. Part II: evolutionary study using a nonhydrostatic axisymmetric numerical model. *J. Atmos. Sci.*, **44**, 542–561.

Rotunno, R., J. B. Klemp, and M. L. Weisman, 1988: A theory for strong, long-lived squall lines. *J. Atmos. Sci.*, **45**, 463–485.

Rutledge, S. A., MacGorman, D. R. 1988: Cloud-to-ground lightning activity in the 10–11 June 1985 mesoscale convective system observed during the Oklahoma–Kansas PRE-STORM Project. *Mon. Wea. Rev.*, **116**, 1393–1408.

Rutledge, S.A., E.R. Williams, and T.D. Keenan, 1992: The Down Under Doppler and Electricity Experiment (DUNDEE): overview and preliminary results. *Bull. Amer. Meteor. Soc.*, **73**, 3-16.

Rutledge, S.A. and W.A. Petersen, 1994: Vertical radar reflectivity structure and cloud-to-ground lightning in the stratiform region of MCS's: Further evidence for in-situ charging in the stratiform region. *Mon. Wea. Rev.*, **122**, 1760-1776.

Samsury, C.E., and E.J. Zipser, 1995: Secondary wind maxima in hurricanes: airflow and relationship to rainbands. *Mon. Wea. Rev.*, **123**, 3502-3517.

Samsury, C.E., and R.E. Orville, 1994: Cloud-to-ground lightning in tropical cyclones: a study of hurricanes Hugo (1989) and Jerry (1989). *Mon. Wea. Rev.*, **122**, 1887-1896.

Sang N. V., and R. K. Smith, 2004: A numerical study of the effects of shallow convection on tropical cyclone intensification. Preprints, *26th Conference on Hurricanes and Tropical Meteorology, American Meteorological Society, Miami, FL*, 2 pp.

Saunders, C. P. R., L. S. Peck, G. G. Aguirre Varela, E. E. Avila and N. E. Castellano, 2001: A Laboratory study of the influence of water vapour on the charge transfer during collisions between ice crystal and graupel. *J. Atmos. Res.*, **58**, 187–203.

Saunders, C. P. R., H. Bax-Norman, and E. E. Avila, 2003: Laboratory studies of the effect of cloud conditions on charge transfer in thunderstorm electrification. *Preprints 12<sup>th</sup> International Conference on Atmospheric Electricity, Versailles, France*. Vol I, pp. 111–114.

Schubert, W. H., M. T. Montgomery, R. K. Taft, T. A. Guinn, S. R. Fulton, J. P. Kossin, and J. P. Edwards, 1999: Polygonal eyewalls, asymmetric eyecontraction, and potential vorticity mixing in hurricanes. *J. Atmos. Sci.*, **56**, 1197–1223.

Schuur, T. J., B. F. Smull, W. D. Rust and T. C. Marshall, 1991: Electrical and kinematic structure of the stratiform precipitation region trailing an Oklahoma squall line. *J. Atmos. Sci.*, **48**, 825-842.

Schuur, T. J., and S. A. Rutledge, 2000: Electrification of stratiform regions in mesoscale convective systems. Part II: Two-dimensional numerical model simulations of a symmetric MCS. *J. Atmos. Sci.*, **57**, 1983–2006.

Shapiro, L. J., 1983: The asymmetric boundary layer flow under a translating hurricane. *J. Atmos. Sci.*, **40**, 1984-1998.

Shapiro, Lloyd J., Montgomery, Michael T. 1993: A Three-dimensional balance theory for rapidly rotating vortices. *J. Atmos. Sci.*, **50**, 3322–3335.

Shapiro, L. J., and J. L. Franklin, 1999: Potential vorticity asymmetries and tropical cyclone motion. *Mon. Wea. Rev.*, **127**, 124-131.

Shay K. L., G. J. Goni and P. G. Black. 2000: Effects of a warm oceanic feature on Hurricane Opal. *Mon. Wea. Rev.*, **128**, 1366–1383.

Shelton K., 2004: Thermodynamic structure of tropical cyclones from aircraft reconnaissance. Preprints, *26th Conference on Hurricanes and Tropical Meteorology*, American Meteorological Society, Miami, FL, 2 pp.

Simpson R. H., 1974: The hurricane disaster potential scale. *Weatherwise*, **27**, 169 and 186.

Simpson, J., R.F. Adler, and G. North, 1988: A proposed Tropical Rainfall Measuring Mission (TRMM), *Bull. Amer. Meteor. Soc.*, **69**, 278-295.

Simpson, J., C. Kummerow, W.-K. Tao, and R.F. Adler, 1996: On the Tropical Rainfall Measuring Mission (TRMM). *Meteor. Atmos. Phys.*, **60**, 19-36

Simpson, J., and J. B. Halverson, 1998: Cloud physics and electrification in forming Tropical Cyclone Oliver, 1993. Preprints, *Conference on Cloud Physics, American Meteorological Society*, Everett, WA, 185-188.

Skamarock W. C. and J. B. Klemp, 1992: The stability of time-split numerical methods for the hydrostatic and the nonhydrostatic elastic equations. *Mon. Wea. Rev.*, **120**, 2109–2127.

Solorzano N. N., Jeremy N. T. and R. H. Holzworth, 2007: Studying intense tropical cyclones using the World Wide Lightning Detection Network. Preprints, *13<sup>th</sup> International Conference on Atmospheric Electricity, American Meteorological Society*, Beijing, China.

Stith, J. L., J. E. Dye, A. Bansemer, A.J. Heymsfield, C.A. Grainger, W.A. Petersen, and R. Cifelli, 2002: Microphysical Observations of Tropical Clouds. *J. Appl. Meteor.*, **41**, 97-117.

Stolzenburg, M., W. D. Rust, and T. C. Marshall, 1998: Electrical structure in thunderstorm convective regions: 3. Synthesis, **103**, 14,097-14,108

Straka, J. M. and E. R. Mansell, 2005: A bulk microphysics parameterization with multiple ice precipitation categories. *J. Appl. Meteor.*, **44**, 445–466.

Suszcynsky D. M., Jacobson A. R., Linford J., Light T. E., and A. Musfeldt, 2005: VHF lightning detection and storm tracking from GPS orbit. Preprint, *Conference on Meteorological Applications of Lightning Data, American Meteorological Society, San Diego, CA*, pp. 10.

Takahashi, T., 1978: Riming electrification as a charge generation mechanism in thunderstorms, *J. Atmos. Sci.*, **35**, 1536-1548.

Takahashi, T., 2003: Lightning and in-cloud ice phases in the East Asian Monsoon. Preprints, 12<sup>th</sup> *International Conference on Atmospheric Electricity, American Meteorological Society, Versailles, France*, 115-118.

Tao, W.-K., J. Simpson, and M. McCumber, 1989: An ice-water saturation adjustment. *Mon. Wea. Rev.*, **117**, 231-235.

Tao, W. K., and J. Simpson, 1993: Goddard Cumulus Ensemble Model. Part I: Model description. *TAO*, **4**, 35–72.

Thorpe, A. J., M. J. Miller, and M. W. Moncrieff, 1982: Two-dimensional convection in non-constant shear: A model of mid-latitude squall lines. *Quart. J. Roy. Meteor. Soc.*, **108**, 739-762.

Tremback C. J., J. Powell, W. R. Cotton and R. A. Pielke, 1987: The forward-in-time upstream advection scheme: extension to higher orders. *Mon. Wea. Rev.*, **115**, 540–555.

Trier S. B., W. C. Skamarock, M. A. LeMone, D. B. Parsons, and D. P. Jorgensen, 1996: Structure and evolution of the 22 February 1993 TOGA COARE squall line: Numerical simulations. *J. Atmos. Sci.*, **53**, 2861–2886

Trier, S.B., W.C. Skamarock, and M.A. LeMone, 1997: Structure and Evolution of the 22 February 1993 TOGA COARE Squall Line: Organization Mechanisms Inferred from Numerical Simulation. *J. Atmos. Sci.*, **54**, 386–407.

Velden, C.S., and L.M. Leslie, 1991: The basic relationship between tropical cyclone intensity and the depth of the environmental steering layer in the Australian region. *Wea. Forecasting*, **6**, 244-253.

Vigh J., 2006: Formation of the hurricane eye. Preprints, *27th Conference on Hurricanes and Tropical Meteorology*, American Meteorological Society, Monterey, CA, 16 pp.

Wang H., and W. M. Frank, 1999: Two modes of tropical cyclogenesis: An idealized simulation. Preprints, *23d Conf. on Hurricanes and Tropical Meteorology*, American Meteorological Society, Dallas, TX, 923–924.

Wang Y., and G. J. Holland, 1999: On intensity changes of landfalling tropical cyclones. Preprints, *23th Conference on Hurricanes and Tropical Meteorology*, American Meteorological Society, Dallas, TX, 493-496.

Wang P. Y., 1999: Numerical study on mesoscale structures of typhoon and orographic effects. Preprints, *23<sup>rd</sup> Conference on Hurricanes and Tropical Meteorology*, American Meteorological Society, Dallas, TX, 305-307.

Wang, Y., 2002: An explicit simulation of tropical cyclones with a triply nested movable mesh primitive equation model: TCM3. Part II: model refinements and sensitivity to cloud microphysics parameterization. *Mon. Wea. Rev.*, **130**, 3022-3036.

Wang, Y., and C. C. Wu, 2004: Current understanding of tropical cyclone structure and intensity changes-A review. *Meteor. Atmos. Phys.*, **87**, 257–278.

Weatherford, C. L., and W. M. Gray, 1988: Typhoon structure as revealed by aircraft reconnaissance. Part II: Structural variability. *Mon. Wea. Rev.*, **116**, 1044–1056.

Webster, P.J., Holland, G.J., Curry, J.A. and H.-R. Chang, 2005. Changes in tropical cyclone number, duration, and intensity in a warming environment. *Science*, **309**, 1844-1846.

Weisman, M. L., and J. B. Klemp, 1984: The structure and classification of numerically simulated convective storms in directionally varying wind shears. *Mon. Wea. Rev.*, **112**, 2479-2499.

Whitehead, J. C., 2003: One million dollars a mile? The opportunity costs of hurricane evacuation. *Ocean and Coastal Management*, **46**, 1069–1089.

Wiens, K. C., Rutledge S. A. and S. A. Tessendorf, 2005: The 29 June 2000 Supercell observed during steps. part II: lightning and charge structure. *J. Atmos. Sci.*, **62**, 4151–4177.

Williams E. R. (1989) The tripole structure of thunderstorms. *J Geophys Res* 94: 13151-13167.

Williams E. R. and S. A. Rutledge, 1990: Studies of electrification and lightning in deep tropical precipitation systems. *Conference on Cloud Physics, American Meteorological Society*, San Francisco, CA, 290-294.

Williams, E.R. and S. Stanfill, 2002: The physical origin of the land-ocean contrast in lightning activity. *Comptes Rendus—Physique*, **3**, 1277-1292, 2002.

Willis P. T. and A. J. Heymsfield, 1989: Trajectories of hydrometeors in hurricane Emily. Preprints, 16<sup>th</sup> *Conference on Hurricanes and Tropical Meteorology. American Meteorological Society*, San Diego, CA, 192-196.

Willoughby, H. E., J. A. Clos, and M. G. Shoreibah, 1982: Concentric eye walls, secondary wind maxima, and the evolution of the hurricane vortex. *J. Atmos. Sci.*, **39**, 395–411.

Willoughby, H. E., 1990a: Temporal changes of the primary circulation in tropical cyclones. *J. Atmos. Sci.*, **47**, 242–264.

Willoughby, H.E., 1990b: Gradient Balance in Tropical Cyclones. *J. Atmos. Sci.*, **47**, 265–274.

Willoughby, H.E., 1998: Tropical cyclone eye thermodynamics. *Mon. Wea. Rev.*, **126**, 3053-3067.

Witcraft, N.C., Y. L. Lin, and Y.H. Kuo, 2003. Sensitivity of tropical cyclone track, intensity, and orographic precipitation to cumulus and microphysical parameterization. Preprints, *10th Conference on Mesoscale Processes, American Meteorological Society*, Portland, OR, 94-97.

Wolff D. B., 2000: Vertical reflectivity profile and lightning characteristics of landfalling hurricane and tropical storms. Preprints, *24th Conference on Hurricanes and Tropical Meteorology, American Meteorological Society*, Ft. Lauderdale, FL, 298-297.

Wu C., K. A. Emanuel, 1993: Interaction of a baroclinic vortex with background shear: application to hurricane movement. *J. Atmos. Sci.*, **50**, 62-76.

Wu, L. and Bin Wang, 1999: Numerical study of tropical cyclones propagation in the presence of diabatic heating. Preprints, *23<sup>rd</sup> Conference on Hurricanes and Tropical Meteorology, American Meteorological Society*, Dallas, TX, 91-94.

Wu, L. and Bin Wang, 2000: A potential vorticity tendency diagnostic approach for tropical cyclone motion. *Mon. Wea. Rev.*, **128**, 1899-1911.

Xue, M., 1990: Towards the environmental condition for long-lived squall lines: vorticity versus momentum. Preprints, *16th Conference on Severe Local Storms, American Meteorological Society*, Alberta, Canada, 24-29.

Xue, M., 2000: Density current in two-layer shear flows. *Quart. J. Roy. Meteor. Soc.*, **126**, 1301-1320.

Yau M. K. and Y. Chen, 2002: Asymmetric structure of a landfalling hurricane. Preprints, *25th Conference on Hurricanes and Tropical Meteorology*, American Meteorological Society, San Diego, CA.

Zehnder J. A., 1993: The Influence of Large-Scale Topography on Barotropic Vortex Motion, *J. Atmos. Sci.*, **50**, 2519-2532.

Zehnder, J.A. and M.J. Reeder, 1997: A numerical study of barotropic vortex motion near large scale mountain ranges with application to the motion of tropical cyclones approaching the Sierra Madre. *Met.Atmos.Phys.* **64**, 1-19.

Zehr, R. M., 1992: Tropical cyclogenesis in the western North Pacific. NOAA Tech. Rep. NESDIS 61, 181 pp. [Available from U.S. Department of Commerce, NOAA/NESDIS, 5200 Auth Rd., Washington, DC 20233.].

Zhu, H. and R. K. Smith, 2002: The importance of three physical processes in a three-dimensional tropical cyclone model. *J. Atmos. Sci.*, **59**, 1825-1840.

Ziegler, C. L., D. R. MacGorman, J. E. Dye, and P. S. Ray, 1991: A model evaluation of non-inductive graupel-ice charging in the early electrification of a mountain thunderstorm. *J. Geophys. Res.*, **96**, 12833-12855.

Zipser, E. J., and M. LeMone, 1980: Cumulonimbus vertical velocity events in GATE. Part II: Synthesis and model core structure. *J. Atmos. Sci.*, **37**, 2458–2469.

Zipser, E.J., and K.R. Lutz, 1994: The Vertical Profile of Radar Reflectivity of Convective Cells: A Strong Indicator of Storm Intensity and Lightning Probability? *Mon. Wea. Rev.*, **122**, 1751–1759.

Zipser, E. J., and H. Jiang, 2003: Variability of ice and liquid precipitation contents and shape of radar reflectivity profiles in tropical cyclones. Preprints, *31st International Conference on Radar Meteorology, American Meteorology Society*, Seattle, WA, 375-379.

## IX. Nomenclature and symbols used

$\langle \rangle$  = Reynolds averaging (grid volume)

$x''$  = perturbation quantities (deviation from average in a Reynolds sense)

$\bar{x}$  = base state or mean quantities

$x'$  = perturbation quantities (deviation from mean)

$\varepsilon_{ijk}$  = Alternating (permutation) unit tensor

$\delta_{ij}$  = Kronecker Delta tensor

$C_p$  = Specific heat of air at constant pressure

$C_v$  = Specific heat of air at constant volume

$q_x$  = mixing ratio of specie x (e.g., water vapor, graupel,..etc)

$K_M$  = Eddy diffusion coefficient for momentum

$K_H$  = Eddy diffusion coefficient for scalars

$e$  = turbulent kinetic energy

$l$  = mixing length

$\theta$  = potential temperature

$p$  = pressure

$u_i$  = three dimensional wind component

$g$  = acceleration due to gravity

$\Omega$  = Earth angular momentum

$\rho$  = air density

$C_{\text{sound}}$  = phase speed of sound

$L$  = Latent heat of vaporization

$V_{Tx}$  = hydrometeor terminal fall speed

$\xi$  = vertical component of vorticity vector